

## THÈSE

Pour obtenir le grade de

## DOCTEUR DE L'UNIVERSITÉ DE GRENOBLE

Spécialité : **PHYSIQUE/NANOPHYSIQUE**

Arrêté ministériel : 7 août 2006

Présentée par

**Samuel TARDIF**

Thèse dirigée par **Dr. Joël CIBERT**

et codirigée par **Dr. Salia CHERIFI** et par **Dr. Vincent FAVRE-NICOLIN**

préparée au sein de l'**Institut Néel, CNRS-UJF**

et de l'**Institut Nanoscience et Cryogénie, CEA-GRENOBLE**

dans l'**Ecole Doctorale de Physique de Grenoble**

## **Nanocolonnes de GeMn :** propriétés magnétiques et structurales à la lumière du synchrotron

Thèse soutenue publiquement le **27 janvier 2011**,  
devant le jury composé de :

**Pr. Alain SCHUHL**

Professeur des Universités, UJF et Institut Néel (Grenoble), Président

**Pr. Mébarek ALOUANI**

Professeur des Universités, UdS et IPCMS (Strasbourg), Rapporteur

**Pr. Václav HOLÝ**

Professor Doctor, Charles University (Prague), Rapporteur

**Dr. Kevin EDMONDS**

Faculty, University of Nottingham (Nottingham), Examineur

**Dr. Joël CIBERT**

Directeur de Recherche, Institut Néel (Grenoble), Directeur de thèse

**Dr. Salia CHERIFI**

Chargée de Recherche, IPCMS (Strasbourg), Co-Directeur de thèse

**Dr. Vincent FAVRE-NICOLIN**

Maître de Conférences, UJF et CEA (Grenoble), Co-Directeur de thèse





# *Acknowledgements*

Ce travail de thèse, financé par le projet ANR GEMO, s’est déroulé au sein de deux laboratoires : d’un côté dans l’équipe MicroNanoMagnétisme du département NANOSciences de l’Institut Néel (CNRS et UJF), et de l’autre dans le laboratoire Nanostructure et Rayonnement Synchrotron du Service de Physique des Matériaux et des Microstructures de l’Institut Nanosciences et Cryogénie (CEA-Grenoble). Je souhaiterais donc exprimer mes plus vifs remerciements à mon équipe d’encadrement : Salia Cherifi et Joël Cibert au CNRS et Vincent Favre-Nicolin au CEA. Ils ont su à la fois aiguiller mes recherches tout en me laissant une large marge de manoeuvre et m’ont permis de mener de front les différents aspects de mon travail de thèse. Leur contact fut des plus enrichissant, tant sur les plans scientifiques que humains.

I would also like to express my deep gratitude to the members of my PhD jury : Pr Alain Schuhl, Pr Mébarek Alouani and Pr Václav Holý, and Dr Kevin Edmonds, who kindly accepted to be respectively president of the jury, referees of this manuscript, and examiner of the PhD defense.

Je voudrais remercier ici tous les gens avec qui j’ai eu la chance de travailler au cours de ces trois années et demi : Salia Cherifi, dont j’espère avoir appris la détermination, même lorsque l’expérience semble ne pas vouloir fonctionner et qu’il ne reste que quelques heures de temps de faisceau ; Vincent Favre-Nicolin, son enthousiasme et son efficacité, même à 4h du matin après une semaine de manip, restent un modèle pour moi ; Joël Cibert, dont la charge de direction de département n’a jamais été un obstacle à ce que sa porte me soit toujours ouverte pour la discussion. Un grand merci à tous les proches collaborateurs, permanents, post-doctorants et doctorants : Thibaut Devillers, qui a défriché le terrain et posé de nombreuses bases dans l’étude du système ; Matthieu Jamet, avec qui les échanges, notamment sur le magnétisme dans les nanocolonnes, ont toujours été très constructifs ; André Barski, Clément Porret et Abi Jain, dont j’ai pu profiter des échantillons et du soutien lors des expériences de diffraction ; Pascale Bayle-Guillemaud et Cédric Prestat, dont les clichés de microscopie électronique en transmission ont été déterminants dans l’étude structurale par rayonnement synchrotron des nanocolonnes ; Emmanuel Arras, Pascal Pochet et Frédéric Lançon, dont les calculs *ab initio* ont permis à la fois de définir des structures théoriques

possible dans les nanocolonnes et dans la matrice de germanium environnante ; El-Kébir Hlil, Yves Joly et Oana Buneau, qui m'ont introduit aux calculs de structures électroniques et de spectres d'absorption de rayons X, ainsi qu'Andrey Titov, avec qui nous avons pu aller le plus loin possible avec ces mêmes calculs et les structures théoriques précédemment proposées ; Francesco d'Acapito et Mauro Rovezzi, dont la complémentarité de la technique EXAFS a permis de projeter un autre éclairage sur la structure des nanocolonnes ; Ing-Song Yu, dont les travaux sur le transport dans les nanocolonnes permettent de compléter la vue d'ensemble. Je n'oublierais pas non plus le personnel des différentes lignes de lumières utilisées : D2AM, BM32, ID01, ID11 et ID31 à l'ESRF, ainsi que UE46 et UE56 à Bessy. Il est difficile d'exprimer en quelques mots tous les apports, scientifiques et humains, de toutes ces collaborateurs, qu'ils en soit néanmoins profondément remerciées. De la même manière, je remercie tous ceux qui, sans intervenir directement dans mon sujet de thèse, ont interagi avec moi au cours de mon séjour au laboratoire et en particulier toute l'équipe MNM ainsi que les différents occupants du bâtiment K. Un grand merci à tous ceux qui ont fait que mon travail au laboratoire a pu se dérouler dans les meilleures conditions, tant d'un point de vue technique (l'équipe de Nanofab et Jean-François Jacquot au CEA) qu'administratif (Sabine Gadale, Marielle Lardato, Louise Infuso et Véronique Fauvel). Merci aussi à toutes les personnes dont j'ai partagé le bureau au cours de mon séjour : Rodrigo Della Noce, Frank Balestro et Laurent Cagnon. Je remercie par ailleurs tous les thésards et post-docs des différents départements, tant au CNRS qu'au CEA, avec qui j'ai pu interagir au cours de cette thèse pour l'atmosphère qu'ils ont su créer au laboratoire. J'aurais une pensée particulière pour grand Micka et nos discussions animées lors de nos retours tardifs du labo à vélo.

Enfin, je voudrais remercier tous ceux qui m'ont soutenu au cours de ce travail de thèse, en particulier Arnaud et Julie pour m'avoir offert à multiple reprise le couvert lors de la phase critique de la rédaction du manuscrit ; Hugo et Géraldine, pour m'avoir offert de nombreux bols d'air à la montagne ou à Agricola ; mes compatriotes exilés de la Réunion au bastion de la rue des Eaux Claires, merci zot toute ! J'aurais une pensée également pour Pêche qui a assisté à l'intégralité de la rédaction du manuscrit, avec même une certaine insistance à l'heure de remplir sa gamelle. Last but not least, je voudrais remercier ma famille, et en particulier mes parents, pour leur soutien et leurs encouragements ; ainsi que celle qui a partagé avec moi tous les hauts et les bas de cette thèse et m'a toujours supporté et soutenu : merci à toi Bilkisse. Cette thèse vous est dédiée.







# Table des matières

<b>Acknowledgements</b>	<b>ii</b>
<b>Contents</b>	<b>vi</b>
<b>List of Figures</b>	<b>xii</b>
<b>List of Tables</b>	<b>xvi</b>
<b>General Introduction</b>	<b>2</b>
<b>Introduction Générale</b>	<b>4</b>
<b>1 Spintronics, Magnetic Semiconductors, and GeMn nanocolumns</b>	<b>8</b>
1.1 Spintronics : applications and the spin-injection issue . . . . .	9
1.1.1 Giant MagnetoResistance . . . . .	9
1.1.2 Tunnel MagnetoResistance . . . . .	10
1.1.3 The Spin Transistor . . . . .	10
1.1.4 Spin-injection : current issues and possible solutions . . . . .	11
1.1.5 A new class of materials : the Ferromagnetic Semiconductors	12
1.1.5.1 Concentrated Magnetic Semiconductors . . . . .	12
1.1.5.2 Diluted Magnetic Semiconductors . . . . .	13
1.1.5.3 Heterogeneous Magnetic Semiconductors . . . . .	14
1.2 The (Ge,Mn) system : state of the art . . . . .	14
1.2.1 The Ge :Mn binary phase diagram . . . . .	15
1.2.2 Theoretical studies of the GeMn system . . . . .	15
1.2.3 Experimental studies of the GeMn system . . . . .	18
1.2.3.1 GeMn as a DMS . . . . .	18
1.2.3.2 GeMn as a heterogeneous semiconductor contain- ing stable intermetallic precipitates . . . . .	21
1.2.3.3 GeMn as a heterogeneous semiconductor contain- ing containing metastable phases . . . . .	22
1.2.3.4 GeMn in nanostructures . . . . .	23
1.2.3.5 Quick summary . . . . .	25
1.3 The GeMn nanocolumns . . . . .	25
1.3.1 An out-of-equilibrium growth mode . . . . .	26
1.3.2 GeMn nanocolumns : a family picture . . . . .	28

1.3.3	Intriguing magnetic properties of the GeMn nanocolumns . .	33
1.3.4	What is left to be known about the nanocolumns? . . . . .	34
1.4	Conclusion . . . . .	36
1.5	Résumé du chapitre 1 . . . . .	37
<b>2</b>	<b>X-ray scattering</b>	<b>38</b>
2.1	X-ray scattering in matter . . . . .	38
2.1.1	Elastic scattering by a free electron . . . . .	39
2.1.2	Elastic scattering by a cloud of electrons . . . . .	39
2.1.3	The complex atomic scattering factor . . . . .	40
2.1.4	The atomic scattering factor in a crystal and the Kramers-Kronig relations . . . . .	43
2.2	X-ray scattering and diffraction by a crystal . . . . .	44
2.2.1	The structure factor . . . . .	44
2.2.2	The reciprocal lattice . . . . .	45
2.2.3	The form factor . . . . .	45
2.2.4	Extinction rules . . . . .	46
2.2.5	Bragg's law . . . . .	47
2.2.6	Ewald's sphere . . . . .	47
2.3	Grazing-incidence x-ray scattering . . . . .	48
2.3.1	The total reflection condition and the critical angle . . . . .	49
2.3.2	Scattering depth . . . . .	51
2.4	Diffuse x-ray scattering from defects . . . . .	52
2.4.1	Diffuse scattering <i>vs</i> diffraction . . . . .	52
2.4.2	Quick overview of the available literature on diffuse scattering	53
2.4.3	Huang diffuse scattering . . . . .	53
2.5	Experimental setups . . . . .	54
2.5.1	Synchrotron experimental setups . . . . .	54
2.5.1.1	The ID01 beamline . . . . .	55
2.5.1.2	The BM32 beamline . . . . .	56
2.5.1.3	The D2AM beamline . . . . .	58
2.5.2	Detectors . . . . .	58
2.5.3	Measurement procedure : grazing incidence reciprocal space maps . . . . .	63
2.5.4	Data processing . . . . .	64
2.6	Conclusion . . . . .	65
2.7	Résumé du chapitre 2 . . . . .	66
<b>3</b>	<b>X-ray absorption spectroscopy and magnetic circular dichroism</b>	<b>68</b>
3.1	Theoretical aspects . . . . .	68
3.1.1	Quantum description of the x-ray absorption : Fermi's Golden Rule and the dipole approximation . . . . .	69
3.1.2	X-ray absorption cross-section . . . . .	71
3.1.3	Interaction matrix elements in terms of spherical harmonics and the dipole selection rules . . . . .	71

3.1.4	X-ray magnetic circular dichroism : a semi-relativistic approach . . . . .	72
3.1.5	The XMCD sum rules . . . . .	74
3.1.5.1	The orbital moment sum rule . . . . .	75
3.1.5.2	The spin moment sum rule . . . . .	77
3.1.5.3	The orbital to spin ratio sum rule . . . . .	77
3.2	X-ray absorption spectroscopy : Experimental considerations . . . .	78
3.2.1	How to measure x-ray absorption . . . . .	78
3.2.1.1	The transmission mode . . . . .	79
3.2.1.2	The fluorescence yield mode . . . . .	79
3.2.1.3	The total electron yield mode . . . . .	81
3.2.2	Synchrotron experimental setups . . . . .	82
3.2.2.1	A XAS-XMCD beamline : UE46-PGM1 at the Helmholtz Centre Berlin . . . . .	83
3.2.2.2	Experimental setups and data acquisition . . . . .	85
3.3	Conclusion . . . . .	86
3.4	Résumé du chapitre 3 . . . . .	87
<b>4</b>	<b>Structural analysis of the GeMn system by x-ray scattering and diffraction</b>	<b>88</b>
4.1	Study of the atomic structure in the GeMn nanocolumns . . . . .	89
4.1.1	X-ray scattering by the GeMn nanocolumns : a grazing incidence study . . . . .	89
4.1.1.1	Methodology . . . . .	90
4.1.1.2	Dense and small nanocolumns (low growth temperature) . . . . .	91
4.1.1.3	Very large amorphous nanocolumns (medium to high growth temperature and large Mn concentration) . . . . .	93
4.1.1.4	Ge <sub>3</sub> Mn <sub>5</sub> clusters (high growth temperature or annealing) . . . . .	95
4.1.1.5	Medium-to-large-sized nanocolumns (medium-range growth temperatures and Mn concentrations) . . . .	97
4.1.1.6	GeMn on GaAs substrates . . . . .	100
4.1.2	Enhancing the GISAXS sensitivity : the Bragg-GISAXS technique . . . . .	102
4.1.3	Chemical contrast and anomalous scattering . . . . .	103
4.2	Strain in the Germanium matrix . . . . .	105
4.2.1	First approach : a simple analytical model . . . . .	105
4.2.1.1	Expression of the scattered intensity . . . . .	105
4.2.1.2	Scattering from a single nanocolumn . . . . .	107
4.2.1.3	Positional correlations term . . . . .	108
4.2.1.4	Calculated X-ray scattering from the analytical model . . . . .	110
4.2.2	Simulation of the strain using an atomistic model . . . . .	111

4.2.2.1	The atomistic model . . . . .	112
4.2.2.2	Calculated X-ray scattering from the atomistic model	113
4.2.2.3	Quantitative analysis of the strain in the Ge matrix	116
4.2.2.4	Oxidation-induced strain relaxation . . . . .	116
4.3	Conclusion . . . . .	122
4.4	Résumé du chapitre 4 . . . . .	124
<b>5</b>	<b>Magnetic and electronic properties of the GeMn nanocolumns : experiment and theory</b>	<b>126</b>
5.1	Probing magnetism in the GeMn nanocolumns by XAS-XMCD . .	126
5.1.1	Magnetic semiconductors probed by XAS-XMCD . . . . .	126
5.1.2	A metallic-like absorption spectrum . . . . .	128
5.1.3	Towards a quantitative analysis : validity of the sum rules and experimental considerations . . . . .	133
5.1.4	Magnetic (an)isotropy in the GeMn nanocolumns . . . . .	135
5.1.5	Surface <i>vs</i> bulk measurement : comparison between XMCD and SQUID . . . . .	140
5.1.6	Temperature dependence of the XAS-XMCD spectra . . . .	142
5.1.7	Which manganese atoms are being measured ? . . . . .	145
5.2	Influence of the surface oxide . . . . .	146
5.2.1	Evidencing the surface oxide . . . . .	146
5.2.2	Probing the oxide/GeMn layer interface . . . . .	148
5.2.3	Oxide and exchange bias in the nanocolumns . . . . .	149
5.3	Conclusion about the experimental XAS-XMCD analysis in the GeMn nanocolumns . . . . .	150
5.4	Calculation of the XAS-XMCD spectra . . . . .	152
5.4.1	Calculation of the spectra . . . . .	153
5.4.2	The Ge <sub>3</sub> Mn <sub>5</sub> structure : a benchmark . . . . .	153
5.4.2.1	Structural and magnetic properties of the Ge <sub>3</sub> Mn <sub>5</sub> phase . . . . .	153
5.4.2.2	Calculation details . . . . .	154
5.4.2.3	Total and Mn-projected densities of states . . . . .	155
5.4.2.4	Absorption spectra : experiment <i>vs</i> theory . . . . .	156
5.4.2.5	Quantitative analysis of the magnetic moments . .	159
5.4.2.6	Conclusion . . . . .	160
5.4.3	Simple defects . . . . .	161
5.4.3.1	Structural properties of the Ge crystalline phase with simple defects . . . . .	161
5.4.3.2	Calculation details . . . . .	162
5.4.3.3	Total and Mn-projected densities of states . . . . .	163
5.4.3.4	Absorption spectra : experiment <i>vs</i> theory . . . . .	164
5.4.3.5	Quantitative analysis of the magnetic moments . .	167
5.4.3.6	Conclusion . . . . .	168
5.4.4	Crystalline phases . . . . .	169
5.4.4.1	Structural properties of the GeMn crystalline phases	170

5.4.4.2	Calculation details for the GeMn crystalline phases	173
5.4.4.3	Total and Mn-projected densities of states . . . . .	173
5.4.4.4	Absorption spectra and magnetic moment in the Hex2 and C16 structures . . . . .	175
5.4.4.5	Particularities of the calculation for the $\alpha$ phase . .	177
5.4.4.6	Conclusion . . . . .	184
5.4.5	Systematic error in the sum rules . . . . .	185
5.4.6	Conclusion of the theoretical XAS-XMCD analysis and how to obtain further insights . . . . .	187
5.5	Résumé du chapitre 5 . . . . .	190
<b>General Conclusion and Outlook</b>		<b>194</b>
	General Conclusion . . . . .	194
	Short summary . . . . .	197
	Outlook . . . . .	197
<b>Conclusion Générale et Perspectives</b>		<b>200</b>
<b>A Synchrotron radiation : generalities</b>		<b>202</b>
<b>B Exchange bias in GeMn nanocolumns : The role of surface oxida- tion</b>		<b>204</b>
<b>Bibliographie</b>		<b>208</b>
<b>Abstract</b>		<b>237</b>





# Table des figures

1.1	The GMR effect . . . . .	10
1.2	The SPINFET device . . . . .	11
1.3	The Ge :Mn binary phase diagram . . . . .	16
1.4	Different types of nanocolumns obtained in different groups . . . . .	24
1.5	Schematic view of the low temperature MBE setup . . . . .	27
1.6	Different types of nanocolumns obtained in different groups . . . . .	29
1.7	Morphological characteristics of the GeMn nanocolumns as a function of the growth parameters . . . . .	30
1.8	High-resolution TEM and filtered image of the nanocolumns . . . . .	31
1.9	Cluster formation in the nanocolumns . . . . .	33
1.10	SQUID magnetometry in the GeMn nanocolumns . . . . .	35
2.1	Scattering geometry . . . . .	39
2.2	Scattering geometry with two scatterers . . . . .	40
2.3	Atomic scattering factors $f_0$ for Mn and Ge . . . . .	41
2.4	Real and imaginary parts of the atomic scattering factors for Mn and Ge . . . . .	42
2.5	Experimental and tabulated $f'$ and $f''$ around the Mn K edge . . . . .	44
2.6	Bragg' law . . . . .	47
2.7	Ewald's sphere . . . . .	48
2.8	Snell-Descartes law of refraction, total reflection and evanescent wave . . . . .	50
2.9	The ID01 beamline . . . . .	57
2.10	The BM32 beamline . . . . .	59
2.11	The D2AM-BM02 beamline . . . . .	60
2.12	PSD detector in grazing incidence . . . . .	62
2.13	2-D detectors . . . . .	62
2.14	Radial and angular scans . . . . .	64
2.15	$q_r$ , $q_a$ and $q_z$ . . . . .	65
3.3	Principle of transmission XAS measurement . . . . .	80
3.4	Principle of fluorescence yield XAS measurement . . . . .	81
3.5	Principle of total electron yield XAS measurement . . . . .	82
3.6	UE46-PGM1 beamline at the Helmholtz Centre Berlin . . . . .	83
3.7	APPLE II undulator . . . . .	84
3.8	XAS-XMCD measurement geometry . . . . .	86

4.1	RSM and TEM in small and dense GeMn nanocolumns . . . . .	92
4.2	RSM and TEM in very large amorphous GeMn nanocolumns . . . . .	94
4.3	RSM in a sample containing $\text{Ge}_3\text{Mn}_5$ clusters . . . . .	96
4.4	RSM and TEM in medium-sized GeMn nanocolumns . . . . .	98
4.5	RSM and TEM in large GeMn nanocolumns . . . . .	99
4.6	RSM in GeMn nanocolumns grown on GaAs . . . . .	101
4.7	Bragg-GISAXS in GM173 . . . . .	103
4.8	Surface roughness and nanocolumns positions correlations . . . . .	104
4.9	Anomalous scattering in GeMn nanocolumns . . . . .	106
4.10	Mechanical anisotropy in Ge . . . . .	108
4.11	Correlations in the positions of the nanocolumns . . . . .	109
4.12	Analytical model of the strain in the Ge matrix . . . . .	110
4.13	Atomic structure of the amorphous nanocolumns and of the matrix in the atomistic simulations . . . . .	113
4.14	Atomic structure of the amorphous nanocolumns and of the matrix in the atomistic simulations . . . . .	114
4.15	Simulation of the strain in the Ge matrix using an atomistic model	114
4.16	Calculated RSM (1%) . . . . .	117
4.17	Calculated RSM (4%) . . . . .	118
4.18	Calculated RSM (amorphous) . . . . .	119
4.19	Calculated RSM ( $\alpha$ ) . . . . .	120
4.20	Intensity profile around the 220 Bragg peak . . . . .	121
4.21	3D RSM around the 111 Bragg peak . . . . .	123
5.1	XAS-XMCD in (Ga,Mn)As . . . . .	127
5.2	TEM micrographs of a typical sample for the XAS-XMCD study . .	129
5.3	XAS-XMCD in the GeMn nanocolumns . . . . .	130
5.4	Comparison of the XAS in the GeMn nanocolumns and in Mn metal	131
5.5	Shirley background correction of the XAS . . . . .	132
5.6	Fit of the XAS in the GeMn nanocolumns using similar $L_3$ and $L_2$ absorption edges. . . . .	133
5.7	Comparison of the XAS-XMCD in the GeMn nanocolumns and in $\text{Ge}_3\text{Mn}_5$ . . . . .	134
5.8	Magnetization <i>vs</i> temperature for different GeMn systems . . . . .	135
5.9	XAS-XMCD in GeMn samples by Ahlers <i>et al.</i> . . . . .	136
5.10	XAS and XMCD spectra measured at different incidence angles . .	137
5.11	Orbital and spin magnetic moment <i>vs</i> incidence angle . . . . .	138
5.12	Corrected orbital and spin magnetic moment <i>vs</i> incidence angle . .	139
5.13	Magnetization curves measured by SQUID and XMCD . . . . .	141
5.14	XAS spectra as a function of temperature . . . . .	142
5.15	Amplitude of the XAS at the $L_3$ and $L_2$ absorption edge and BR as a function of temperature . . . . .	143
5.16	Normalized XMCD spectra <i>vs</i> temperature . . . . .	144
5.17	XMCD <i>vs</i> temperature . . . . .	144
5.18	Corrected XMCD <i>vs</i> temperature . . . . .	145

5.19	Influence of surface oxidation on the XAS-XMCD spectra . . . . .	147
5.20	XAS in Mn oxides . . . . .	148
5.21	SQUID <i>vs</i> XMCD magnetization curves for an oxidized sample . . .	149
5.22	XMCD in a partially oxidized sample . . . . .	150
5.23	Ferromagnetic and paramagnetic components in a partially oxidized sample . . . . .	151
5.24	the $\text{Ge}_3\text{Mn}_5$ unit cell . . . . .	154
5.25	DOS and PDOS in $\text{Ge}_3\text{Mn}_5$ . . . . .	156
5.26	Integrated DOS in $\text{Ge}_3\text{Mn}_5$ . . . . .	157
5.27	XAS-XMCD for each individual core level in $\text{Mn}_1$ in $\text{Ge}_3\text{Mn}_5$ . . .	158
5.28	Comparison between experimental and theoretical XAS-XMCD spec- tra in $\text{Ge}_3\text{Mn}_5$ . . . . .	159
5.29	$\text{Mn}_S$ and $\text{Mn}_T$ unit cells . . . . .	162
5.30	DOS and integrated DOS in $\text{Mn}_T$ . . . . .	164
5.31	DOS and integrated DOS in $\text{Mn}_S$ . . . . .	165
5.32	Comparison between experimental and theoretical XAS-XMCD spec- tra in $\text{Mn}_T$ . . . . .	166
5.33	Comparison between experimental and theoretical XAS-XMCD spec- tra in $\text{Mn}_S$ . . . . .	167
5.34	Hex2, C16 and $\alpha$ unit cell . . . . .	170
5.35	Contruction of the $\alpha$ structure . . . . .	171
5.36	DOS and integrated DOS for the Hex2, the C16 and the $\alpha$ crystal- line phases . . . . .	174
5.37	Comparison between experimental and theoretical XAS-XMCD spec- tra in the Hex2 crystalline structure . . . . .	176
5.38	Comparison between experimental and theoretical XAS-XMCD spec- tra in the C16 crystalline structure . . . . .	177
5.40	Mn $2p_{3/2}$ core-level splitting (between $ \frac{3}{2}, +\frac{3}{2}\rangle$ and $ \frac{3}{2}, -\frac{3}{2}\rangle$ ) as a function of the SPRKKR calculated magnetic moment for different structures . . . . .	180
5.41	Simple picture of the core-level shifting procedure . . . . .	181
5.42	XAS-XMCD for each individual core level in the $\alpha$ crystalline phase	182
5.43	Calculated XAS and XMCD spectra for the $\alpha$ phase for different values of the additional splitting in the $2p$ core states . . . . .	183
5.44	Calculated XAS and XMCD spectra for the interstitial Mn for dif- ferent values of the additional splitting in the $2p$ core states . . . .	184
5.45	Calculated XAS and XMCD spectra for the substitutional Mn for different values of the additional splitting . . . . .	185
5.46	Experimental and calculated XAS-XMCD spectra in the $\alpha$ phase for different values of the additional splitting in the $2p$ core states .	186
5.47	Effective spin magnetic moment extracted from the sum rules ap- plied to the calculated spectra <i>vs</i> the corresponding expectation value of the spin magnetic moment calculated <i>ab initio</i> . . . . .	188
5.48	Experimental and calculated XAS-XMCD spectra for a faulted $\alpha$ phase . . . . .	191

A.1	Layout of the ESRF . . . . .	203
-----	------------------------------	-----

# Liste des tableaux

2.1	CCD <i>vs</i> Pixel detectors . . . . .	61
3.1	Dipole selection rules : conditions on the allowed transitions in the dipole approximation . . . . .	72
3.2	Transition probabilities from the spin-orbit split $2p$ states to the final $3d$ states having $\downarrow$ spin for right (left) circular polarized light. .	74
4.1	Samples studied by grazing incidence x-ray scattering . . . . .	90
5.1	Characteristics of the samples studied in XAS-XMCD . . . . .	128
5.2	Structural parameters of the $\text{Ge}_3\text{Mn}_5$ crystalline phase . . . . .	154
5.3	Calculated and measured magnetic moments in $\text{Ge}_3\text{Mn}_5$ . . . . .	160
5.4	Structural parameters of the Ge diamond crystalline phase with simple defects . . . . .	163
5.5	Calculated magnetic moments for the Mn interstitial and substitutional defect in germanium . . . . .	168
5.6	Structural parameters of the Hex2, the C16 and the $\alpha$ crystalline phases . . . . .	172
5.7	Parameters used for the calculation of the Hex2, the C16 and the $\alpha$ crystalline phases . . . . .	173
5.8	Number of $3d$ holes for the Hex2, the C16 and the $\alpha$ crystalline phases	173
5.9	Magnetic moments in the Hex2, C16 and $\alpha$ crystalline phases . . .	178



# General Introduction

Classically, electronic devices make use of the charge of the electrons to process information using electric fields, and of the spin of the electrons to store information using magnetic fields. Spintronics, an emerging field of electronics, aims at bridging the gap between the two technologies by using both spins and charges within the same devices. The perspective of faster and smaller devices is even more interesting when seen as a way to circumvent the predicted upcoming limit in Moore's law.

The importance of spintronics today has been illustrated by the 2007 Nobel prize in physics, awarded to Albert Fert and Peter Grünberg for their discovery of the *Giant MagnetoResistance* (GMR) in the late 80's. Up to now, the most important application of the GMR is the spin-valve device. It is widely used in hard disk drive readheads and has allowed for a tremendous increase in data storage capacity, from tens of megabytes in the mid 80's to a few terabytes nowadays in a typical hard disk drive. New devices, such as the non-volatile *Magnetic Random Access Memory*, are expected to be as widely used in a very near future.

Spintronics requires a strong interplay between electric and magnetic properties and therefore new materials have to be considered and even designed. A possible solution that is widely studied is the relatively new family of *ferromagnetic semiconductors* (FMS). In particular FMS based on group IV semiconductors would be compatible with the existing Si-based technology, and therefore they appear as very promising. A modern approach is to consider not only semiconductors where the magnetic impurities have been diluted in the semiconducting host, but also heterogeneous materials where the local concentration in magnetic impurities may greatly vary. The (Ge,Mn) system is one of such systems in which inhomogeneities can be in the form of self-assembled nanostructures (nanocolumns). Self-assembly is particularly interesting in view of possible future bottom-up processes.

The study of nanostructures is now greatly aided by the recent development of synchrotron radiation-based techniques. The intense light produced at synchrotron radiation facilities can be used as a versatile tool to probe electronic, magnetic or structural properties of nano-sized materials. The potential of synchrotron techniques is further illustrated by the recent widespread development of new synchrotron radiation facilities, especially in Europe.

The work presented in this manuscript is mostly based on different synchrotron techniques. It aims at characterizing the magnetic and structural properties of GeMn nanocolumns with an additional theoretical effort to support interpretation. The manuscript is organized in five chapters, described hereafter :

- The first chapter is a broad introduction to spintronics and its applications. It presents an overview of the different types of ferromagnetic semiconductors and a more specific review of the results in the (Ge,Mn) system. The GeMn nanocolumns system is introduced.
- The second chapter presents the different x-ray scattering techniques used, both from a theoretical and experimental point-of-view. Grazing incidence is shown to be a method of choice.
- Similarly, the third chapter presents the x-ray absorption spectroscopy technique and the x-ray magnetic circular dichroism technique. Both theoretical and experimental aspects are described.
- The fourth chapter summarizes the different results obtained by x-ray scattering in different types of nanocolumns. The aim is to find a possible crystalline structure in the nanocolumns, to characterize their morphological parameters and to study the strain in the Ge matrix.
- The fifth chapter contains a detailed analysis of the magnetic properties of the GeMn nanocolumns using experimental XAS-XMCD results. Additional results from a theoretical XAS-XMCD study are also presented and used to provide insights about the local nanostructure in the nanocolumns.



# Introduction Générale

Les dispositifs électroniques classiques se basent d'une part sur la charge de l'électron pour traiter l'information en utilisant des champs électriques et d'autre part sur le spin des électrons pour stocker l'information en utilisant des champs magnétiques. La spintronique, un domaine émergent de l'électronique, cherche à relier ces deux technologies en utilisant à la fois spins et charges au sein des mêmes dispositifs. Une telle approche pourrait permettre des dispositifs plus petits et plus rapides, tout en offrant une alternative à l'approche de la limite prévue de la loi de Moore.

L'importance actuelle de la spintronique a récemment été illustrée par le prix Nobel de Physique en 2007, décerné conjointement à Albert Fert et Peter Grünberg pour leur découverte simultanée et indépendante de la *MagnétoResistance Géante* (GMR) à la fin des années 80. Jusqu'à maintenant, l'application la plus répandue de la GMR est le dispositif de valve de spin. Celui-ci est couramment utilisé dans les têtes de lecture de disques durs et a permis un fort accroissement de la capacité de stockage de l'information, depuis quelques dizaines de mégaoctets au milieu des années 80 jusqu'à quelque téraoctets de nos jours dans un disque dur typique. On s'attend dans un avenir proche à ce que de nouveaux dispositifs soient largement utilisés, tels que les mémoires magnétiques à accès aléatoire (MRAM) non-volatiles.

La spintronique requiert un fort couplage des propriétés électriques et magnétique, de sorte que de nouveaux matériaux doivent être envisagés, voire même fabriqués. Une solution possible et très largement étudiée, repose sur la famille relativement nouvelle des semi-conducteurs ferro-magnétiques (FMS). En particulier, les FMS basés sur des semi-conducteurs de type IV sont compatible avec la technologie actuelle à base de silicium et donc semblent particulièrement prometteurs. Une approche récente consiste à ne pas considérer seulement des matériaux semi-conducteurs dans lesquels les impuretés magnétiques auraient été diluées, mais plutôt des matériaux hétérogènes dans lesquels la concentration locale en

impuretés magnétiques peut varier grandement. Le système (Ge,Mn) est ainsi considéré dans cette approche car les inhomogénéités y prennent la forme de nanostructures auto-assemblées (nanocolonnes), l'auto-assemblage étant par ailleurs particulièrement intéressant du point de vue de process de fabrication de type *bottom up*.

L'étude de nanostructures bénéficie grandement du développement récent des techniques utilisant le rayonnement synchrotron. La lumière intense produite dans une source de rayonnement synchrotron peut être utilisée comme un outil multifonctions pour sonder les propriétés électroniques, magnétiques et structurales de matériaux de taille nanométrique. Le potentiel des techniques synchrotron est d'autant plus illustré par le récent développement global de nouvelles sources de lumière, en particulier en Europe.

Le travail présenté dans ce manuscrit est principalement basé sur différentes techniques synchrotron. L'objectif est la caractérisation des propriétés électroniques, magnétiques et structurales des nanocolonnes de GeMn, avec un effort théorique supplémentaire afin d'aider à l'interprétation. Le manuscrit est organisé en cinq chapitres, décrits ci-après :

- Le premier chapitre est une introduction générale à la spintronique et à ses applications. Une vue d'ensemble des différents types de semi-conducteurs ferromagnétique est présentée, ainsi qu'une revue plus spécifique des connaissances sur le système (Ge,Mn). Enfin, le système étudié, les nanocolonnes de GeMn, est introduit.
- Le second chapitre présente les différentes méthodes de diffusion de rayons X utilisées, à la fois d'un point de vue expérimental et théorique. On montre que la géométrie d'incidence rasante est particulièrement adaptée à l'étude des nanocolonnes de GeMn.
- De façon similaire, le troisième chapitre présente les techniques de spectroscopie d'absorption de rayons X et de dichroïsme magnétique circulaire de rayons X. Les aspects théoriques et expérimentaux sont discutés.
- Le quatrième chapitre résume les différents résultats obtenus par l'étude de la diffusion de rayons X par différents types de nanocolonnes de GeMn. L'objectif est de déterminer la possible structure cristalline des nanocolonnes, de caractériser leurs paramètres morphologiques et enfin d'étudier la déformation induite dans la matrice de Ge.

- 
- Le cinquième chapitre est dédié à l'analyse détaillée des propriétés magnétiques des nanocolonnes de GeMn à partir de résultats XAS-XMCD expérimentaux. Les résultats additionnels provenant d'une étude théorique sont aussi présentés et discutés dans le cadre de la nanostructure locale dans les nanocolonnes.



# Chapitre 1

## Spintronics, Magnetic Semiconductors, and GeMn nanocolumns

The broad context of this PhD thesis is the study of a spintronic-related material. Spintronics is a relatively recent field of study in condensed matter. It takes advantage of the coupling of magnetic (spin) and electronic (charge) properties of the electrons in the same material. As such, it offers a broad range of new applications, some of which are already widely used (*e.g.*, in today's hard disk drive read head). Hence, new materials have to be designed to fulfill the requirement of spintronics, such as, *e.g.*, an efficient spin injection in a semiconductor. This has led to the development of a new class of materials, described as *ferromagnetic semiconductors* (FMS). Different types of FMS have been studied over the last decade or so, yet reaching ordering temperature above room temperature (RT) is still an issue. Heterogeneous materials, obtained using out-of-equilibrium growth techniques, appear as a promising solution. In particular, Curie temperatures above RT have been reported in GeMn nanocolumns.

In this chapter, I will first give a quick overview of the current issues in spintronics, followed by the possible studied solutions. Ferromagnetic Semiconductors are introduced and current achievements in the (Ge,Mn) system are described. A particular emphasis is put on GeMn nanocolumns, which will be the system studied in this thesis. The out-of-equilibrium growth technique as well as previous structural and magnetic results are also recalled.

## 1.1 Spintronics : applications and the spin-injection issue

Current solid-state electronics is based on only one intrinsic property of the electron : its charge. Spintronics, a short for *spin electronics*, aims at introducing an additional degree of freedom by using the electron spin as well. Spin manipulation of electrons offers new possibilities in devices design, bridging the gap between information processing (electronics) and information storage (magnetism).

The main applications of spintronics are the Giant MagnetoResistance (GMR) and the Tunnel MagnetoResistance (TMR) effects, which have led to tremendous advances in spintronic device design. Both effects are described hereafter, along with the proposed *SPINFET* transistor device, which also introduces the problem of spin injection in a semiconductor.

### 1.1.1 Giant MagnetoResistance

GMR was simultaneously and independently discovered by Fert *et al.* [1] and Grünberg *et al.* [2] in 1988 and was worth the 2007 Physics Nobel for both of them. The GMR is observed in stacks of metallic materials, alternatively magnetic and non-magnetic, as illustrated in figure 1.1. Depending on the relative orientations of the magnetization in the two magnetic layers, the transverse resistance can be tuned. This is due to the inequivalency of the spins up and spin down densities of states near the Fermi level in the ferromagnetic materials. A widespread application of this phenomenon is the spin-valve device used in the hard disk drive (HDD) read heads [3]. Such a device consists in the simplest stack (two magnetic layer separated by a non-magnetic layer) : one of the magnetic layer can be switched in either way by the magnetic domains in the plates of the HDD and the corresponding switching of resistance is read. This device has allowed for a large increase of the memory density in HDDs.

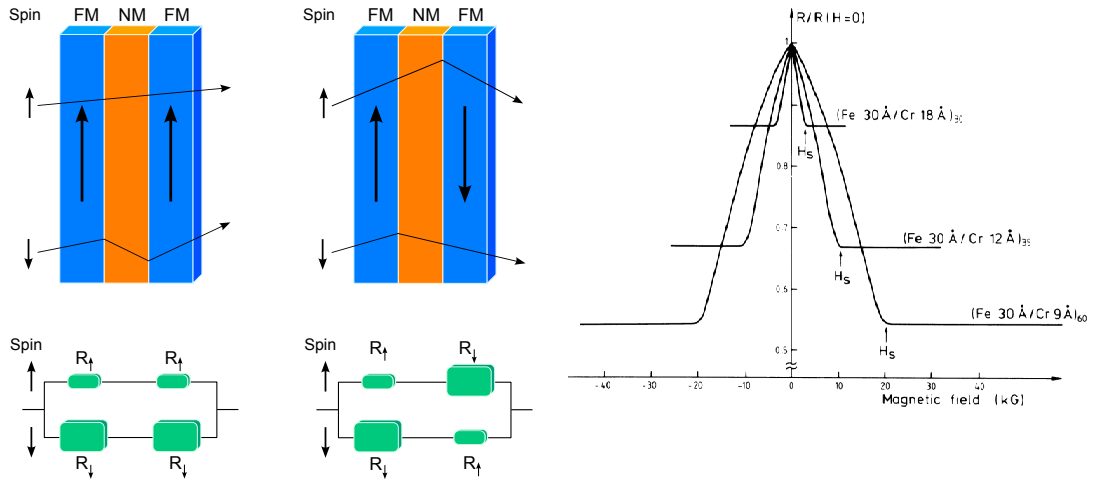


FIGURE 1.1: (left) Simple sketch of the GMR process. Picture adapted from [4]. (right) First GMR results in different triple superlattices, as reported by Fert *et al.* [1].

### 1.1.2 Tunnel MagnetoResistance

Another extensively studied topic in spintronics is the Tunnel MagnetoResistance (TMR), where the non-magnetic spacer is no longer metallic but rather insulating. The corresponding stack FM-metal/NM-insulator/FM-metal is known as a Magnetic Tunnel Junction (MTJ). The TMR effect was historically discovered before the GMR by Jullière *et al.* in 1975 [5]. The principle is slightly different from that in GMR, in the sense that in TMR the electrons *tunnel* through the insulating barrier. The amplitude of the effect was rather limited (on the order of 10% change in resistance) at room temperature in early designs, where the insulating barrier was amorphous (typically aluminum oxide). In recent MTJ, however, the use of a crystalline MgO as a barrier has led to TMR of more than few hundreds of percents, even at room temperature (see, *e.g.*, ref. [6]). Upcoming applications in Magnetic Random Access Memories (MRAM) are expected in the very near future.

### 1.1.3 The Spin Transistor

The GMR and TMR effect can be used to increase information storage density, yet they have not been applied to information processing devices. Probably the most famous device to such an end is the spin transistor proposed by Datta and

Das in 1989 [7]. The device is depicted in figure 1.2. In the SPINFET transistor, the current is injected in the channel (a two dimensional electron gas) by a ferromagnetic source electrode and it is collected in the ferromagnetic drain electrode. Hence the current is spin polarized and the magnetization in the drain electrode is used to analyze the polarization. The control of the polarization in the channel is done by applying a voltage on the gate electrode. The resulting electric field in the channel interacts with the spins *via* the Rashba-Bychkov effect and makes the spins precess. The final orientation (upon reaching the drain) can then be tuned and one expects oscillating current through the transistor as a function of the gate voltage.

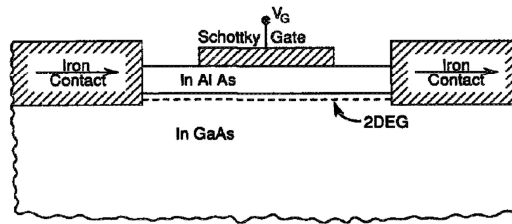


FIGURE 1.2: Original sketch of the spin transistor (SPINFET), as proposed by Datta and Das in ref. [7].

Many other devices have been proposed but the spin transistor described here has the advantage to illustrate one of the most important requirement : the ability to inject efficiently spins from the ferromagnetic source in the channel. The origin of this issue is discussed in more details in the next section.

#### 1.1.4 Spin-injection : current issues and possible solutions

Spin injection can easily be done using so-called optical pumping : the material is illuminated with circularly polarized light, as a result electrons excited to the valence band have a preferential spin orientation. This was demonstrated in direct gap semiconductors (*e.g.* GaAs [8]) but also in indirect gap semiconductors (*e.g.* Si [9]). However, optical pumping is not a viable means in terms of industrial applications, one would rather use all-electric phenomena. The most simple design is then to stick a ferromagnetic electrode on a semiconductor and inject spin-polarized electrons through the interface. However, a fundamental obstacle has been opposed to this simple design : it has been demonstrated [10, 11] that the conductivity mismatch between the metallic FM electrode and the semiconductor



(typically a few orders of magnitude) leads to a spin accumulation at the interface that prevents any injection of a polarized current.

Two possible solutions to this issue are currently being studied :

- **injection through a tunnel barrier** : In that case, the FM electrode and the semiconductor are separated by a thin tunnel barrier. Experimental results have proven the feasibility [12, 13], however the process seems rather hard to scale industrially.
- **injection from a resistive ferromagnet** : if one could adapt the resistivity of the FM electrode to that of the semiconductor, then the injection process might be possible. Magnetic semiconductors could then be a way to circumvent the spin injection issue. The quest for room-temperature ferromagnetism in semiconductors has then been on for over a decade now and it is within this framework than the study GeMn nanocolumns may offer new insights.

### 1.1.5 A new class of materials : the Ferromagnetic Semiconductors

GeMn nanocolumns belong to a wide class of materials, known as the ferromagnetic semiconductors (FMS). These materials are being developped for the field of spintronics and aim at coupling electronic and magnetic properties within the same material. As such, they are basically obtained by alloying or doping semiconductors with magnetic atoms.

FMS can be roughly classified in three different families according to the distribution of the magnetic atoms : (i) concentrated, (ii) diluted or (iii) heterogeneous magnetic semiconductors. Informations given in this subsection and the following ones are very general and only serve a descriptive purpose. However, more specific informations, as well as an up-to-date review of current results in the field of FMS, can be found on the *Ferromagnetic Semiconductor Spintronics Website* of the Czech Insitute of Physics (see ref. [14])

#### 1.1.5.1 Concentrated Magnetic Semiconductors

Concentrated Magnetic Semiconductors (CMS) consist in alloys of magnetic atoms in semiconducting materials. The magnetic atoms sit in well defined lattice sites

and the material is an homogeneous single crystal. Typical examples are  $\text{CdCr}_2\text{Se}_4$  or  $\text{CuCr}_2\text{S}_4$ , where the proportion of magnetic atoms is 28.6%. However, such materials are quite hard to integrate in existing industrial processes which rely mostly on III-V (*e.g.* GaAs) or group IV (*e.g.* Si, Ge) semiconductors.

### 1.1.5.2 Diluted Magnetic Semiconductors

Due to their high potential compatibility with existing micro-electronics, ferromagnetic Diluted Magnetic Semiconductors (DMS) have been extensively studied over the last decade or so. The approach in DMSs is to dope the semiconductor with small amount of magnetic atoms (a few percent at most) and to mediate the ferromagnetism *via* the charge carriers.

Historically, the first semiconductors to be doped with magnetic atoms were II-VI (*e.g.* ZnTe, CdTe) in the 1980's. The advantage is that doping Mn atoms have the same valence as the cation (Zn or Cd) and therefore they are highly soluble in such matrices. However, early II-VI DMSs appeared to be either paramagnetic or antiferromagnetic. It is only in the 1990's and during the study of the III-V DMS (Ga,Mn)As that the carrier density appeared as a critical parameter in the mediation of ferromagnetism. A common model was proposed in 2000 to explain magnetism in II-VI and III-V DMS, deriving a strong dependence of  $T_C$  on both the concentration in magnetic atoms and the carrier density [15]. Since Mn atoms have the same valence as the cations they replace in a II-VI DMS, they act as localized magnetic moments without changing the carrier density. Thus, additional conventional doping is required to achieve the tuning of carrier density. Despite those advances, experimental results in such systems have shown rather low  $T_C$  and focus moved on to III-V and IV semiconducting hosts.

The archetypical III-V DMS is the well-known (Ga,Mn)As, where Mn atoms sit on Ga positions. In opposition to the II-VI case, Mn atoms provide both magnetic moments and holes, due to their valence different from Ga. Other DMS based on InAs, GaN, AlN, and Si have been extensively studied as well. The particular group IV DMS (Ge,Mn) has recently received a lot of attention and an overview of the different studies about this material as a DMS will be given in section 1.2.3.1.

The main drawbacks in DMSs are that (i) Curie temperatures are limited below room temperature and (ii) there is high probability of formation of intermetallic

precipitates during the growth of DMS. Such precipitates can be ferromagnetic with  $T_C$  near room temperature (*e.g.* MnAs,  $\text{Ge}_3\text{Mn}_5$ ), which requires constant efforts to rule out their contribution to the magnetic properties. It also means that out-of-equilibrium growth techniques are required to achieve the synthesis of a true DMS.

### 1.1.5.3 Heterogeneous Magnetic Semiconductors

Heterogeneous Magnetic Semiconductors (HMS) are the most recent group of magnetic semiconductors to be studied. They stem originally from DMS : as out-of-equilibrium growth techniques are required, the formation of unknown, metastable phases is possible. Such phases can be fully coherent with the surrounding matrix but still show locally higher concentration of magnetic atoms. Ferromagnetism and coupling with the charge carrier may then be expected. A theoretical study of the nanoscale spinodal decomposition occurring during the growth of HMS was first given by Sato *et al.*, who calculated an increase of the  $T_C$  upon phase decomposition due the extended magnetic networks in the system [16]. The authors also investigated the phase separation in spherical regions, so-called *Daireseki*-phases<sup>1</sup>, and in columnar-like structures, so-called *Konbu*-phases<sup>2</sup> [17, 18]. Several experimental results confirmed the decomposition process in different II-VI, III-V and IV systems, such as, *e.g.*, in (Zn,Cr)Te by Kuroda *et al.* [19], in (Ga,N)Fe by Bonanni *et al.* [20], in (Ga,Mn)As by Hai *et al.* [21], or in (Ge,Mn) by Jamet *et al.* [22]. The GeMn nanocolumns studied in this thesis belong to the *Konbu*-phase and are typical of such HMS. An overview of experimental results in (Ge,Mn) system as a HMS will be given in the section 1.2.3.3.

## 1.2 The (Ge,Mn) system : state of the art

The (Ge,Mn) system combines both a well-known semiconductor and a well-known magnetic transition metal in the same material. Therefore, it appears as a very promising system for ferromagnetic semiconductor applications. In this section, I will first give an overview of the known stable (Ge,Mn) phases and show why out-of-equilibrium are requested to form either a diluted system or at least a system

---

1. Daireseki is the japanese word for marbble.

2. Konbu is the japanese name of a kind of seaweed.

free of intermetallic precipitates. Then I will give an extensive overview of previous theoretical and experimental work on the (Ge,Mn) system, in particular in the case of out-of-equilibrium systems.

### 1.2.1 The Ge :Mn binary phase diagram

Prior to any further description of the GeMn system, let us take a look at the Ge :Mn binary phase diagram, as shown in figure 1.3. One can see that there exist no known Ge :Mn single phase with less than 58% Mn. All stable phases are on the high Mn content side of the phase diagram. This already shows that Mn atoms in Ge have a strong tendency to aggregate and form high Mn concentration compounds. In particular, the solubility limit of Mn in Ge has been measured to be around  $10^{-6}\%$  [23], preventing any dilution of Mn atoms in Ge by using equilibrium growth techniques.

At room temperature, going from pure Ge diamond to pure  $\text{Mn}_\alpha$ , the known stable phases are :  $\theta\text{-Ge}_8\text{Mn}_{11}$  [25](formerly identified as  $\text{Ge}_2\text{Mn}_3$ ),  $\eta\text{-Ge}_3\text{Mn}_5$  [26],  $\kappa\text{-Ge}_3\text{Mn}_7$  [27], and  $\varepsilon_1\text{-GeMn}_{3.4}$  [27, 28]. All these phases are metallic and therefore not suited as ferromagnetic semiconductors. However, the first two phases, *i.e.*  $\text{Ge}_8\text{Mn}_{11}$  and  $\text{Ge}_3\text{Mn}_5$ , are interesting because (i) they are magnetic and (ii) they are the most likely to appear as precipitates when dealing with out-of-equilibrium growth of (Ge,Mn) with Mn contents between 1 and 10%. Experimental results showing precipitation of intermetallic compounds will be discussed in subsection 1.2.3.

### 1.2.2 Theoretical studies of the GeMn system

Most of the theoretical work performed in the GeMn system was done within the DMS approach, *i.e.* Mn atoms sitting randomly on substitutional sites in a Ge diamond host matrix. Early results by Dietl *et al.* in 2000 have shown, using the Zener model, that in the case of Ge enriched with 2.5 at.%  $\text{Mn}^{2+}$  and with a hole concentration of  $3.5 \times 10^{20} \text{ cm}^{-3}$ , a Curie temperature of about 80 K may be expected [15, 29].

In 2001, Schultess and Butler have shown that the magnetic moment on a substitutional Mn atom was not  $5 \mu_B$  as in the case of the isolated  $\text{Mn}^{2+}$  atom, but

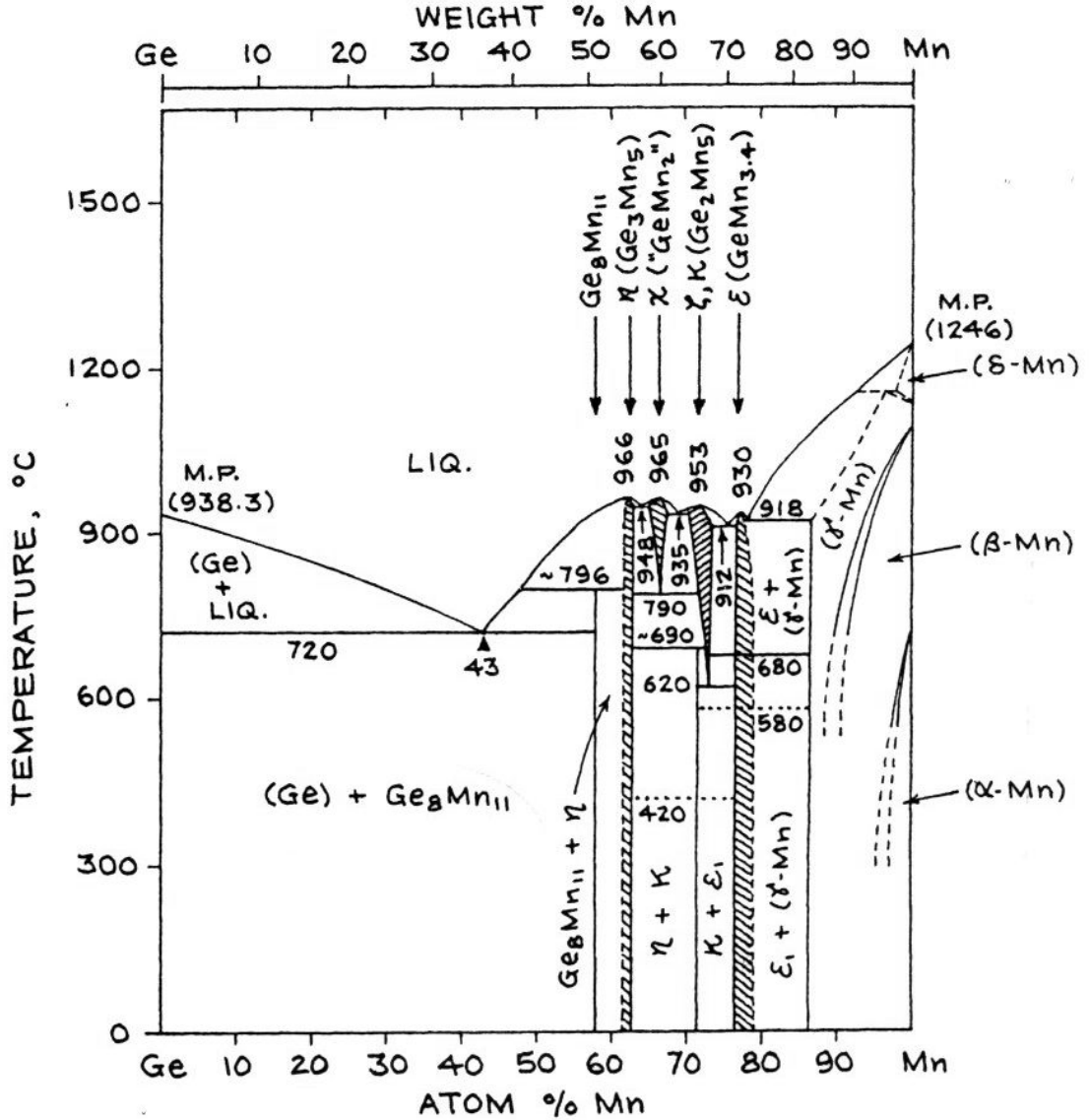


FIGURE 1.3: Ge :Mn binary phase diagram, adapted from [24].

rather  $3 \mu_B$  due to the hybridization of the Mn  $d$  orbitals with the Ge  $p$  orbitals [30]. In particular, the Mn  $d$  states should have the configuration  $e_{\uparrow 2, \uparrow}^2 t_{2, \uparrow}^1 t_{2, \downarrow}^1$ .

In 2003, Zhao *et al.* have calculated oscillating exchange interactions, corresponding to the RKKY theory, for a system of 2 Mn atoms diluted among 62 Ge atoms [31].

In 2006, Continenza *et al.* have shown that “Mn in Ge is expected to be the most promising magnetic impurity to obtain spintronic materials, since it is able to ensure the desired ferromagnetic alignment and high magnetic moment” [32]. In particular, they found a magnetic moment of about  $3 \mu_B$  on the substitutional Mn atoms, as previously predicted. They have also confirmed a tendency towards

cluster formation of the Mn atoms [33, 34]. The arrangement of the Mn atoms in the Ge matrix critically affects the magnetic properties, especially on the high-doping side (around 10%), as shown by Picozzi *et al.* [35].

Very recently (mid-october 2010), interest for other-than-substitutional positions for Mn in Ge was revived by Decoster *et al.* [36]. In particular, the authors have shown that the bond-centered (BC) position, associated to a Mn-Vacancy complex, explains experimental results of electron emission channeling. The authors highly recommend further theoretical studies taking into account the BC position.

Further studies by Continenza *et al.* have also extended to amorphous materials (Si and Ge) and shown that (i) Mn-doping in amorphous Ge leads to a half-metallic system with exactly  $3 \mu_B$  on the Mn atoms<sup>3</sup>, (ii) disorder enhances Mn solubility, as the heat of formation is reduced by 0.5 eV with respect to the value in diamond [39].

Some recent work also focussed on nanostructured GeMn, and in particular, on GeMn nanocolumns : Caprara *et al.* have studied ferromagnetic columns in a semiconducting host using an effective semi-phenomenological Hamiltonian describing the coupling [40]. Due to the confinement of the carriers in the metallic columns, they predict the formation of quasi-one-dimensional spin-polarized subbands inside the band gap. Excitation between these states and the band edges should mediate the intercolumns exchange. The authors described the coupling as a *carrier-confinement-mediated* mechanism. This mechanism can explain both FM or AFM coupling, depending on the intercolumns distances or on the filling of the quasi-one-dimensional spin-polarized subbands. Further work is still required to confirm the role of residual impurities in the semiconducting host.

Arantes *et al.* have performed *ab initio* studies of free-standing [110]-oriented Ge nanowires doped with 2% Mn atoms [41]. Typical diameters ranged between 2.7 and 3.5 nm. The authors found that Mn atoms were energetically favored inside the nanowires, as opposed to near the surface. This behavior is reversed if the surface of the nanowires is saturated with H atoms. They also found ferromagnetic alignment of the magnetic moment as soon as the Mn-Mn distance was larger than  $4 \text{ \AA}$ , with magnetic moments values around  $3.5 \mu_B$ .

---

3. This is at variance with experimental results where the magnetic moment on the Mn atoms in amorphous Si was measured to be critically reduced [37, 38]. Continenza *et al.* suggest that it may due to defects that destroy the local tetrahedral configuration, even though the authors in refs. [37, 38] claim tetrahedral coordination of the Si atoms using EXAFS.

### 1.2.3 Experimental studies of the GeMn system

The first experimental evidence of (Ge,Mn) as ferromagnetic semiconductor was published by Park *et al.* in 2002 [42]. These results spurred intensive research about the (Ge,Mn) system and since the initial publication of ref. [42], several other groups have investigated the (Ge,Mn) system by many different means. I shall give here an overview of these results and present them in their context : whether (i) the research aimed at investigating a DMS, or (ii) on the opposite investigating a heterogeneous material with metallic precipitates or (iii) with metastable phases, or (iv) eventually in the case of the growth of nanostructures (such as nanowires or quantum wells).

#### 1.2.3.1 GeMn as a DMS

Park *et al.* have used low-temperature molecular beam epitaxy to grow out-of-equilibrium solutions of  $\text{Ge}_{1-x}\text{Mn}_x$  with  $x$  in the range 0.6–3.5% [42]. The films were ferromagnetic, with a Curie temperature scaling with the Mn concentration, from 25 to 116 K. Furthermore, they have shown that the ferromagnetism was indeed mediated by the charge carriers (holes) by observing an extraordinary Hall effect (EHE) that could be modulated by applying a gate voltage (*i.e.* tuning the hole concentration). The magnetic moment measured on the Mn atoms were lower than expected, around 1.4–1.9  $\mu_B$ .

Following the results of Park *et al.*, a group at the University of Camerino and at the University of L'Aquila in Italy (and co-workers) have published between 2004 and 2006 many experimental results in MBE grown diluted (Ge,Mn) systems [43–50]. In particular, ferromagnetism was observed up to room temperature and an interpretation of the transport and magnetic properties based on bound magnetic polaron (BMP) was given.

At the same time, another group at the same universities investigated ion-implanted Ge films [51–53]. They observed cluster formation at depth larger than the projected range (32 nm). However, using TEM, XRD, and EXAFS, it is claimed that the Mn atoms in the subsurface layer occupy only substitutional positions. In particular, XAS measurements at the Mn  $L_{2,3}$  edges show broad absorption edges just after the implantation and a multiplet structure ascribed to predominant  $\text{Mn}^{2+}$

substitutional atoms after annealing [53]. The broad absorption edges are attributed to clustered Mn atoms. Upon annealing those atoms move to energetically more favorable substitutional sites and yield *in fine* the  $\text{Mn}^{2+}$ -like spectra. Another possible explanation proposed here, is that upon annealing the clusters move towards the bulk, as observed by Devillers *et al.*, leaving only single atoms in the subsurface region. It is worth noting that the absence of oxygen was monitored throughout the whole process [53]. The same samples were studied by Morgunov *et al.* [54] and the authors were able to discriminate the magnetic properties due to ferromagnetic  $\text{Ge}_3\text{Mn}_5$  inclusions and to explain the behavior of the diluted  $\text{Mn}^{2+}$  ions with a magnetic polaron model. In particular they observed spin-wave resonance at low temperature (below 13 K).

A group at the University of Queensland in Australia and at the University of California, Los Angeles reported in 2008 the low temperature MBE growth of  $\text{Ge}_{0.96}\text{Mn}_{0.04}$  films [55]. They found that the top layer of the film was amorphous and, at variance with the previously cited results, a diffusion of Mn atoms towards the surface.

In 2002, a group in South Korea has published magnetization and transport measurements in (Ge,Mn) samples grown by powder mixing in a furnace [56]. Surprisingly, no indication of secondary phases could be observed in x-ray powder diffraction pattern. Yet a double transition AFM-FM-PM was observed as the temperature rose from 4.2 to 400 K. Such a transition would be expected in the case of  $\text{Ge}_8\text{Mn}_{11}$ . The Curie temperature was 285 K (like in  $\text{Ge}_8\text{Mn}_{11}$ ) and the authors predicted it could be further increased with additional carrier doping. Hence, all magnetic clues of the presence of a  $\text{Ge}_8\text{Mn}_{11}$  phase were gathered, yet no structural evidence could be put forward. This may indicate the limitation of conventional XRD technique when dealing with extremely small clusters embedded in a crystalline matrix.

More recently, another group in South Korea obtained polycrystalline  $\text{Ge}_{0.7}\text{Mn}_{0.3}$  films by radio frequency magnetron sputtering of Ge and Mn on sapphire at  $500^\circ\text{C}$  [57]. Besides desoriented Ge grains, no peaks from different (Ge,Mn) phases could be evidenced. Furthermore, ferromagnetism up to more than 350 K was observed, which is higher than the  $T_C$  in  $\text{Ge}_8\text{Mn}_{11}$  or  $\text{Ge}_3\text{Mn}_5$  ( $\sim 285$  K and  $\sim 300$  K respectively).



Another way to synthesize homogeneously doped (Ge,Mn) was proposed by a group at the University of Tennessee and Oak Ridge National Laboratory under the name “subsurfactant epitaxy” [58]. They used very low temperature MBE (150 K) with a sequential protocol : firstly, they evaporate only Mn atoms on Ge, most of the atoms sit on substitutional sites, but some remain at other positions. Lateral diffusion and clustering are inhibited by the low temperature. Secondly they cover the surface with Ge atoms. As a result interstitial Mn float on the new Ge surface due to a surfactant effect, while substitutional Mn atoms stay uniformly distributed in the Ge. In that way, the authors reached 0.25% homogeneous Mn doping levels and Curie temperature higher than 400 K. In particular, a DMS-type anomalous Hall effect was observed.

A Chinese group published in 2007 [59] experimental evidence of ferromagnetism up to 213 K in highly concentrated  $\text{Ge}_{0.43}\text{Mn}_{0.57}$  (*i.e.* the same stoichiometry as  $\text{Ge}_8\text{Mn}_{11}$ ) films, with magnetic moments of about  $1 \mu_B$  per Mn atom . The samples were obtained by the alternate sputtering of thin Mn and Ge layer over a sequence of 60 repetitions and appeared homogeneous. No AFM-FM transition upon temperature rise was observed, excluding a possible  $\text{Ge}_8\text{Mn}_{11}$  phase. Semiconducting transport properties as well as small magnetoresistance were also reported.

The same group also considered amorphous materials as a way to increase the Mn solubility [60]. They coevaporated Mn and Ge atoms on liquid nitrogen-cooled substrates. A ferromagnetic, homogeneous phase with  $T_C$  up to 220 K was obtained for Mn concentration up to 52%. Higher concentrations resulted in phase separation and formation of  $\text{Ge}_8\text{Mn}_{11}$  clusters.

Amorphous (Ge,Mn) films were obtained at the Institute of Physics of Sao Carlos in Brazil by radio frequency co-sputtering of Ge and Mn on substrate kept at 150°C [61]. The Mn content reached up to 24%, yet the films appeared homogeneous as-deposited and no secondary phases could be evidenced prior to the annealing.

A group of the University of Tokyo investigated the magneto-optical and the magnetotransport properties of amorphous (Ge,Mn) thin film grown by low temperature MBE on  $\text{SiO}_2$  [62]. By comparing magnetization, magneto-optical, and magnetotransport measurements, they concluded that the films were magnetically homogenous, *i.e.* they were single-phase ferromagnetic.

### 1.2.3.2 GeMn as a heterogeneous semiconductor containing stable intermetallic precipitates

Most of the groups than have studied diluted (Ge,Mn) were confronted to phase separation during the growth and have studied the results of the precipitation. In most cases, the precipitates were the expected  $\text{Ge}_8\text{Mn}_{11}$  or  $\text{Ge}_3\text{Mn}_5$  phases.

Park *et al.* have already reported in 2001 on the formation of  $\text{Ge}_8\text{Mn}_{11}$  precipitates in films grown between 250–300°C [63].

The groups at the University of Camerino and at the University of L'Aquila have shown that their samples contained mostly  $\text{Ge}_3\text{Mn}_5$  clusters and some  $\text{Ge}_8\text{Mn}_{11}$ , embedded in a Ge matrix containing up to 1.5% Mn [64–70].

Similarly, Biegger *et al.* [71] observed precipitation of  $\text{Ge}_3\text{Mn}_5/\text{Ge}_8\text{Mn}_{11}$  in a Mn-poor (1–3%) Ge matrix in samples grown by powder mixing in a furnace (in the same fashion as Cho *et al.* [56]). In their case, the presence of clusters with a different crystalline phase could be observed in XRD.

In 2007, one group from South Korea reported the RF magnetron sputtering growth of  $\text{Ge}_3\text{Mn}$  amorphous thin films with ferromagnetic order up to 350 K that contained  $\text{Ge}_3\text{Mn}_5$  and/or  $\text{Ge}_8\text{Mn}_{11}$  clusters. The magnetic signal measured above 300 K is explained as stemming only from the amorphous  $\text{Ge}_3\text{Mn}$ .

As mentionned in the previous section, the group at the Shandong University in China observed the precipitation of  $\text{Ge}_8\text{Mn}_{11}$  clusters, embedded in the amorphous matrix [60]. As a side note, they were able to evidence exchange bias in the ferromagnetic, low Mn-content matrix due to the exchange coupling with the antiferromagnetic  $\text{Ge}_8\text{Mn}_{11}$  clusters.

The group at the University of Queensland in Australia and at the University of California, Los Angeles have shown evidence of  $\text{Ge}_8\text{Mn}_{11}$  and  $\text{Ge}_2\text{Mn}_5$  clusters [72], as well as metallic  $\text{Mn}_\alpha$  [55] which is much less common.

Bihler *et al.* investigated the structural and magnetic properties of  $\text{Ge}_3\text{Mn}_5$  clusters embedded in Ge matrix [73]. They have observed a coherent incorporation of the hexagonal clusters in the diamond matrix with a preferential alignment of the *c*-axis of both lattices. The matrix displayed a DMS-like behavior. Lechner *et al.* [74] further performed a depth-resolved study of the  $\text{Ge}_3\text{Mn}_5$  clusters in Ge. They

found two types of clusters : a majority is buried in the layer and  $c$ -axis aligned and a minority lies close to the surface with different but well defined orientations.

Similarly, a German group at Munich observed precipitation of  $\text{Ge}_3\text{Mn}_5$  clusters in Ge during the low temperature MBE growth of (Ge,Mn) films [75, 76]. In their case, the clusters are also mainly located near the bottom of the (Ge,Mn) layer.

A group from Dresden reported on different measurements in  $\text{Ge}_3\text{Mn}_5$  clusters in Ge [77, 78]. In particular they have shown a remarkable temperature-dependent magnetic memory effect in the clusters. They explain the observed spin-glass-like features by the finite size distribution of the clusters, rather than by coupling through the Mn-poor matrix.

### 1.2.3.3 GeMn as a heterogeneous semiconductor containing metastable phases

Fewer groups also observed the formation of Mn-rich regions, without any evidence of phase separation. In most cases, the regions have a columnar shape, as theoretically calculated by Katayama-Yoshida, Sato *et al.* [17, 18]. This *Konbu*-phase formation can be explained by the combination of a 2D growth mode with a nanoscale spinodal decomposition phenomenon.

In 2005, the group at the University of Tokyo reported on the formation of amorphous, columnar-like, and Mn-rich regions in Mn-doped Ge films [79]. A clear ferromagnetic signal was observed, yet no intermetallic compound was evidenced.

Since 2006, the group from Munich reported on the formation of Mn-rich cubic clusters in  $\text{Ge}_{0.95}\text{Mn}_{0.05}$  films free of intermetallic precipitates [80]. In 2009 the same group used atom probe tomography to investigate the position of Mn atoms in the columnar or “string-of-pearls”-like objects [81]. In particular they found strong structural disorder inside the nanocolumns.

At the same time, in 2006, our group in Grenoble published its first results on GeMn nanocolumns [22]. The initial publication, demonstrating Curie temperature above room temperature, was followed by additional characterization of the nanocolumns [82–89]. In particular it is shown that upon a fine tuning of the low temperature MBE growth parameters (substrate temperature and growth rate), (Ge,Mn) films consisting of Mn-rich nanocolumns embedded in a Mn-poor matrix

can be obtained. The nanocolumns extend continuously from the buffer to the substrate. The surrounding matrix is almost pure Mn ( $<1\%$ ). Typical sizes are 3–5 nm in diameter and typical densities are on the order of  $10^4 \mu\text{m}^{-2}$ . Similar results were also obtained on GaAs substrates.

In 2007, the group at the University of Tennessee and Oak Ridge National Laboratory also reported on the formation of coherent, nanometer-sized, Mn-rich region in (Ge,Mn) [90]. In particular they found Mn concentration in nanocolumns to be in the range 17–30% and the magnetic moment on the Mn atoms to be in the range  $1.0\text{--}1.5 \mu_B$ . Such values are consistent with those reported by our group.

Lastly, a group at the University of California, Los Angeles, reported on the growth of “tadpole”-like (*i.e.* distorted columnar-like) Mn-rich regions in (Ge,Mn) grown on Si [91] and on the assembly of nanocolumns by piling up of Mn-rich quantum wells [92], as previously proposed by Devillers *et al.* [82]. In both cases, the presence of additional  $\text{Ge}_3\text{Mn}_5$  clusters was also evidenced.

The corresponding Mn-rich regions (shaped like nanocolumns) obtained by the different groups are shown in figure 1.4 for comparison. Striking similarities between the nanocolumns obtained in our group, in the group from Munich, and in the group at the University of Tennessee and Oak Ridge National Laboratory can be observed.

#### 1.2.3.4 GeMn in nanostructures

Several groups have extended the study to other (Ge,Mn) nanostructures, such as quantum dots or nanowires.

The group at the University of California, Los Angeles, has recently reported on the growth of high-Curie-temperature quantum dots in Ge with 5% Mn [93]. Interestingly, they were able to tune the magnetic properties by applying a gate voltage.

Mn-doped Ge nanowires were also studied by Kazakova *et al.* [94]. They reported room-temperature ferromagnetism in 35 nm-wide (Ge,Mn) film with 1–5% Mn, grown in the pores of anodized aluminium oxide membranes. The nanowires are crystalline and no secondary phase could be evidenced.

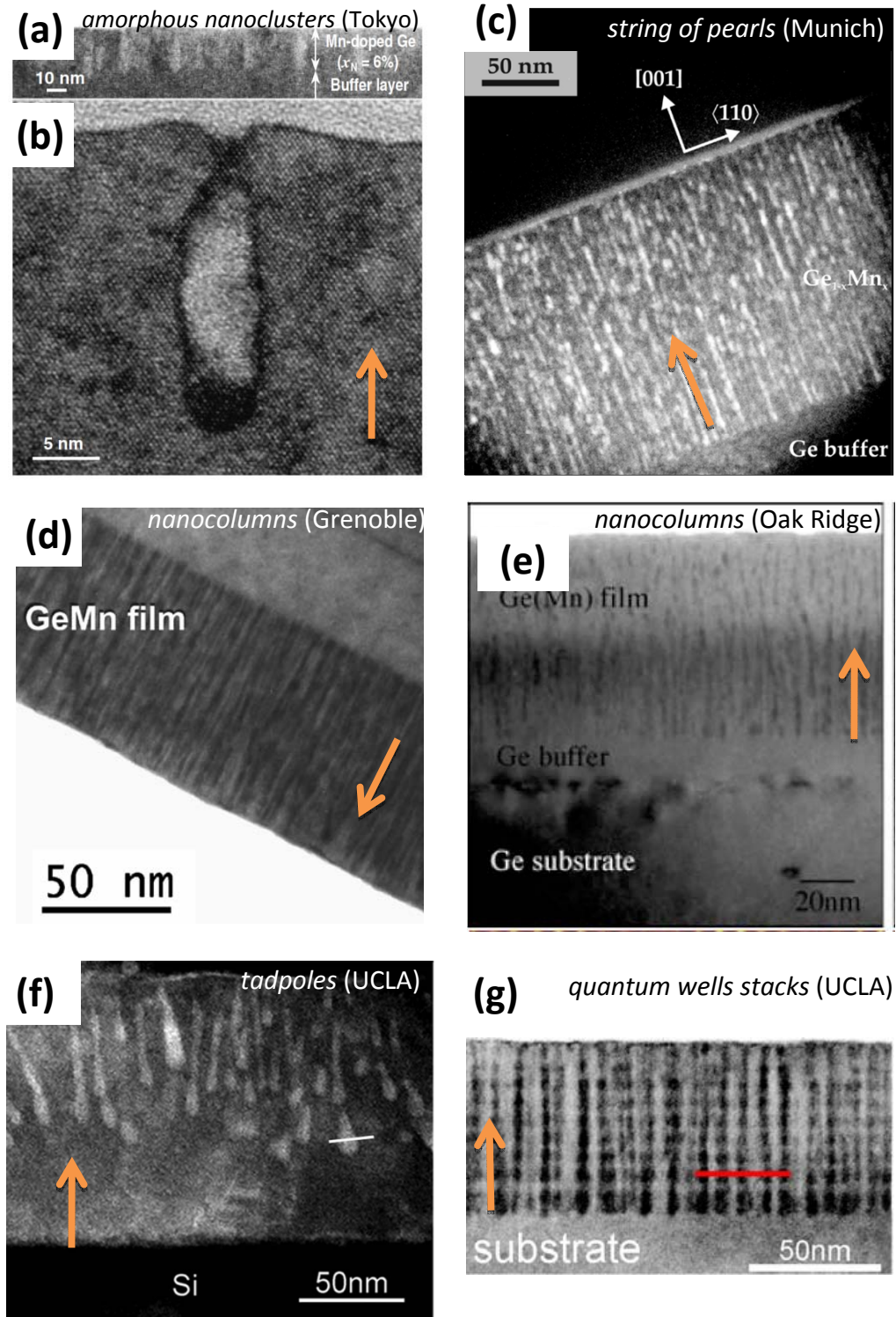


FIGURE 1.4: Cross-sectional TEM micrographs showing the different types of nanocolumns obtained in different groups. (a) and (b) are from the group at the University of Tokyo [79], (c) is from the group from Munich [81], (d) is from our group in Grenoble [82], (e) is from the group at the University of Tennessee and Oak Ridge National Laboratory [90], (f) and (g) are from the group at the University of California, Los Angeles [91, 92] (respectively). In all cases the growth direction is indicated by an orange arrow.

(Ge,Mn) nanowires grown using the Vapor-Liquid-Solid (VLS, or thermal vapor transport) technique by a group in South Korea [23] were shown to be free of intermetallic precipitates. Typical diameters were around 60 nm and the nanowires can be 20  $\mu\text{m}$ -long. Elemental mapping has shown that the Mn atoms are homogeneously diluted in the nanowire. Ferromagnetism is observed above room-temperature, even in undoped nanowires (though much less pronounced)<sup>4</sup>.

### 1.2.3.5 Quick summary

As this broad review of theoretical and experimental results in the (Ge,Mn) shows, there is a major trend not to consider only a perfectly diluted system anymore but rather to shift to a new paradigm, considering both a Mn-poor Ge matrix and inclusions that can be either known metallic compounds or new unknown phases. As such, the GeMn nanocolumns appear as a very interesting way towards a better understanding of self-assembled inhomogeneous magnetic semiconductors, which were proposed as a relevant alternative for spintronics materials [95]. In particular, the spinodal decomposition in the GeMn nanocolumns allows for a possible optimization of (i) the magnetic properties of the HMS (*e.g.*, by extending the network of magnetic atoms in the Mn-rich regions), and (ii) of the interphase coupling (*e.g.* by maximizing the interfaces between the columns and the matrix, or by a carrier-confinement effect in the nanocolumns).

## 1.3 The GeMn nanocolumns

Most of the results reported in the previous section indicate that the coherent Mn-rich inclusions in Ge (*e.g.* the GeMn nanocolumns) are metastable and precipitate in intermetallic clusters upon annealing. This emphasizes the fact that GeMn nanocolumns can only be obtained by out-of-equilibrium growth techniques. The samples used in my thesis were grown by André Barski, Thibaut Devillers, Clément Porret and Abhinav Jain at the INAC-CEA Grenoble. I was given the opportunity to participate in a few samples growth and the growth process will be described in the following. The different types of nanocolumns obtained as well as

---

<sup>4</sup>. Quantum confinement and surface contribution are suggested by the authors as a possible explanation for the magnetism in the undoped nanowires. Further work is still required for a complete understanding.

their intriguing properties will be also described hereafter. Most of this work was reported in ref. [96] and references therein.

### 1.3.1 An out-of-equilibrium growth mode

The GeMn nanocolumns are obtained by low-temperature molecular beam epitaxy (MBE). This out-of-equilibrium growth method is the most suited for the growth of metastable phases, such as the GeMn nanocolumns. The experimental setup is a RIBER 2300 model and its main element consists in an ultra-high vacuum chamber (pressure on the order of  $10^{-11}$  mbar), as depicted in figure 1.5. Several Knudsen cells are connected to the chamber, each containing one specific element. Using filaments, the cells can be heated to establish a solid-gas phase equilibrium (or liquid-gas phase equilibrium if the temperature rises above the melting point). As a result, the pressure of the gas phase in the cell can be adjusted by the temperature of the cell. Atoms in the gas phase are then evaporated on the sample. The ratio of pressures between different cells with different elements will control the stoichiometry of the sample. Two sets of shutters are used to turn on and off the flux of gas-phase atoms from the cell to the sample. The first set consists in individual shutters for each cell (*e.g.*, Mn or Ge), that allow for selective deposition of the elements. The second set is a large shutter that covers the whole sample and that is used to precisely control the start and stop of the growth. A silicon gun is also available on the setup. Silicon evaporation temperatures cannot be reached in a typical Knudsen cell. Instead, a silicon lump is heated by sweeping it with a 10 keV electron beam and local melting is achieved. The flux of the silicon gun is measured using a quartz crystal microbalance. The start and stop of the Si flux on the sample are also controlled using a dedicated shutter.

The growth rate is calibrated using Reflection High-Energy Electron Diffraction (RHEED). This technique uses a beam of high-energy electrons (20 keV) impinging on the sample surface at grazing incidence (incidence angle on the order of 0.5–3°). The grazing incidence limits the interactions of the electrons to the first few atomic planes and ensures surface sensitivity. The diffraction pattern is observed on a phosphorescent screen and recorded by a camera. Due to the different patterns corresponding to a flat surface, terraces or 3D islands, one can follow the growth mode *in situ*. In particular, in the case of a layer-by-layer, 2D growth mode (*Frank-van der Merwe* growth mode), the intensity of the diffracted spots oscillates as

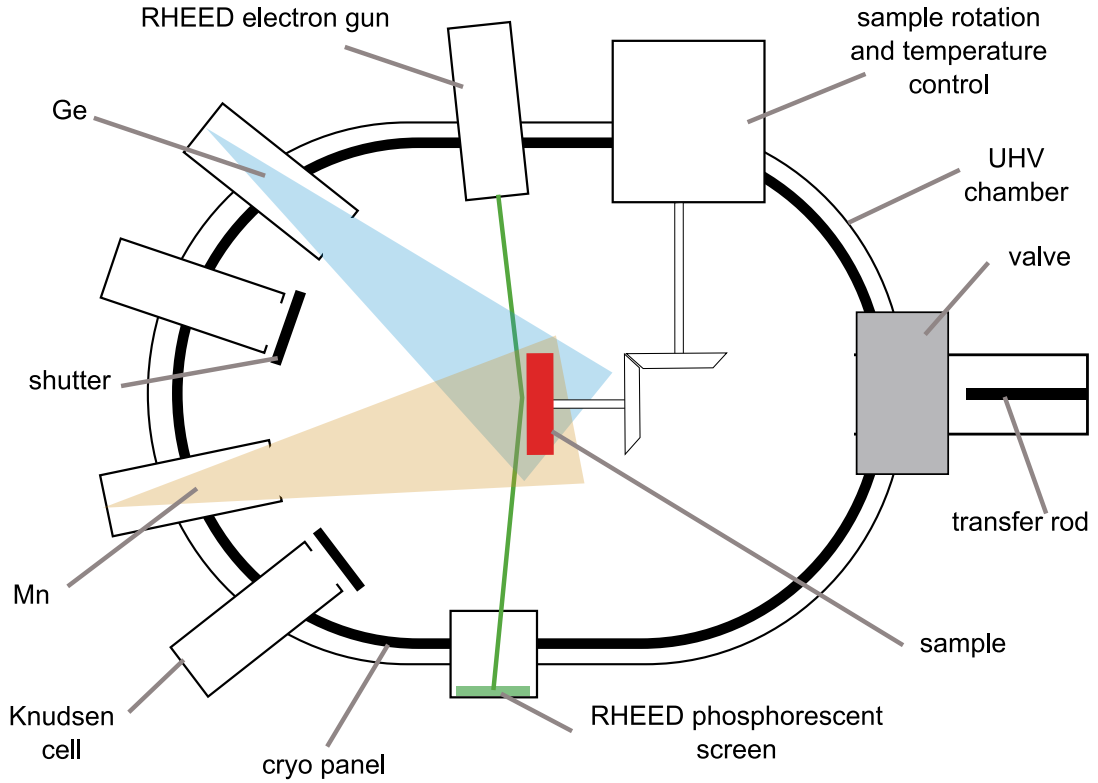


FIGURE 1.5: Schematic view of the low-temperature molecular beam epitaxy setup used for the GeMn nanocolumns growth. For clarity the main shutter (see text), the Si gun and the pumping system have not been represented.

a function of the layer coverage : it is maximum for a full layer and minimum for a half-covered layer. Hence one may follow the growth with a layer-by-layer resolution and calibrate the impinging flux accordingly.

Prior to the growth, the substrates (typically Ge(001)) are glued on molybdenum Molyblocks using indium. This ensures good mechanical stability of the sample and a good thermal conductivity with the sample holder. The substrates are introduced into a glove-box, where they can undergo chemical treatment (such HF acid etch) in a controlled  $N_2$  atmosphere. The substrates are then transferred to a sas connected via UHV modules to the growth chamber. During the growth, the sample surface is maintained at a low-temperature (between 100 and 150°C)<sup>5</sup> using a small heating filament. The low temperature is used to prevent the system to go over thermodynamical barriers and form stable alloys, such as  $Ge_3Mn_5$ .

5. Those temperatures are low compared to typical MBE temperatures that are usually above 500°. Note also that they are too low to be read directly in the sample using a pyrometer, as usually done. Instead, a thermocouple is used and mounted on the sample holder as close as a possible to the sample. The temperatures reported here are thus only indicative of this particular setup and can only be used as qualitative guidelines when comparing with other setups.



At the beginning of my PhD thesis, the growth chamber was located at the ESRF and physically connected to beamline BM32. This allowed for *in situ* x-ray characterization of the samples. After one year, the whole setup was disconnected from the beamline and transferred to the CEA-Grenoble site.

### 1.3.2 GeMn nanocolumns : a family picture

Initial studies in the GeMn nanocolumns were performed by Devillers during his PhD and are presented in his manuscript [96] and the relevant publications [22, 82, 83]. In the following I will give a quick overview of these results in the GeMn nanocolumns system. More details can be found in the previously cited references.

During the low temperature MBE growth of Ge and Mn, a spinodal decomposition occurs and results in Mn rich regions, embedded in a Mn-poor Ge matrix. These results were obtained by analyzing the local chemical composition in a transmission electron microscope using electron energy loss spectroscopy (EELS) and energy-filtered TEM imaging. A typical classical TEM micrograph is shown in figure 1.6(a), along with its energy-filtered equivalent in figure 1.6(b) and an energy-filtered plane view TEM micrograph in figure 1.6(c). Quantitative EELS analysis, assuming a homogeneous atomic density, suggests a local concentration of about 30–40% Mn in the nanocolumns (*i.e.* close to  $\text{Ge}_2\text{Mn}$ ) and less than 1% (below the detection threshold) in the matrix.

Depending on the growth parameters, *i.e.*, on the substrate temperature during the growth ( $T_{\text{growth}}$ ) and the Mn concentration, different types of nanocolumns can be obtained, as it is clearly visible in figure 1.6(d). Smaller Mn concentrations and/or smaller  $T_{\text{growth}}$  result in smaller and denser nanocolumns, coherent with the Ge matrix. Larger concentration and larger  $T_{\text{growth}}$  result in larger, amorphous nanocolumns. In addition, upon growth at higher substrate temperature,  $\text{Ge}_3\text{Mn}_5$  metallic clusters precipitate. Such clusters can be seen in the RHEED pattern during the growth or as Moiré pattern in TEM micrograph, due to their different crystalline structure.

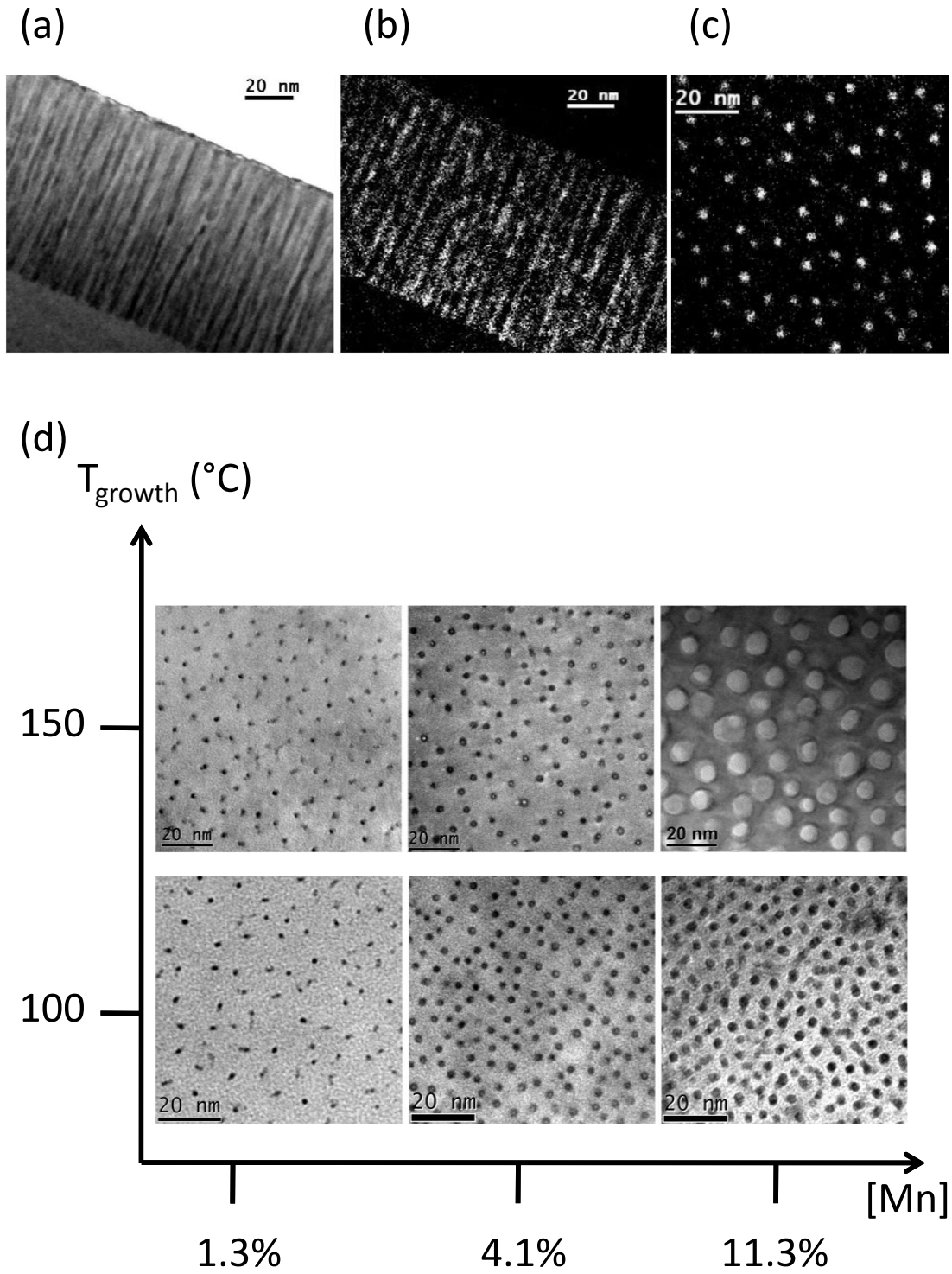


FIGURE 1.6: Cross-sectional TEM micrographs in (a) classical mode and EF-TEM mode in cross-section (b) and plane-view (c). Bright pixels are Mn-rich regions. (d) Overview of the different types of (Ge,Mn) nanocolumns obtained by low temperature MBE by tuning the Mn concentration and the growth temperature. All pictures adapted from [82].

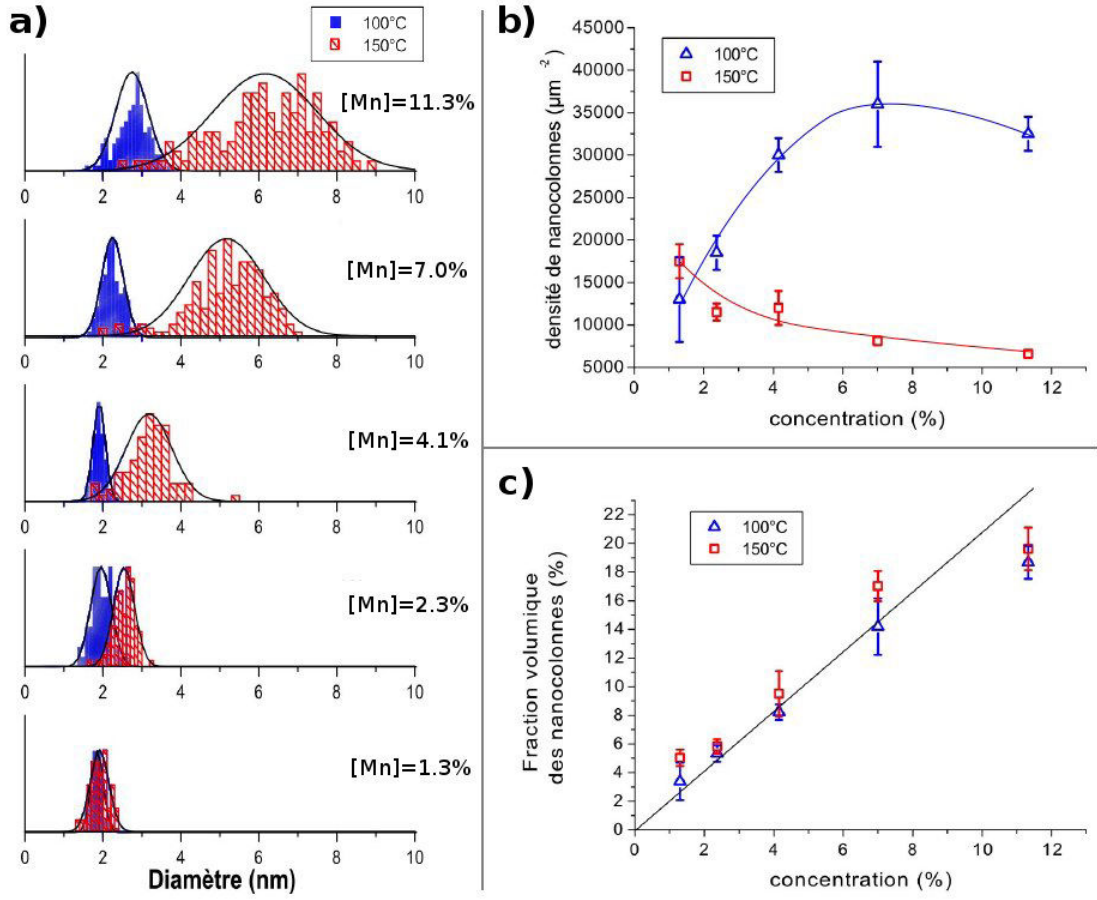


FIGURE 1.7: Morphological characteristics of the GeMn nanocolumns as a function of the growth parameters. (a) diameters distribution, (b) density, and (c) volumic fraction of the nanocolumns as a function of the growth temperature and of the Mn concentration. All pictures adapted from [82].

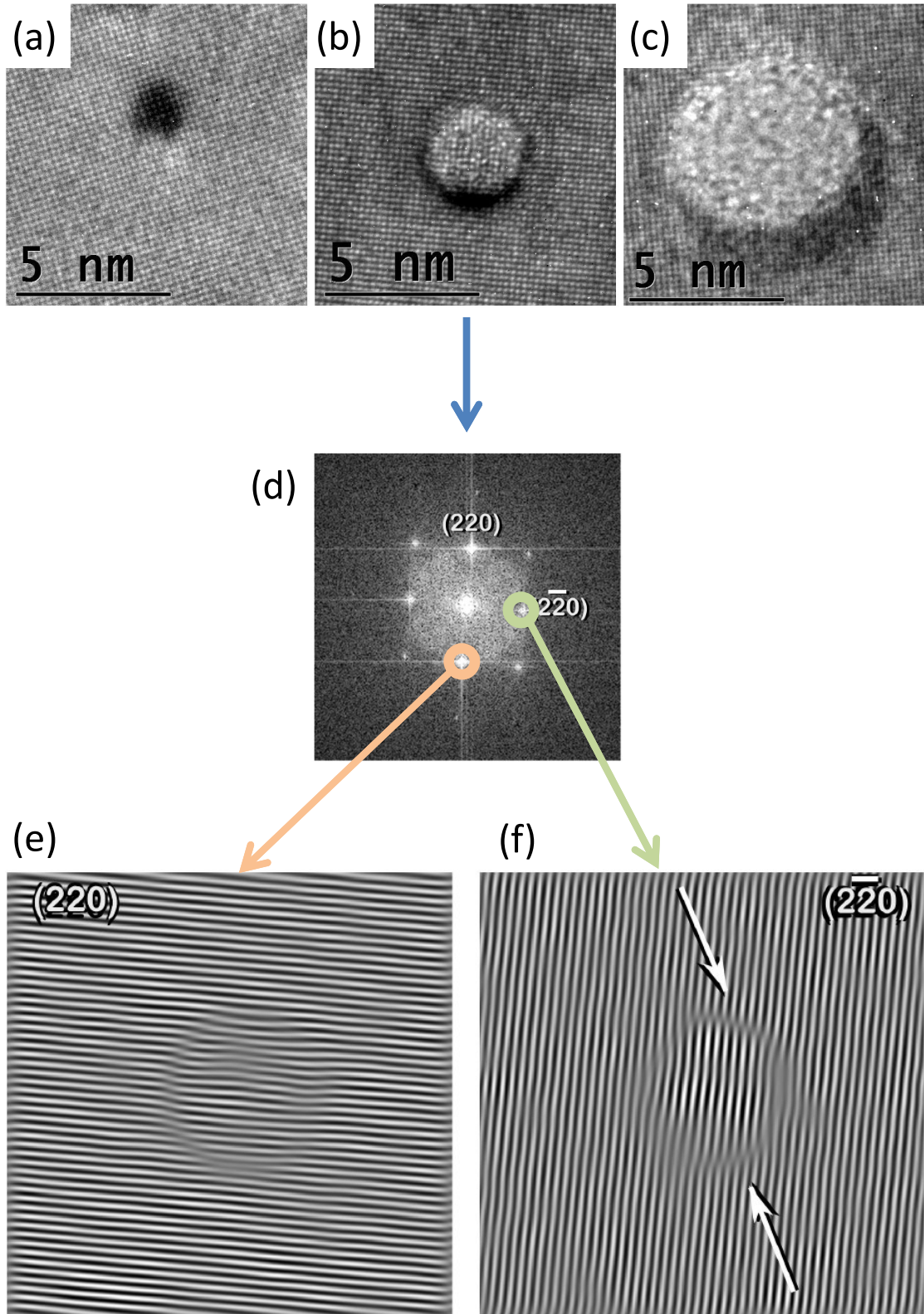


FIGURE 1.8: High-resolution TEM images of (a) small, (b) medium, and (c) large-sized nanocolumns. (d) Diffraction pattern corresponding to (b). Filtered image using (e) the  $220$  and (f) the  $\bar{2}\bar{2}0$  reflections : a pair of dislocations can be seen at the nanocolumn/matrix interface. All pictures adapted from [82].

The influence of the growth parameters on the morphological properties (diameters, densities) of the nanocolumns are more quantitatively shown in figure 1.7. These results can be summarized as follows : at low  $T_{\text{growth}}$  the diameters remain almost constant while the density increases (and saturates) with increasing [Mn]. On the opposite, at high  $T_{\text{growth}}$  the diameters increase while the density slowly decreases with increasing [Mn]. This can be simply explained by the fact that at low temperature surface mobility is hindered, then the maximum diameters are easily reached and additional Mn atoms will rather result in new nucleation sites. At high temperature surface diffusion is dominant and increasing the number of Mn atoms results in a increase of the size of the nanocolumns.

It can also be seen in figure 1.7(c) that the volumic fraction of the nanocolumns scales almost linearly with the Mn concentration, suggesting a constant Mn concentration in the nanocolumns and a similar incorporation mechanism over  $T_{\text{growth}}$  and [Mn].

High-resolution TEM provided additional information about the structure in and around the nanocolumns, as seen in figure 1.8. Small and medium-sized nanocolumns appear rather coherent with the matrix, while large nanocolumns, as stated before, are clearly amorphous. No particular structural defects can be seen in small nanocolumns, except for the contrast variation. Medium-sized nanocolumns show a pair of dislocations in the  $2\bar{2}0$  planes. This is likely due to strain relaxation in the nanocolumns, and shows that the lattice parameter inside the nanocolumn is 4% larger than in the matrix.

EXAFS measurements by Rovezzi *et al.* in small to medium-sized nanocolumns indicated some disorder in the nanocolumns [85]. Interpretation of the spectra is a very arduous task, but the authors concluded about the observation of structures similar to one the building blocks in the  $\text{Ge}_3\text{Mn}_5$  crystalline structures and shaped as a Ge3-Mn tetrahedron.

Upon annealing, the nanocolumns appear to collapse and form spherical  $\text{Ge}_3\text{Mn}_5$  clusters that sink toward the interface with the buffer, as shown in figure 1.9 and similarly to results reported by Lechnert *et al.* [74]. The resulting clusters are much larger than the nanocolumns they replace and have much smaller surface-to-volume ratio. This indicates that the precipitation is driven not only by formation energy differences but also by interface energy minimization.

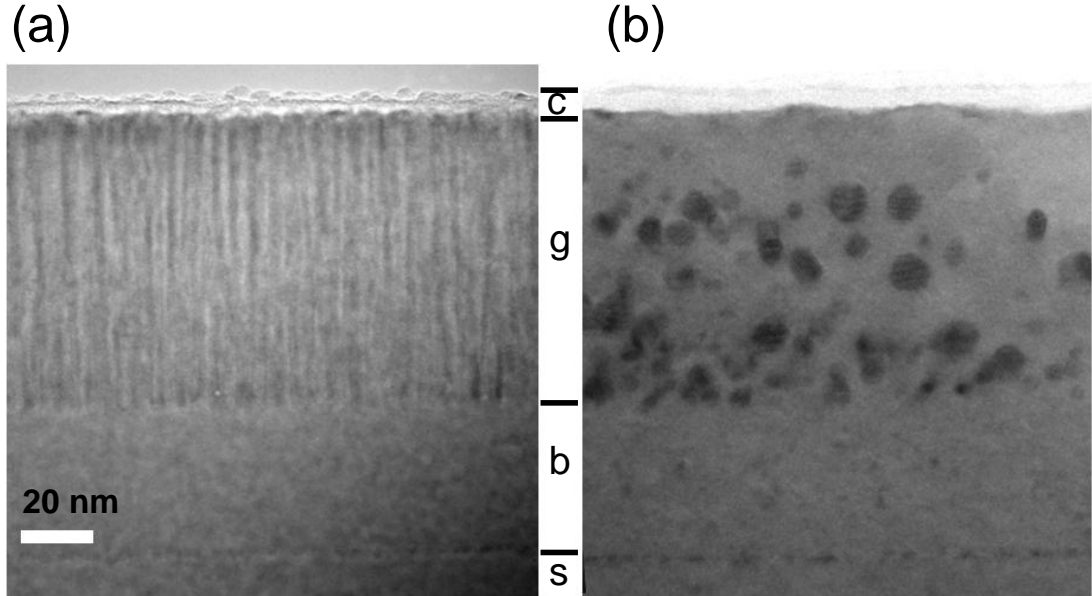


FIGURE 1.9: TEM images in cross-section for the same sample, (a) before and (b) after annealing. Upon annealing, the nanocolumns collapse in larger spherical clusters, located towards the buffer interface. The labels are : c = capping, g = GeMn layer, b = Ge buffer and s = Ge substrate. Micrographs measured by Devillers.

A theoretical work on the structure inside the nanocolumns using *ab initio* methods was performed at the same time as this thesis by Arras at the CEA-Grenoble [97]. The corresponding results will be discussed along those from this work in the next chapters.

### 1.3.3 Intriguing magnetic properties of the GeMn nanocolumns

Magnetic properties of the nanocolumns were also performed by Devillers *et al.* using SQUID magnetometry mostly. The relevant results have been published in refs. [22, 82, 83] and shall be recalled here.

SQUID magnetometry provides information about the magnetization in the complete sample. Hence, two main contributions have been observed, stemming from (i) ferromagnetic nanocolumns and (ii) paramagnetic interstitial Mn atoms. The

corresponding measurements and interpretations are shown in figure 1.10(a) and (b). In ref. [82], Devillers *et al.* have extended the interpretation to the contribution of (iii) high- $T_C$  FM nanocolumns, and (iv)  $\text{Ge}_3\text{Mn}_5$  clusters, in specific samples.

Zero-Field-Cooled–Field-Cooled (ZFC-FC) magnetometry showed a superparamagnetic behavior of the clusters and of the nanocolumns. The process is illustrated in figure 1.10(c) and (d) for a sample containing  $\text{Ge}_3\text{Mn}_5$  clusters (see ref. [82] for other examples). Since the blocking temperature is related to the anisotropy and to the volume of the superparamagnetic objects, it also allowed for a determination of their *magnetic size*. It appeared that such sizes in the analyzed nanocolumns were four times smaller than the nanocolumns themselves, suggesting a magnetic discontinuity along the nanocolumns.

No magnetic anisotropy could be evidenced in the coherent nanocolumns. This result is quite unexpected since shape anisotropy should be predominant, given the aspect ratio of the objects. A possible explanation is that the shape anisotropy is compensated by the magnetocrystalline anisotropy. This is further supported by the fact that in amorphous nanocolumns, the expected out-of-plane anisotropy is observed. It was also suggested that some anisotropy may exist in coherent nanocolumns along orientations that are neither in-plane nor out-of-plane.

### 1.3.4 What is left to be known about the nanocolumns ?

The different magnetic and structural characterizations performed in the GeMn nanocolumns system have given some very interesting answers but also risen many questions. Among those, the crystal structure *inside* the nanocolumns is still unknown. The origin of the magnetic coupling between the nanocolumns has also yet to be established. The magnetic measurements have only provided bulk properties and detailed informations about the magnetic properties on the Mn atoms are still missing. Hence my PhD thesis was dedicated to the analysis of the *local* electronic, magnetic, and structural properties of the Mn atoms in the GeMn nanocolumns system, using to that end synchrotron radiation-base techniques.



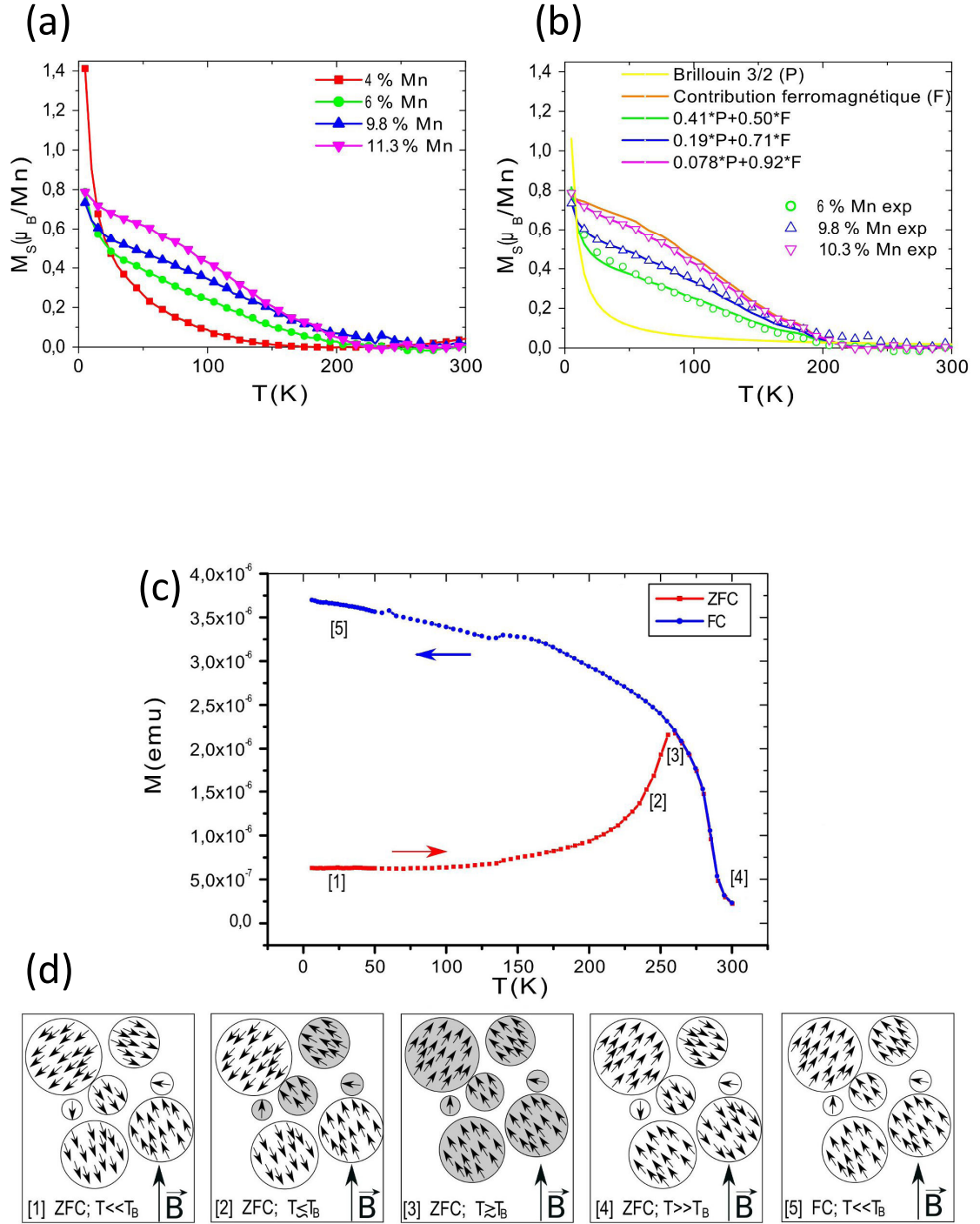


FIGURE 1.10: (a) Magnetic moment per Mn atom as function of the temperature in GeMn nanocolumns with different Mn concentrations. (b) Corresponding fit as the sum of a paramagnetic phase (P, diluted Mn atoms in the matrix) and of a ferromagnetic phase (F, GeMn nanocolumns). (c) Zero-Field-Cooled-Field-Cooled measurements in a sample containing  $\text{Ge}_3\text{Mn}_5$  clusters. The magnetization process is illustrated in (d). All pictures adapted from [82].



## 1.4 Conclusion

In this chapter, we have described the current issues in the field of spintronics, with a direct connection to applications. We have seen that ferromagnetic semiconductors are considered as a viable solution for the different problems currently encountered in spintronics. It was shown in particular that heterogeneous systems may offer new research routes towards above-room-temperature carrier mediated ferromagnetism. We have reviewed the (Ge,Mn) system and shown that out-of-equilibrium growth techniques were required to obtain the metastable coherent GeMn nanocolumns. A overview of the current knowledge about the GeMn nanocolumns at the begin of this thesis was given. It was stressed that an experimental analysis of the *electronic*, *magnetic*, and *structural* properties of the Mn atoms in the GeMn nanocolumns system is required, which is the primary aim of this thesis. It is underlined that to achieve the high sensitivity required for nano-sized objects and the chemical selectivity required for local measurements, synchrotron radiation-based techniques are highly suited and have been used in during this thesis.

## 1.5 Résumé du chapitre 1

Le chapitre 1 présente le contexte général de la thèse, depuis le domaine de l'électronique de spin (ou spintronique) jusqu'au cas particulier du matériau semi-conducteur ferromagnétique (Ge,Mn).

Dans ce chapitre, nous avons décrit les problématiques actuelles dans le domaine de la spintronique, en connexion directe avec les applications. Nous avons vu que les semiconducteurs ferromagnétiques sont considérés comme une solution viable aux différents problèmes rencontrés par la spintronique. En particulier, il a été montré que les systèmes hétérogènes peuvent offrir une nouvelle voie de recherche vers la maîtrise du ferromagnétisme à température ambiante médié par les porteurs de charges. Une revue du système (Ge,Mn) a été présentée et nous avons vu que des techniques de croissance hors-équilibre étaient nécessaire pour obtenir les nanocolonnes de GeMn métastables. Nous avons également décrit l'état général des connaissances sur le système (Ge,Mn) au moment du début de cette thèse. Nous avons ainsi montré qu'une étude des propriétés électroniques, magnétiques et structurales des atomes de Mn dans les nanocolonnes de GeMn était nécessaire, ce qui a constitué l'objectif principal de cette thèse. Nous avons aussi souligné que les techniques synchrotron, principaux outils expérimentaux de cette thèse, étaient nécessaires pour obtenir à la fois la haute sensibilité requise pour l'étude de nano-objets et la sélectivité chimique pour des mesures locales.

# Chapitre 2

## X-ray scattering

X-ray scattering is the method of choice to study structural and dynamic properties at an atomistic level. The rapid development of intense synchrotron radiation sources and of new detectors has allowed for faster measurements over larger areas. Informations about the size, shape, density, internal atomic structure or strain in nanoobjects (*e.g.*, GeMn nanocolumns) can be obtained using x-ray scattering techniques, as described in this chapter.

This chapter is divided in four sections. First, I introduce a few basic concepts in x-ray scattering theory, such as the atomic scattering factor, and show how anomalous scattering can be used to enhance the chemical contrast. Second, I give a quick overview of the grazing incidence x-ray scattering technique and show how this technique is particularly adapted to thin films. In the third section, I review a few important results on the diffuse scattering from defects. Finally, I describe the different experimental setups that have been used at the ESRF, as well as the principal measurement and data processing procedures.

### 2.1 X-ray scattering in matter

In this section, we start from the scattering of an electromagnetic wave by free electron to finally describe the scattering of x-ray by matter, in terms of atomic scattering factor. The basic tools for the description of x-ray diffraction are also introduced.

### 2.1.1 Elastic scattering by a free electron

Let us start with the most simple case of the elastic scattering (Thomson scattering) of a photon by a free electron. The elastic scattering can be seen classically as the emission of radiation by the electron accelerated by the oscillating electric field of the incident electromagnetic wave. The intensity scattered  $I_f$  in a unit solid angle  $d\Omega$  (figure 2.1) can be written as a function of the incident intensity  $I_i$  as

$$I_f = Pr_e^2 I_i \quad (2.1)$$

where  $r_e = \frac{e^2}{4\pi\epsilon_0 m_e c^2}$  is the classical radius of the electron,  $m_e$  its mass<sup>1</sup>,  $e$  its charge,  $c$  the celerity of light and  $\epsilon_0$  the vacuum permittivity. The factor  $P$  represent the dependence of the scattered intensity on the polarization of the incident wave and on the scattering direction.

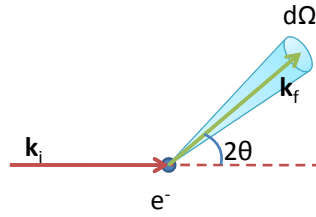


FIGURE 2.1: Scattering of an incident wave with wavevector  $\mathbf{k}_i$  in an elementary solid angle  $d\Omega$ .

### 2.1.2 Elastic scattering by a cloud of electrons

We now consider a second scatterer, at distance  $\mathbf{r}$  from the first one, as depicted in figure 2.2. The incoming wave is seen as a plane wave, with wavevector  $\mathbf{k}_i = \frac{1}{\lambda}\mathbf{x}$  (we use the crystallographer's notation), where  $\lambda$  is the wavelength and  $\mathbf{x}$  an unitary vector pointing along the propagation direction. Let us consider the scattered wave at angle  $2\theta$  with wavevector  $\mathbf{k}_f$ . The phase shift between the two scatterers is

$$\delta = \frac{2\pi}{\lambda}(O'B - OA) = 2\pi(\mathbf{k}_f - \mathbf{k}_i) \cdot \mathbf{r} = 2\pi\mathbf{Q} \cdot \mathbf{r} \quad (2.2)$$

---

1. The mass of the proton is three orders of magnitude larger, therefore when we will consider the scattering by an *atom*, we can safely restrict ourselves to the scattering by its electrons only.

where  $\mathbf{Q} = \mathbf{k}_f - \mathbf{k}_i$  is the scattering vector. The amplitude  $Q$  of the scattering vector  $\mathbf{Q}$  is  $\frac{2 \sin \theta}{\lambda}$ .

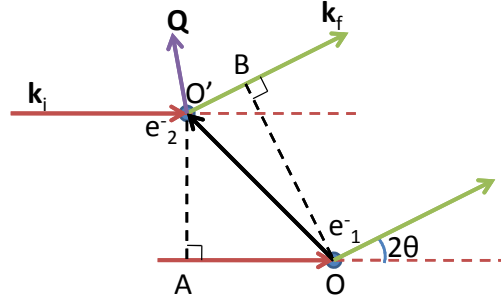


FIGURE 2.2: Scattering of an incident plane wave with wavevector  $\mathbf{k}_i$  by two distant scattering electrons ( $e_1^-$  and  $e_2^-$ ).

Let us extend to a cloud of scatterer, with density  $\rho(\mathbf{r})$ . The intensity scattered along  $\mathbf{k}_f$  (i.e., with scattering vector  $\mathbf{Q}$ ) can be written as an integral over all the scatterers :

$$I_f = Pr_e^2 \int \rho(\mathbf{r}) e^{i\delta} d\mathbf{r} = Pr_e^2 \int \rho(\mathbf{r}) e^{i2\pi\mathbf{Q}\cdot\mathbf{r}} d\mathbf{r} \quad (2.3)$$

It appears that the scattering by a cloud of electrons is proportional to the Fourier transform of the electron density  $\rho(\mathbf{r})$ . If we consider this electron cloud to be that of an atom and to be a spherically symmetric, the intensity scattered by this atom, called the *atomic scattering factor* (noted  $f$ ), depends only on  $\frac{\sin \theta}{\lambda}$ . The atomic scattering factors for Ge and Mn are plotted in figure 2.3. Note that in the forward scattering limit ( $\theta = 0$ ),  $f$  is equal to the number of electrons  $Z$  of the atom.

### 2.1.3 The complex atomic scattering factor

In the previous subsection, we have seen that the atomic scattering factor is equal to the Fourier transform of the electron density. However, when considering electrons that are bound to the atoms, the oscillating electric field of the incoming photon is not the only applied force on the electron. In fact, we may model the electron as a damped oscillator, satisfying the second-order differential equation

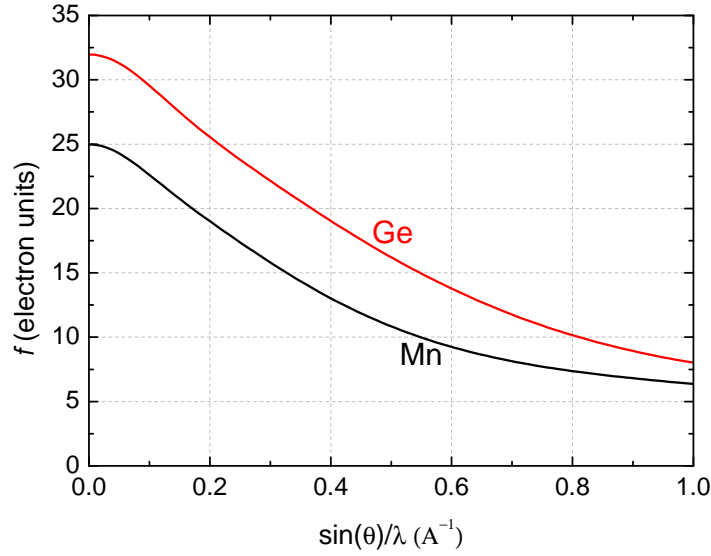


FIGURE 2.3: Atomic scattering factors for Mn and Ge, calculated using the Cromer–Mann coefficients [98, 99].

$$\frac{d^2 \mathbf{x}}{dt^2} + g \frac{d\mathbf{x}}{dt} + \omega_0^2 \mathbf{x} = \frac{e}{m_e} \mathbf{E}_{0i} e^{i\omega t} \quad (2.4)$$

where  $\mathbf{x}$  is the electron position,  $g$  a damping parameter,  $\omega_0$  the undamped angular frequency and  $\mathbf{E}_{0i} e^{i\omega t}$  the oscillating electric field of the photon with angular frequency  $\omega$ . A solution to this equation is

$$\mathbf{x} = \frac{1}{(\omega_0^2 - \omega^2 + ig\omega)} \frac{e}{m_e} \mathbf{E}_{0i} e^{i\omega t} \quad (2.5)$$

The oscillating electron radiates an electric field with the same frequency as the electric field of the incoming photon. In a plane perpendicular to the plane of the electric field of the incoming wave, the amplitude of the radiated electric field at distance  $r$  is

$$A = \frac{r_e}{r} \frac{\omega^2}{(\omega_0^2 - \omega^2 + ig\omega)} E_{0i} \quad (2.6)$$

In the same condition, a free electron would radiate an electric field with amplitude  $A_0 = \frac{r_e}{r} E_{0i}$ . The ratio  $\frac{A}{A_0}$  defines the electron scattering factor  $f_e$ :

$$f_e = \frac{\omega^2}{(\omega_0^2 - \omega^2 + ig\omega)} = 1 + f'(\omega) + if''(\omega) \quad (2.7)$$

$$f'(\omega) = \frac{\omega_0^2(\omega^2 - \omega_0^2) - g^2\omega^2}{(\omega_0^2 - \omega^2)^2 + g^2\omega^2} \quad (2.8)$$

$$f''(\omega) = \frac{g\omega^3}{(\omega_0^2 - \omega^2)^2 + g^2\omega^2} \quad (2.9)$$

As a result, the atomic scattering factor will be a complex number. It is usually written

$$f(\theta, \lambda) = f^0\left(\frac{\sin \theta}{\lambda}\right) + f'(\lambda) + if''(\lambda) \quad (2.10)$$

The first term  $f^0$  is the Thomson scattering factor introduced in section 2.1.2. The second and third terms are the anomalous or resonant contributions. They describe the absorption due to the photoelectric effect in the atom and therefore they vary greatly around absorption edges. In figure 2.4 are plotted the real ( $f_1 = f_0 + f'$ ) and the imaginary ( $f_2 = f''$ ) part of the atomic scattering factor. A clear enhancement of  $f_2$  can be seen at the different absorption edges. Such large variations of the atomic scattering factor at given energies can be used to enhance the chemical contrast in the scattered signal. It is the basis of anomalous scattering experiments.

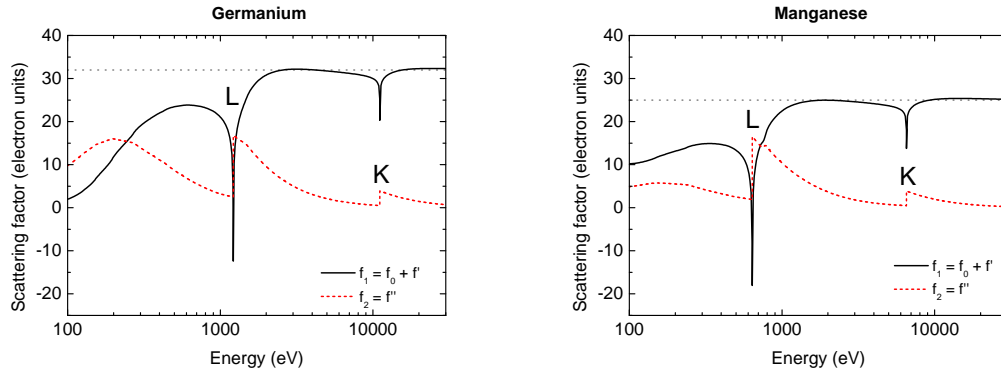


FIGURE 2.4: Real ( $f_1 = f_0 + f'$ ) and imaginary parts ( $f_2 = f''$ ) of the atomic scattering factors for Ge and Mn, (data taken from ref. [100]). The dotted grey line indicates the number  $Z$  of electrons in the atom. Large variations of  $f_1$  and  $f_2$  can be seen around the K,  $L_1$ ,  $L_2$  and  $L_3$  absorption edges.

### 2.1.4 The atomic scattering factor in a crystal and the Kramers-Kronig relations

The atomic scattering factor derived in equation 2.10 is valid for an *isolated* atom. For an atom in condensed matter, *e.g.*, in a crystal, interferences between neighboring atoms will occur. In fact, near an absorption edge, the photoelectron emitted by the photoelectric effect from a core level may be backscattered from neighboring atoms and interfere with the emitted wave, resulting in a local modification of the absorption and diffusion. This phenomenon is well known and experimentally measured in the X-ray Absorption Near Edge Structure (XANES) and Extended X-ray Absorption Fine Structure (EXAFS) techniques. Such techniques are not the topic of this manuscript<sup>2</sup>, however it is worth mentioning that using such core-level absorption spectroscopies, one may measure the absorption coefficient of a given species in a sample, and therefore access the  $f''$  coefficient of that species.

The  $f'$  coefficient can be accessed using the Kramers-Kronig relations. These relations link the dispersive ( $f'$ ) and the absorptive ( $f''$ ) parts of the atomic scattering factor, as a consequence of the principle of causality : there cannot be absorption without dispersion [102]. The expressions of the relations are

$$f'(\omega_0) = \frac{2}{\pi} \text{p.v.} \int_0^\infty \frac{\omega}{\omega^2 - \omega_0^2} f''(\omega) d\omega \quad (2.11)$$

$$f''(\omega_0) = \frac{2}{\pi} \text{p.v.} \int_0^\infty \frac{-1}{\omega^2 - \omega_0^2} f'(\omega) d\omega \quad (2.12)$$

where p.v. indicates the Cauchy principal value. An exemple<sup>3</sup> of  $f'$  and  $f''$  for Mn in  $\text{Ge}_3\text{Mn}_5$  is shown in figure 2.5. Oscillations, *i.e.*, the fine structure, due to the interferences with the neighboring atoms are clearly visible in the experimental data.

---

2. The reader may find more details on these techniques applied to the GeMn system in the PhD manuscript by M. Rovezzi [101] and ref. [85], as well as additional interpretation in the PhD manuscript by E. Arras [97].

3. Measurement of  $f''$  and calculation of  $f'$  by M. Rovezzi.



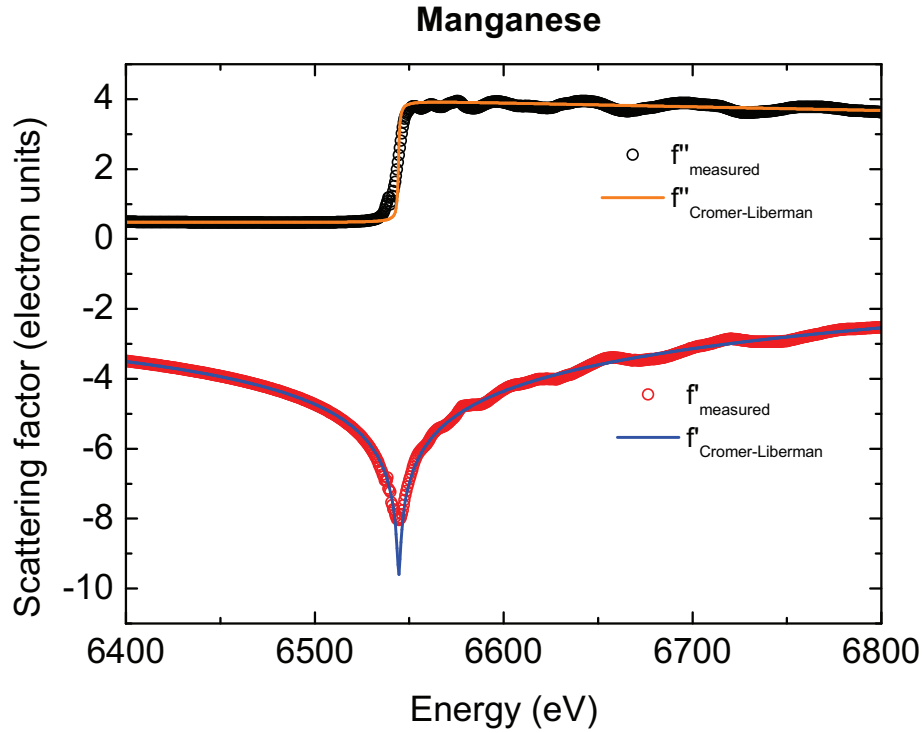


FIGURE 2.5: Experimental and Cromer-Liberman calculated [103]  $f'$  and  $f''$  around the Mn K edge in  $\text{Ge}_3\text{Mn}_5$ . Measurements and calculations using the DIFFKK code [104] by M. Rovezzi.

## 2.2 X-ray scattering and diffraction by a crystal

### 2.2.1 The structure factor

In a crystal, all atoms will act as scatterers. Let us first consider the unit cell of the crystal. The amplitude  $F$  of the wave scattered with scattering vector  $\mathbf{Q}$  by the unit cell is proportional to the sum of all individually scattered wave by each atom  $i$  in the unit cell, with atomic scattering factor  $f_i$ , and taking into account the respective phase shifts (see figure 2.2)

$$F(\mathbf{Q}) = \sum_{\text{atoms } i} f_i(\theta, \lambda) e^{i2\pi\mathbf{Q}\cdot\mathbf{r}_i} \quad (2.13)$$

For example, in Ge diamond there are 8 Ge atoms in the unit cell at the fractional coordinates  $\left\{ (0, 0, 0); (0, \frac{1}{2}, \frac{1}{2}); (\frac{1}{2}, 0, \frac{1}{2}); (\frac{1}{2}, \frac{1}{2}, 0); (\frac{3}{4}, \frac{1}{4}, \frac{3}{4}); (\frac{3}{4}, \frac{3}{4}, \frac{1}{4}); (\frac{1}{4}, \frac{1}{4}, \frac{1}{4}); (\frac{1}{4}, \frac{3}{4}, \frac{3}{4}) \right\}$ , with the cubic lattice parameter  $a = 5.657 \text{ \AA}$ . Hence the structure factor can be written

$$F(\mathbf{Q}) = f_{Ge}(\theta, \lambda) (1 + e^{i\pi(k+l)} + e^{i\pi(h+l)} + e^{i\pi(h+k)} + e^{i\frac{\pi}{2}(3h+k+3l)} + e^{i\frac{\pi}{2}(3h+3k+l)} + e^{i\frac{\pi}{2}(h+k+l)} + e^{i\frac{\pi}{2}(h+3k+3l)}) \quad (2.14)$$

where we note  $(\mathbf{a}, \mathbf{b}, \mathbf{c}) = a(\mathbf{x}, \mathbf{y}, \mathbf{z})$  the basis vector of the unit cell.

### 2.2.2 The reciprocal lattice

The reciprocal lattice is defined using the following basis vectors

$$\begin{aligned} \mathbf{a}^* &= \frac{\mathbf{b} \times \mathbf{c}}{V} \\ \mathbf{b}^* &= \frac{\mathbf{c} \times \mathbf{a}}{V} \\ \mathbf{c}^* &= \frac{\mathbf{a} \times \mathbf{b}}{V} \end{aligned} \quad (2.15)$$

where  $V = \mathbf{a} \cdot \mathbf{b} \times \mathbf{c}$  is the volume of the unit cell.

In that basis, the scattering vector  $\mathbf{Q}$  is written

$$\mathbf{Q} = h\mathbf{a}^* + k\mathbf{b}^* + l\mathbf{c}^* \quad (2.16)$$

such that

$$\begin{aligned} \mathbf{Q} \cdot \mathbf{a} &= h \\ \mathbf{Q} \cdot \mathbf{b} &= k \\ \mathbf{Q} \cdot \mathbf{c} &= l \end{aligned} \quad (2.17)$$

It is easily verified that  $\mathbf{Q}$  written as in equation 2.16 complies with equations 2.17.

### 2.2.3 The form factor

In order to take into account *all* scatterers in the crystal, the sum in equation 2.13 must be extended to all the cells  $j$  (at positions  $R_j$ ) of the crystal to calculate the *total* amplitude of the scattered wave

$$A(\mathbf{Q}) = \sum_{cell} \sum_j \sum_{atoms} f_i(\theta, \lambda) e^{i2\pi\mathbf{Q} \cdot (\mathbf{r}_i + \mathbf{R}_j)} \quad (2.18)$$

$$= \left( \sum_{cell} e^{i2\pi\mathbf{Q} \cdot \mathbf{R}_j} \right) \left( \sum_{atoms} f_i(\theta, \lambda) e^{i2\pi\mathbf{Q} \cdot \mathbf{r}_i} \right) \quad (2.19)$$

$$= D(\mathbf{Q})F(\mathbf{Q}) \quad (2.20)$$

The factor  $D(\mathbf{Q})$  is the form factor. We note  $\mathbf{R}_j = n_x\mathbf{a} + n_y\mathbf{b} + n_z\mathbf{c}$ , hence, using equations 2.17,  $\mathbf{Q} \cdot \mathbf{R}_j = n_x h + n_y k + n_z l$ . In the particular case of a parallelepipedic crystal, let  $(N_x, N_y, N_z)$  be the total number of cells in the crystal along  $(\mathbf{x}, \mathbf{y}, \mathbf{z})$ . The form factor can be written

$$D(\mathbf{Q}) = \frac{\sin \pi N_x h}{\sin \pi h} \frac{\sin \pi N_y k}{\sin \pi k} \frac{\sin \pi N_z l}{\sin \pi l} \quad (2.21)$$

In the case of an infinite crystal ( $N_{x,y,z} \rightarrow \infty$ ), the limit of  $D(\mathbf{Q})$  is a Dirac comb, with non-zero values for integer values of  $(h, k, l)$ , *i.e.* when the scattering vector  $\mathbf{Q}$  joins two reciprocal lattice points (equation 2.16). In that case all cells interfere constructively, the crystal is in *diffraction* condition. If the crystal is not infinite, equation 2.21 indicates that there will be an interference pattern and non zero-values around the integer values of  $(h, k, l)$  (*i.e.* around the nodes of the reciprocal lattice). The broadening of the corresponding Bragg peak in a given direction is on the order of  $\frac{1}{N}$ , *e.g.* for nanocolumns with a diameter of 5 Ge diamond unit cells ( $\approx 2.8$  nm), the broadening should be about 0.2 reciprocal lattice units (r.l.u.).

## 2.2.4 Extinction rules

We now go back to the structure factor  $F(\mathbf{Q})$ . We know that  $(h, k, l)$  must be integers to obtain a diffracted intensity. However  $F(\mathbf{Q})$  may also contain some specific rules on  $(h, k, l)$  to obtain a non-zero factor, due to the symmetry of the atoms *inside* the unit cell. In fact, in the example of Ge diamond described in equation 2.14, it can be shown that  $(h, k, l)$  must have the same parity<sup>4</sup>. Additionally, it can be verified that  $h + k + l$  must be either odd or a multiple of 4 for  $F(\mathbf{Q})$  to be

4. This condition is typical of the face-center cubic crystal structure, indeed diamond is composed of two fcc structures, shifted by  $(\frac{1}{4}, \frac{1}{4}, \frac{1}{4})$

non-zero. Such rules are known as the extinction conditions and are characteristic of a given crystal structure.

### 2.2.5 Bragg's law

The general diffraction conditions can be seen in an equivalent way as the reflection on the set of parallel planes defined by their normal  $\mathbf{h} = h\mathbf{a}^* + k\mathbf{b}^* + l\mathbf{c}^*$ , as depicted in figure 2.6. The diffraction angle can be put a simple form, known as the Bragg's law :

$$2d \sin \theta = \lambda \quad (2.22)$$

where  $\theta$  is the usual angle of reflexion and  $d$  is the distance between the planes. In the cubic lattice

$$d(h, k, l) = \frac{a}{\sqrt{h^2 + k^2 + l^2}} \quad (2.23)$$

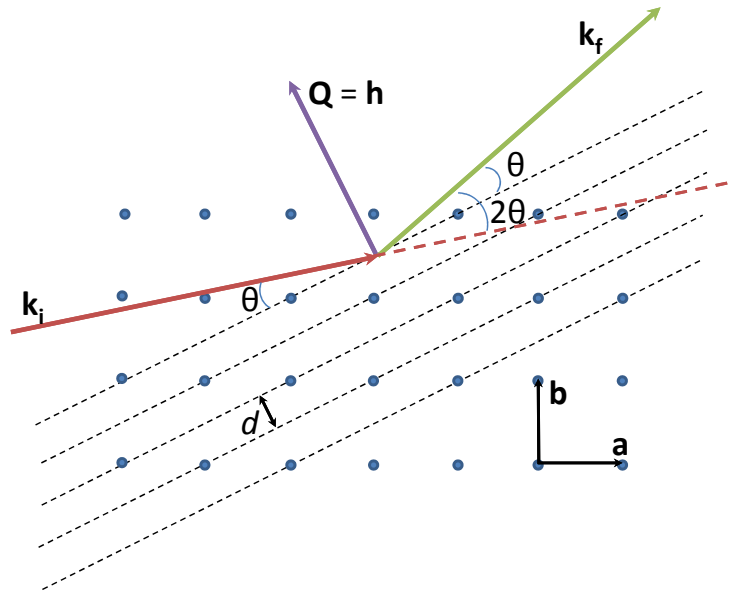


FIGURE 2.6: Simple sketch of the Bragg condition of diffraction in a cubic crystal. The x-rays are reflected on the family of reticular planes for which the normal is  $\mathbf{h}$ . The incident and reflected angle with respect to the planes is the Bragg angle  $\theta$ .

### 2.2.6 Ewald's sphere

The Ewald's sphere is a simple graphical construction, illustrated in figure 2.7 that allows for the determination of the diffraction condition. One considers a sphere,

centered on the crystal  $C$  and with radius  $\frac{1}{\lambda}$ . We can set a point  $A$  on the sphere such that  $\mathbf{AC}=\mathbf{k}_i$ . We now construct the reciprocal lattice, *i.e.* all the points (nodes)  $h\mathbf{a}^* + k\mathbf{b}^* + l\mathbf{c}^*$  such that  $(h, k, l)$  are integers (*i.e.* all the extremities of the  $\mathbf{h}$  vectors). The origin  $O^*$  of the reciprocal lattice is also set on the sphere, such that  $\mathbf{AC}=\mathbf{CO}^*$ . All the accessible scattering vectors  $\mathbf{Q}$  are now located on the sphere. If a node  $N$  lies on the sphere  $\mathbf{Q}=\mathbf{O}^*\mathbf{N}=\mathbf{h}$  : it is in diffraction condition for  $\mathbf{k}_f=\mathbf{CN}$ .

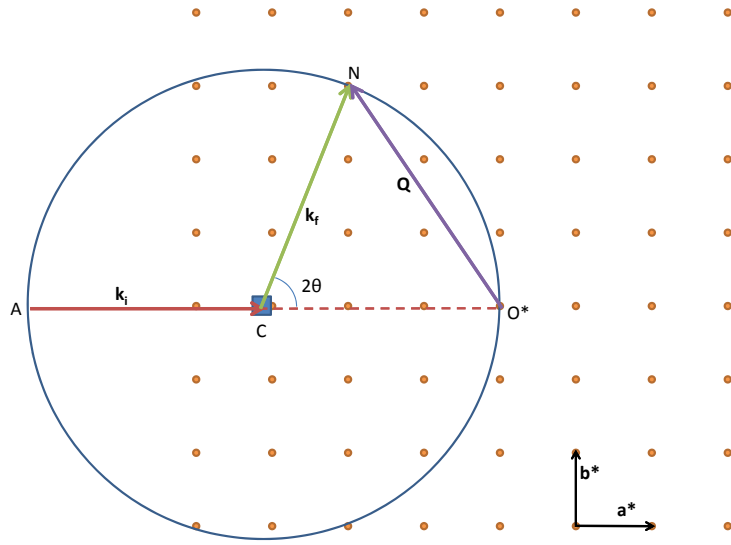


FIGURE 2.7: Construction of the Ewald's sphere in 2D. The crystal is centered in  $C$ , the incoming wavevector is  $\mathbf{AC}=\mathbf{k}_i$ . During a diffraction experiment, the crystal is rotated around its position  $C$ . As a result, the reciprocal lattice rotates around its origin  $O^*$ . Diffraction will occur every time a node of the reciprocal lattice intersects the Ewald's sphere. In the case depicted here, the node  $N$  of the reciprocal lattice is in diffraction condition, the diffracted intensity is measured along  $\mathbf{k}_f=\mathbf{CN}$  and the corresponding scattering vector is  $\mathbf{Q}=\mathbf{O}^*\mathbf{N}$ .

## 2.3 Grazing-incidence x-ray scattering

In this section, the total reflection condition is recalled and the critical angle of total reflection is defined, based on the refraction index and the atomic scattering factor. The scattering depth is calculated and it is shown that grazing incidence x-ray scattering can be used as probe of the surface layer of a few nanometers.

### 2.3.1 The total reflection condition and the critical angle

When an electromagnetic wave arrives at an interface between two different media, it undergoes a well known refraction phenomenon. To describe it, we will use the following approximations, known as the Fresnel approach [105] : the interface between the media is supposed to be sharp, and each medium is taken as homogeneous and characterized by a refraction index  $n$ . The refraction index contains the information of the interaction of the electromagnetic wave with the medium. For example, the refraction index in vacuum is equal to one. In matter, the refraction index depends on the energy of the electromagnetic wave. Certain specific frequencies give rise to resonant phenomena due to electronic transitions in the medium (the photoelectric effect). In the case of x-rays, their energy is higher than most electronic transitions, except K- and L-edge transitions which correspond to core electrons. In order to take account both dispersion ( $\delta$ ) and absorption ( $\beta$ ) phenomena in matter, it is necessary to write the refraction index as a complex number [106]

$$n = 1 - \delta + i\beta \quad (2.24)$$

with, far from any absorption edge,

$$\delta = \frac{\lambda^2}{2\pi} r_e \rho_e \quad (2.25)$$

$$\beta = \frac{\lambda}{4\pi} \mu \quad (2.26)$$

where  $\lambda$  is the wavelength of the x-ray radiation,  $r_e$  is the classical radius of the electron,  $\rho_e$  is the averaged electronic density and  $\mu$  the absorption coefficient. Typical values for the unitless quantities  $\delta$  and  $\beta$  are  $10^{-5}$  and  $10^{-6}$ – $10^{-7}$  respectively.

Equations 2.25 and 2.26 give a macroscopic description of  $n$ . It can be seen that  $n$  depends on  $\mu$  and  $\rho_e$ , and thus is related to the atomic scattering factor of the atoms in the material. A microscopic description of the refraction index  $n$  using the atomic scattering factors is given by the following equations [107]

$$n = 1 - \frac{\lambda^2}{2\pi} r_e \rho_a f \quad (2.27)$$

$$= 1 - \frac{\lambda^2}{2\pi} r_e \rho_a (f^0 + f' + if'') \quad (2.28)$$

where  $\rho_a$  is the atomic density (*i.e.* the number of atoms per unit volume, or the ratio of the number of atoms in the unit cell to the unit cell volume). Hence, using equation 2.24

$$\delta = \frac{\lambda^2}{2\pi} r_e \rho_a (f^0 + f') \quad (2.29)$$

$$\beta = -\frac{\lambda^2}{2\pi} r_e \rho_a f'' \quad (2.30)$$

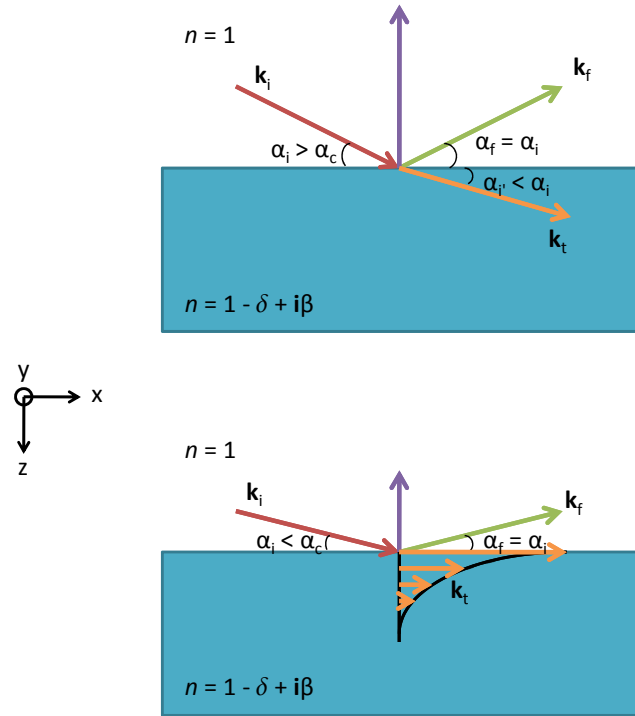


FIGURE 2.8: Schematic view of the total reflection condition between vacuum and condensed matter for incident x-rays. An incident and a reflected wave are pictured, with the same angle with respect to the surface. If the incidence angle  $\alpha_i$  is larger than the critical angle  $\alpha_c$  (*top*), the transmitted wave is refracted at angle  $\alpha'_i$  in the material. The angles  $\alpha_i$  and  $\alpha'_i$  are linked by equation 2.31. If the incidence angle is smaller than the critical angle (*bottom*), then the refracted wave is an evanescent wave, travelling parallel to the surface. The amplitude of the evanescent wave decreases exponentially with the depth.

The critical angle for total reflection can be obtained from the Snell-Descartes law of refraction, illustrated in figure 2.8. It relates the incident angle  $\alpha_i$  to the refracted angle in the material  $\alpha'_i$  through

$$\cos \alpha_i = n \cos \alpha'_i \quad (2.31)$$

Since  $n < 1$  for x-rays, there is a value of  $\alpha_i$  such that  $\alpha'_i = 0$ . This value is the critical angle of total reflection  $\alpha_c$ . It is simply derived from equation 2.31 in the small incident angle regime, setting  $\alpha'_i = 0$  and neglecting the  $\beta$  part in  $n$ . Then, one finds

$$\alpha_c = \sqrt{2\delta} \quad (2.32)$$

$$= \lambda \sqrt{r_e \rho_{el}} \quad (2.33)$$

It can be seen in equation 2.33 that the critical angle will increase for heavier atoms and decrease for more higher energy x-rays. Typical values are the order of a few tenths of a degree, *e.g.* in Ge,  $\alpha_c = 0.38^\circ$  at the Mn K-edge ( $\sim 6.5$  keV) and  $\alpha_c = 0.21^\circ$  just below the Ge K-edge ( $\sim 11$  keV).

### 2.3.2 Scattering depth

For an incident wave vector  $\mathbf{k}_i$  at angle  $\alpha_i$ , the transmitted (refracted) wave vector  $\mathbf{k}_t$  and reflected wave vector  $\mathbf{k}_r$  are (figure 2.8) [105]

$$\mathbf{k}_i = k_0 \begin{pmatrix} \cos \alpha_i \\ 0 \\ \sin \alpha_i \end{pmatrix} \quad (2.34)$$

$$\mathbf{k}_t = k_0 \begin{pmatrix} \cos \alpha_i \\ 0 \\ A_i - iB_i \end{pmatrix} \quad (2.35)$$

$$\mathbf{k}_r = k_0 \begin{pmatrix} \cos \alpha_i \\ 0 \\ -\sin \alpha_i \end{pmatrix} \quad (2.36)$$

In the limit of small incidence angle [105],

$$A_i = \frac{1}{\sqrt{2}} \left( \sqrt{(\alpha_i^2 - 2\delta)^2 + 4\beta^2} + \alpha_i^2 - 2\delta \right)^{1/2} \quad (2.37)$$

$$B_i = \frac{1}{\sqrt{2}} \left( \sqrt{(\alpha_i^2 - 2\delta)^2 + 4\beta^2} + 2\delta - \alpha_i^2 \right)^{1/2} \quad (2.38)$$

The transmitted wave in the medium is proportional to  $e^{-i2\pi\mathbf{k}_t\mathbf{r}}$ . As seen in equation 2.35,  $\mathbf{k}_t$  is complex when  $\alpha_i < \alpha_c$ , hence  $-i2\pi\mathbf{k}_t\mathbf{r} = -i2\pi k_0 A_i z - 2\pi k_0 B_i z$ .



Therefore, the amplitude of the transmitted wave is exponentially reduced by the factor  $e^{-2\pi k_0 B_i z}$ .

The characteristic penetration distance of the transmitted wave in the medium is

$$l = \frac{1}{2\pi k_0 B_i} \quad (2.39)$$

$$= \frac{\lambda}{2\pi B_i} \quad (2.40)$$

As a result, the transmitted wave is limited to a region close to the surface. Typical scattering depths lie in the 1–10 nm range below the critical angle. In the limit of  $\alpha_i \rightarrow 0$  in Ge, just below the Ge K-Edge,  $l \approx 5$  nm. Note however, than in real crystal the surface roughness at the interface increases significantly the penetration of the waves in the medium.

Therefore, by using grazing incidence, one can dramatically enhance the sensitivity of x-ray scattering techniques to the surface. In particular, one may also vary the probing depth simply by tuning the incidence (and/or exit) angles.

## 2.4 Diffuse x-ray scattering from defects

We have seen in the previous section that using grazing incidence, one can limit the probe to a shallow layer of the sample. The influence of the substrate is then greatly reduced. We shall now see how defects in the probed layer may affect the scattered intensity.

### 2.4.1 Diffuse scattering *vs* diffraction

As shown in section 2.1, a perfect infinite crystal will scatter – or more precisely *diffract* – x-rays in only some well-defined orientations. The resulting intensities are the well-known Bragg peaks (BP). However, in actual experiments one deals with real crystals. Such crystals have a finite size and are at a non-zero temperature, which results in a broadening of the Bragg peaks from their ideal Dirac shape. Real crystals also contain defects. The effects of defects on the scattered intensity are multiple : the intensity of the BP is reduced, the position in reciprocal space of the BP can be shifted either way and some intensity appears in-between the

BP. The latter is known as the *diffuse* scattering and contains information about the defects in the crystal [108].

## 2.4.2 Quick overview of the available literature on diffuse scattering

The first studies of point defect-induced x-ray scattering were published by Huang in 1947 [109]. The theory was further expanded by Krivoglaz when he published in 1969 the first english version of its monograph on x-ray and thermal neutron scattering in *real* crystals [110]. A reedition of this work was published in 1996 under the title *x-ray and neutron diffraction in non-ideal crystals* [108]. Two years later, Holý *et al.* published a comprehensive book on the subject [111], which was further completed in a more recent edition [112]. In this section, a quick overview of the principal equations describing the diffuse scattering and in particular the Huang diffuse scattering (HDS) will be given.

## 2.4.3 Huang diffuse scattering

Krivoglaz classified defects in crystal in two categories, *weak* and *strong* defects, depending on the value of the static Debye-Waller factor. In the case of crystal containing volume defects, the static Debye-Waller factor can be written [112]

$$D = \exp \left( -n \int 1 - i2\pi \mathbf{h} \cdot \boldsymbol{\nu}(\mathbf{r}) - e^{-i2\pi \mathbf{h} \cdot \boldsymbol{\nu}(\mathbf{r})} d\mathbf{r} \right) \quad (2.41)$$

where  $n$  is the defect density,  $\mathbf{h}$  is the vector joining the origin and the lattice point  $H$  in reciprocal space and  $\boldsymbol{\nu}(\mathbf{r})$  is the displacement field of a defect, *i.e.* the variation in position of the atom located at  $\mathbf{r}$  when no defect is present. If equation 2.41 converges to a finite value, the defects are weak; if on the opposite it diverges, the defects are strong. In fact, the most important criterion in this classification is the asymptotic behavior of the displacement field  $\boldsymbol{\nu}$ . In the case of finite defects (such as inclusions), the displacement field decreases as  $\frac{1}{r^2}$  and equation 2.41 converges.

Holý *et al.* have shown that the defect can be treated in two separate ways : (i) the defect core, sensibly different from the matrix, and (ii) the deformed matrix around the defect where the the crystal can be described as a simple deformation

from its bulk structure [111, 112]. Near a reciprocal lattice point of the unstrained bulk lattice, *i.e.* for small  $\mathbf{q}$  (where  $\mathbf{q}=\mathbf{Q}-\mathbf{h}$ ), the diffuse scattering is mostly due to the elastic deformation of the matrix around the defect core and is known as Huang scattering.

A clear derivation of the Huang scattering intensity can be found in ref. [112]. In particular, it is shown that the intensity of the Huang scattering at  $\mathbf{Q}$  in reciprocal space is

$$J_{Huang}(\mathbf{Q}) \propto |\mathbf{h} \cdot \boldsymbol{\nu}^{FT}(\mathbf{q})|^2 \quad (2.42)$$

where  $\boldsymbol{\nu}^{FT}(\mathbf{q})$  is the Fourier transform of the displacement field of a defect (inclusion). In particular, in the case of inclusions with displacement fields decaying as  $\frac{1}{r^2}$ , one finds  $|\mathbf{h} \cdot \boldsymbol{\nu}^{FT}(\mathbf{q})|^2 \propto \left| \frac{\mathbf{h} \cdot \mathbf{q}}{q^2} \right|^2$ . This translates in a zero intensity plane (*nodal plane*) for  $\mathbf{h}$  perpendicular to  $\mathbf{q}$ , characteristic of Huang scattering. The nodal plane is a consequence of the symmetry of the displacement field and should vanish in an anisotropic material [112].

There are a few approximations behind the derivation of the analytical intensity of the Huang scattering. The most important one, in our case, is the fact that defect positions are assumed to be uncorrelated. We will show in chapter *Chapter 4* that this approximation is too restrictive in the case of the GeMn nanocolumns.

## 2.5 Experimental setups

In this section, details about the different experimental setups used on the different beamlines are given. A short description of synchrotron radiation is given in the Appendices.

### 2.5.1 Synchrotron experimental setups

During this PhD thesis, mostly three beamlines – all at the European Synchrotron Radiation Facility – were used for x-ray scattering experiments : beamlines ID01, BM32 and D2AM (BM2). The characteristics of each these beamlines will be

given below. Additional measurements were also performed on beamline ID31 (Pair Distribution Function) and ID11 (Total Scattering), also at the ESRF.

### 2.5.1.1 The ID01 beamline

The purpose of beamline ID01 at the ESRF (known as the "anomalous scattering beamline") is to measure grazing incidence x-ray scattering at small and wide angles with the possible use of the anomalous x-ray scattering technique [113, 114].

The x-ray source on ID01 has recently been upgraded to three insertion devices : two 35 mm and one 42 mm undulators give access to energy range of 2.1–40 keV. A schematic view of the beamline is shown in figure 2.9(a). The energy selection is made on Si(111) monochromator. The resolution is  $\Delta E/E = 10^{-4}$ , *i.e.* about 1 eV at the Ge K-edge. Typical energies between 6.5 and 16 keV were used during this work. Higher harmonic rejection ( $\lambda/3$ ,  $\lambda/5$ ... etc) is performed using a pair of Si mirror with Pt or Rh coating available, depending on the energy used. The second mirror of the monochromator can be bent sagittally to achieve horizontal focussing, while the second mirror can be bent in the direction of the beam to achieve vertical focussing. In both cases, focussing increases the photon flux at the sample position. Typical photon flux at 11 keV on a  $0.1 \times 0.1$  mm<sup>2</sup> area when the storage ring current is at 200 mA is on the order of  $10^{13}$  photon.s<sup>-1</sup>.

The experimental hutches are housed in a large (diameter = 2.8 m) vacuum vessel with a 4+2-circle diffractometer that we have used with a Huber tower setup (figure 2.9). In order to reduce unwanted scattering by air, the vacuum vessel can be evacuated down to  $\sim 7 \times 10^{-3}$  mbar. Then, using two stages of differential pumping, the beamline can be used with a physical connection between the x-ray source in the storage ring and the detector (*i.e.* without any beryllium window in the beam path). An alternative to the total evacuation of the vessel is to use so-called "flight tubes" (kapton sealed and evacuated tubes) along the path of the beam, as shown in figure 2.9(d). It is usually faster to set up than to pump down the whole vessel and it is generally sufficient when higher energies are used, *e.g.* at the Mn or Ge K-edges.

The sample is mounted on a goniometer head. It is then placed in a He-filled kapton cone in order to reduce scattering due to air and to avoid enhanced oxidation due to x-ray-induced ozone. The sample is usually oriented vertically (*i.e.*

$\chi = 90^\circ$ ). This defines a vertical scattering plane and takes advantage of the fact that the polarization factor of the x-ray beam is  $P=1$  in that orientation. It also takes advantage of the small vertical divergence of the beam, allowing for a higher angular resolution resolution in the sample plane.

### 2.5.1.2 The BM32 beamline

The BM32 beamline, known as the *InterFace* (IF) beamline, is part of the French Collaborating Research Group (CRG). It offers three endstations : the *Surface under Ultra-high Vacuum* (SUV) instrument (that we have used), the *MultiTechnic Goniometer* (GMT) instrument, and the *MicroDiffraction Setup*. The SUV endstation is dedicated to study of surfaces and interfaces under ultra-high vacuum and offers the possibility to perform *in situ* studies during the sample growth [115, 116].

As the name indicates, the x-ray source at BM32 is a bending magnet. As such, it produces a white spectrum of x-rays. The wavelength selection and beam focussing are performed in the same fashion as at ID01 : respectively by using a Si(111) monochromator and a set of mirrors, and by bending the second crystal of the monochromator and the second mirror, as shown in figure 2.10(a). Accessible energies are in the 5–30 keV range, with the typical  $\Delta E/E = 10^{-4}$  resolution. The focused beam size at the sample position is about  $0.25 \times 0.18 \text{ mm}^2$  (H×V). Due to the use of a bending magnet, the photon flux is lower than on ID01 with approximately  $10^{11} \text{ photon.s}^{-1}$ .

The experimental hutch contains an ultra-high vacuum chamber with a base pressure as low as  $10^{-11}$  mbar. Beryllium windows are used as entry and exit ports for the x-ray beam. Standard surface-science tools are available on the chamber, as well as evaporation cells. More importantly, at the beginning of my PhD thesis, the ultra-high vacuum chamber was connected via a Riber-type modutrack transfer module to the molecular beam epitaxy chamber used to grow the GeMn samples, as shown in figure 2.10(b). This allowed for *in situ* characterization of the GeMn nanocolumns.

The diffractometer is a “z-axis” 6-circle diffractometer, as shown in figure 2.10(c). In the same fashion as at ID01, the sample is mounted vertically to allow surface diffraction while avoiding zero-polarization factor at  $2\theta = 90^\circ$ . Adjustment of the

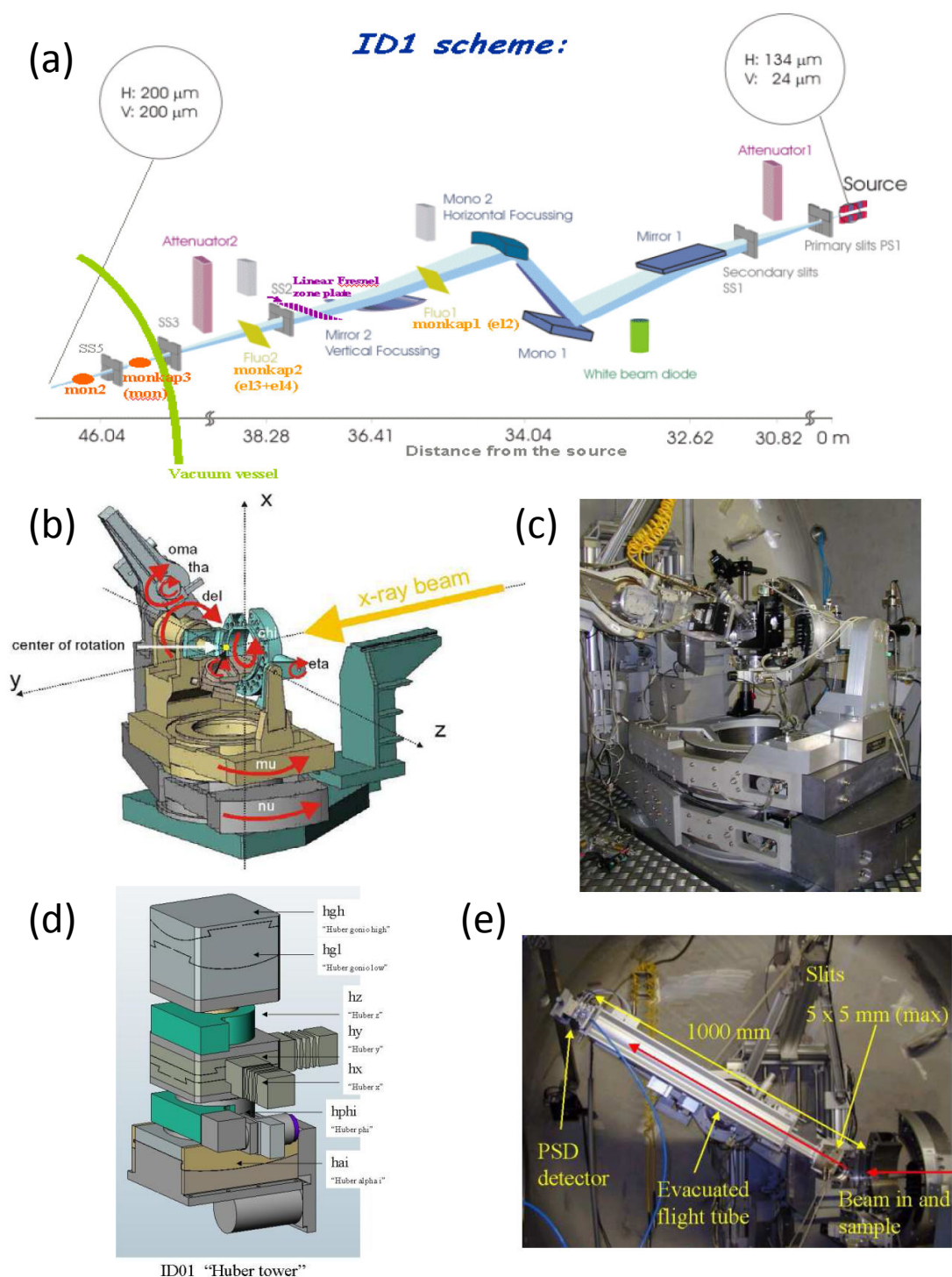


FIGURE 2.9: The ID01 beamline : (a) schematic view of the beamline, from the x-ray source to the sample. (b) Schematic view of the 4+2-circle diffractometer and (c) actual set up. (d) Huber tower used in place of some circles of the diffractometer to control the orientation of the sample. (e) Detector arm with an evacuated flight tube. All pictures are adapted from [114].

incidence angle  $\alpha_i$  is done by rotating the whole diffractometer about the  $x$ -axis. Alignment of the surface of the sample perpendicular to the  $\omega$  axis is performed using a pair of cradles ( $\chi_1$  and  $\chi_2$ ). A translation along  $z$  is also possible to adjust the position of the sample in the beam with 10  $\mu\text{m}$  accuracy. The samples are mounted on molybdenum molybblocks, as used during the MBE growth.

### 2.5.1.3 The D2AM beamline

The beamline BM02 is called the *Multiwavelength Anomalous Diffraction and Scattering* (D2AM in french). Like BM32, it is part of the French CRG beamlines at the ESRF. Its endstation features two instruments : a 8-circle diffractometer and a small angle scattering camera, allowing both small and wide angle scattering experiments [118].

The x-ray source of D2AM is a bending magnet, giving access to energies between 5 and 25 keV. Energy selection and sagittal focussing is done by a two crystal Si(111) monochromator. Two mirrors are used for both higher harmonics rejection and horizontal focussing as shown in figure 2.10(a,b).

The experimental hutch in D2AM is rather larger can house both the 8-circle diffractometer and rail for small angle x-ray scattering at large distances (fig. 2.10(b)). The 7-circle diffractometer has three rotations for the orientation of the sample ( $\chi$ ,  $\varphi$  and  $\theta$ ), as shown in figure 2.10(c,d). As described for ID01 and BM32 beamlines, the  $\chi$  angle is usually set such that the surface of the sample lies vertically, in the plane where the polarization factor of the beam is always  $P=1$ . Two additional rotations are used to orient the detector arm ( $2\theta$  and  $\alpha$ ). The last two circles ( $2\theta_a$  and  $\theta_a$ ) are used on the detector arm to set the energy of the analyser.

A beryllium dome can be put over the sample and evacuated to reduce air scattering and air ionization over the sample due the radiation. *Flight tubes* may also be used on the beam path to reduce background scattering from the air.

## 2.5.2 Detectors

Two different types of detectors were used during my PhD thesis. The first type consisted in a Vantec position sensitive detector (PSD), *i.e.* a 1-D detector. This

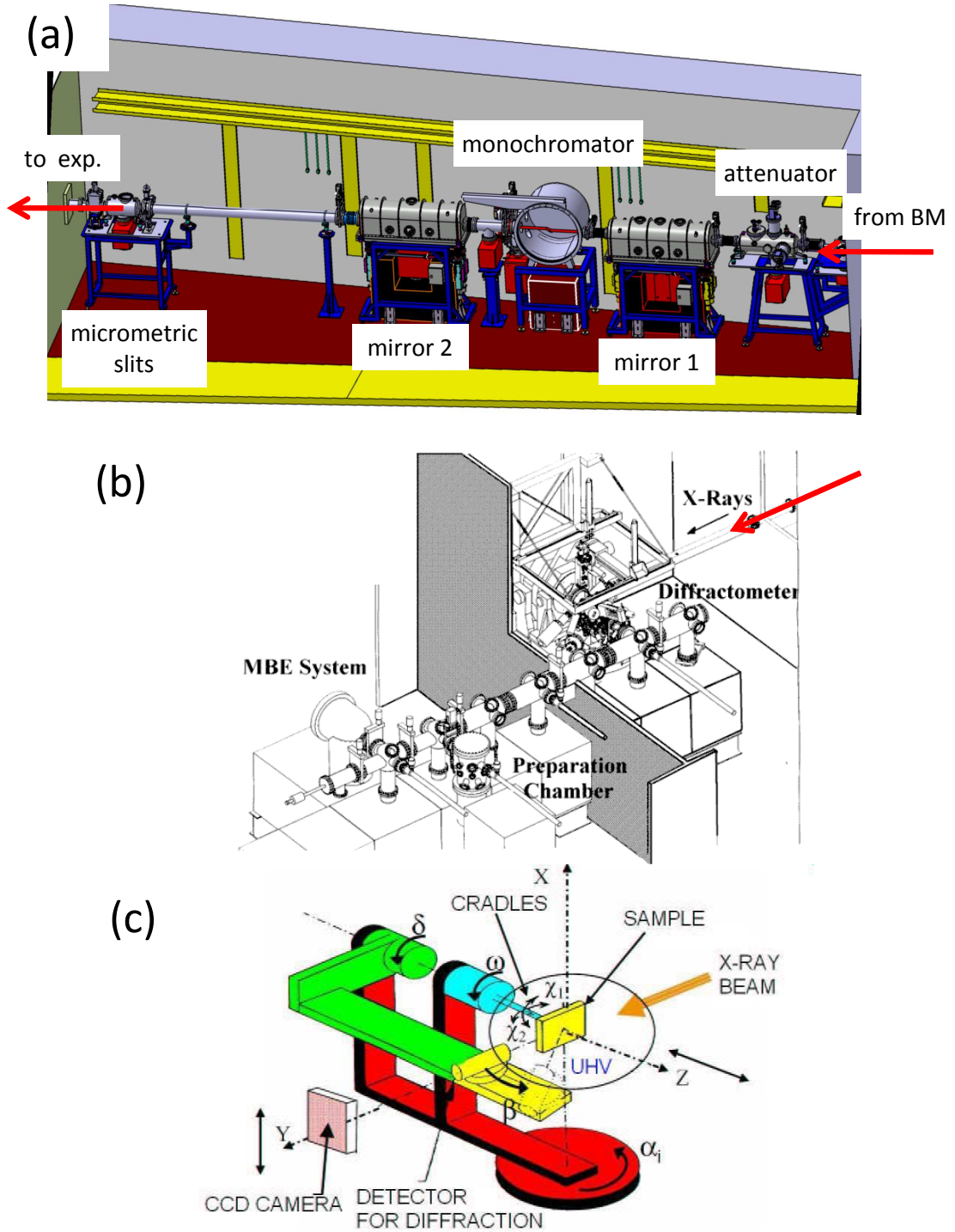


FIGURE 2.10: The BM32 beamline : (a) schematic view of the optics at the BM32 beamline, after the bending magnet and before the experimental hutches. (b) Schematic view of the experimental hutches at SUV and the UHV connection to the GeMn growth chamber. (c) Sketch of the 6-circle diffractometer. Pictures (a) and (b) are adapted from [116], picture (c) is adapted from [117].



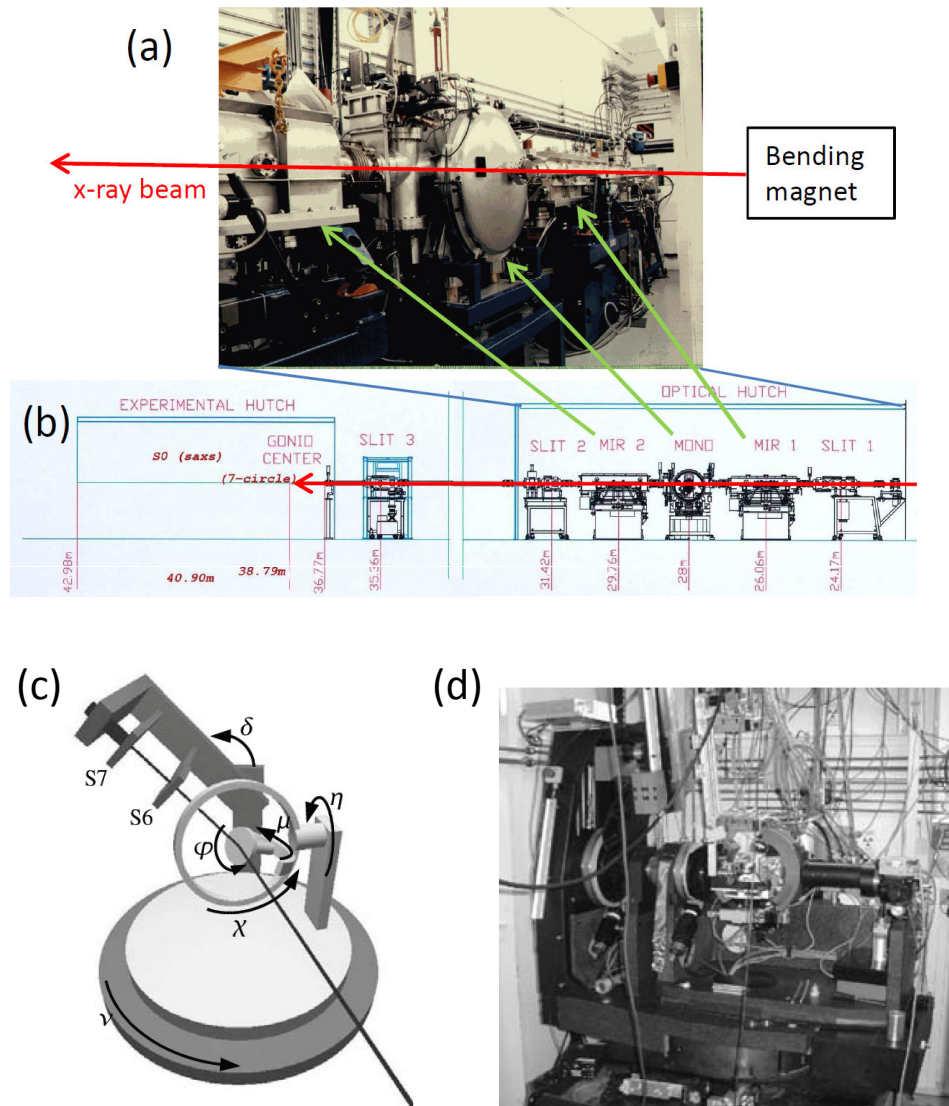


FIGURE 2.11: The D2AM-BM02 beamline : (a) picture of the optics hutch, after the bending magnet and before the experimental hutch. (b) Blueprint of the D2AM beamline. (c) Sketch and (d) actual picture of the 8-circle diffractometer.

Pictures (a–b) are adapted from ref. [118], (c–d) from ref. [119]

kind of linear detector can be used perpendicular to the sample surface to provide exit-angle resolution, as sketched in figure 2.12. The PSD detector features 1400 channels. At the sample-detector distance used, the typical angular resolution was measured to be  $2.46 \times 10^{-3} \text{ }^\circ/\text{pixel}$ .

TABLE 2.1: Comparison between the advantages and drawbacks of the different types of 2-D detectors.

CCD	Pixels
<b>Advantages</b>	
<ul style="list-style-type: none"> <li>– large area of detection</li> <li>– large number of pixels (the FReLON 4M CCD camera at the ESRF has about <math>4.2 \times 10^6</math> pixels)</li> <li>– insensitivity to the radiation (passive detector)</li> <li>– small pixel size (typically <math>50 \text{ } \mu\text{m}</math>)</li> </ul>	<ul style="list-style-type: none"> <li>– high dynamic range (<math>&gt; 10^6</math> cps)</li> <li>– fast acquisition/reading procedure</li> <li>– very-low-to-zero noise (photon counting)</li> </ul>
<b>Drawbacks</b>	
<ul style="list-style-type: none"> <li>– low dynamic range</li> <li>– limited resolution at high intensities (saturated pixels tend to affect neighboring pixels)</li> <li>– rather slow read-out times</li> <li>– background level and noise (<i>dark</i> images, <i>i.e.</i> without no beam, have to be measured prior to the experiment to calibrate the detector)</li> </ul>	<ul style="list-style-type: none"> <li>– damage to the electronics due to exposure to radiation (<i>e.g.</i> pixels start degrading under <math>10^{12} \text{ photons.s}^{-1}</math> at 10 keV)</li> <li>– bigger pixel sizes (<math>55 \text{ } \mu\text{m}</math> for the MAXIPIX to <math>130 \text{ } \mu\text{m}</math> for the XPAD)</li> <li>– less than 100% pixel area coverage in some cases (due to the embedded electronics)</li> </ul>

The second type of detector used are 2-D detectors. A wide range of 2-D detectors are available at the different beamlines at the ESRF. In addition to the exit-angle resolution, 2-D detectors also allow lateral angle resolution when used perpendicular to the surface of the sample in grazing incidence. In particular they allows single acquisition of small angle x-ray scattering measurements. Due to their large area of detection (typically on the order of several  $\text{cm}^2$ ), they also allow for fast mapping of large portions of reciprocal space, in particular when one wants to achieve *total scattering* measurements. 2-D detectors can be further divided into two subgroups : the charge-coupled device (CCD) detectors and the pixel detectors. Very basically, x-ray CCD detectors consist in a layer opaque to visible light

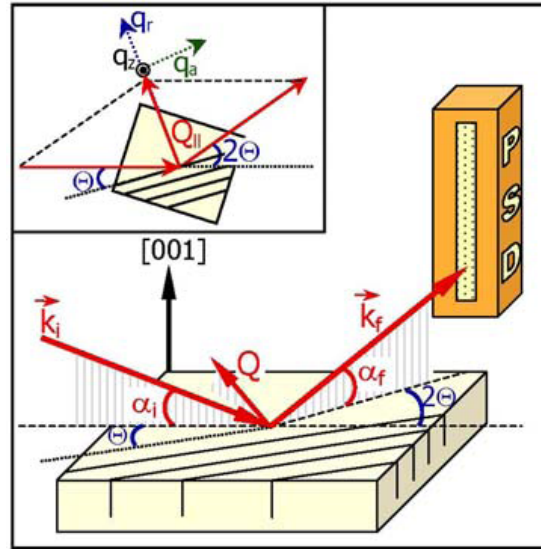


FIGURE 2.12: Sketch of the scattering geometry in grazing incidence (incidence angle  $\alpha_i$ ) using a PSD detector with exit-angle  $\alpha_f$  resolution. Insert : Top-view of the scattering geometry with reduced scattering vectors ( $\mathbf{q}_r$ ,  $\mathbf{q}_a$  and  $\mathbf{q}_z$ ). Adapted from [120].

but transparent to x-rays. A scintillator then transforms x-rays to visible light, which is conducted through optical fibers to a classic CCD detector. This detector measures the signal due to electron-hole pairs created in a semi-conducting layer by the photoelectric effect.

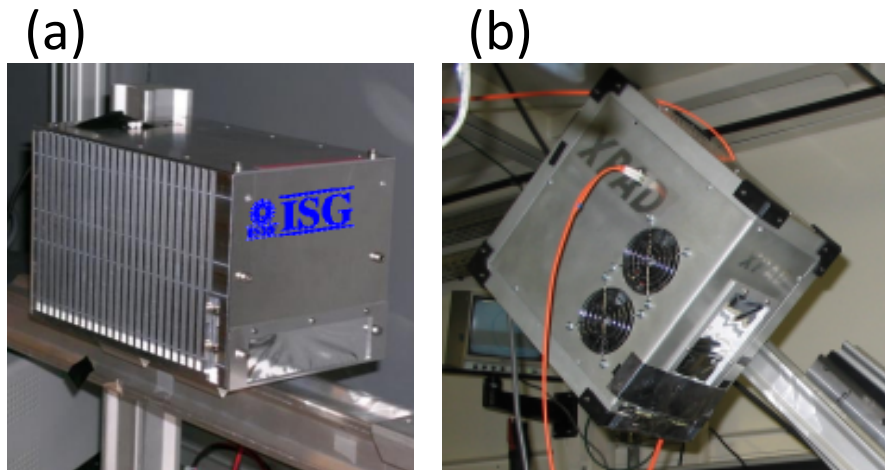


FIGURE 2.13: Pictures of (a) the MAXIPIX and (b) the XPAD pixel detectors. Pictures respectively adapted from [121] and [122]

X-ray pixel detectors have appeared more recently in synchrotron facilities and aim at reducing the drawbacks of CCD detectors. They consist in arrays of diode sensors with a dedicated amplifying and reading electronic circuit for each pixel.

The separation of detecting and reading allows for very fast measurements : the next image can be taken while the previous one is being read-out.

The main advantages and draw backs of each type of detectors have been roughly summarized in table 2.1. Two pixel detectors were used during my PhD thesis : the MAXIPIX, developped at the ESRF by the Detector Group, and the XPAD, developped jointly by the D2AM-CRG beamline, the CNRS and the Institut National de Physique Nucléaire et de Physique des Particules (IN2P3). Both are illustrated in figure 2.13(a) and (b) respectively.

### 2.5.3 Measurement procedure : grazing incidence reciprocal space maps

Two types of scans in reciprocal space were mainly used : (i) scans along a  $\mathbf{Q}$  direction (*radial scan*) and scans at constant  $|\mathbf{Q}|$  (*angular scans*). Both types of scans are illustrated in reciprocal space in figure 2.14.

Reciprocal space maps were performed by first setting a value for  $\mathbf{Q}$ . Then a series of one angular scan followed by a small increase in  $|\mathbf{Q}|$  were performed. Values of  $|\mathbf{Q}|$  were chosen to include the Ge diamond Bragg reflection 220 and 040. The angular sector scanned was chosen by symetry to be the smallest irreducible angular sector, *i.e.*  $45^\circ$ <sup>5</sup> between the 220 and 040 Bragg reflections.

When measuring the scattering around a Bragg reflection in grazing incidence, we may write  $\mathbf{Q} = \mathbf{h} + \mathbf{q}$  where  $\mathbf{h} = (h, k, l)$  is the vector to the  $hkl$  Bragg reflection. Then  $\mathbf{q}$  may be decomposed in  $\mathbf{q}_r$ ,  $\mathbf{q}_a$  and  $\mathbf{q}_z$ , as illustrated in figure 2.12. Let us write  $\Theta_{hkl}$  the Bragg angle corresponding to the  $hkl$  reflection and  $\Delta\Theta$  the deviation to the Bragg angle ( $\Delta\Theta = \Theta_{hkl} - \Theta$ ). Then, in the limit of the small angles (see figure 2.15) :

$$\mathbf{q}_r = \frac{2}{\lambda} \cos(\Theta_{hkl}) \Delta\Theta \quad (2.43)$$

$$\mathbf{q}_a = \frac{2}{\lambda} \Delta\Theta \quad (2.44)$$

$$\mathbf{q}_z = \frac{1}{\lambda} (\alpha_i + \alpha_f) \quad (2.45)$$

---

5. about  $2.5^\circ$  were added at each end for safety

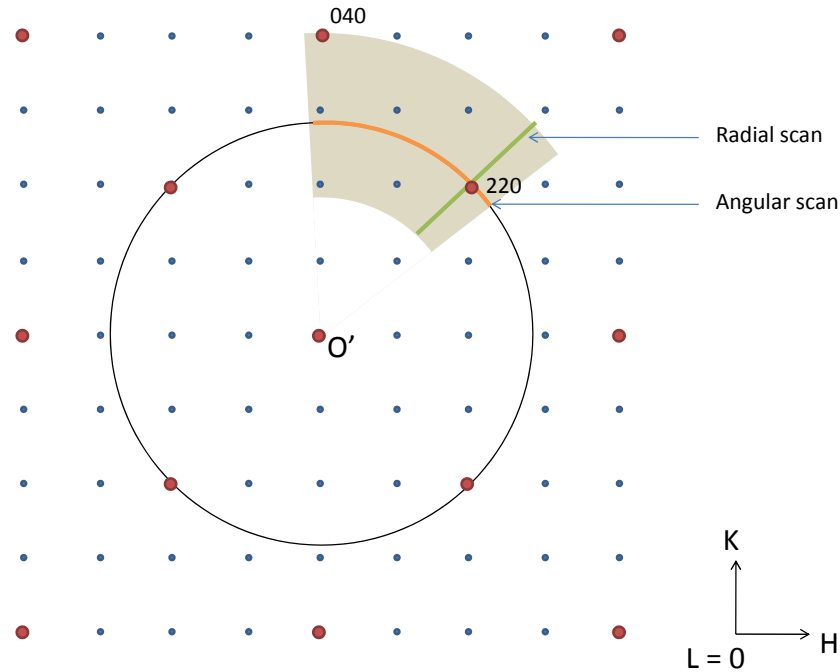


FIGURE 2.14: Schematic view of the angular and radial scans in the Ge diamond reciprocal space, in the particular case when they come across the 220 Bragg reflection. The grey area is the area mapped using a succession of angular scans in this work.

### 2.5.4 Data processing

Once acquired, the data have to be processed before further analysis. A few corrections are necessary. First the measured intensity has to be normalized at each point by the corresponding incident beam intensity (measured by the monitor value). In the case of too intense or too low intensity during the measurement, absorbing metal foils may be added or removed from the beam path. The absorbing coefficient of the foils has to be measured prior to the experiment at the energy used. Correction of the absorption of the foils is then taken into account when normalizing the data. As discussed in the description of the experimental setups, vertical alignment of the surface of the sample results in a polarization factor correction  $P=1$  for surface diffraction in the vertical plane.

Quantitative analysis may require further corrections, such as a correction by the illuminated area or by the Lorentz factor. The latter takes into account the different speed at which the reciprocal space crosses the Ewald sphere for a given orientation.

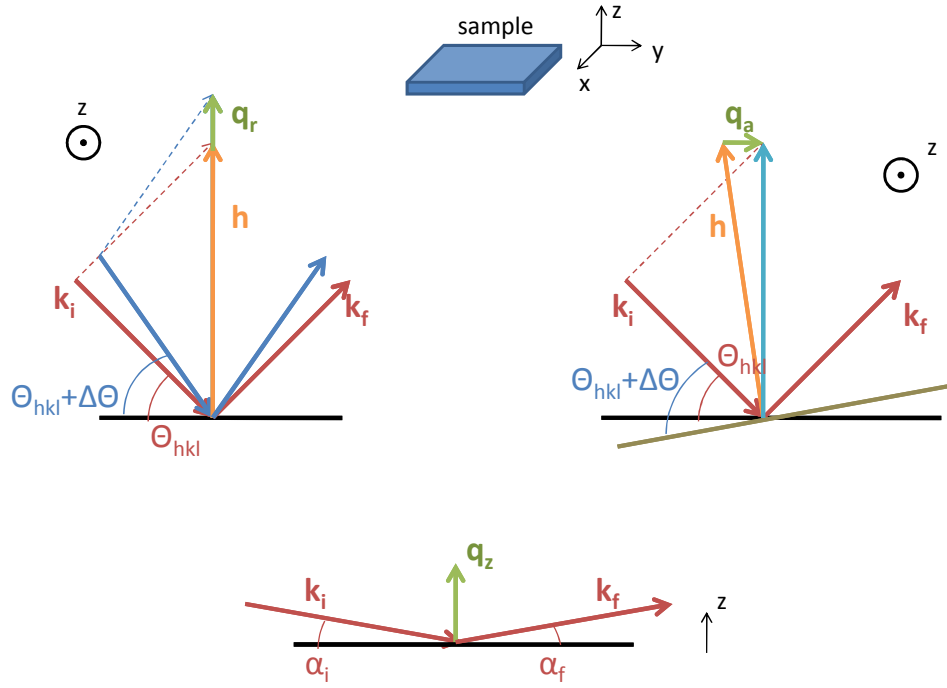


FIGURE 2.15: Derivation of  $q_r$ ,  $q_a$  and  $q_z$ .  $q_r$  and  $q_a$  lie parallel to the surface, while  $q_z$  is perpendicular to the surface.

## 2.6 Conclusion

We have seen that x-ray scattering is the method of choice for the structure determination of new materials. In particular, it allows to measure the atomic positions, as well as deviations from the average values, due the strain in the crystal. Surface sensitivity may also be achieved by using grazing incidence and limiting the scattering to the topmost part of the sample. Therefore, x-ray scattering appears as a method of choice to probe the structural properties of the GeMn nanocolumns. Different experimental setups have been used at the European Synchrotron Radiation Facility, each with its specific advantages. Beamline BM32 allowed for *in situ* characterization of the nanocolumns, avoiding any surface contamination. Beamline BM02 allowed for an easy change of the beam energy for anomalous scattering experiments and large detectors were available for fast acquisition of large maps in reciprocal space. Beamline ID01 provides a higher photon flux and is adapted for lower energies and anomalous scattering. Other less conventional experiments were also tried, such as 2D-Pair Distribution Function measurements on beamline ID31 or 3D mapping of the reciprocal space (*total scattering* experiments) on beamline ID11. Such experiments are not described here.

## 2.7 Résumé du chapitre 2

Le chapitre 2 présente le cadre théorique et expérimental des techniques de mesures de diffusion et de diffraction de rayons X.

Dans ce chapitre, nous avons vu que la mesure de diffusion de rayons X est particulièrement adaptée à la détermination de la structure de nouveaux matériaux. En particulier, il est possible de déterminer les positions atomiques, ainsi que les écarts aux positions moyennes dus à la déformation du cristal. L'utilisation d'un faisceau de rayons X incident rasant permet par ailleurs d'obtenir une sensibilité accrue à la surface en limitant la diffusion à la partie supérieure de la couche étudiée. Ainsi, la mesure de diffusion de rayons X en incidence rasante apparaît comme une méthode de choix pour la détermination des propriétés structurales des nanocolonnes de GeMn. Les différents dispositifs expérimentaux utilisés à l'ESRF (European Synchrotron Radiation Facility), ainsi que leurs avantages spécifiques, ont été décrits. La ligne de lumière BM32 a ainsi permis la caractérisation *in situ* des nanocolonnes, permettant donc d'éviter toute contamination de la surface. La ligne de lumière BM02 a été utilisée pour sa capacité à changer facilement l'énergie incidente autour des seuils d'absorptions afin de réaliser des mesures de diffusion anormale. L'utilisation de grands détecteurs bidimensionnels a aussi permis l'acquisition rapide de vastes cartographies de l'espace réciproque. Enfin, la ligne de lumière ID01 a été utilisée pour son fort flux de photons incidents et sa capacité à mesurer la diffusion anormale à de plus faibles énergies (seuil du Mn). D'autres expériences, moins conventionnelles, ont aussi été menées, telles que des mesures de fonction de distribution de paires 2D sur ID31, ou encore de cartographies tridimensionnelles de l'espace réciproque (mesure de *diffusion totale*) sur ID11. De telles expériences ne sont pas décrites ici.





# Chapitre 3

## X-ray absorption spectroscopy and magnetic circular dichroism

The development over the last few decades of synchrotron radiation facilities has provided the scientific community with intense, energy and polarization tunable, x-ray sources. This has led, in particular, to the development of x-ray absorption techniques such as x-ray absorption near-edge spectroscopy (XANES), extended x-ray absorption fine structure (EXAFS) or x-ray magnetic circular (or linear) dichroism (XMC(L)D). Such techniques have attracted much attention due to their element-specificity, their high sensitivity and the wealth of information they can provide. For example, in the case of the GeMn nanocolumns system, an investigation of the chemical ordering has been performed by Rovezzi *et al.* using EXAFS [101]. During my PhD I have used the synchrotron radiation in the soft x-ray regime to probe the manganese electronic structure and magnetic properties in the GeMn nanocolumns. More specifically, I have used x-ray absorption spectroscopy and magnetic circular dichroism at the Mn  $L_{2,3}$  photo-ionization edges. I shall give in this chapter a quick reminder of the underlying theory followed by a general description of the experimental realization.

### 3.1 Theoretical aspects

In this part I recall a few theoretical concepts to the reader. I start from the semi-classical model and derive the polarization-dependent transition selection rules

from the interaction Hamiltonian. The expression of the sum rules are given along some theoretical limitations in the case of Mn.

### 3.1.1 Quantum description of the x-ray absorption : Fermi's Golden Rule and the dipole approximation

The photon absorption by the absorbing atom yields a transition from the initial state  $|i\rangle$  at time  $t$  to the final state  $|f\rangle$  at time  $t + dt$ . The expression of the transition rate (probability per unit time)  $T_{i \rightarrow f}$  obtained by using a time-dependent perturbation calculation is known as *Fermi's Golden Rule*<sup>1</sup>[123]

$$T_{i \rightarrow f} = \frac{2\pi}{\hbar} |\langle f | \mathbf{H}_{int} | i \rangle|^2 \rho(E_f) \delta(E_f - E_i - \hbar\omega) \quad (3.1)$$

The term  $\delta(E_f - E_i - \hbar\omega)$  describes the conservation of the energy,  $\hbar\omega$  being the energy of the absorbed photon,  $\rho(E_f)$  is the energy density of the final state  $|f\rangle$ .  $\mathbf{H}_{int}$  is the photon-electron interaction operator and the squared matrix element gives the transition probability. The photon-electron interaction operator can be derived from a time-dependent perturbation of the Hamiltonian of the absorbing atom  $\mathbf{H}_0$  : we replace  $\mathbf{p}$  (the momentum operator of the electron) by  $\mathbf{p} - \frac{e}{c}\mathbf{A}$ , where  $\mathbf{A}$  is the vector potential related to the photon, representing its electric field  $\mathbf{E}$ . The perturbed Hamiltonian is written as

$$\mathbf{H} = \mathbf{H}_0 + \mathbf{H}_{int} \quad (3.2)$$

$$= \frac{1}{2m} \left( \mathbf{p} - \frac{e}{c}\mathbf{A} \right)^2 + \mathbf{V}_0 \quad (3.3)$$

$$= \frac{1}{2m} \mathbf{p}^2 + \mathbf{V}_0 - \frac{e}{2mc} \mathbf{p} \mathbf{A} - \frac{e}{2mc} \mathbf{A} \mathbf{p} + \frac{e^2}{2mc^2} \mathbf{A}^2 \quad (3.4)$$

$$= \mathbf{H}_0 - \frac{e}{2mc} \mathbf{p} \mathbf{A} - \frac{e}{2mc} \mathbf{A} \mathbf{p} + \frac{e^2}{2mc^2} \mathbf{A}^2 \quad (3.5)$$

The prefactors are the charge of the electron  $e$ , its mass  $m$  and the speed of light  $c$ . Hence the interaction Hamiltonian :

$$\mathbf{H}_{int} = -\frac{e}{2mc} \mathbf{p} \mathbf{A} - \frac{e}{2mc} \mathbf{A} \mathbf{p} + \frac{e^2}{2mc^2} \mathbf{A}^2 \quad (3.6)$$

---

1. It can be noted that an early expression of the transition rate was given by Paul Dirac, yet it was Enrico Fermi who coined the term “*Golden Rule*”.

Fixing the Coulomb gauge  $\mathbf{p}\mathbf{A} = 0$  and ignoring the last term in equation 3.6 (*i.e.* the term relative to two-photons absorption/emission processes), we can write

$$\mathbf{H}_{int} = -\frac{e}{2mc} \mathbf{A}\mathbf{p} \quad (3.7)$$

The vector potential can be written as a plane wave

$$\mathbf{A} = A_0 e^{i(\mathbf{k}\mathbf{r} - \omega t)} \boldsymbol{\varepsilon} \quad (3.8)$$

where  $\boldsymbol{\varepsilon}$  is the polarization vector of the electromagnetic wave. The product  $\mathbf{k} \cdot \mathbf{r}$  can be seen as the ratio of the radial extension of the electron to the wavelength of the photon. In the case of the  $L_{2,3}$  absorption edge of Mn,  $\hbar\omega_{edge}$  is about 650 eV, hence  $\lambda \approx 1.9$  nm. The Mn  $2p$  orbital is a core orbital, therefore it has a very limited spatial extension, on the order of 0.01 nm. So the term  $\mathbf{k} \cdot \mathbf{r}$  is on the order of  $10^{-2}$  and it will be further reduced by the squaring of the matrix element. Therefore the Taylor expansion of  $e^{i(\mathbf{k}\mathbf{r} - \omega t)}$  can be limited to the first term. This approximation is called the *dipole approximation* because higher order terms (*e.g.* quadripolar interactions) are neglected and only dipolar interaction are taken into account. Physically, it means that the photon electromagnetic wave does not vary rapidly over the spatial extent of the electron. Considering only the dipole transition, the interaction Hamiltonian becomes :

$$\mathbf{H}_{int} = -\frac{e}{2mc} A_0 e^{-i\omega t} \boldsymbol{\varepsilon}\mathbf{p} \quad (3.9)$$

Hence the squared matrix element

$$|\langle f | \mathbf{H}_{int} | i \rangle|^2 = \frac{|A_0|^2 e^2}{4m^2 c^2} |\langle f | \boldsymbol{\varepsilon}\mathbf{p} | i \rangle|^2 \quad (3.10)$$

Considering now the relation  $\mathbf{p} = \frac{m}{i\hbar} [r, \mathbf{H}_0]$ , we can rewrite equation 3.1 as

$$T_{i \rightarrow f} = \frac{\pi}{\hbar} \frac{|A_0|^2 e^2}{2c^2} \frac{(E_f - E_i)^2}{\hbar^2} |\langle f | \boldsymbol{\varepsilon}\mathbf{r} | i \rangle|^2 \rho(E_f) \delta(E_f - E_i - \hbar\omega) \quad (3.11)$$

### 3.1.2 X-ray absorption cross-section

The absorption cross-section  $\sigma(\hbar\omega)$  is defined as the ratio of the amount of energy absorbed from the incident photon beam per unit time ( $T_{i \rightarrow f} \hbar\omega$ ) to the incident energy flux ( $\frac{|A_0|^2 \omega^2}{8\pi c}$ ), thus

$$\sigma(\hbar\omega) = 4\pi^2 \alpha \hbar\omega |\langle f | \boldsymbol{\varepsilon} \mathbf{r} | i \rangle|^2 \rho(E_f) \delta(E_f - E_i - \hbar\omega) \quad (3.12)$$

where  $\alpha = \frac{e^2}{\hbar c}$  is the fine structure constant.

### 3.1.3 Interaction matrix elements in terms of spherical harmonics and the dipole selection rules

Equation 3.12 shows that the x-ray absorption process is dependent on the tensor operator  $\boldsymbol{\varepsilon} \mathbf{r}$ . According to the orientation of the polarization, the tensor operator can be written as

$$\text{linear polarization : } \boldsymbol{\varepsilon}_z \mathbf{r} = z = r \sqrt{\frac{4\pi}{3}} Y_1^0 \quad (3.13)$$

$$\text{circular left polarization : } \boldsymbol{\varepsilon}_+ \mathbf{r} = \frac{1}{\sqrt{2}}(x + iy) = -r \sqrt{\frac{4\pi}{3}} Y_1^1 \quad (3.14)$$

$$\text{circular right polarization : } \boldsymbol{\varepsilon}_- \mathbf{r} = \frac{1}{\sqrt{2}}(x - iy) = r \sqrt{\frac{4\pi}{3}} Y_1^{-1} \quad (3.15)$$

where  $Y_l^{m_l}$  are the well known spherical harmonics [123]. Then, according to the Wigner-Eckart theorem, the matrix element  $|\langle f | \boldsymbol{\varepsilon} \mathbf{r} | i \rangle|^2$  will be non zero under the conditions summarized in table 3.1. These conditions are known as the dipole selection rules.

It can be seen in particular that the spin is unaffected by the absorption process. The orbital part, however, is increased or decreased by unity during the same process. This can be interpreted as the conservation of the total angular momentum of the (*photon+electron*) system. This means, in the case of the absorption at the Mn  $L_{2,3}$ , that the transition processes will occur between, on the one hand, the

TABLE 3.1: Dipole selection rules : conditions on the allowed transitions in the dipole approximation

Polarization	$\Delta s$	$\Delta m_s$	$\Delta l$ ( $\Delta j$ ) <sup>a</sup>	$\Delta m_l$ ( $\Delta m_j$ ) <sup>a</sup>
linear	0	0	$\pm 1$ ( $\pm 1$ )	0 (0)
circular left	0	0	$\pm 1$ ( $\pm 1$ )	+1 (+1)
circular right	0	0	$\pm 1$ ( $\pm 1$ )	-1 (-1)

<sup>a</sup> In the case of spin-orbit coupling in the initial state,  $l$  and  $s$  are not good quantum numbers anymore and one uses instead  $j = l + s$

spin-orbit split  $2p_{3/2}$  and  $2p_{1/2}$  initial states, and on the other hand, the empty  $4s$  and  $3d$  final states with similar spins.

### 3.1.4 X-ray magnetic circular dichroism : a semi-relativistic approach

The absorption in a magnetized material depends on the relative orientation of the polarization of the incident radiation with respect to the direction of magnetization. It has been shown in the previous section that for a given initial state and polarization of the incident photons, only certain transitions are allowed. In particular, as it will now be shown, for a given energy one may observe two different absorption rates depending on the relative orientations of  $\boldsymbol{\epsilon}$  and  $\mathbf{M}$  (the magnetization). This phenomenon is called *magnetic dichroism*. In particular, when circular polarized light is used, one uses the term *magnetic circular dichroism*. Eventually, when dealing with transitions metals  $L_{2,3}$  absorption edges, incident photons have to be roughly in the range of 600–800 eV, *i.e.* x-rays. Hence the denomination *x-ray magnetic circular dichroism* (XMCD) for this particular phenomena, which is also by extension the name given to the technique aiming at measuring it.

The first calculations of the XMCD at the  $M_{2,3}$  absorption edges of Ni were performed by Erskine and Stern [124] using a one-electron model. This model is treated semi-relativistically, *i.e.* spin-orbit coupling is considered only in the initial state, and both the initial and final states are treated as atomic wave functions. Thus

$$|i\rangle = |R_{n,l}; j, m_j, l, s\rangle = \sum_{m_l, m_s} |R_{n,l}; l, m_l, s, m_s\rangle \langle l, m_l, s, m_s | j, m_j\rangle \quad (3.16)$$

$$|f\rangle = |R_{n',l'}; l', m_{l'}, s', m_{s'}\rangle = R_{n',l'} Y_{l'}^{m_{l'}} \chi_{s',m_{s'}} \quad (3.17)$$

where  $R_{n,l} = R_{n,l}(r)$  is the radial part,  $Y_l^{m_l} = Y_l^{m_l}(\nu, \phi)$  is the angular part, and  $\chi_{s,m_s}$  the spin part.

The matrix element can be written

$$\left| \sum_{m_l} C_{l,m_l} \langle R_{n',l'}; l', m'_l, s', m'_s | \boldsymbol{\varepsilon} \mathbf{r} | R_{n,l}; l, m_l, s, m_s \rangle \right|^2 \quad (3.18)$$

where  $C_{l,m_l}$  are the Clebsh-Gordan coefficients. We have already shown that the tensor operator  $\boldsymbol{\varepsilon} \mathbf{r}$  could be written in the form of spherical harmonics (equations 3.13, 3.14 and 3.15). The spherical harmonic operators only act on the angular part of the wave function, so we may separate the radial  $\langle R_{n',l'} | r | R_{n,l} \rangle$ , the angular  $\langle l', m'_l | \frac{\boldsymbol{\varepsilon} \mathbf{r}}{r} | l, m_l \rangle$  and the spin  $\delta m'_s, m_s$  components. The spin part translates the conservation of the spin ( $\Delta m_s = 0$ ), while the radial part represents the overlap of the initial and final wave function, localized in the core region.

The polarization dependent absorption comes from the angular part  $\langle l', m'_l | \frac{\boldsymbol{\varepsilon} \mathbf{r}}{r} | l, m_l \rangle$ . In the case of  $p \rightarrow d$  transitions, one needs to project the initial states on the spherical harmonics basis. As an illustration, let us cite the exemple exposed in ref. [125] : consider the transition from the spin-orbit split initial state

$$|i\rangle = \left| \frac{1}{2} \frac{1}{2} \right\rangle \quad (3.19)$$

$$= \sqrt{\frac{2}{3}} Y_1^1 |\downarrow\rangle + \sqrt{\frac{1}{3}} Y_1^0 |\uparrow\rangle \quad (3.20)$$

to the final state

$$|f\rangle = Y_2^2 |\downarrow\rangle \quad (3.21)$$

Say we consider right circular polarized light ( $\boldsymbol{\varepsilon}_- \mathbf{r} = \frac{1}{\sqrt{2}}(x - iy) = r \sqrt{\frac{4\pi}{3}} Y_1^{-1}$ ) and knowing that  $\langle \downarrow | \uparrow \rangle = 0$ , we can write

$$|\langle f | \boldsymbol{\varepsilon} \mathbf{r} | i \rangle|^2 = \left| \int_{\nu, \phi} Y_2^{2*} \sqrt{\frac{4\pi}{3}} Y_1^{-1} \sqrt{\frac{1}{3}} Y_1^0 \right|^2 \quad (3.22)$$

$$= \frac{4}{15} \quad (3.23)$$

All transition probabilities are reported on table 3.2 [125].

TABLE 3.2: Transition probabilities from the spin-orbit split  $2p$  states to the final  $3d$  states having  $\downarrow$  spin for right (left) circular polarized light.[125]

	$ 2, 2\rangle$	$ 2, 1\rangle$	$ 2, 0\rangle$	$ 2, -1\rangle$	$ 2, -2\rangle$
$ \frac{1}{2}, +\frac{1}{2}\rangle$	$\frac{12}{45}$		$(\frac{2}{45})$		
$ \frac{1}{2}, -\frac{1}{2}\rangle$		$\frac{3}{45}$		$(\frac{3}{45})$	
$ \frac{3}{2}, +\frac{3}{2}\rangle$					
$ \frac{3}{2}, +\frac{1}{2}\rangle$	$\frac{6}{45}$		$(\frac{1}{45})$		
$ \frac{3}{2}, -\frac{1}{2}\rangle$		$\frac{6}{45}$		$(\frac{6}{45})$	
$ \frac{3}{2}, -\frac{3}{2}\rangle$			$\frac{3}{45}$		$(\frac{18}{45})$

The XMCD process for a  $2p$  electron with spin  $\downarrow$  is further illustrated in figure 3.1. The transition probabilities in fig. 3.1 are calculated from those reported in table 3.2. In the case of a metal, final states are no longer simple single atomic orbitals but rather a linear combination of them. The corresponding absorption process is shown in figure 3.2. If the metal is magnetized, the valence band is split by the exchange interaction and spin up and down accessible empty states are not equivalent. The XMCD originates from the difference in transition probabilities for spin  $\uparrow$  and  $\downarrow$ . However, it is worth noting that in XMCD, the spins are not probed directly but rather indirectly through the spin-orbit coupling.

### 3.1.5 The XMCD sum rules

The sum rules were first derived in 1992 by Thole *et al.* [127] for the orbital magnetic moment, and in 1993 by Carra *et al.* [128] for the spin magnetic moment. Within a few approximations, these magneto-optical sum rules allow for the determination of the expectation value of the orbital and spin operators from the relative amplitude of the polarization dependent transition probabilities. In a word, they allow for the simultaneous determination of the orbital and spin magnetic moments from the measurements of the absorption of left and right circular polarized x-rays (XAS, for x-ray absorption spectra) and their difference (the XMCD spectrum).

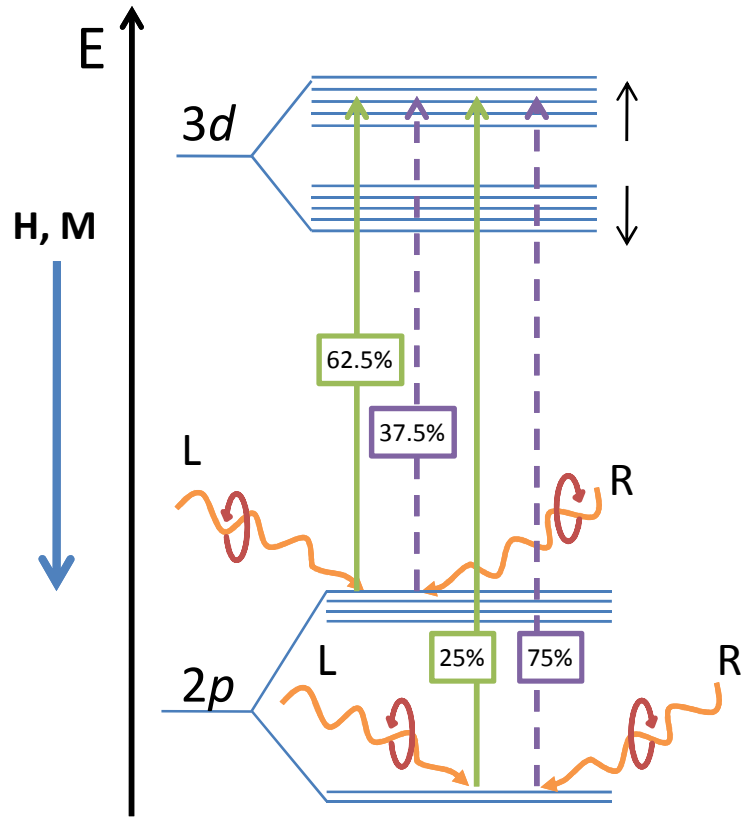


FIGURE 3.1: Simple picture of the  $2p \rightarrow 3d$  XMCD effect in an atomic-like system, for an electron with spin  $\downarrow$ , excited by left (L) or right (R) circularly polarized. The weights are given for the spin-orbit split core states  $2p_{3/2}$  and  $2p_{1/2}$ . Adapted from ref [126].

### 3.1.5.1 The orbital moment sum rule

The first sum rule states that the integrated intensity of the XMCD spectrum over the whole absorption edge (*e.g.*  $L_2 + L_3$ ) is proportional to the expectation value of the orbital operator. Let us write  $\mu_+(E)$  ( $\mu_-(E)$ ) the absorption coefficient for the circular polarisation of the light parallel (antiparallel) to the magnetization. The quantity  $\mu_+ + \mu_-$  is the isotropic absorption<sup>2</sup>. The quantity  $\mu_+ - \mu_-$  is the XMCD signal. It is conventional to use the following notations [129]

2. more rigorously, the isotropic absorption is given by  $\frac{1}{2}(\mu_+ + \mu_- + \mu_0)$ , where  $\mu_0$  is the absorption for  $z$ -linearly polarized light. However, in symmetric systems,  $\mu_0 = \frac{1}{2}(\mu_+ + \mu_-)$  and only the circular polarized absorption needs to be measured



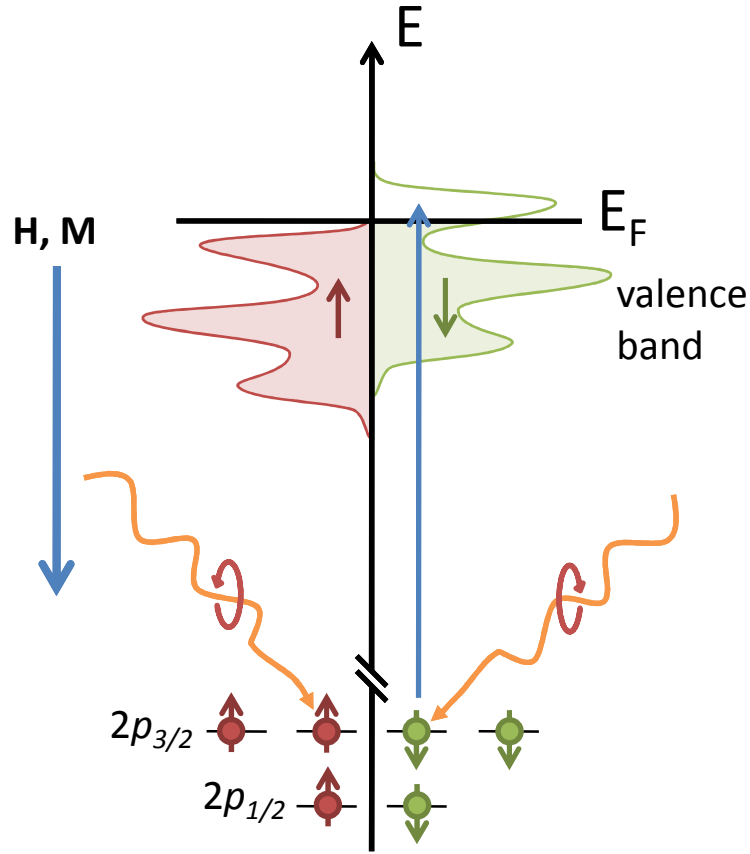


FIGURE 3.2: Simple picture of the  $2p \rightarrow 3d$  XMCD effect in a magnetic metal, for an electron with spin  $\downarrow$ , excited by left (L) or right (R) circularly polarized. The final states are the empty states in the valence band. Adapted from ref [125].

$$p = \int_{L_3} \mu_+ - \mu_- dE \quad (3.24)$$

$$q = \int_{L_3+L_2} \mu_+ - \mu_- dE \quad (3.25)$$

$$r = \int_{L_3+L_2} \mu_+ + \mu_- dE \quad (3.26)$$

Writing  $n_h$  the number of holes in the  $3d$  band, the orbital moment sum rule gives the orbital magnetic moment ( $m_l$ ) in  $\mu_B/\text{atom}$  as

$$m_l = -\frac{4}{3} \frac{q}{r} n_h \quad (3.27)$$

The most important approximations here are :

- For the transition metals, the  $L_2$  and  $L_3$  absorption edges can be well separated. However it is only true for the heavier ones ( $Z \geq 26$ , *e.g.* Fe, Co, Ni), manganese is on the onset of the separation of both edges.
- Only  $p \leftarrow d$  transitions are considered, however experimental spectra always contain contributions from transitions to other allowed states, as well as background absorption from the environment of the absorbing atoms.
- The number of  $3d$  holes is supposed to be known, however it is not an easily accessible value and often approximation or complementary calculations have to be made.

### 3.1.5.2 The spin moment sum rule

The second sum rule gives the expectation values of both the spin and magnetic dipole operators. The effective spin magnetic moment ( $m_{s,eff} = m_s + 7\langle T_z \rangle$ ) is given in  $\mu_B/atom$  by the spin moment sum rule as

$$m_{s,eff} = -\frac{6p - 4q}{r} n_h \quad (3.28)$$

The dipole operator describes the anisotropy of the spin distribution around the absorbing atom, due *e.g.* to the interaction with the orbit. Highly symmetric systems, such as bulks cubic crystal for example, are expected to have negligible dipolar contribution with respect to the spin component.

The same approximations as for the orbital moment sum rule applies, with the addition of the vanishing  $\langle T_z \rangle$  when one writes  $m_{s,eff} = m_s$ .

### 3.1.5.3 The orbital to spin ratio sum rule

A very interesting way to reduce the number of approximations (and therefore the possible errors) is to consider the *ratio* of the orbital to the spin magnetic moment

$$\frac{m_l}{m_{s,eff}} = \frac{2q}{9p - 6q} \quad (3.29)$$

This value is independent of the number of  $3d$  holes and also of the isotropic absorption ( $\mu_+ + \mu_-$ )

The different sum rules have been first successfully applied experimentally by Chen *et al.* [129]. They measured orbital and spin magnetic moment values in Fe and Co thin films within 7% to those reported using gyromagnetic ratio measurements [130]. The orbital to spin magnetic moment ratio was found to be in even better agreement (3%), as expected from the smaller number of approximations in the orbital to spin ratio sum rule.

These results have revealed the validity of the sum rule analysis, which, along with the development of synchrotron radiation sources, have made the XAS-XMCD technique a powerful tool for investigating the magnetic properties of materials.

## 3.2 X-ray absorption spectroscopy : Experimental considerations

In order to apply the sum rules and extract quantitative informations on the magnetic moments, one needs to measure the x-ray absorption spectra in the considered sample. In this section I will describe how one can measure such spectra, as well as the different synchrotron experimental setups that were used during this thesis. In the last subsection I will give a step by step description of the data processing used.

### 3.2.1 How to measure x-ray absorption

There are several ways to measure the absorption of x-rays by matter. I will describe here the three most common techniques : one that is direct, the ‘transmission mode’, and two that are indirect, respectively the so-called ‘total electron yield’ and the ‘fluorescence yield’. Details about the experimental possibilities as well as the technical and physical limitations of all three techniques are also given below. During my thesis, I had the opportunity to experiment all three techniques, yet only the indirect ones were suited for the characterization of the GeMn nanocolumns.

### 3.2.1.1 The transmission mode

The most straightforward way to measure the absorption coefficient is to use the Beer-Lamber's law :

$$I(E) = I_0(E)e^{-\mu(E)t} \quad (3.30)$$

where  $I_0(E)$  and  $I(E)$  respectively are the incoming and outgoing intensity on the sample, usually measured using photodiodes;  $t$  is the sample thickness and  $\mu(E)$  is the absorption coefficient. The energy  $E$  of the incoming beam is usually set to a precision of  $\frac{\Delta E}{E} \sim 10^{-4}$  using a monochromator. A simple sketch of the principle is shown in figure 3.3. The length over which the signal is attenuated by a factor  $1/e$  defines the attenuation length  $\lambda_x = \frac{1}{\mu}$ . The main advantage of this technique is that it provides a direct measurement of  $\mu = \frac{1}{t} \ln(\frac{I_0(E)}{I(E)})$ .

Due to the enhancement of the absorption coefficient near the resonance,  $\lambda_x$  varies rapidly around the absorption edges. For example, in the case of Mn-metal  $\lambda_x$  is more than  $0.5 \mu m$  below the  $L_3$  edge, less than  $70 \text{ nm}$  at the edge and about  $80 \text{ nm}$  after the  $L_2$  edge [100]. This is one of the main limitation of this technique since the sample must be thin enough – on the order of  $100 \text{ nm}$  – so that some signal can still be measured through at the absorption edges. Moreover, the  $L_{2,3}$  absorption edges of the 3d transition metals are in the soft x-ray regime where the absorption by air is significant, therefore the experiments have to be conducted in vacuum. This issue vanishes in the case of  $K$ -edge measurements where hard x-rays, *i.e.* energies above  $1 \text{ keV}$  are required.

As transmission measurements, by definition, are measured through the whole thickness of the sample, one should also take care to measure the transmission through a clean substrate. That way, background signal from the substrate may be properly removed and does not need to be modeled.

### 3.2.1.2 The fluorescence yield mode

A second way to measure the x-ray absorption of the sample is to detect the photons emitted during the desexcitation of the absorbing atoms, that is the fluorescence yield (FY). In this case, one places the detector on the same side of the

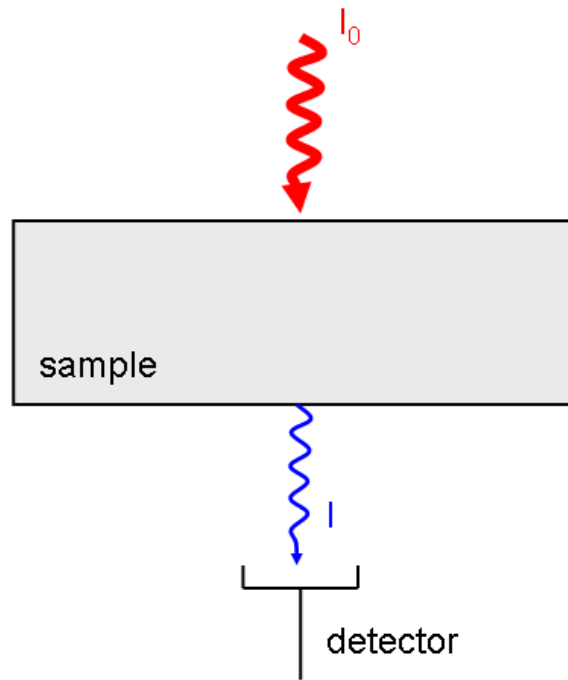


FIGURE 3.3: Principle of transmission XAS measurement.  $I_0$  is the intensity of the incoming light (x-rays) and  $I$  the transmitted intensity that is measured.

sample as the incoming beam (figure 3.4) and one assumes the proportionality between the number of absorbed photons and the number of photons emitted by fluorescence over the considered energy range. Similarly to what was discussed in the previous paragraph, the probing depth is limited by both the attenuation length (or *penetration length*) and the photon escape length. In this case they are both equal to  $\lambda_x$  and the probing depth is typically of a few tens of nanometers in the soft x-ray regime. There are two major issues with this technique. The first one is a poor signal-to-noise ratio (SNR), due to the small contribution of the fluorescence channel in the soft x-ray range. The second issue is known as ‘self-absorption’. It occurs in the case of concentrated samples, *i.e.* when there are more than a few percent of absorbing atoms : for energies close the absorption edge, the fluorescence photon can be re-absorbed and remain undetected. As a result, the signal at the absorption edges is weaker than what it should be. Correction for this effect have been proposed [131], but they rely on a self-consistent equation and its solution requires high-quality data.

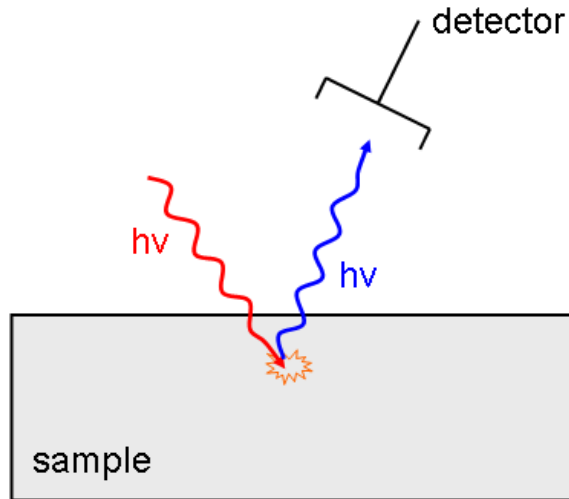


FIGURE 3.4: Principle of fluorescence yield XAS measurement.

### 3.2.1.3 The total electron yield mode

The last way to measure the x-ray absorption of the sample is known as the ‘total electron yield’. It consists in measuring the proportion of Auger electrons that cascade up to the surface of the sample and escape in the vacuum. The probability of Auger decay is considered constant over the considered energy range, as well as the cascading process. To detect the escaping electrons, one connects the sample to the ground through a pico-ammeter and simply measures the current flowing back from the sample as can be seen in figure 3.5. In this case the probing depth is mostly limited by the escaping depth of the electrons  $\lambda_e$ , which is typically of only a few nanometers for 3d metals. The main limitations of this technique are : (i) the requirement for conductive samples (and the good connection between the surface and the ground), (ii) in some cases the signal measured maybe affected by the applied magnetic field (XMCD measurements) due to its effect of the electrons trajectory [132] and (iii) the saturation effect. The latter can be observed when measurements are done for several angles of incidence : when the incidence angle over the surface is small enough, the projected penetration depth of the x-rays becomes comparable to the escaping depth of the electrons. The signal is then strongly affected by variations of  $\lambda_x$  around the absorption edge. This can be corrected, as demonstrated by Nakajima *et al.*[133, 134], however the correction requires a good knowledge of  $\lambda_e$  and the solution of a self-consistent equation. Despite these limitations, the TEY technique is still a quite simple way to measure the x-ray absorption spectra and it is the technique we have mostly used in the

case of the GeMn nanocolumns. It can be noted that we were also able to measure the FY at the same time on the different setups we have conducted experiences on (beamlines UE46-PGM at the Helmholtz Center Berlin and ID08 at the European Synchrotron Radiation Facility).

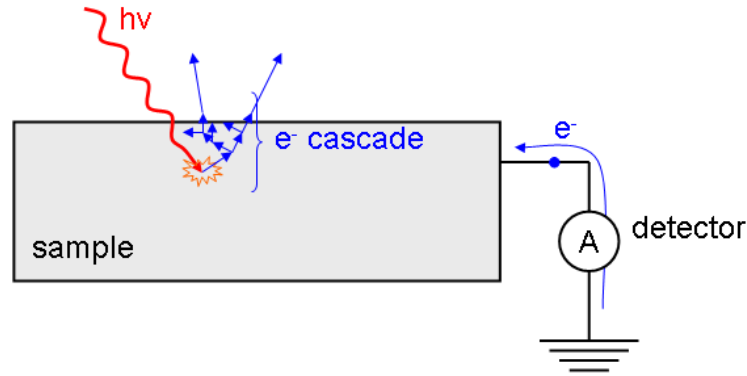


FIGURE 3.5: Principle of total electron yield XAS measurement.

### 3.2.2 Synchrotron experimental setups

In order to apply the XAS-XMCD technique to the L absorption edge in  $3d$  transition metals, x-ray in the soft x-ray regime (on the order of 1 keV) are required. The photon beam needs to be monochromatic and tunable to perform high-resolution spectroscopy. A large photon flux is preferable, in order to measure the absorption spectra as fast as possible (and before any modification of the sample). In the case of diluted systems, with concentration in magnetic element on the order of a few percent, further requirements include (i) a large experimental sensitivity due to the very small signal (typical signal currents are in the picoampere range), (ii) low accessible temperatures (few Kelvin) and (iii) large magnetic fields (few Tesla) to increase as much as possible the magnetic signal.

All these different features are typically found on XAS-XMCD beamlines in synchrotron radiation facilities. During this thesis, two of such beamlines were used : UE46-PGM1 at the Helmholtz Centre Berlin (formerly BESSY-II), and ID08 at the ESRF in Grenoble.

### 3.2.2.1 A XAS-XMCD beamline : UE46-PGM1 at the Helmholtz Centre Berlin

As an illustration of a typical XAS-XMCD beamline, I shall give here a quick overview of the UE46-PGM1 beamline at the Helmholtz Centre Berlin (formerly BESSY). A sketch of the different elements is shown in figure 3.6(a).

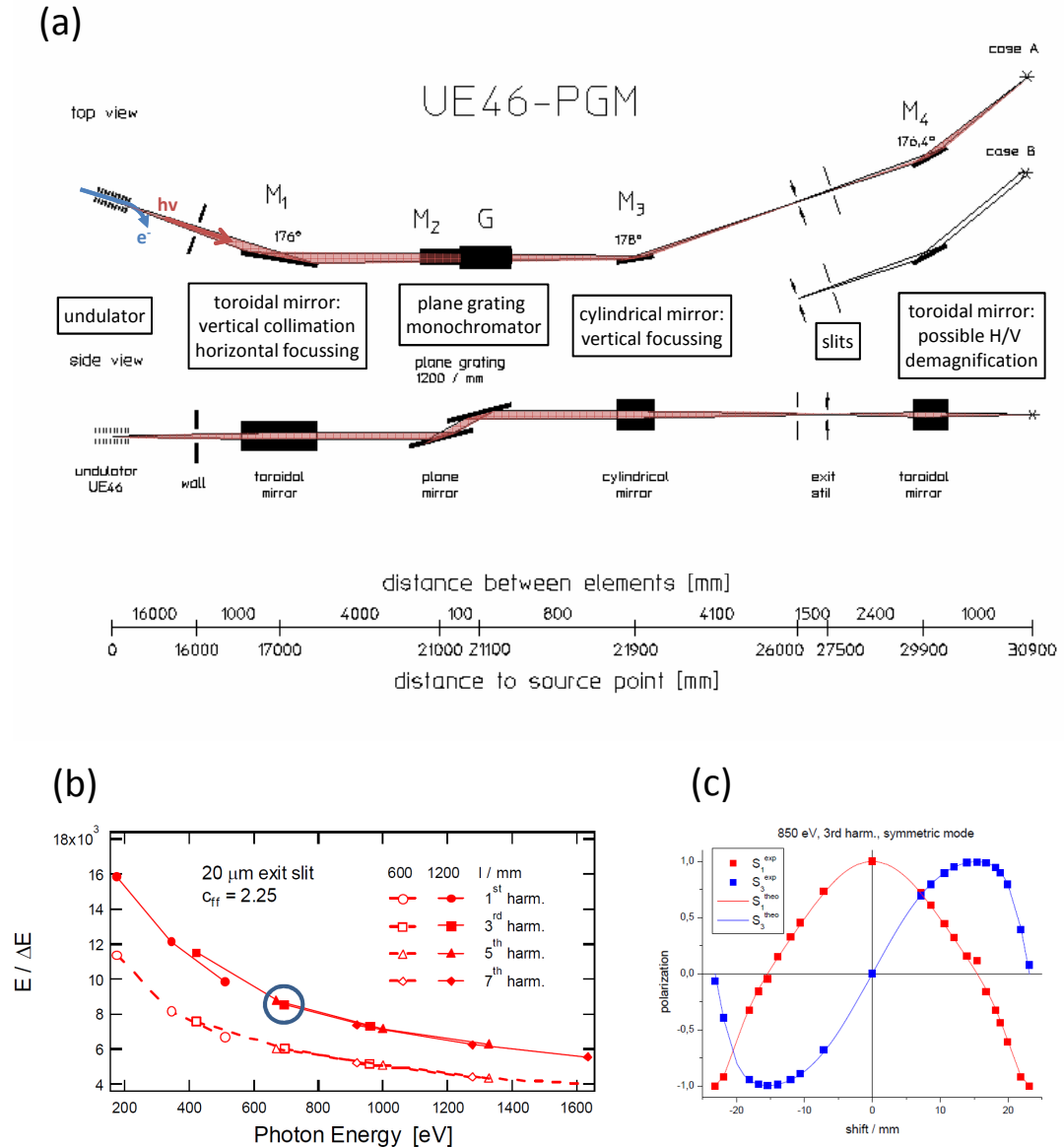


FIGURE 3.6: Characteristics of the UE46-PGM1 beamline at the Helmholtz Centre Berlin. (a) Schematic view of the organisation of the different elements in the beamline. (b) Calculated and experimentally verified energy resolution of the monochromator. (c) Calculated and measured polarization. Adapted from refs. [135, 136].



The x-ray source is a type APPLE II (Advanced Planar Polarized Light Emitter II) undulator [137], such undulators are also present at beamline ID08 at the European Synchrotron Radiation Facility. An undulator consists in arrays of permanent magnets that modify the path of the electrons going through it into an helix. The radiation is then emitted coherently in a narrow energy range that can be tuned by adjusting the vertical *gap* between the two magnet arrays. As a result, the emitted radiation has a very large photon flux and more specifically a very large brilliance (*i.e.* the number of photons/s/mm<sup>2</sup>/mrad<sup>2</sup> per 0.1% bandwidth). Typical values are the order of 10<sup>18</sup> (more than a billion times the brilliance of the sun). Additionally, the polarization (linear, circular or elliptical) can be tuned by adjusting the horizontal *shift* between the magnet arrays, as illustrated in figure 3.6(c). A schematic view and the modes of operations of an APPLE II undulator are shown in figure 3.7.

### **APPLE-II type undulator: 4 different modes**

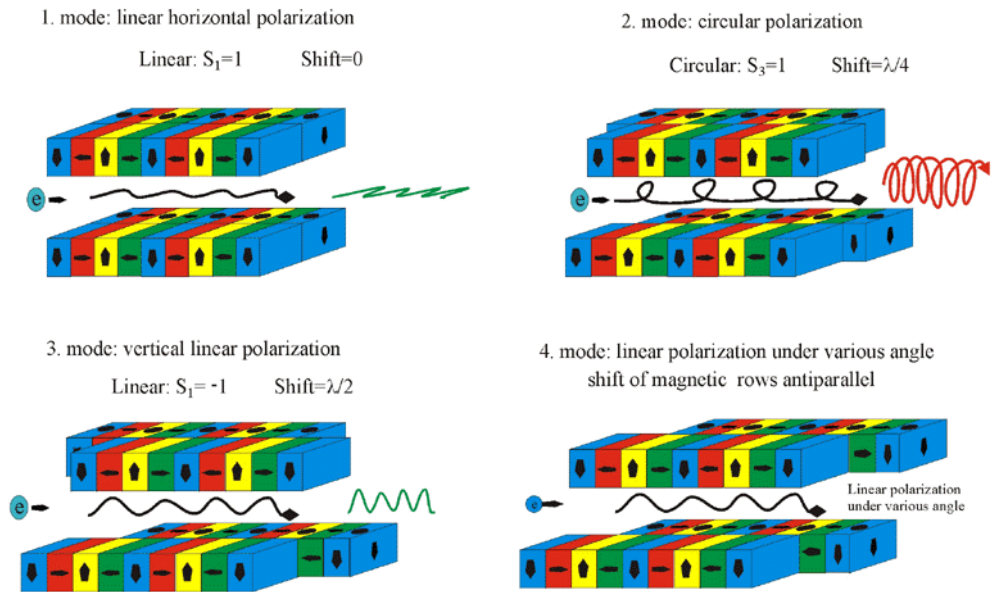


FIGURE 3.7: Schematic view and modes of operation of an APPLE II undulator such as those at the Helmholtz Center Berlin and the ESRF. From ref. [138].

The first mirror is used to focus the beam in the horizontal plane and to perform vertical collimation just before the monochromator. The beam energy is selected using a plane grating monochromator [139]. The energy resolution at the Mn L-edge is  $\frac{\Delta E}{E} \approx 10^{-4}$ , as shown in figure 3.6(b). A second mirror is used after the

monochromator to focus the beam in the vertical plane. A pair of slits placed before the sample defines the beam size on the sample.

### 3.2.2.2 Experimental setups and data acquisition

Both endstations at beamlines UE46-PGM at the Helmholtz Center Berlin and ID08 at the European Synchrotron Radiation Facility share features allowing XAS-XMCD measurements for *ex situ* samples. As exposed in the previous sections, the magnitude of the XMCD signal is proportional to the local magnetic moment. Hence, large magnetic fields are suitable to measure magnetic moments as close as possible to the saturation, especially in diluted systems. At both endstations, the high magnetic field ( $> 5$  Tesla) was provided by a liquid-helium cooled superconducting magnet. The amplitude of the applied can be modulated by changing the current in the superconducting loop. This allows for element-specific hysteresis loop measurements and magnetization curves measurements. Such cryomagnets may also be rotated along with the sample around the  $z$ -axis (fig. 3.8) to study anisotropy effects. Note that under grazing incidence saturation effects may occur, due to small projected depth compared to the electron escape depth [133]. A cryostat is used to achieve low temperature ( $\sim 5$  K) on the sample and enhance the magnetic signal. A heating element coupled to a temperature sensor can be used to set a stable temperature in the range 5–300 K, allowing for the measurement of the temperature dependence of the magnetic signal. At all point during the experiment, the sample is kept in a UHV environment to prevent surface contamination. The results presented in this thesis were obtained using the TEY mode. Such measurements were obtained after gluing the sample to the conducting sample holder using silver paste and making sure that the surface was contacted as well.

The data acquisition protocol was slightly different between the measurements at UE46-PGM and ID08. At beamline UE46, the *stop and go* was used : is consists in defining a table of energies to be measured and to have the setup go to each energy, stop and measure the absorption, before moving to the next energy point. The applied magnetic field is kept constant as well as the circular polarization. Once the scan is done (about 15 min), the polarization was reversed at the undulator (on the order of a minute) and the corresponding symetric scan was acquired. The procedure was repeated several times for averaging.

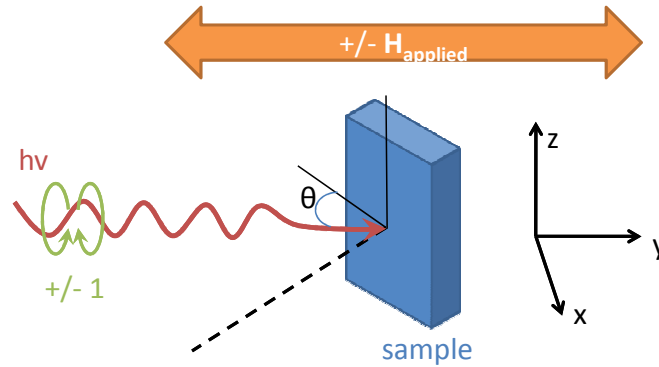


FIGURE 3.8: Schematic drawing of the measurement geometry. The x-ray beam and the magnetic field direction are parallel to the  $y$ -axis. The sample can be rotated about the  $z$ -axis and the angle between the surface of the sample and the  $y$ -axis is noted  $\theta$ . The applied magnetic field and/or the beam circular polarization can be reversed.

At beamline ID08, the slightly different setup allowed for *flyscan* measurements. Such measurements are obtained by continuously moving the energy while simultaneously recording the absorption. This allowed for much faster measurements. As a result, data were not acquired at specific energies. A simple interpolation was then further needed for data processing. Typically, four scans were acquired with polarization sequence  $+ - +$ . Since measurements were much faster, we also performed the same sequence after reversing the applied magnetic field. As a result, the noise in our spectra was much reduced.

### 3.3 Conclusion

We have seen in this chapter that the x-ray absorption spectroscopy and the x-ray magnetic circular dichroism techniques allow for the probing of the magnetic moment with chemical selectivity. The use of theoretical sum rules within the dipolar approximation (*i.e.* incident wavelength much larger than the spatial extent of the probed  $3d$  orbitals) allows for a specific determination of both orbital and spin components of the magnetic moment. A typical experimental setup was illustrated by the beamline UE46-PGM1 at the Helmholtz Centre Berlin (formerly BESSY) and some particularities of the beamline ID08 at the European Synchrotron Radiation Facility were given, both of them having been used during this thesis.

## 3.4 Résumé du chapitre 3

Le chapitre 3 présente le cadre théorique et expérimental des techniques de mesures de spectroscopie d'absorption de rayons X et de dichroïsme circulaire magnétique de rayons X.

Nous avons vu que les techniques de spectroscopie d'absorption de rayons X et de dichroïsme circulaire magnétique de rayons X permettent la mesure du moment magnétique avec une sensibilité chimique. Par ailleurs, les composantes orbitales et de spin du moment magnétique peuvent être déterminées par l'utilisation de règles de somme théoriques dans la limite de l'approximation dipolaire (c'est à dire pour des longueurs d'ondes incidentes bien plus grandes que l'étendue spatiale des orbitales  $3d$  sondées). La ligne de lumière UE46-PGM1 au Centre Helmholtz de Berlin (Helmholtz Centre Berlin) illustre le montage expérimental typique pour les mesures XAS-XMCD. Les particularités de la ligne de lumière ID08 à l'ESRF (European Synchrotron Radiation Facility) ont aussi été discutées, ces deux lignes ayant été utilisées durant cette thèse.

## Chapitre 4

# Structural analysis of the GeMn system by x-ray scattering and diffraction

X-ray scattering techniques are the tool of choice for investigating unknown crystalline structure. Such techniques can make use of the high intensity synchrotron radiation and are therefore highly suited for the study of nano-objects, such as the GeMn nanocolumns. A good description of the crystalline structure in the nanocolumns is of primary interest, *e.g.* for further modelization and *ab initio* calculations of magnetic or electronic properties, or for further growth optimization.

In this chapter, I describe the most important results on the structural properties of the nanocolumns obtained using various grazing-incidence and diffuse scattering techniques. We investigated the crystalline structure both *in* the nanocolumns, as well as *around* them, in the Ge matrix. In particular we have determined the influence of the nanocolumns, as inclusions, in the Ge matrix and the resulting strain. A large amount of work was put into measuring the x-ray scattering from the nanocolumns on various experimental setups, mostly on different beamlines at the European Synchrotron Radiation Facility. For the sake of clarity, only the most relevant results are presented in this chapter.

## 4.1 Study of the atomic structure in the GeMn nanocolumns

It has previously been shown [96] that specular  $\theta - 2\theta$  scans (*i.e.* in the [001] direction, perpendicular to the surface) for GeMn samples grown at low temperature (100°C) show only the Ge (004) Bragg reflection, whereas in samples grown at higher temperature (130°C) or annealed, one can also observe the forbidden Ge (002) and (006) reflections. Two explanations have been proposed and can be further discussed : the origin of these forbidden Bragg reflections could be due to crystal defects induced symmetry breaking, or to local chemical ordering in the case of alloys.

In order to get more insights on the possible crystalline order inside the nanocolumns, we have turned to grazing incidence techniques. Such techniques, described in more details in chapter 2, make use of the critical angle of total reflection (on the order of a few tens of a degree for hard x-rays in Ge) in order to maximize the scattering from the top layer and minimize that of the substrate.

### 4.1.1 X-ray scattering by the GeMn nanocolumns : a grazing incidence study

Using the techniques described in Chapter 2, we have measured the intensity of the x-rays scattered by the GeMn nanocolumns under grazing incidence. We have considered different samples, depending on the structural parameters of the nanocolumns (diameters and density). We have also considered nanocolumns grown on typical Ge(001) substrate as well as nanocolumns grown on GaAs substrates. Nanocolumns grown on GaAs substrates are interesting from the point of view of magnetotransport measurements (GaAs substrates are more resistive than commercial Ge substrates) and from the point of view of future realization of Spin-LED devices. We will show here that no fundamental difference between Ge- or GaAs-grown nanocolumns can be observed and that, in fact, they show the same structural features (*i.e.* correlated deformations of the Ge matrix).

#### 4.1.1.1 Methodology

Different types of experiments were carried out to understand the crystalline structure in the GeMn samples. Most techniques were based on grazing incidence to maximize the signal from the GeMn layer. In particular, we have used GISAXS<sup>1</sup> and GISAXS-type techniques to probe the different correlation lengths in the GeMn samples. We also measured the scattering at wide angles (including out-of-plane) to investigate the signs of a new crystalline phase in the nanocolumns. Small-angle measurements around the Ge diamond Bragg were also carried out to probe the strain in the Ge matrix. Those techniques relied on the mapping of reciprocal space, as described in chapter 2. The most typical results for various samples are presented in figures 4.2, 4.3, 4.1, 4.4, 4.5, 4.6. All the relevant parameters are summarized in table 4.1.

TABLE 4.1: Structural (nanocolumns density and diameter) and growth (growth temperature and Mn concentration) parameters of the GeMn nanocolumns samples studied by grazing incidence x-ray scattering.

	Density	Diameter	$T_{\text{growth}}$	$x_{\text{Mn}}$	Notes
Sample	( $\mu\text{m}^{-2}$ )	(nm)	( $^{\circ}\text{C}$ )	(%)	
GM259	$24,000 \pm 4,000$	$2.1 \pm 0.4$	100	10	
GM154	$28,000 \pm 2,000$	$3.0 \pm 0.5$	100	11.3	
GM197	$20,000 \pm 2,000$	$3.2 \pm 0.6$	130	10	<sup>a</sup>
GM173	$8,500 \pm 300$	$5.0 \pm 0.7$	150	6	<sup>b</sup>
GM169	$6,800 \pm 400$	$6.1 \pm 1.7$	150	11.3	<sup>c</sup>
GM267			100	10	<sup>d</sup>

<sup>a</sup> Efficiently capped with 0.5 nm Ge + 3 nm amorphous Si. Similar results were obtained *in situ* for similar uncapped samples.

<sup>b</sup> This sample was measured after several months of exposure to air.

<sup>c</sup> This sample contains amorphous nanocolumns.

<sup>d</sup> Grazing incidence x-ray scattering measured *in situ*. Similar grazing incidence reciprocal maps were obtained for a similar sample grown at  $130^{\circ}\text{C}$ .

---

1. See, *e.g.*, ref. [107] for a recent review on this technique

#### 4.1.1.2 Dense and small nanocolumns (low growth temperature)

High-resolution TEM micrographs have suggested that smaller nanocolumns ( $\sim 2$  nm in diameter) would be more crystalline and show less disorder [96]. However, reciprocal space maps (RSM) measured in such samples – shown in figure 4.1(a) – show no sign of a crystalline phase different from Ge diamond. In fact, only the expected 220 and 040 Bragg reflections can be seen in that portion of reciprocal space. A low intensity curve can be observed in figure 4.1(a) corresponding to a constant  $\omega$  angle, due to the absorption of the kapton cone protecting the sample. No particular diffusion around the Bragg peaks could be observed, as shown in figures 4.1(c-f).



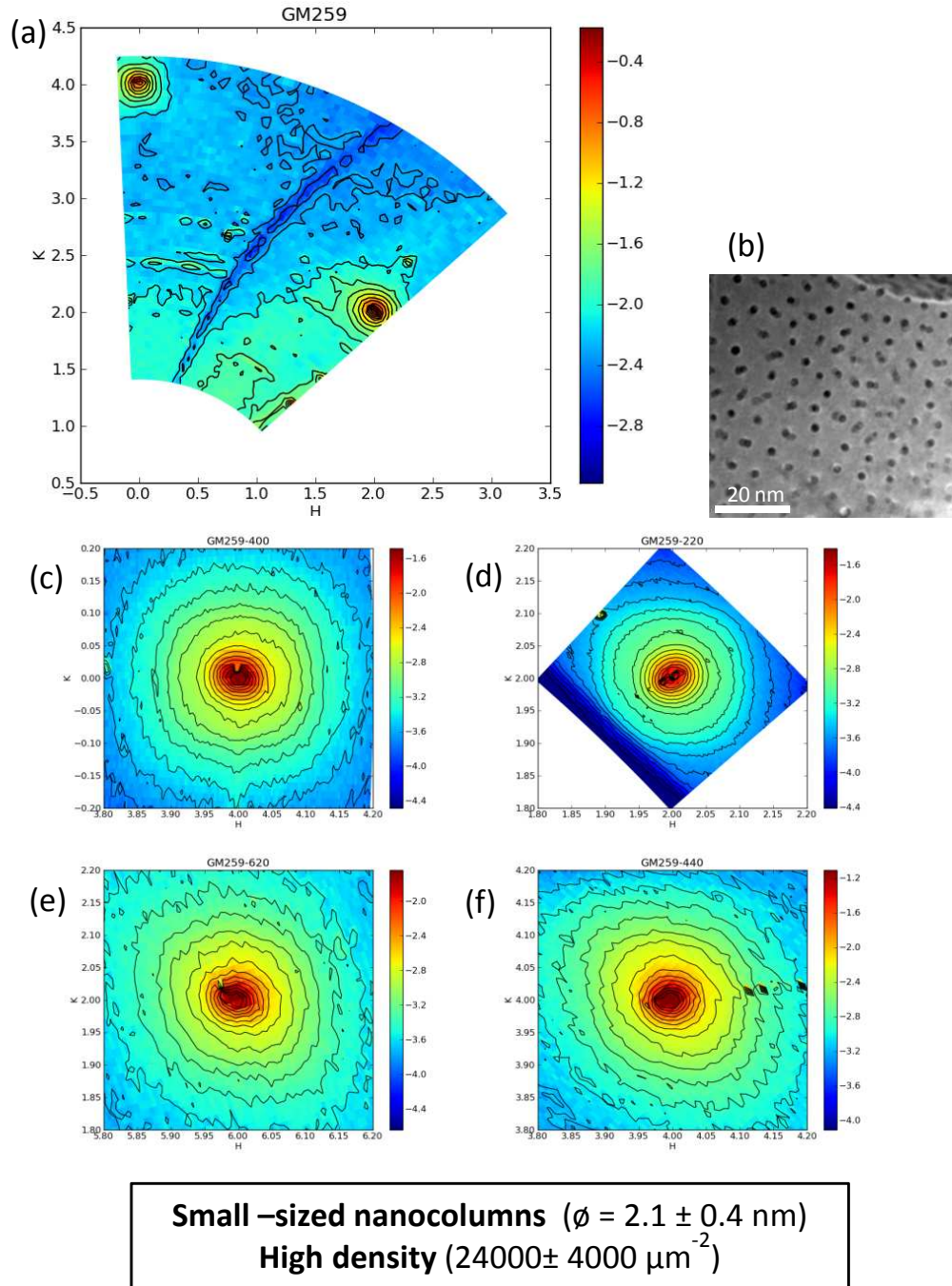


FIGURE 4.1: (a) Grazing incidence reciprocal space map (GI-RSM) of the measured intensity in the  $hk0$  plane. (b) Plane-view TEM micrograph. (c,d,e,f) GI-RSM around the 400, 220, 620, 440 Bragg reflections. In (a) and (c–f) the intensity is represented as a logarithmic color scale, the full scale corresponding to 3 orders of magnitude for all plots (2 above and 1 below the median value in each plot). There are respectively 15 and 20 equally spaced contour lines in (a) and (c–f). All plots were normalized to the brightest pixel.

#### **4.1.1.3 Very large amorphous nanocolumns (medium to high growth temperature and large Mn concentration)**

In heavily disordered samples, containing large amorphous nanocolumns, the RSM shown in figure 4.2(a) exhibits amorphous rings superposed to a faint Ge diamond diffraction pattern. Two orientations of the Ge diffraction pattern can be observed at  $45^\circ$  of each other, as can be inferred by the two sets of  $\{220, 400, 440\}$  reflections indicated by the gray circles and gray squares in figure 4.2(a). Such nanocolumns also appear amorphous when inspected in TEM, as shown in figure 4.2(c). As a side note, magnetic measurements have shown that the anisotropy is out-of-plane, as expected from their shape and no magnetocrystalline component seems to be present [96].

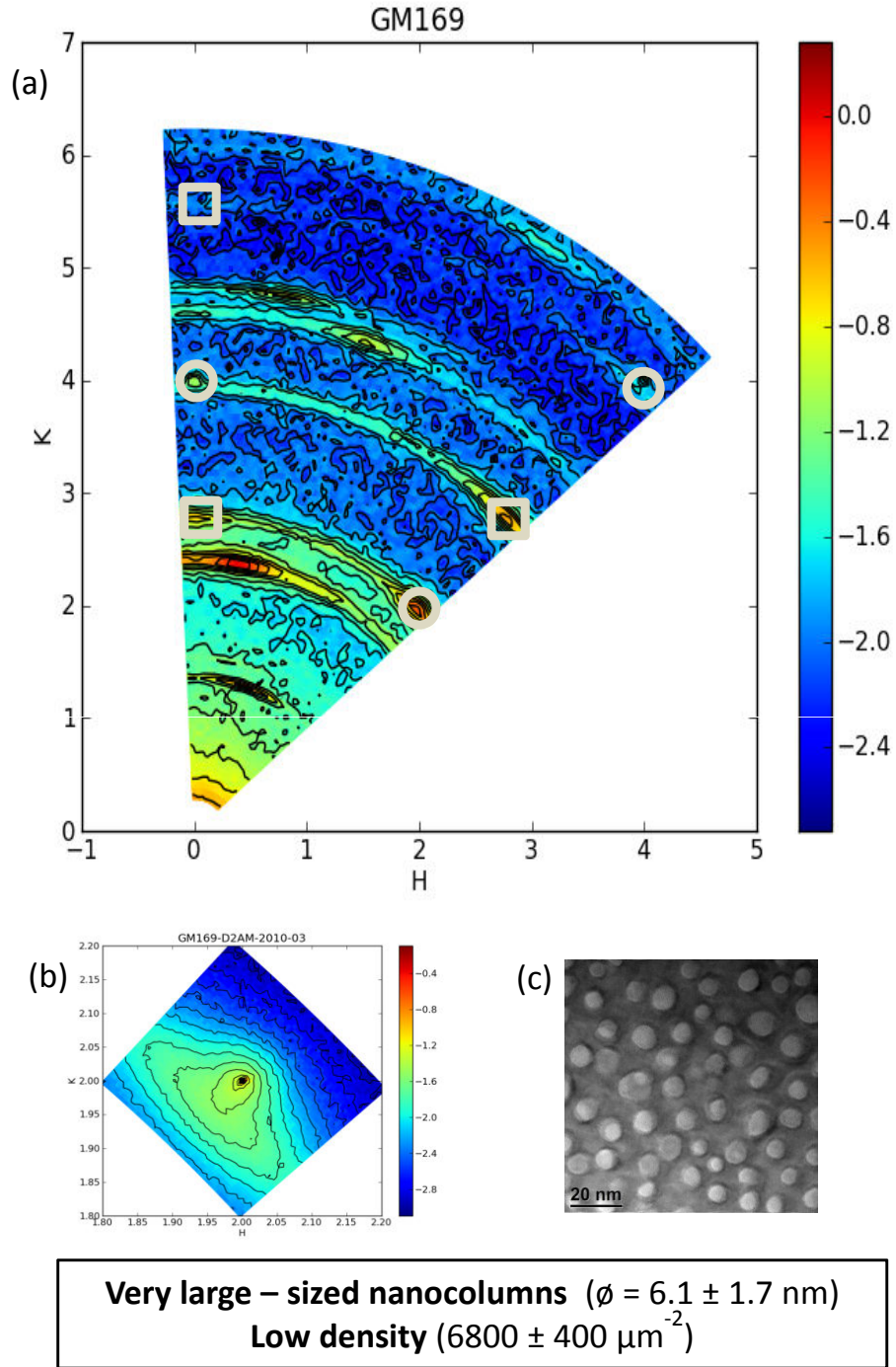
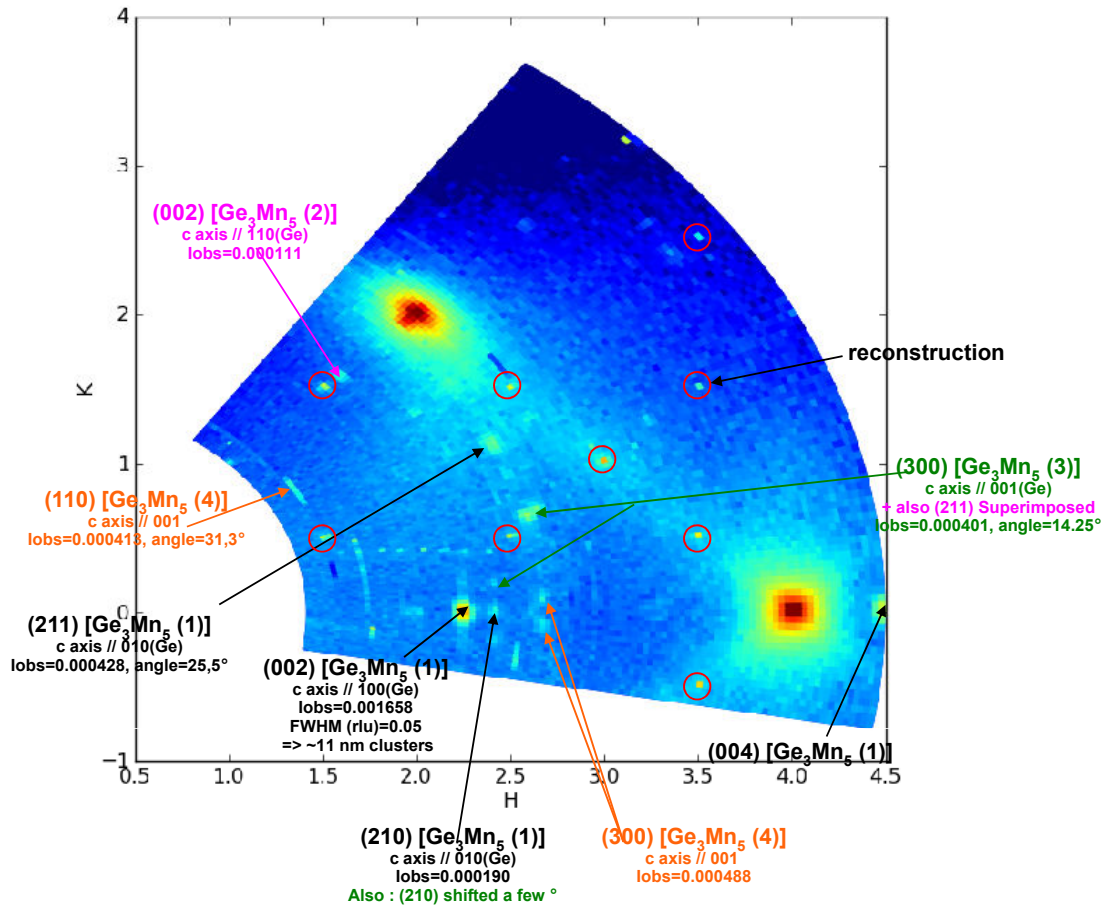


FIGURE 4.2: (a) Grazing incidence reciprocal space map (GI-RSM) of the measured intensity in the  $hk0$  plane. (b) GI-RSM around the 220 Bragg reflections. (c) Plane-view TEM micrograph. In (a,b) the intensity is represented as a logarithmic color scale, the full scale corresponding to 3 orders of magnitude for all plots (2 above and 1 below the median value in each plot). There are respectively 15 and 20 equally spaced contour lines in (a) and (b). All plots were normalized to the brightest pixel.

#### 4.1.1.4 $\text{Ge}_3\text{Mn}_5$ clusters (high growth temperature or annealing)

When  $\text{Ge}_3\text{Mn}_5$  clusters are present, specific Bragg peaks can be seen in the reciprocal space maps. Different sizes and orientations of the clusters may be observed, as shown in figure 4.3, measured in a GeMn sample after *in situ* annealing. We observed a preferential alignment of the  $\text{Ge}_3\text{Mn}_5$   $c$ -axis in-plane, along that the Ge diamond (100) orientation ( $(001)_{\text{Ge}_3\text{Mn}_5} // (100)_{\text{Ge}}$ ). A small percentage of the clusters appeared to have their  $c$ -axis parallel to the (110) direction in Ge. An even smaller fraction had their  $c$ -axis oriented perpendicular to the plane, with either their (210) or (100) orientation parallel to the (100) orientation of Ge. These results are in agreement with a recent study by Lechner *et al.*, who have published a depth-resolved analysis of the orientation of the  $\text{Ge}_3\text{Mn}_5$  clusters in GeMn [74]. They found two types of clusters : deeply buried ( $>10$  nm) clusters, with their  $c$ -axis parallel to that of Ge and that we did not observe because our sample was only 10 nm thick, and shallow clusters, with different inclinations of the  $c$ -axis (up to  $90^\circ$ ).



#### Clusters orientation summary :

- |     |  |
|-----|--|
| (1) | $c$ // (100) Ge<br>(210) // (010)Ge<br>Population: $\sim 1$                                  |
| (2) | $c$ // (110) Ge<br>(210) in-plane (we see 211)<br>Population: 0.07                           |
| (3) | $c$ // (001) Ge<br>(210) $\sim$ // (100)Ge (a few $^\circ$ off axis)<br>Population: $< 0.05$ |
| (4) | $c$ // (001) Ge<br>(100) $\sim$ // (100)Ge<br>Population: $< 0.05$                           |

HKL	Nominal F <sup>2</sup>
100	1020
110	2400
200	2000
111	6000
002	50000
210	1700
102	670
121	7500
300	12000
112	2000

FIGURE 4.3: Grazing incidence reciprocal space map (GI-RSM) of the measured intensity in the  $hk0$  plane for a  $\text{GeMn}$  sample annealed *in situ*. Well-defined additional Bragg peaks can be observed and can be indexed on the  $\text{Ge}_3\text{Mn}_5$  crystalline structure. In particular, different orientations of the nanoclusters can be observed, though clusters with their (001) axis parallel to the (100) orientation of Ge are predominant.

#### 4.1.1.5 Medium-to-large-sized nanocolumns (medium-range growth temperatures and Mn concentrations)

In the case of samples containing nanocolumns with intermediate diameters ( $2 \leq d \leq 7$  nm), some additional features may be seen in the RSM. A diffuse line can be observed between the Ge diamond 220 and 040 Bragg reflections in nanocolumns with diameters in the lower range, as seen in figure 4.4(a). The diffuse intensity is also larger around the face-centered-cubic forbidden 310 Bragg reflection. A diffuse ring can also be seen below the Ge 220 reflection. A tentative interpretation is that the intensity observed around the 310 reflection comes from disorder in the Ge diamond lattice, that partially lifts the extinction condition on this reflection. In the same fashion, we first attributed the observed diffuse line between the 220 and 040 reflections to possible dislocations in the Ge diamond structure, at the interface with the nanocolumns. The diffuse ring that is observed below the Ge 220 reflection may be attributed to disordered regions in the sample, *e.g.* in the core of the nanocolumns or their interfaces with the matrix. The small peaks on the ring at exactly the 220 distance are attributed to randomly oriented crystallites on the surface, probably coming from sample manipulation. We will show further other RSM measured during a different experiment where such parasite peaks have disappeared.

A closer look at the accessible Ge diamond Bragg reflections, *i.e.* the 220, 040, 440 and 620 reflections, reveals a very specific diffuse scattering around those Bragg peaks, as can be seen in figures 4.4(c–f) and figures 4.5(c–d). This diffuse scattering consists in a ring around the BP, whose intensity is larger on the high- $q$  side of the BP. In particular, the rings are *polarized*, *i.e.* the intensity is not constant around it, and stronger along the H and K directions. It will be shown in the next section that such features are in fact due to the correlated strain in the Ge matrix from the GeMn nanocolumns. The correlation comes from the correlated positions of the nanocolumns in the matrix.



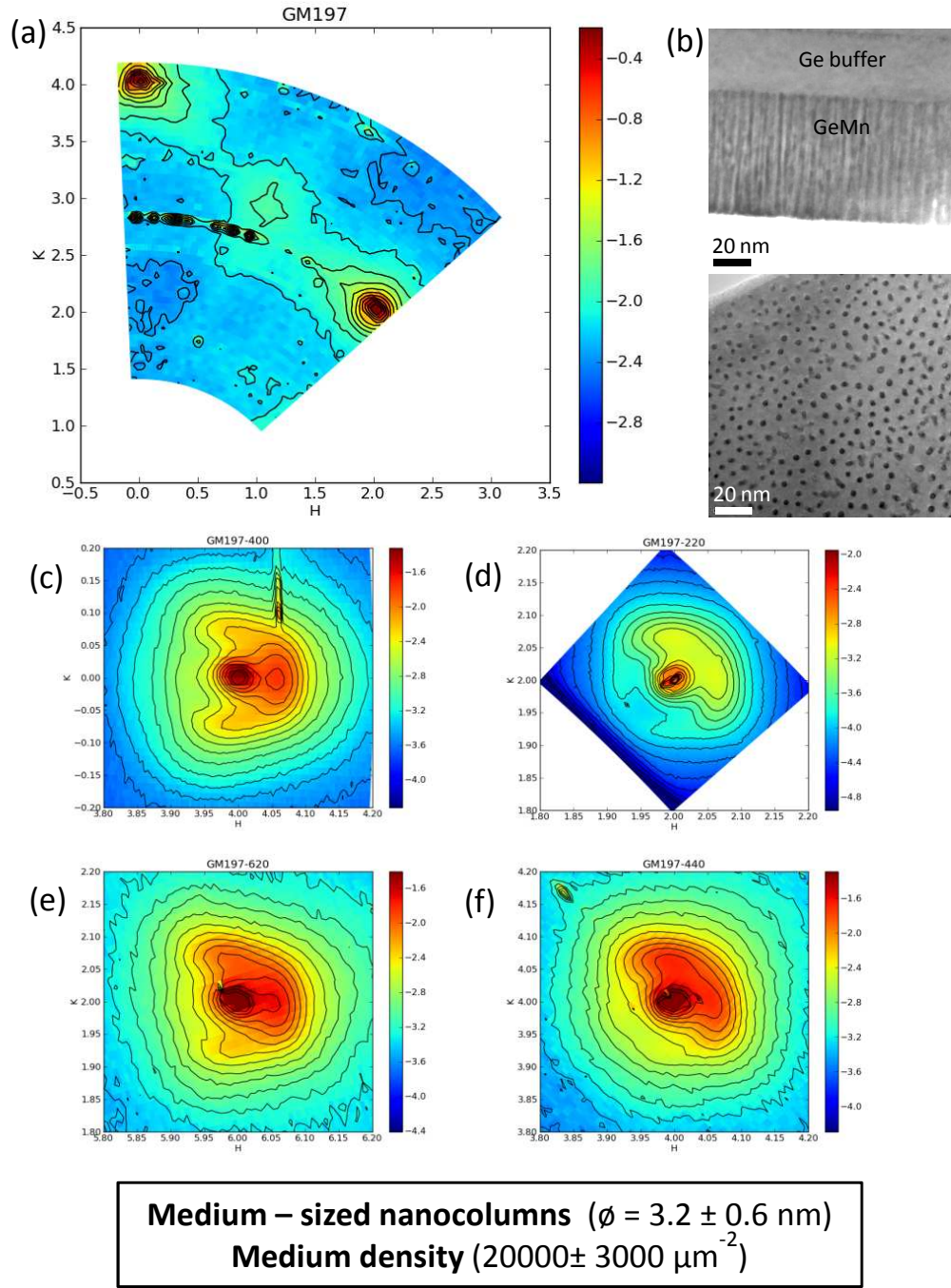
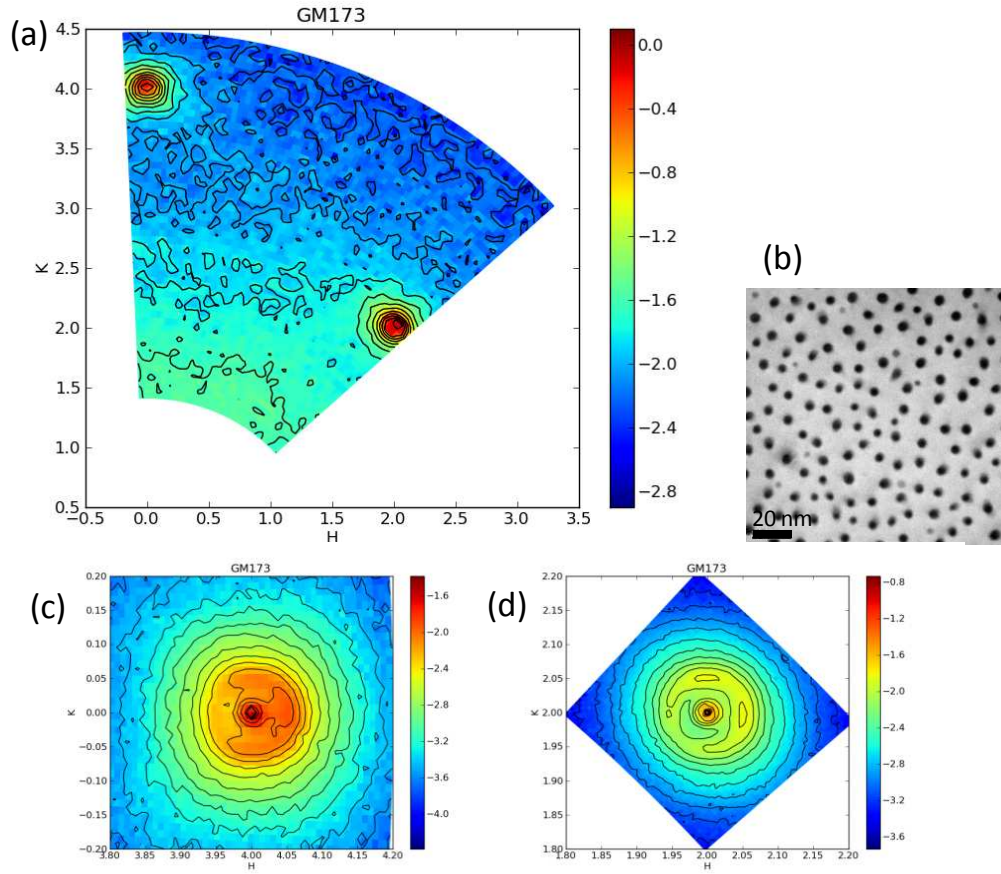


FIGURE 4.4: (a) Grazing incidence reciprocal space map (GI-RSM) of the measured intensity in the  $hk0$  plane. (b) Cross-sectional (top) and plane-view (bottom) TEM micrograph. Both micrographs are on the same scale. (c,d,e,f) GI-RSM around the 400, 220, 620, 440 Bragg reflections. In (a) and (c–f) the intensity is represented as a logarithmic color scale, the full scale corresponding to 3 orders of magnitude for all plots (2 above and 1 below the median value in each plot). There are respectively 15 and 20 equally spaced contour lines in (a) and (c–f). All plots were normalized to the brightest pixel.



**Large – sized nanocolumns ( $\phi = 5.0 \pm 0.7$  nm)**  
**Low density ( $8500 \pm 300 \mu\text{m}^{-2}$ )**

FIGURE 4.5: (a) Grazing incidence reciprocal space map (GI-RSM) of the measured intensity in the  $hk0$  plane. (b) Plane-view TEM micrograph. (c,d) GI-RSM around the 400, 220 Bragg reflections. In (a) and (c, d) the intensity is represented as a logarithmic color scale, the full scale corresponding to 3 orders of magnitude for all plots (2 above and 1 below the median value in each plot). There are respectively 15 and 20 equally spaced contour lines in (a) and (c, ). All plots were normalized to the brightest pixel.



#### 4.1.1.6 GeMn on GaAs substrates

Grazing incidence measurements were also performed in samples grown on GaAs. The main interests of GaAs substrates have been described at the beginning of this section, note also that the GaAs lattice parameter  $a = 5.65 \text{ \AA}$  is extremely close to that of Ge ( $5.66 \text{ \AA}$ ). The results of the grazing incidence x-ray scattering measurements are shown in figure 4.6(a–e). No substantial difference with GeMn samples grown on Ge(001) with medium-to-large nanocolumns can be seen. In fact, all diffuse features are present. The RSM around the Bragg peaks also show the same shape of the diffuse signal as in 4.4(c–f). Therefore, all conclusions drawn from the measurements in GeMn/Ge(001) samples will also apply to GeMn/GaAs samples.

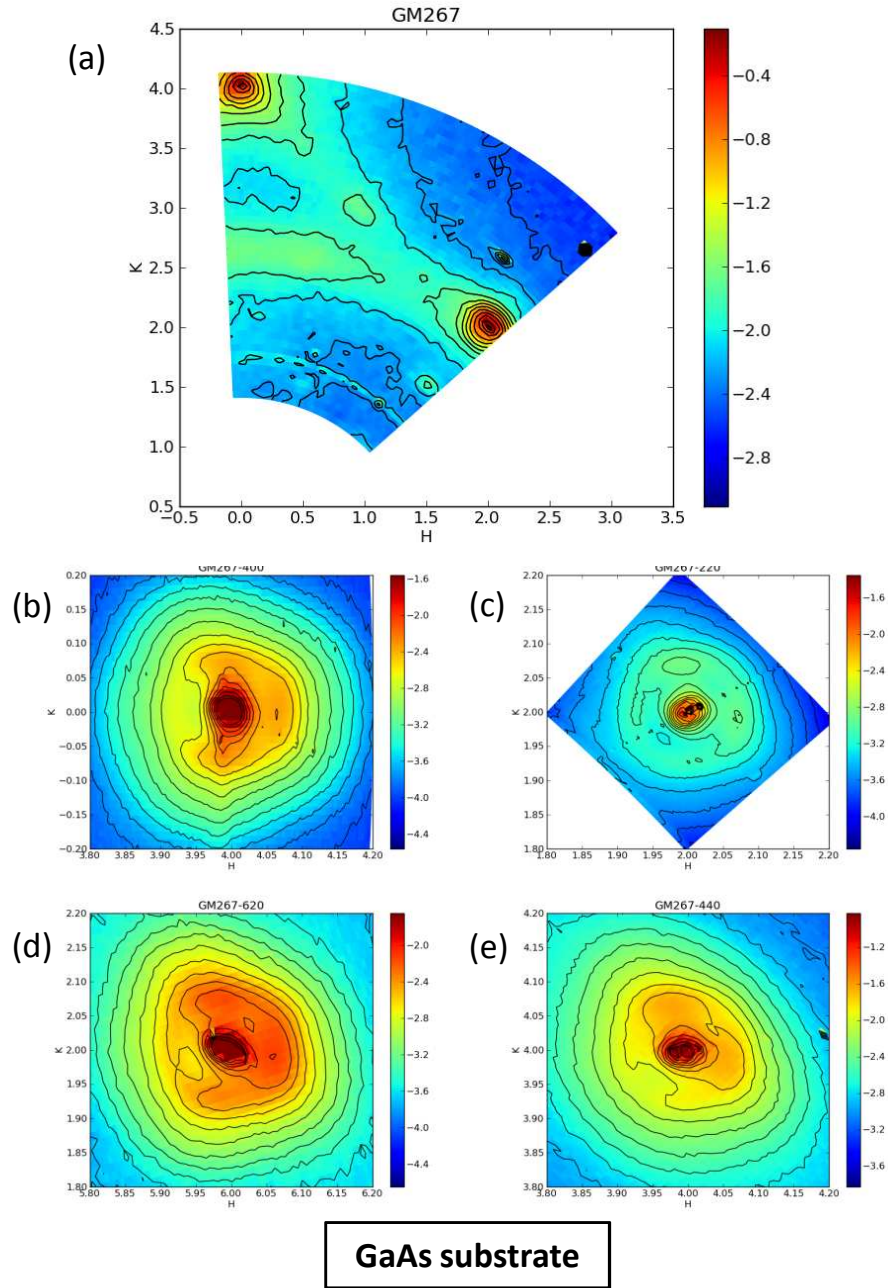


FIGURE 4.6: (a) Grazing incidence reciprocal space map (GI-RSM) of the measured intensity in the  $hk0$  plane. (b,c,d,e) GI-RSM around the 400, 220, 620, 440 Bragg reflections. The intensity is represented as a logarithmic color scale, the full scale corresponding to 3 orders of magnitude for all plots (2 above and 1 below the median value in each plot). There are respectively 15 and 20 equally spaced contour lines in (a) and (c-f). All plots were normalized to the brightest pixel.

### 4.1.2 Enhancing the GISAXS sensitivity : the Bragg-GISAXS technique

The Grazing-Incidence Small-Angle X-ray Scattering (GISAXS) technique consists in measuring the intensity scattered at small angles around the direct beam. Due to the very small  $Q$  value, this technique is sensitive to larger distances, typically on the order of a few to a few tens of nanometers. Thus, it allows the probing of the morphological properties of nanoobjects, such as their size or orientation. See *e.g.*, reference [107] for a recent review on the technique. The contrast in GISAXS is due to the local variations in the electron density, *i.e.* it depends strongly on the Z-contrast between the different species. Therefore, it is very sensitive *e.g.*, in the case of Ge quantum dots ( $Z_{Ge} = 32$ ) in Si ( $Z_{Si} = 14$ ) [117]. In the case of the GeMn nanocolumns, the low Z-contrast between Ge and Mn ( $Z_{Ge} = 32$  and  $Z_{Mn} = 25$ ) reduces the sensitivity of the GISAXS technique, especially considering the expected higher atomic density inside the nanocolumns.

In order to increase the sensitivity to the nanocolumns, we measured the signal diffused at small angles around the Bragg reflections (BR). The grazing incidence x-ray diffuse scattering is then strongly affected by any deformation in the Ge diamond lattice, in particular due to the GeMn nanocolumns. Such measurements were made at the same time as the measurement of the RSM shown in figure 4.5(d) by using a position-sensitive detector (1D detector) perpendicular to the sample plane, thus resolving the exit angle.

As can be seen in the ‘Bragg-GISAXS’ image in figure 4.7, the intensity measured as function of the exit angle ( $\alpha_f$ ) and as a function of the angle around the BR is very similar to a typical GISAXS image. Two sets of symmetric peaks can be seen, one (with  $d \approx 40$  nm) corresponding to the surface roughness correlation (as already reported by Holý *et al.*[140]) and another (with  $d \approx 9$  nm) corresponds to the average distance between neighboring columns. Both distances are confirmed using plane-view TEM imaging and atomic force microscopy as shown in figure 4.8(a) and (b) respectively.

In addition, the peak corresponding to the nanocolumns also exhibits fringes with a period corresponding to the thickness of the GeMn layer (60 nm). This is only

possible because the columns are continuous over the whole thickness of the layer.<sup>2</sup>

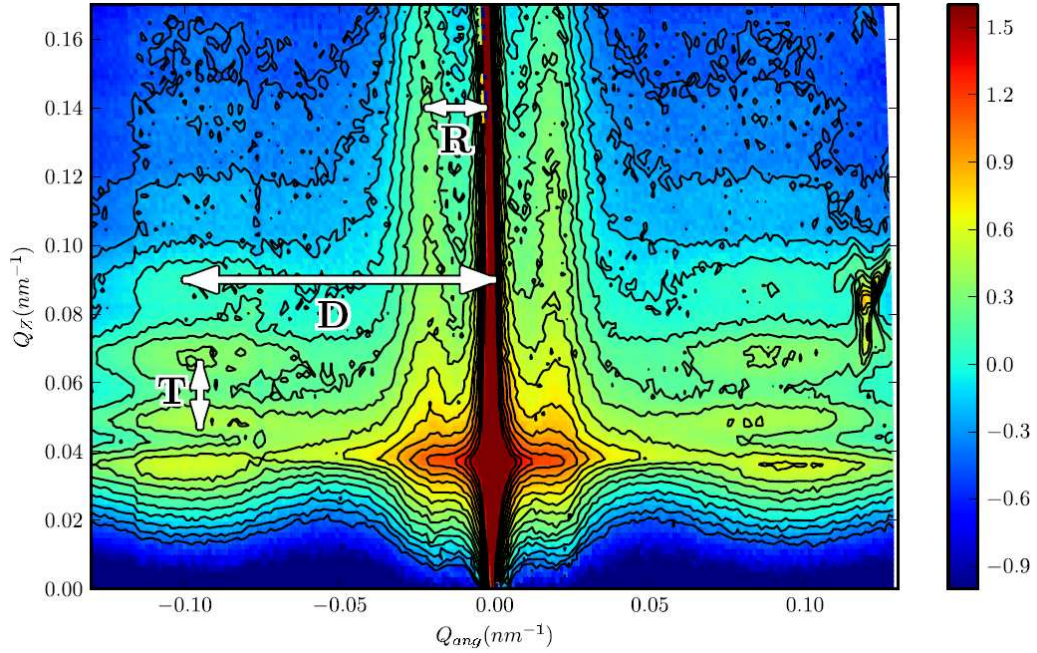


FIGURE 4.7: Bragg-GISAXS map measured in sample GM173 by an angular scan around the in-plane (220) Bragg reflection (during the measurement of figure 4.5(d)), using a Vantec position-sensitive detector, at  $E=6.5$  keV and  $\alpha_i = 0.4^\circ$  (intensity plotted on a logarithmic scale, with 8 contour levels per order of magnitude).  $Q_{ang}$  and  $Q_z$  are respectively parallel and perpendicular to the surface, note that we use the crystallographer's convention ( $|\mathbf{Q}| = \frac{2\sin\theta}{\lambda}$ ). Three finite distances effects can be seen, symmetrically about the  $Q_{ang} = 0$  axis : (i) a correlation distances of about 9 to 15nm (marker 'D'), corresponding to the average distance between columns, (ii) the oscillations (marker 'T') along  $Q_z$  (dot-dashed line) are due to the finite thickness of the sample (60 nm), and (iii) the two intense streaks (marker 'R') at very small  $Q_{ang}$  have been attributed to the surface roughness.

### 4.1.3 Chemical contrast and anomalous scattering

As discussed in chapter 2, the atomic scattering factor varies greatly around an absorption edge. One may then take advantage of core level transitions in the hard x-ray regime (Mn or Ge K-edge) to enhance the contrast in the scattered intensity. We have performed such measurements at the Mn K-edge (6.5 keV), as shown in

2. In the small-angle regime, a continuous *average density* in the layer is enough to create oscillation fringes - however in 'Bragg-GISAXS', such fringes can only be present if the *lattice* is continuous throughout the entire layer.

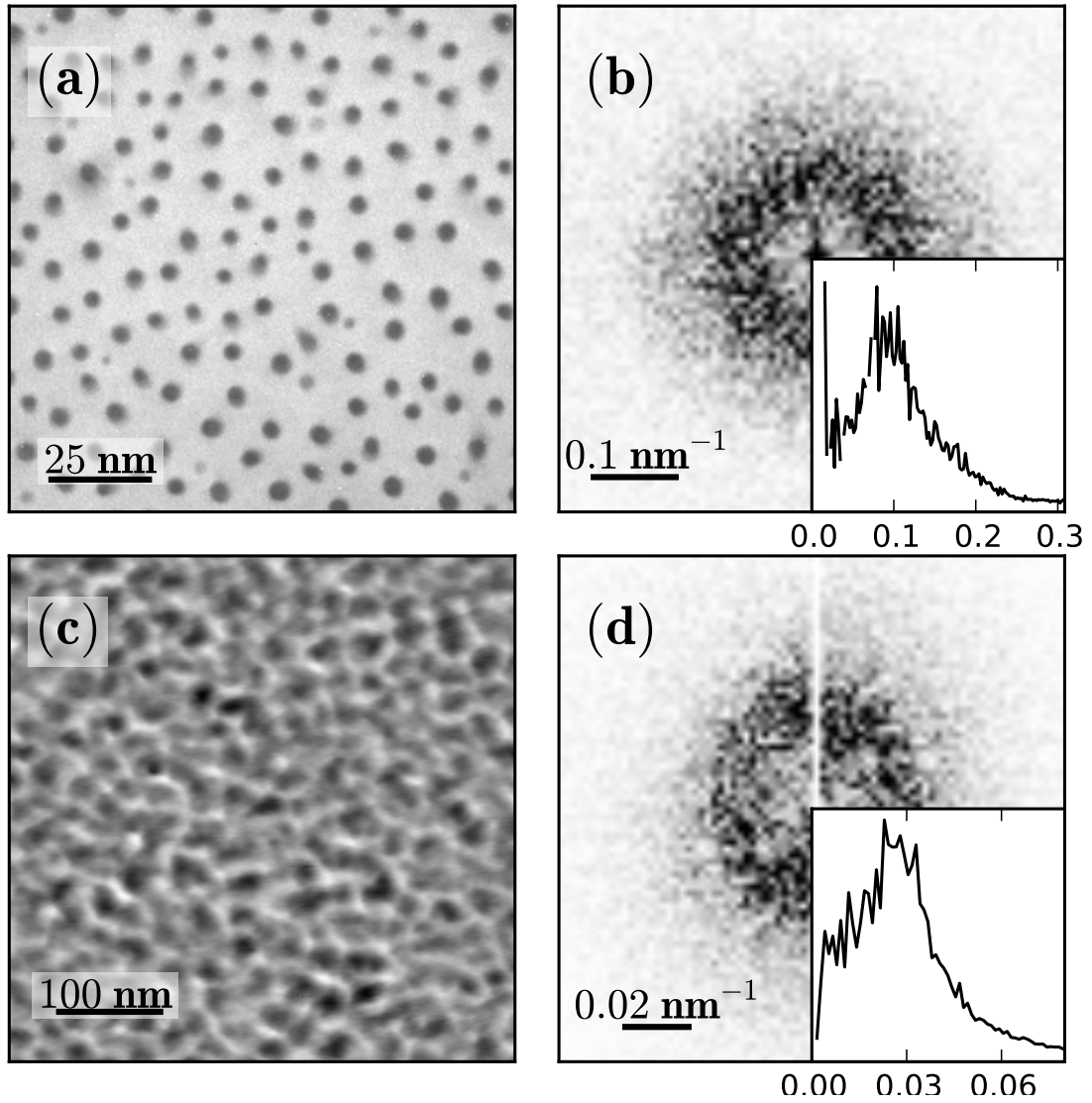


FIGURE 4.8: (a) Plane-view TEM micrograph, (c) surface topography measured by AFM, and (b),(d) the central zones of the corresponding Fourier transforms (FT), each with an inset showing the radial distribution of the FT amplitude (scale in  $\text{nm}^{-1}$ ). All color scales are linear, with the full z-scale for the AFM image corresponding to 2.6 nm. In each FT image a more intense ring can be observed, with correlation distances equal to  $\sim 10$  and  $\sim 40$  nm, respectively in the TEM (inter-column average spacing) and the AFM (surface roughness) images.

figure 4.9. Some differences in the RSM can be observed : above the edge the diffuse scattering is “flattened”, due to the higher level of background noise (*i.e.* the fluorescence), and the diffuse features are no longer discernable (fig. 4.9(top)). No clear difference in scattering can be observed close to the Bragg peaks in figure 4.9(middle). The only small variations can be explained only by resonant absorption, as suggests the similar energy dependance between the measured scattered intensity and calculated absorption coefficient in figure 4.9(bottom)).

## 4.2 Strain in the Germanium matrix

### 4.2.1 First approach : a simple analytical model

In order to understand the origin of the shape of the observed Bragg peaks discussed in section 4.1.1, we have proposed a simple analytical model. In this model we have separated the contribution in the scattered intensity from the strain induced by the nanocolumn as single inclusions and the contribution due to their positional correlations. We have simulated the corresponding diffraction patterns and compared them to the experimental ones.

#### 4.2.1.1 Expression of the scattered intensity

Let us first write the total amplitude  $A(\mathbf{k})$  of the wave scattered by the GeMn sample

$$A(\mathbf{k}) = \sum_i A_0(\mathbf{k}) e^{2i\pi\mathbf{k}\cdot\mathbf{R}_i} \quad (4.1)$$

where the sum goes over all the nanocolumns  $i$ ,  $A_0(\mathbf{k})$  is the scattering due to a single column and the associated distortion of the lattice and  $\mathbf{R}_i$  is the position of column  $i$  in the sample. In this equation we assume that all the nanocolumns have the same size, resulting in the same scattering. This is quite true for small nanocolumns ( $\varnothing \sim 2$  nm) where the deviation from the mean diameter is small, however it is less realistic in the case of larger columns due to the larger dispersion of sizes and shapes.

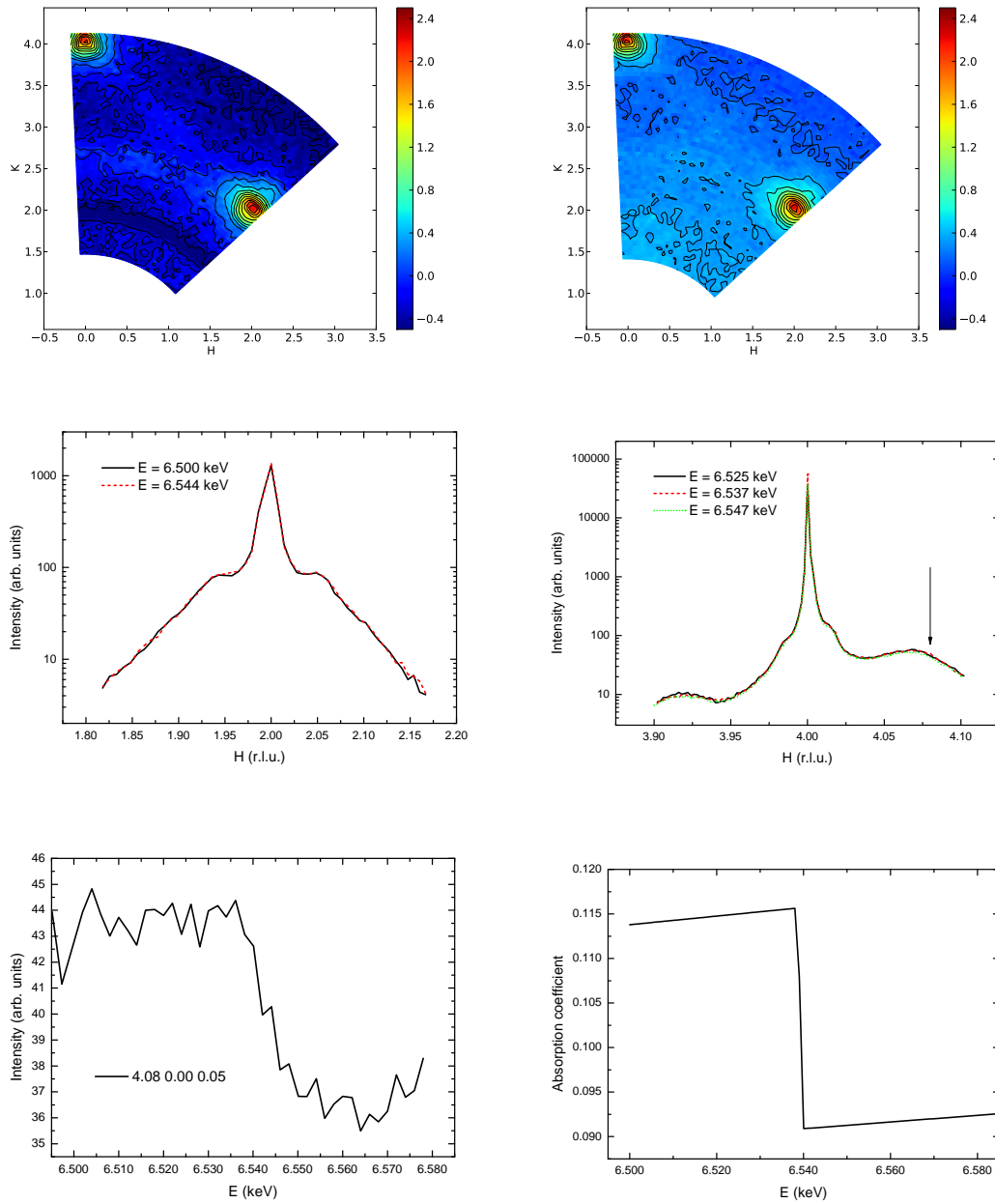


FIGURE 4.9:

(top) Grazing incidence reciprocal space maps in sample GM197, below the Mn K-edge at energy 6.500 keV (left) and above the Mn K-edge at energy 6.544 keV (right). The intensity is represented as a logarithmic color scale, the full scale corresponding to 3 orders of magnitude with 15 equally spaced contour lines.

(middle) Radial scans across the 220 (left) and the 400 (right) Bragg reflections at different energies around the Mn K-edge. The arrow indicates the position of the anomalous scattering measurements.

(bottom) Anomalous scattering measurement near the 400 Bragg reflection around the Mn K-edge (left) and calculated absorption by the Mn at the same energies (right).

The scattered intensity can then be written as

$$I(\mathbf{k}) = |A(\mathbf{k})|^2 = |A_0(\mathbf{k})|^2 \left| \sum_i e^{2i\pi\mathbf{k}\cdot\mathbf{R}_i} \right|^2 \quad (4.2)$$

The square of the absolute value of the sum can be seen as the product with its complex conjugate, then eq. 4.2 can be rewritten as

$$I(\mathbf{k}) = |A_0(\mathbf{k})|^2 \times \left| N + 2 \sum_{i<j} \cos 2\pi\mathbf{k} \cdot (\mathbf{R}_j - \mathbf{R}_i) \right| \quad (4.3)$$

where  $N$  is the total number of nanocolumns. Therefore, with the above approximations the scattered intensity should be proportional to the scattering of a single nanocolumn, multiplied by an interference factor depending on the pair distribution of the columns.

#### 4.2.1.2 Scattering from a single nanocolumn

Let us now look at the first term, *i.e.* the scattering from a single nanocolumn. Let us make the further assumption that the inner part of the column does not contribute to the scattering, because it is either disordered or amorphous. Then the scattering of the single column is the sum of the contribution from the displaced atoms in the Ge matrix and from the ‘hole’ left in the Ge matrix by the column :

$$A_0(\mathbf{k}) = A(\text{displaced atoms}) + A(\text{hole}) \quad (4.4)$$

Because we are only interested in the scattering from the GeMn layer, we can compute it as the difference between the scattering of the distorted and perfect (*i.e.* without deformation or columns) lattices [112]. The advantage of this method is that it avoids most oscillation fringes due to the finite size of the simulated lattice, and also that it allows the superposition of the contributions from several insertions (columns in our case). The only approximation is that the sharp Bragg peak will not be obtained by this calculation. Hence, one can write eq. 4.4 as

$$A_0(\mathbf{k}) = \sum_i^{\text{displ.at.}} f_i e^{2i\pi\mathbf{k}\cdot\mathbf{r}_i^0} (e^{2i\pi\mathbf{k}\cdot\mathbf{u}_i} - 1) - \sum_j^{\text{hole}} f_j e^{2i\pi\mathbf{k}\cdot\mathbf{r}_j^0} \quad (4.5)$$

where  $\mathbf{r}_i^0$  denotes the original position of atom  $i$ , and  $\mathbf{u}_i$  its displacement.



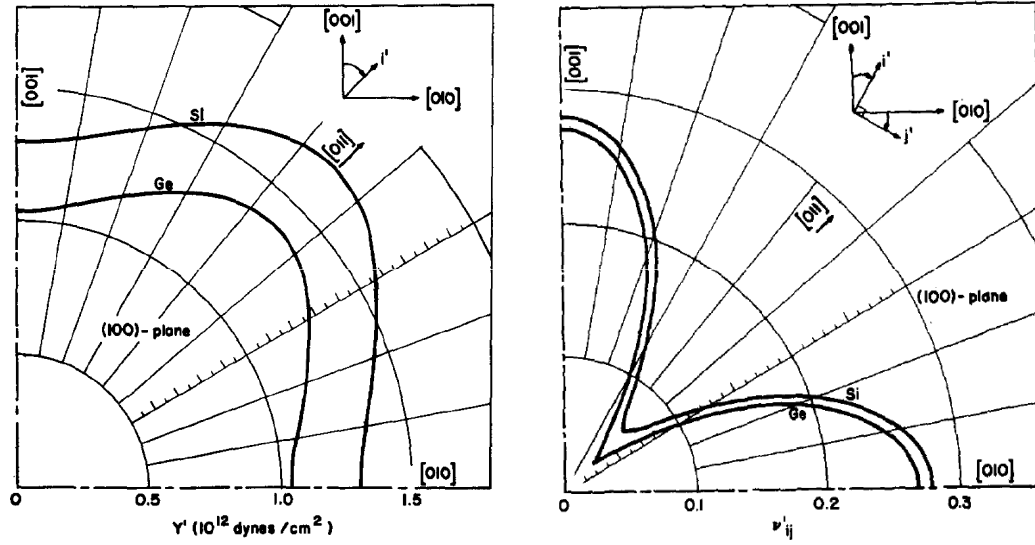


FIGURE 4.10: Anisotropic Young modulus (*left*) and Poisson ratio (*right*) in germanium. Note that  $10^{12}$  dynes.cm $^{-2}$  is CGS is equal to 100 GPa in SI. Adapted from ref. [141].

We shall now need the expression of the displacement  $\mathbf{u}$  to compute the scattered amplitude. In the case of radial displacement due to an axisymmetric inclusion in a homogeneous isotropic matrix, the displacement outside the inclusion can be written as [112]

$$u(r > R) = \frac{\delta(1 + \nu)}{4\pi r^2(1 - \nu)} \quad (4.6)$$

where  $R$  is the column's diameter,  $\delta$  is a parameter giving the extent of the deformation of the matrix, and  $\nu$  is the Poisson coefficient for germanium. The resulting displacement field is plotted in figure 4.12(a). It should be underlined that for the sake of simplicity this simple model does not take into account the elastic anisotropy of germanium, illustrated in figure 4.10 [141].

#### 4.2.1.3 Positional correlations term

We also need the expression of the pair correlation term (second term in the right member of eq. 4.3). Plane-view TEM micrographs seem to show rather random positioning of the GeMn nanocolumns. However, careful inspection of the positions of the nanocolumns show some preferential distances, slightly larger than the nearest neighbor distance, as shown in figure 4.11(a) and (b).

A simple empirical approach to this expression is to model the pair distribution function (PDF) from the measurement of the positions of the nanocolumns in the

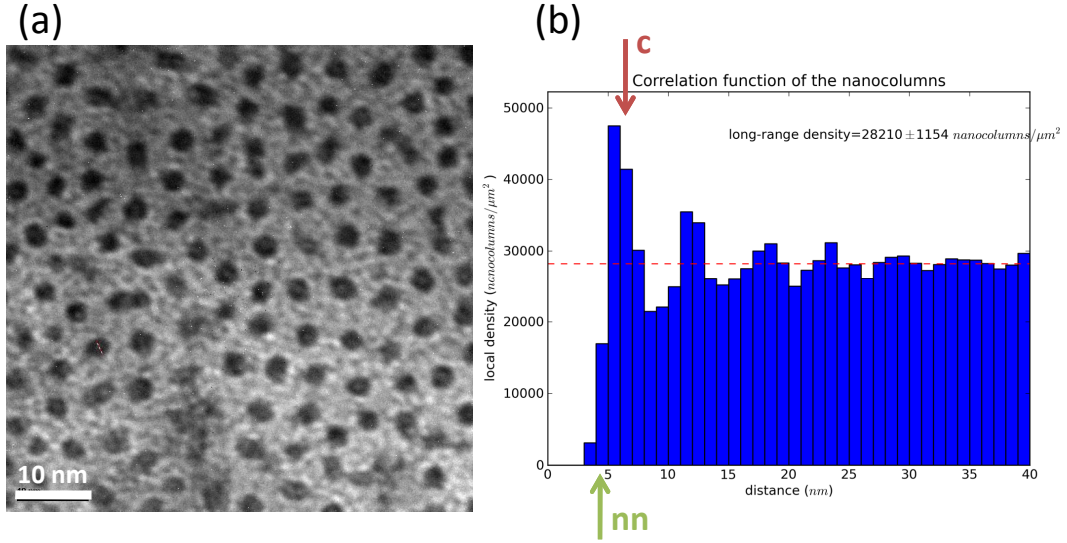


FIGURE 4.11: (a) Plane-view TEM micrograph of a GeMn sample and (b) distribution of inter-columns distances in sample GM154 (see table 4.1). Nearest neighbors lie about 4–5 nm apart (green arrow), however more columns are separated by about 6–7 nm (red arrow). Some oscillations can be seen, due to the nanocolumns that are somewhat aligned. In order to increase the statistics and reduce the noise, inter-columns distances were calculated on a  $3 \times 3$  tiling of the TEM image, considering all orientations of the tiles and only the nanocolumns in the central image. This technique may induce some artificial oscillations, but it does not appear to change the characteristic distances and it gives more accurate long-range densities.

sample and assume it is isotropic. For example, by analysing a  $130 \times 130 \text{ nm}^2$  TEM micrographs, one can measure the positions of 125 nanocolumns. However, due to the edges of the image, if one wants to measure correlations up to a length  $l$ , one cannot take into account the columns that are at a distance less than  $l$  to the edge. Therefore it also reduces the number of pair distances  $\mathbf{R} = \mathbf{R}_j - \mathbf{R}_i$ . In the example cited above, we analyse a sample where the correlation length  $l_{nc}$ , *i.e.* the distance at which the density is maximum, is on the order of 8–10 nm, therefore we want to probe distances up to at least three time  $l_{nc}$ . This means that we look only at the center square with sides equal to  $129.68 - 6l_{nc} = 70 \text{ nm}$ , which represents only 29% of the initial image and contains 35 columns. The total number of unique pair distances measured is then 1451. The resulting (incomplete) PDF is plotted as dots on figure 4.12(b). We can see a main peak at about 10 nm, corresponding to the correlation length of the nanocolumns. At larger distance, the radial PDF tends toward a constant value, with some smaller, decaying oscillations at multiples of the correlation length that probably correspond to more or less aligned nanocolumns. We modeled this experimental radial PDF as the sum of a

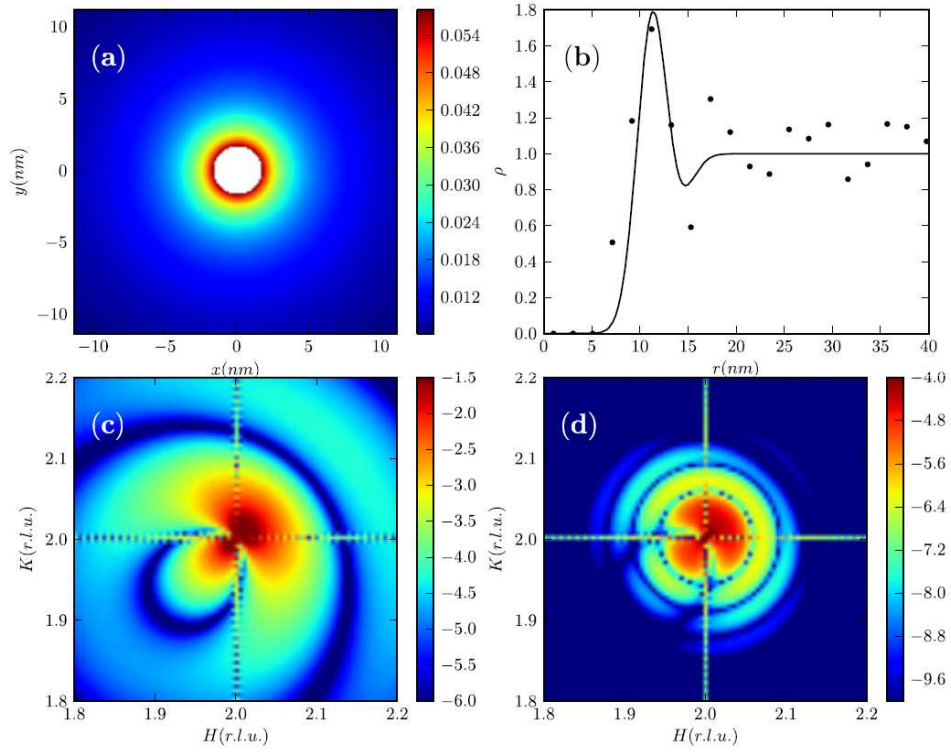


FIGURE 4.12: (a) Amplitude of the atoms radial displacements (in nm), following an isotropic elastic model around a cylindrical inclusion. (b) Radial pair distribution function of the nanocolumns, measured experimentally (dots) and fitted using a gaussian + error function model. (c) Scattering from a single isolated nanocolumn around the (220) reflection, including the scattering contributions from the displaced atoms as well as the missing atoms inside the column (see text for details). (d) Scattering of an assembly of nanocolumns around the (220) reflection, by taking into account their radial distribution function shown in (b). Intensity is plotted with a logarithmic color scale for (c-d).

gaussian function centered at the correlation length and a shifted error function.

#### 4.2.1.4 Calculated X-ray scattering from the analytical model

Within the simple model stated above, we have calculated the grazing incidence x-ray scattering of the GeMn nanocolumns using eq. 4.3. We neglected the transmission coefficients [105] for the incoming and outgoing X-ray beams at the surface, because as the nanocolumns are embedded in the Ge matrix, the GeMn sample exhibits no structure above the surface and therefore the transmission coefficients only affect the scattering as a constant scale factor.

Figure 4.12(c) shows the results of the simulation around a (220) reflection for a single isolated column. One can see a larger intensity at high Bragg angle,

consistent with a Ge matrix under compression by the nanocolumns. In the case of small and coherent inclusions in a single crystal, one would expect to see Huang scattering [109, 112, 142], with a nodal plane (*i.e.* where the intensity vanishes) perpendicular to the scattering vector. However in our case, there is a contribution from the hole in the matrix (as we assume that the nanocolumns do not scatter) in eq. 4.4 and there is no nodal plane anymore.

The intensity scattered by the assembly of nanocolumns is shown in figure 4.12(d). Taking pair correlations into account yields the observed diffuse ring around the Bragg peak, at the right distance. However, due to the simplicity of our model, some differences with the experimental observation still remain and a quantitative analysis cannot be reached. In fact the limiting assumptions in our analytical model are the following :

1. All nanocolumns have the same size – whereas the column diameter distribution is a Gaussian with an FWHM of almost  $\approx 20\%$ .
2. The radial distribution is also the same for all the columns – whereas it should differ, depending on the column's size.
3. The Ge matrix is treated as isotropic – whereas germanium is elastically anisotropic [141], in particular its anisotropy coefficient  $a_c^{Ge} = \frac{2c_{44}}{c_{11}-c_{12}} = 1.65$ , while it is equal to 1 for isotropic materials<sup>3</sup>.
4. The displacement fields are treated independently – whereas the distance between columns (nearest neighbor distance of  $\approx 8 \text{ nm}$ ) is such that the displacement fields generated by all columns will not be independent.

In order to take into account these different parameters, we have turned to more sophisticated models and used atomistic simulations to obtain more realistic atomic positions.

### 4.2.2 Simulation of the strain using an atomistic model

The principle of the atomistic simulations is to get a full picture of all the atomic displacements *ab initio* in a model sample. These approach was led in close collaboration with Frédéric Lançon from the CEA-INAC, who in particular performed all the calculations of the *ab initio* atomic displacements.

---

3. For further comparison, in highly anisotropic Cu  $a_c^{Cu} = 3.21$  and for quasi-isotropic Al  $a_c^{Al} = 1.1$

#### 4.2.2.1 The atomistic model

Atomistic simulations are very helpful when it comes to calculate the diffuse scattering around larger defects. F. Lançon calculated a virtual GeMn sample that we have used to simulate the x-ray scattering. A domain of  $100 \times 100 \times 2$  Ge-diamond unit cell was created with periodic boundary conditions. A total of 42 nanocolumns – corresponding to the experimental density of  $13\,100\,\mu\text{m}^{-2}$  – were added, one after the other, keeping an average exclusion distance between the columns of 6.9 nm (standard deviation = 0.35 nm). The resulting pair correlation peaks at 7.6 nm, close to the experimental values. In the same fashion, the diameter of the nanocolumn was set to the average value of 3.6 nm with a standard deviation 0.5 nm. Interactions between atoms were modeled with a Stillinger-Weber potential [143, 144] for both the atoms in the columns and in the matrix – one advantage of these potentials being that they were developed for both ordered and disordered condensed matter phases. A standard minimization of the energy was performed by conjugate gradient method to reach equilibrium.

#### Crystalline models : Ge diamond and $\alpha$ phase

Different crystalline models were considered for the filling of the nanocolumns. Starting with the simplest model, we first considered a Ge diamond structure where the Ge atoms were “bigger” than those in the surrounding matrix by 1 to 4%, the latter being the mismatch value measured in TEM. The size difference is taken into account in the parameters of the Stillinger-Weber potential.

As a second model, we also considered the  $\alpha$  phase, which is further described in chapter 5. Nanocolumns containing the  $\alpha$  phase are illustrated in figure 4.13. The  $\alpha$  phase also allows for an additional degree of freedom : since the structure is anisotropic, there are different ways to pile the  $\alpha$  unit cells along the  $z$  axis. Such different pilings are called variants and were considered as well.

#### Amorphous nanocolumns

Since we kept our first hypothesis that the nanocolumns participate directly in the scattering only weakly, disorder was introduced in the columns by placing Ge atoms at random positions inside them with the same density as in the diamond structure, resulting in a compressive strain exerted on the Ge matrix. Figure 4.14 shows the resulting assembly of amorphous nanocolumns embedded in a strained Ge matrix. The resulting displacement field can be seen in figure 4.15.

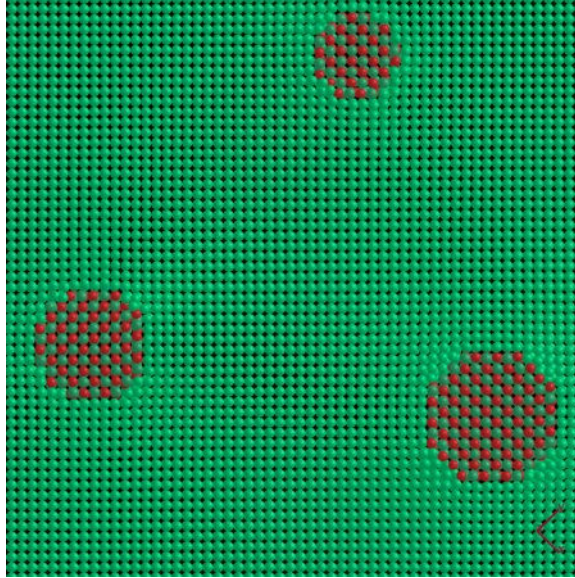


FIGURE 4.13: Atomistic model obtained using a Stillinger-Weber potential, combining columns containing the  $\alpha$  phase (Mn atoms are the red spheres) surrounded by the germanium matrix (Ge atoms are green). Figure from F. Lançon.

A total of 20 different model samples were generated this way and their diffraction patterns were added separately to simulate the incoherent diffraction signal of the different parts of the sample and reduce any speckle effect. A speckle pattern would be expected if only one of the configuration of 42 nanocolumns was used, due to the coherent scattering of the whole domain. In order to avoid interference patterns from the finite size of the simulated domain, we evaluated the scattered intensity at the nodes of the interference function, *i.e.* with increments in reciprocal space equal to  $\frac{1}{N_L}$ , where  $N_L$  is the number of lattices along the considered axis. Performing the simulation over 100 unit cells along  $x$  and  $y$  allowed for a resolution of 0.01 reciprocal lattice units.

#### 4.2.2.2 Calculated X-ray scattering from the atomistic model

In the same fashion as in part 4.2.1.4, the corresponding grazing incidence x-ray scattering was calculated, neglecting the influence of the transmission coefficients for both the incoming and outgoing x-ray beam. The resulting RSM are reported for different cases : diamond nanocolumns with Mn atoms 1% bigger than Ge atoms, figure 4.16 ; diamond nanocolumns with Mn atoms 4% bigger, figure 4.17 ; amorphous nanocolumns (which structure is illustrated in figure 4.14), figure 4.18 and nanocolumns containing a new crystalline phase (the  $\alpha$  phase, described in



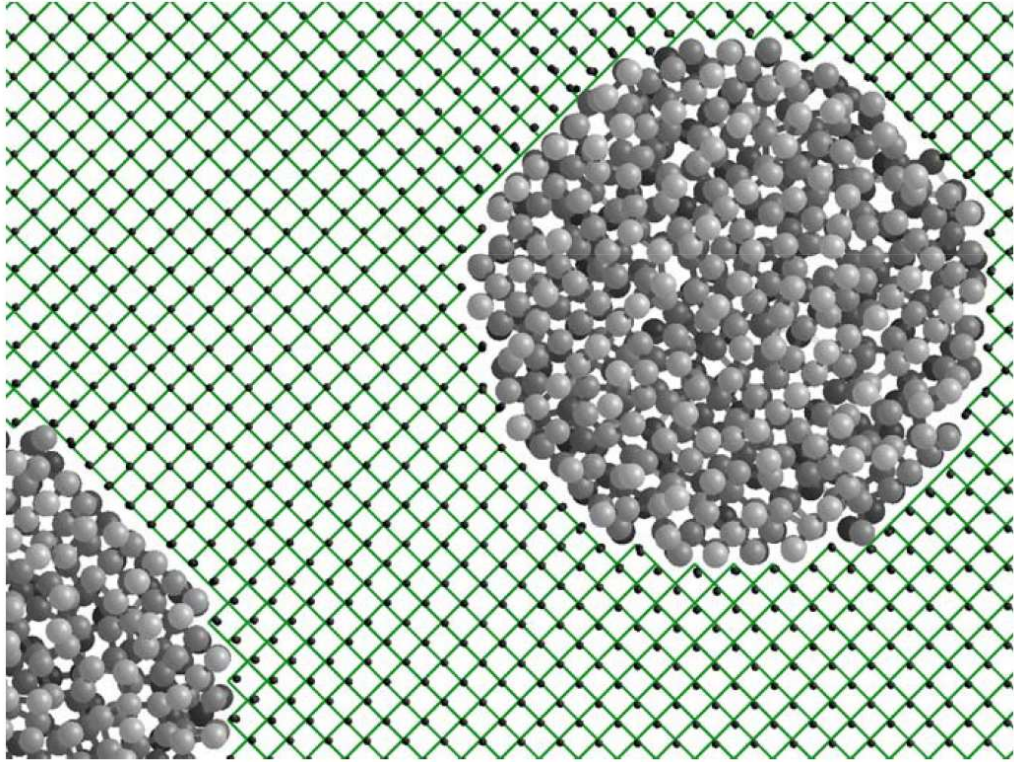


FIGURE 4.14: Atomic model obtained using a Stillinger-Weber potential, combining amorphous columns (grey spheres; darker shade indicates larger depth) surrounded by the germanium matrix (Ge atoms as black disks). Ge-Ge bonds of the perfect (undistorted) lattice are shown in green. Note the atomic displacements of the Ge atoms in the matrix, due to the column expansion. Figure from F. Lançon.

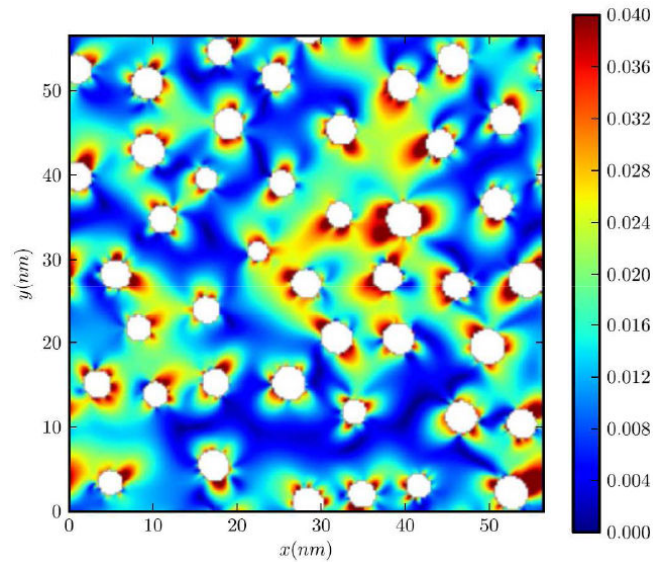


FIGURE 4.15: Mapping of the simulated atomic displacements (from the reference perfect Ge lattice, displacements are given in  $nm$ ), for a simulation with  $100 \times 100$  unit cells and 42 amorphous GeMn nanocolumns. 20 independent atomistic simulations have been averaged to avoid speckle effects.

more details in chapter 5) with disorder<sup>4</sup>, figure 4.19. In all cases, we calculated a wide angle RSM as well as small angles RSM around the Ge (220) and (400) reflections. In order to observe the influence of the inner structure of the nanocolumns, we calculated the RSM with and without the scattering of the inside of the nanocolumns. Additional disorder in the nanocolumns should also decrease the specific scattering from the inside of the nanocolumns.

We observe in all four cases a diffuse ring around the (220) and the (400) Ge Bragg reflections. This ring is more pronounced when the scattering from the nanocolumns is not calculated. This is explained by the fact that this diffuse ring is indeed due to the scattering by the strained matrix. Local maxima are always located at the same position at a distance of about 0.07 *r.l.u.* and the diffuse ring is more intense along the H and K axes. This indicates that the diffuse rings are indeed due to correlations in position of the nanocolumns, or more precisely, to the correlated strain fields due to the different nanocolumns. Smaller strain seems to induce higher order rings (figure 4.16), while more disorder in the nanocolumns results in only one broader ring (figure 4.19), as observed experimentally (figure 4.4). This indicates the presence of some degree of disorder in the GeMn samples.

When considering the inside of the nanocolumns, we observe the characteristic nodal plane of the Huang scattering, due to the central symmetry of the strain field. When the strain is larger, the plane is more deformed, up to the point where it vanishes for amorphous nanocolumns.

Large RSM calculated for the Ge crystalline nanocolumns (figures 4.16 and 4.17) do not show the diffuse line observed experimentally between the (220) and the (040) Bragg reflections. On the opposite, calculations for the  $\alpha$  phase and the amorphous nanocolumns do show this diffuse line, especially when considering the scattering from the inside of the nanocolumns, indicating a contribution from the disordered inner crystalline structure. Additional reflections are observed for the  $\alpha$  structure, due to the cubic (as opposed to diamond) character of the inner part of the nanocolumns. These reflections are weakened by considering simultaneously several variants of the  $\alpha$  structure.

Since no well defined additional Bragg peaks could be observed in the different experimental RSM, we could not conclude on a specific crystalline phase inside the

---

4. The disorder is simulated by considering the presence of several different variants in the nanocolumns.



nanocolumns. However, in light of the atomistic simulations, it appears that a large degree of structural disorder is present in the nanocolumns, even in samples that were expected to be crystalline.

#### 4.2.2.3 Quantitative analysis of the strain in the Ge matrix

Since we can reproduce the experimental results with a good accuracy, we may now turn to a quantitative analysis of the strain in the germanium matrix and study its influence on the scattered intensity. In order to do so, we shall compare the variations of the amplitude of the scattered intensity along the correlation rings (further referred as intensity profiles). The Ge atoms in the matrix are in the elastic regime, so their displacement is proportional to the stress induced by the nanocolumns. Therefore we can tune the amplitude of the displacements by multiplying them with a factor between 0 and 1, calculate the corresponding scattered intensities, and compare the resulting intensity profiles. The results are presented on figure 4.20 :<sup>5</sup> the calculated intensity around the [220] Bragg reflection has been integrated between 0.04 and 0.12 *r.l.u.* and plotted as function of the angle with the [220] scattering vector. The amplitude is maximum at  $\pm 45^\circ$  with respect to the scattering vector, *i.e.* along the [100] and [010] directions around the (220) reflection, both in the simulation and in the experimental data. As the factor tends towards 0 (smaller displacements), the intensity profile is more circular ; on the opposite, larger displacements result in more contrasted intensity profiles.

#### 4.2.2.4 Oxidation-induced strain relaxation

We show in figure 4.20(b) a polar plot of the intensity along the ring around the BP. When the strain is diminished (in the elastic limit), the intensity profile gets more circular. Therefore, smaller strain or strain relaxation would result in more circular shape of the intensity profile. In fact, we have reported in plot 4.20(a) the intensity profiles measured in sample GM197 (capped against oxidation) and shown in figure 4.4(c), and the intensity profile measured in sample GM173 and shown in figure 4.5(c) after a few months of exposure to air. Sample GM173 has larger nanocolumns than GM197, therefore one would expect a larger strain in

---

5. When comparing calculated and measured intensity profiles, one shall keep in mind that the calculated intensity does not include the Bragg peak from the perfect Ge lattice and its possible broadening due to instrumental resolution and crystal quality.

## Diamond Ge 1%

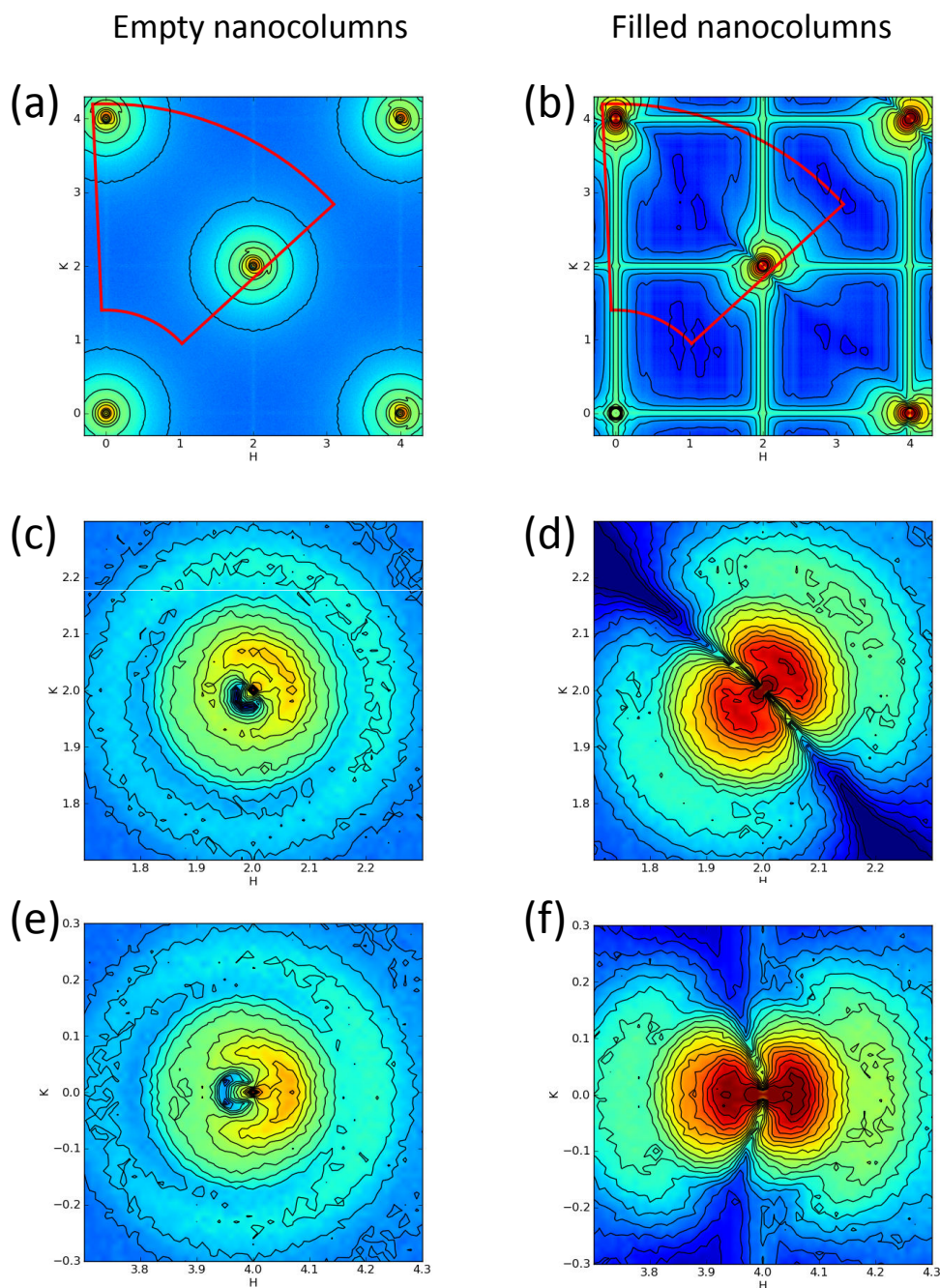


FIGURE 4.16: Calculated wide angle (a–b) and small angle RSM around the (220) (c–d) and the (400) (e–f) Ge diamond Bragg reflections for diamond nanocolumns. Mn atoms are represented by Ge atoms that are 1% bigger than usual. For clarity, a gaussian smoothing was applied to the contours in (a–b).

## Diamond Ge 4%

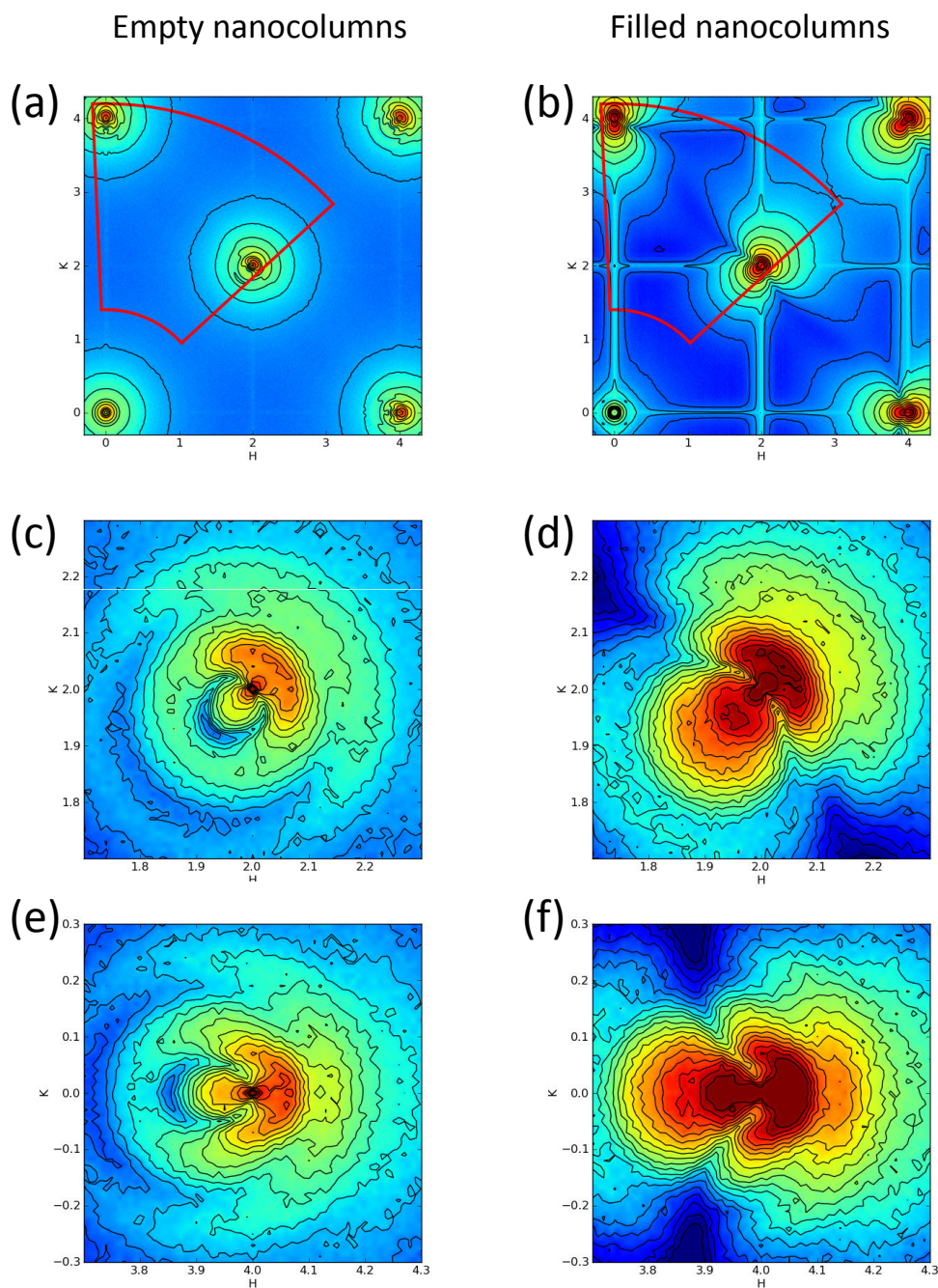


FIGURE 4.17: Calculated wide angle (a–b) and small angle RSM around the (220) (c–d) and the (400) (e–f) Ge diamond Bragg reflections for diamond nanocolumns. Mn atoms are represented by Ge atoms that are 4% bigger than usual. For clarity, a gaussian smoothing was applied to the contours in (a–b).



## Amorphous

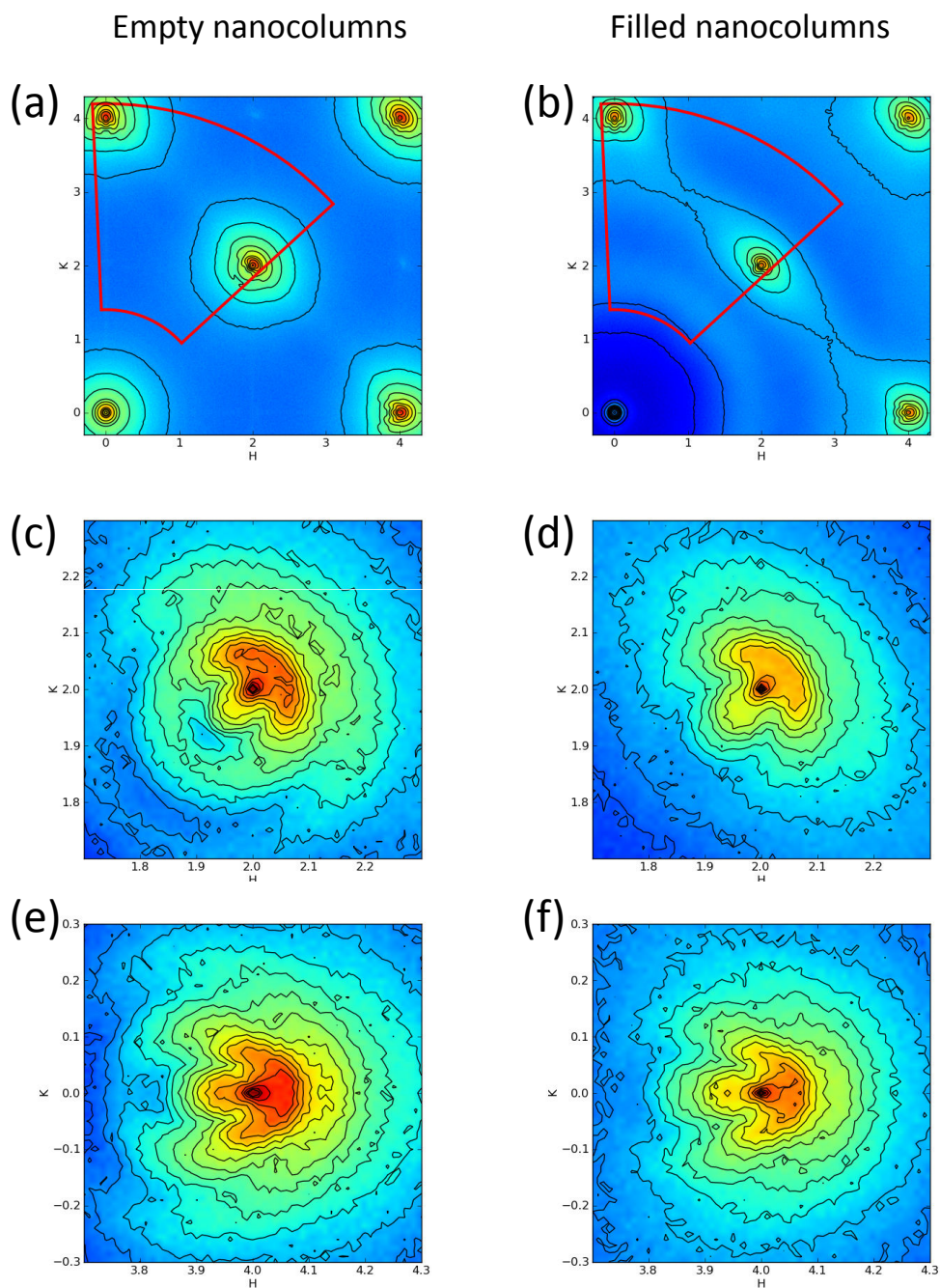


FIGURE 4.18: Calculated wide angle (a–b) and small angle RSM around the (220) (c–d) and the (400) (e–f) Ge diamond Bragg reflections for amorphous nanocolumns. For clarity, a gaussian smoothing was applied to the contours in (a–b).

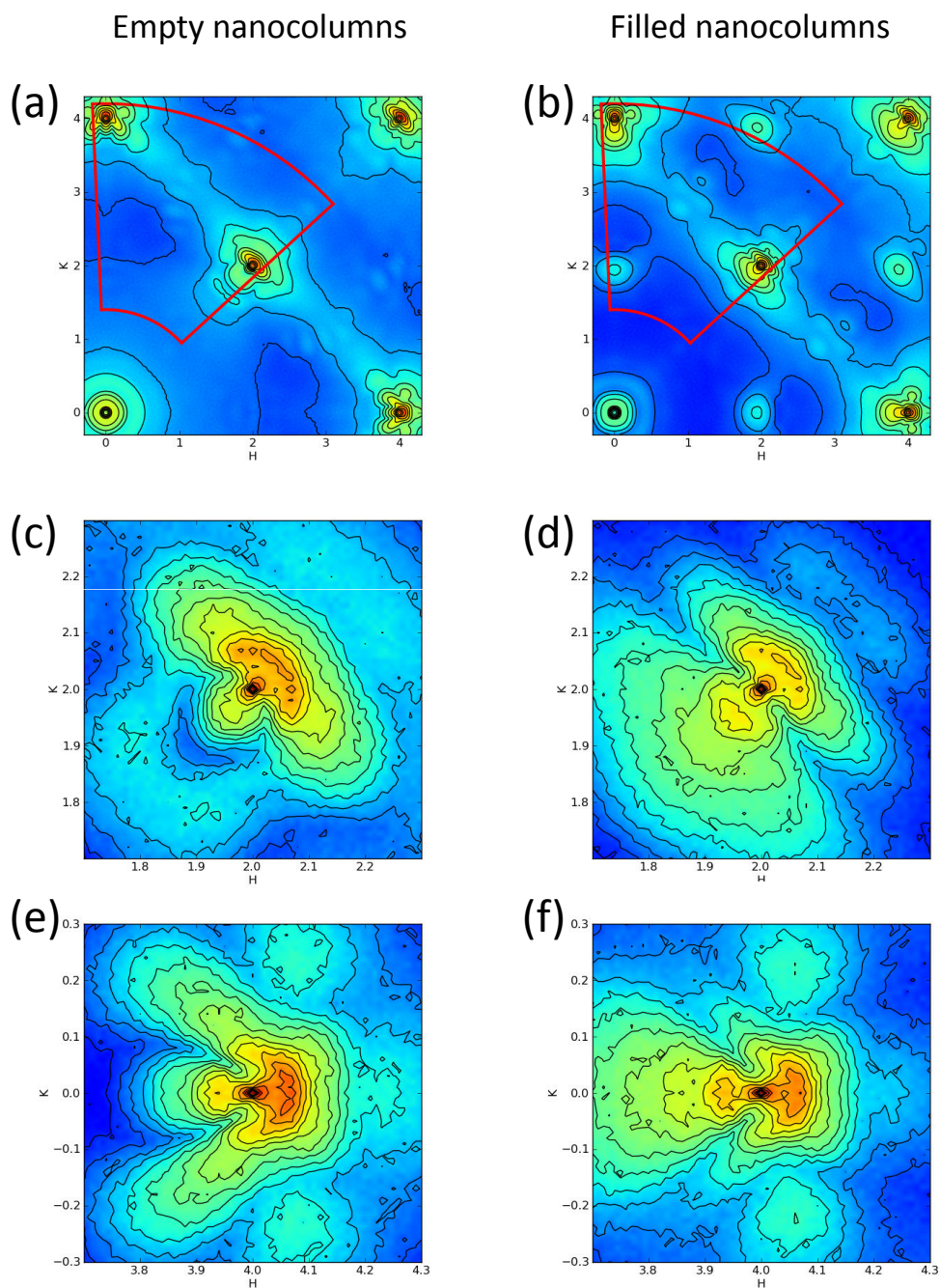
$\alpha$  phase

FIGURE 4.19: Calculated wide angle (a–b) and small angle RSM around the (220) (c–d) and the (400) (e–f) Ge diamond Bragg reflections for nanocolumns containing the  $\alpha$  phase. For clarity, a gaussian smoothing was applied to the contours in (a–b).

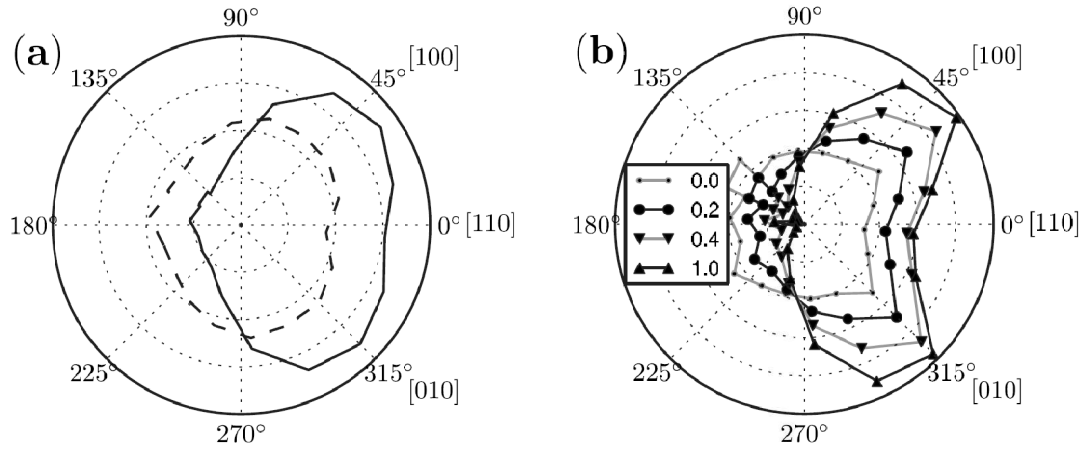


FIGURE 4.20: Normalized angular distribution of the intensity on the ring surrounding the (220) reflection. This distribution is characteristic of the amplitude of deformation of the matrix lattice around the nanocolumns, with a larger asymmetry in the radial direction ( $0$  vs  $180^\circ$ ) for larger deformations : (a) distribution observed for a sample grown in situ (continuous line) and another (dashed line) with oxidized columns; (b) simulated distribution of intensities, using an assembly of nanocolumns, for various amplitudes of deformations - the relative displacement amplitudes around the columns are given in the inset - for the largest amplitude the maximum displacement is  $\approx 0.05$  nm for atoms near the border of the columns.

the Ge matrix. However, the intensity profile in GM173 is more circular than in GM197. We explain that difference by a possible oxidation mechanism in the nanocolumns. Oxidation effects have been described in the previous chapter. Even if the oxidizing mechanism occurring in the nanocolumns is not known, we can infer in light of the previous observations that the oxidation process results in a diminution of the stress due to the nanocolumns and a release of the strain in the germanium matrix. As the stress diminishes, the atomic density in the nanocolumns should also decrease, which probably indicates either a migration of some atoms of the columns to be replaced by oxygens or an expansion of the nanocolumn, integrating nearby strained Ge atoms. As an illustration, the RSM

maps for strain reduced by a factor equal to 0.2 are shown on figure 4.15(d-e), and reproduce well the rings observed for the sample with the oxidized columns on figure 4.5(c-d).

### 4.3 Conclusion

The GeMn nanocolumns were studied using a wide range of x-ray diffraction and diffuse scattering techniques. Grazing-incidence is a method of choice when dealing with thin films, as it dramatically increases the sensitivity to the surface. Diffuse scattering techniques allow for the measurement of the diffuse signal scattered between the Bragg peaks, due to disorder and local variations from the average crystalline structure in the sample. Even though those techniques appeared well-suited for the study of the crystalline structure of the GeMn nanocolumns, they have proven much less straightforward than initially expected. In particular, we could not complete entirely our first two objectives, *i.e.* identifying the crystalline phase in the GeMn nanocolumns and evidencing the influence of dislocations in the Ge matrix at the interface matrix/nanocolumns.

However, we obtained very interesting results while studying the strain the Ge matrix. Using precise measurements of the reciprocal space maps around the Bragg peaks in different types of samples and *ab initio* displacement calculations from a collaboration with Frédéric Lançon, we were able to determine quantitatively the deformation of the Ge matrix around the nanocolumns. We have shown the importance of the correlations in the positions of the columns on the shape of the scattered intensity around the Bragg peaks, as well the importance of the anisotropic nature of the Ge diamond matrix. In particular, we have also shown the effect of aging in the samples and the isotropic relaxation of the strain due to the oxidation of the nanocolumns.

An interesting preview of the possibilities of total scattering techniques is illustrated in figure 4.21 : the total scattering was measured in grazing incidence, using the XPAD detector described in chapter 2 and a 3D zoom on the out-of-plane Ge 111 Bragg reflection is shown. Several features can be observed beside the BP (central red region) : a crystal truncation rod is present along the L axis, with oscillations due to the finite thickness of the GeMn layer and the polarized diffuse ring discussed in this chapter is also observed. In particular, it is confirmed that

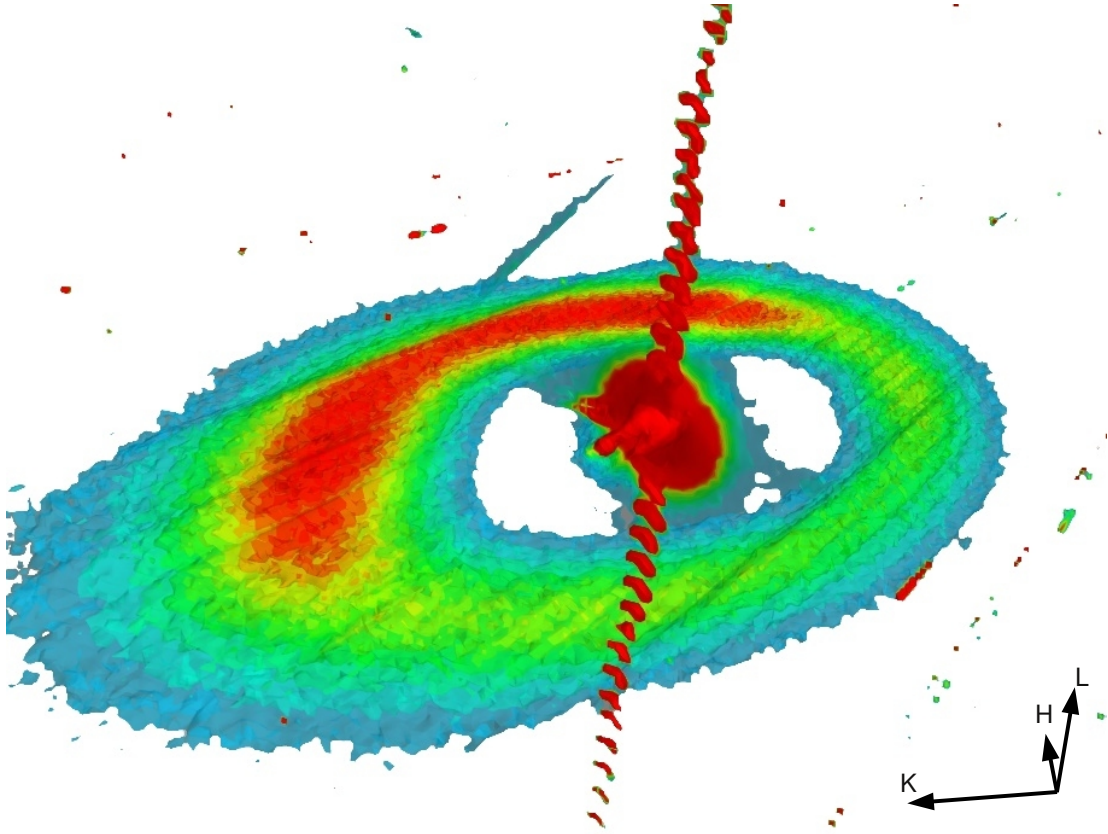


FIGURE 4.21: 3D RSM around the Ge 111 Bragg reflection, measured in grazing incidence with the 2D detector XPAD on beamline BM02. The central red region is the Bragg peak. The streak along the L axis is the crystal truncation rod, due to the finite thickness of the GeMn layer. The polarized diffuse ring around the BP stems from the in-plane correlated strain fields in the Ge matrix, due to the GeMn nanocolumns.

the correlation ring lies in the plane parallel to the surface, since it stems from the in-plane correlated strain fields.



## 4.4 Résumé du chapitre 4

Le chapitre 4 présente les résultats et interprétations des mesures de diffusion de rayons X.

Les propriétés structurales des nanocolonnes de GeMn ont été étudiées à l'aide d'un large ensemble de technique de mesure de la diffusion et diffraction de rayons X. La géométrie d'incidence rasante est particulièrement appropriée lorsque des couches minces sont considérées car la sensibilité à la surface est accrue de façon dramatique. La mesure de la diffusion diffuse, c'est à dire de la diffusion entre les pics de Bragg, permet de déterminer le désordre et les variations locales par rapport aux positions atomiques moyennes. Bien qu'une telle technique semble particulièrement adaptée à l'étude de la structure cristalline des nanocolonnes de GeMn, l'analyse est apparue bien moins directe qu'attendu initialement. En particulier, les deux premiers objectifs n'ont pu être complètement atteints, à savoir l'identification de la phase cristalline dans les nanocolonnes de GeMn et la mise en évidence de l'influence des dislocations à l'interface de la matrice et des nanocolonnes.

Cependant, nous avons obtenus des résultats particulièrement intéressants en étudiant la déformation dans la matrice de Ge. A l'aide de mesures précises de cartographies de l'espace réciproque autour des pics de Braggs dans différents types d'échantillons et de calculs *ab initio* de champs de déplacements dans le cadre d'une collaboration avec Frédéric Lançon, nous avons pu déterminer de façon quantitative la déformation de la matrice autour des nanocolonnes. Nous avons montré l'importance des corrélations de positions des nanocolonnes sur la forme du signal diffus autour des pics de Bragg, ainsi que l'importance de la nature anisotrope de la matrice de germanium en phase diamant. En particulier, nous avons observé l'effet du vieillissement des échantillons et la relaxation isotrope de la déformation due à l'oxydation des nanocolonnes.

Un aperçu intéressant des possibilités offertes par la mesure de la diffusion totale est illustrée par la figure 4.21 : la diffusion totale a été mesurée en incidence rasante, à l'aide du détecteur bidimensionnel XPAD décrit dans le chapitre 2. La figure montre un zoom de la mesure tridimensionnelle autour du pic de Bragg hors-plan (111) du germanium. Plusieurs particularités sont à noter autour du pic de Bragg (région rouge centrale), telle que la présence d'une tige de troncature le long de l'axe L avec des oscillations correspondants à l'épaisseur finie de la couche de GeMn

et un anneau diffus (comme discuté précédemment dans ce chapitre). L'observation de cet anneau dans le plan HK confirme son origine due aux corrélations des champs de déformation dans le plan de la couche de GeMn.

# Chapitre 5

## Magnetic and electronic properties of the GeMn nanocolumns : experiment and theory

In this chapter, the electronic and magnetic properties of the GeMn nanocolumns are discussed. The experimental results, especially those obtained by XAS-XMCD, are qualitatively and quantitatively analyzed. They serve as experimental references in the comparison with the properties theoretically calculated using *ab initio* methods and suggested structural models. In particular, we argue that simple interstitial or substitutional defects can hardly account for the observed properties. However, new crystalline phases, close to the Ge diamond, provide a better agreement between experiments and theory.

### 5.1 Probing magnetism in the GeMn nanocolumns by XAS-XMCD

#### 5.1.1 Magnetic semiconductors probed by XAS-XMCD

Let us first recall the previous results obtained by XAS and XMCD in the magnetic semiconductors systems, and more specifically in the case of the GeMn system.

Early XAS-XMCD measurements in the prototypical system (Ga,Mn)As [145–147] have shown absorption spectra with multiple peaks at the Mn  $L_{2,3}$  absorption edges, as shown for example in figure 5.1(a) from ref. [145]. The pronounced multiplet structure indicated a localized character of the electrons. However quite different results have also been reported from measurements in fluorescence yield mode in similar systems, as shown in figure 5.1(c,d), from ref. [148]. In 2004, a paper by Edmonds *et al.*[149] shed a new light on these results. It appeared that the multiplet structure of the absorption spectra, consistent with a  $\text{Mn}^{2+}$  configuration, was in fact due to the contribution of oxidized Mn atoms on the surface of the sample (fig. 5.1(e,f)). XAS-XMCD spectra measured in clean samples have shown broader absorption peaks and the absence of a multiplet structure in the XAS spectra (fig. 5.1(e)) Similar results were recently obtained in the (Ge,Mn) system by Gambardella *et al.*[150], showing the high sensitivity of the XAS-XMCD technique to the surface composition. It can also be noted that a work by Andrieu and coworkers [151] demonstrated that it is only a matter of hours for a Mn ultra-thin film to be oxidized by residual oxygen in a ultra-high vacuum chamber with a pressure of  $10^{-7}$  mbar.

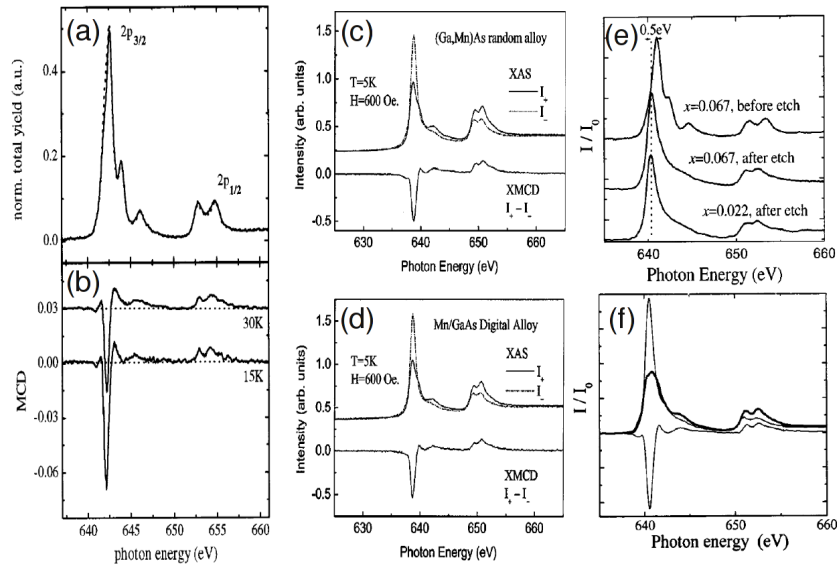


FIGURE 5.1: (a) XAS at the Mn  $L_{2,3}$  absorption edges in  $\text{Ga}_{0.98}\text{Mn}_{0.02}\text{As}$ , measured at 15K and  $15^\circ$  grazing incidence in electron yield mode and (b) corresponding XMCD at 15 and 30 K (ref. [145]). (c) XAS and XMCD spectra in a GaMnAs sample and (d) in a Mn/GaAs digital alloy measured in fluorescence yield mode (from ref. [148]). (e) TEY XAS spectra in a  $\text{Ga}_{1-x}\text{Mn}_x\text{As}$  sample before and after an HCl etch at room temperature and (f) XAS and XMCD spectra in a  $\text{Ga}_{0.933}\text{Mn}_{0.067}\text{As}$  etched sample, at 15 K with an applied magnetic field of  $\pm 0.6\text{ T}$  (from ref. [149]).

Therefore, great care about surface oxidation must be taken when measuring XAS and XMCD spectra, especially when dealing with *ex situ* samples, *i.e.* our case. In order to prevent any misinterpretation, we have capped our sample after the growth *in situ* with a protective layer. Several attempts were made, using Ge, Al, Au and Si. The most efficient capping layer was found to be a 0.5 nm layer of Ge followed by 3 nm of amorphous Si. Figure 5.2(d) shows the good homogeneity of the Si capping. As it can be inferred from the results in single crystal Si [152], a layer of silicon dioxide about 1 nm thick should form on the amorphous silicon during the first few days of exposure to air. Such layer should be enough to hinder further oxidation [152].<sup>1</sup> We will come back in part 5.2 and explain in more details the observation and the role of a surface oxide in the GeMn nanocolumns.

For the XAS-XMCD study of the GeMn nanocolumns, we have considered samples as similar as possible to the high- $T_C$  ones, *i.e.* as summarized in table 5.1. Given such growth parameters, the nanocolumns appear to be quite homogeneously distributed (fig. 5.2(a)) and seem to extend continuously from the buffer layer to the top of the GeMn layer when checked by TEM in cross-section (fig. 5.2(b)). This observation is further supported by imaging the Mn concentration, as shown in figure 5.2(c).

TABLE 5.1: Characteristics of the samples studied in XAS-XMCD.

<b>Growth parameters :</b>	
growth temperature	130 ° C
Mn concentration	10 %
<b>Nanocolumns :</b>	
diameter	$3.2 \pm 0.6$ nm
density	$2.0 \times 10^4 \pm 0.2 \times 10^4$ $\mu\text{m}^{-2}$
spacing (nearest neighbors)	$6.4 \pm 1.3$ nm

### 5.1.2 A metallic-like absorption spectrum

The x-ray absorption spectra measured at the Mn  $L_{2,3}$  edges in a capped GeMn sample are shown in figure 5.3. These spectra have been measured at the lowest accessible temperature (about 5 K) in order to obtain the largest magnetic moment (as suggested by SQUID measurements) and therefore the largest XMCD signal. SQUID measurements also suggested employing a large applied magnetic field

1. In order to prevent exposure to air, the samples were kept in a dessicator as long as possible.

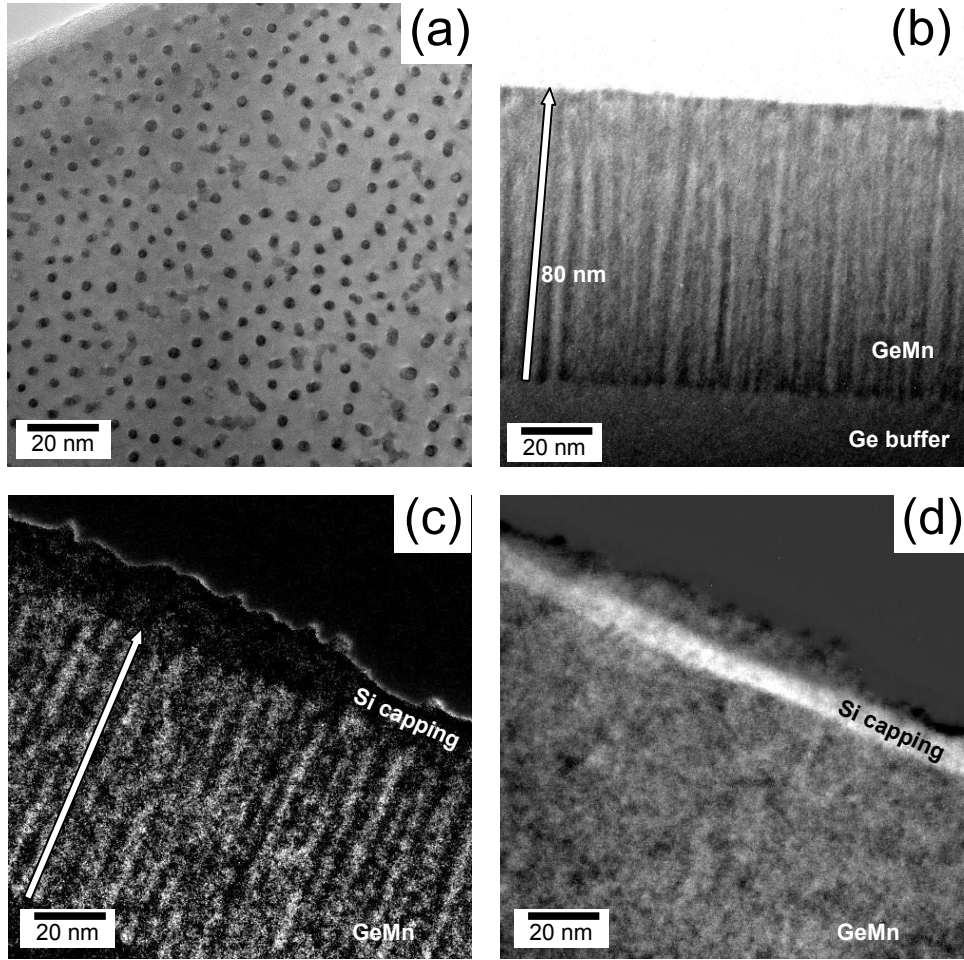


FIGURE 5.2: (a) Plane view and (b) cross-sectional TEM micrograph of a typical sample for the XAS-XMCD study, as detailed in table 5.1. (c) Energy filtered cross-sectional TEM micrograph at the Mn edge and (d) the same picture taken at the Si edge. In cross-sectional views, the growth direction is indicated by a white arrow. Scales are identical for all pictures. Picture (a) was taken by E. Prestat and pictures (b-d) were taken by T. Devillers.

(5 Tesla) in order to get as close as possible to the saturation of the GeMn layer. The small remnant magnetization - about 14% of the signal at 5 T - prevented measurements at remanence. The resulting absorption spectra show two single peaks at 640.5 eV and 651.5 eV and appear very similar to that observed in Mn metal [37], as seen in fig. 5.4.

In order to examine the  $2p \rightarrow 3d$  transitions details, the background corresponding to transitions involving other states has been subtracted. A double arctangent function was used as a model background, with inflexion points at the  $L_3$  and  $L_2$  maximum and with a amplitude ratio of 2 :1. The process is illustrated in fig.5.5.

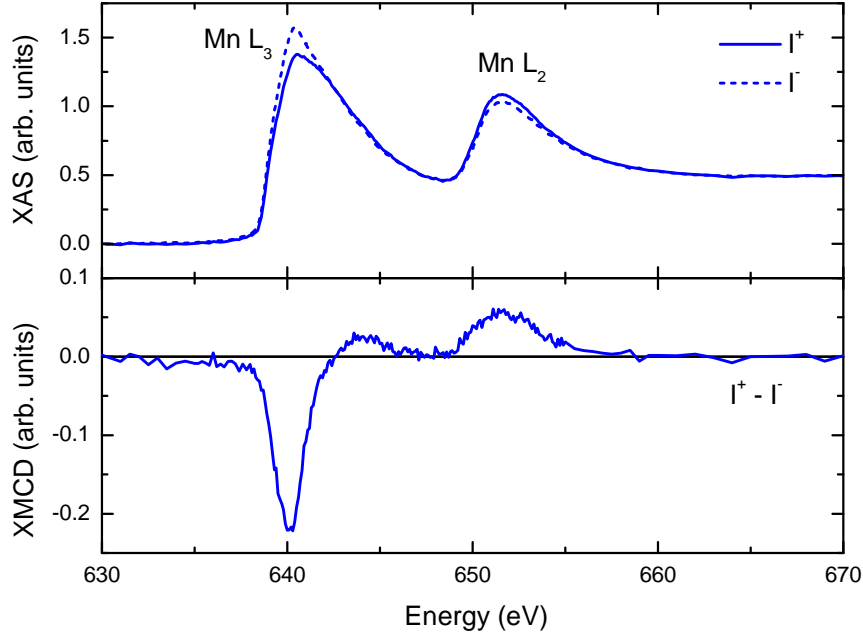


FIGURE 5.3: (top) Corrected and normalized TEY XAS spectra at the Mn  $L_{2,3}$  absorption edges measured at 5 Kelvin with an applied field of 5 Tesla, collinear to the incident photon beam wavevector. The circular polarization of the beam is either parallel (solid line) or antiparallel (dashed line) to the applied magnetic field. (bottom) Corresponding XMCD spectra.

The branching ratio (BR) is defined as :

$$BR = \frac{I(L_3)}{I(L_3) + I(L_2)} \quad (5.1)$$

where  $I(L_x)$  is the intensity of the absorption at the  $L_x$  edge. Since there is a small overlap between the  $L_3$  and the  $L_2$  absorption edge (*i.e.*, non zero absorption around 648 eV), the use of integrated intensities as  $I(L_x)$  is limited. Instead, we simply used the amplitude of the absorption spectrum at the  $L_3$  and  $L_2$  maxima, where the overlap is considered negligible. Thus, in the case of the nanocolumns the BR is equal 0.67, that is the statistical value (2/3). It is worth noting that deviations of the branching ratio from the statistical value have been correlated with deviations in the effective spin moment sum rule [153]. Therefore, rather small correction factors would be expected. We will come back on this last point in the next part.

In order to get an estimation of the overlap induced by the small spin-orbit splitting

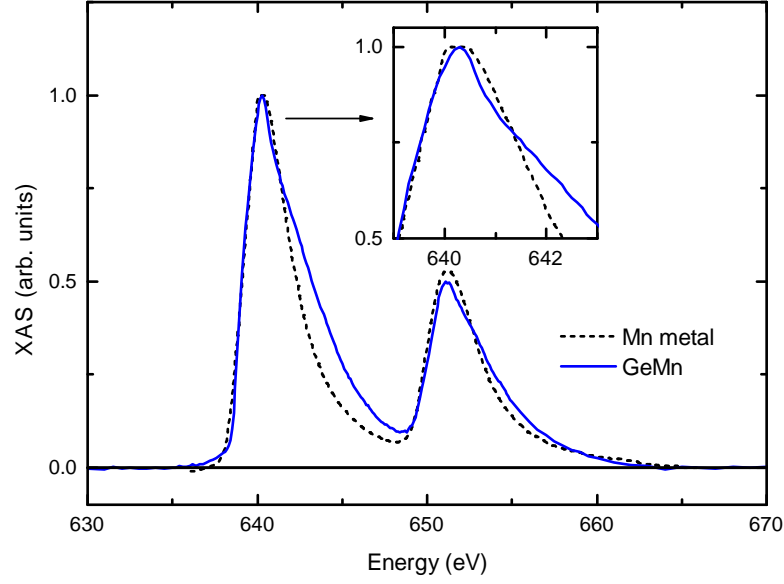


FIGURE 5.4: TEY isotropic x-ray absorption spectra at the Mn  $L_{2,3}$  edges for Mn metal (dashed black line, digitized from [37]) and GeMn nanocolumns. Both spectra have been corrected for the continuum background (see text). In both cases, the  $L_3$  edge was normalized to unity and set at the same energy value (640.5 eV). No comparison of the absolute energy position can be made between the two samples because they have been measured on different beamlines (ALS beamline 6.3.1 for the Mn metal sample, BESSY beamline UE46\_PGM-1 for the GeMn nanocolumns).

of the Mn  $2p_{1/2}$ - $2p_{3/2}$  states ( $\sim 11$  eV), a procedure similar to that proposed by Goering [154] was applied to the GeMn results. The experimental XAS spectrum shown in figure 5.3 could be fitted quite accurately as the sum of two *identical* peaks, only separated in energy (11 eV) and with a 2 :1 ratio of amplitudes, as well as a double arctangent function accounting for the transitions to the continuum (fig. 5.6). As seen in figure 5.6, the  $L_3$ - $L_2$  edge overlap is rather small (on the order of 1% of the total area under the peaks) and the value of  $BR = 0.67$  measured in the previous paragraph is relevant. Using the formula reported in ref. [154] with a value of  $r_{23} = \frac{L_2}{L_3} = 0.50 \pm 0.01$ , we obtained a spin correction factor  $SC = 1.00 \pm 0.03$ . Such value is in agreement with previous comparable results [154, 155].

The peaks observed in the GeMn sample ( $FWHM(L_3) = 4.2\text{eV}$ ,  $FWHM(L_2) = 4.1\text{eV}$ ) are also broader than those observed in Mn metal ( $FWHM(L_3) = 3.2\text{eV}$ ,



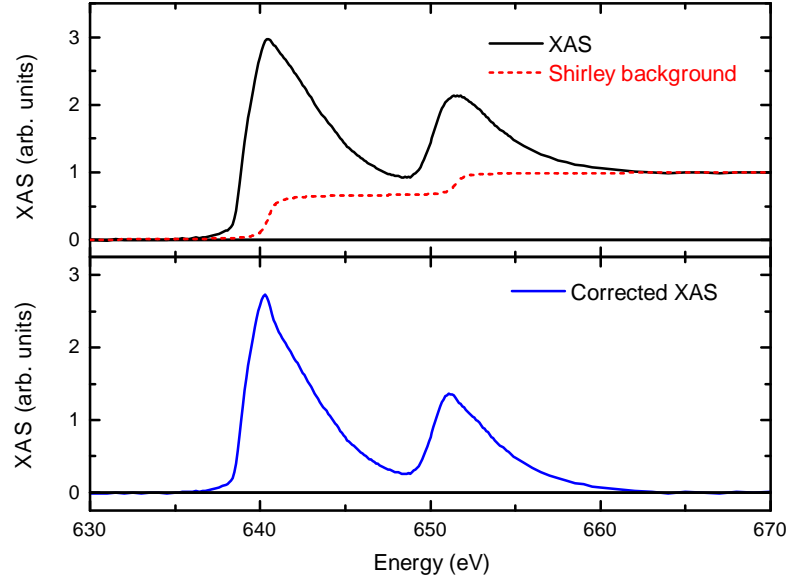


FIGURE 5.5: (top) TEY isotropic x-ray absorption spectrum at the Mn  $L_{2,3}$  edges for GeMn nanocolumns (solid black line) and model background for transitions other than  $2p \rightarrow 3d$  (red dashed line). (bottom) Corresponding corrected absorption spectrum (blue solid line)

$FWHM(L_2) = 3.7\text{eV}$ .<sup>2</sup> These broad, metallic absorption edges show that the Mn  $d$  states in the GeMn samples are delocalized and most likely hybridized with Ge orbitals into bands.

Similarly, the XMCD spectrum (fig. 5.3) consists in a single negative peak at 640.2 eV and a much smaller positive peak, both at the  $L_3$  edge, and a single positive peak at the  $L_2$  edge, very different from what can be observed *e.g.* in GaMnAs (fig.5.1). Bulk Mn-metal is an antiferromagnet with a Néel temperature of 90 K [156], so no comparison of the XMCD spectra is possible. However, as shown in figure 5.7, we found that the XAS and XMCD spectra measured in the GeMn nanocolumns look very similar to those experimentally observed in  $\text{Ge}_3\text{Mn}_5$  [69, 157].

$\text{Ge}_3\text{Mn}_5$  is a stable phase in the Ge :Mn binary phase diagram, however we could not evidence the presence of  $\text{Ge}_3\text{Mn}_5$  clusters in the considered GeMn sample by using x-ray diffraction or transmission electron microscopy. Furthermore,  $\text{Ge}_3\text{Mn}_5$

2. Note that all values for the full width at half maximum given here are slightly affected by the overlap between the  $L_3$  and  $L_2$  absorption edges. The overestimated is of about 0.2 eV, as deduced from fig. 5.6. Note also that given the shape of the spectra in fig. 5.4, the error should be about the same for Mn-metal and GeMn.

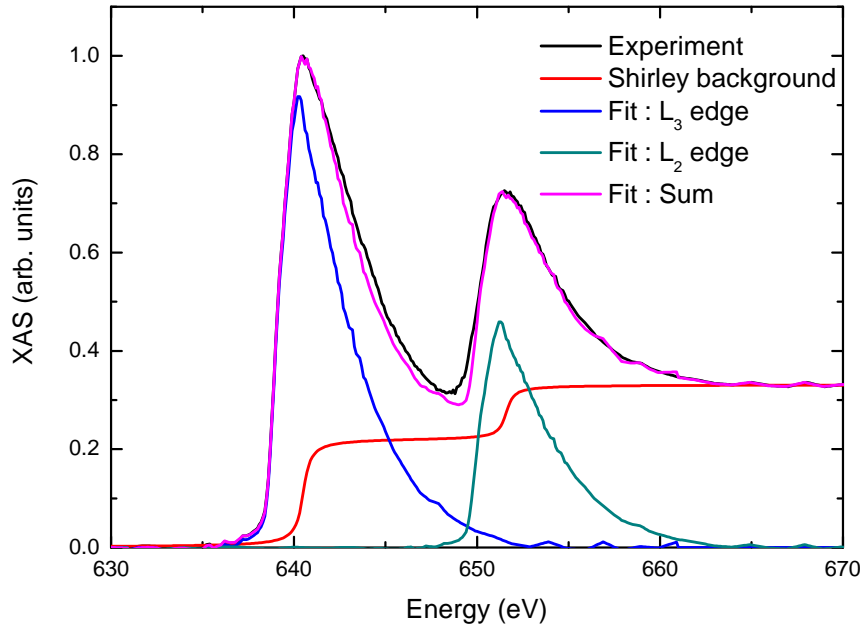


FIGURE 5.6: Experimental XAS spectrum (black line) and its fit into two similar peaks for the  $L_3$  (blue line) and  $L_2$  (green line) absorption edge, only separated in energy and with different amplitudes, as well as a double arctangent (red line) for the transitions to the continuum. The result of the fit (sum of the three contributions) is also plotted (pink line).

has a Curie temperature of about 300 K, yet no magnetic signal was measurable in the GeMn nanocolumns sample at room temperature in SQUID, as shown in fig. 5.8 or by XMCD. In contrast, the contribution of such  $\text{Ge}_3\text{Mn}_5$  clusters was clearly observed in other samples and further supported by XRD and TEM. Thus, the spectra shown in fig. 5.3 are intrinsic to the GeMn nanocolumns and not due to other metallic inclusions. Similar results were obtained by Alhers *et al.* from Munich : they also observed striking similar XAS and XMCD spectra in samples containing GeMn columnar inclusions and in sample containing also  $\text{Ge}_3\text{Mn}_5$  clusters (as shown in figure 5.9) and a decreasing XMCD signal when the amount of  $\text{Ge}_3\text{Mn}_5$  clusters was reduced [158].

### 5.1.3 Towards a quantitative analysis : validity of the sum rules and experimental considerations

Following the qualitative analysis described in section 5.1.2, we have performed a more quantitative analysis of the XAS-XMCD spectra using the corresponding

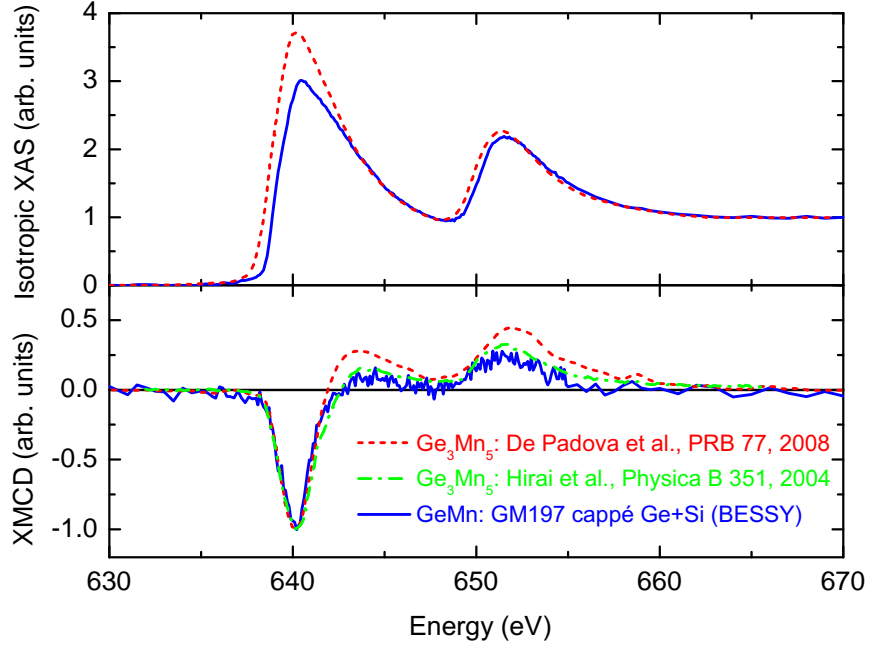


FIGURE 5.7: (top) Corrected and normalized isotropic x-ray absorption spectra in the GeMn nanocolumns (solid blue line) and in  $\text{Ge}_3\text{Mn}_5$  (dashed red line, digitized from [69]). (bottom) X-ray circular magnetic dichroism spectra in the GeMn nanocolumns (solid blue line) and in  $\text{Ge}_3\text{Mn}_5$  (dashed red line, digitized from [69] and dot-dashed green line, digitized from [157]). All spectra were measured in total electron yield mode. The GeMn nanocolumns were measured at 5 K with an applied magnetic field of 5 T. De Padova *et al.* measured in a  $\text{Ge}_3\text{Mn}_5$  thin film *in situ* at MAX-Lab, at remanence and at a temperature of 80 K. Hirai *et al.* measured in a  $\text{Ge}_3\text{Mn}_5$  single crystal at SPring-8 after *in situ* scrapping of the surface, using 1.4 T applied magnetic field at 110 K.

XMCD sum rules. The magneto-optical sum rules (SR) were introduced in 1992 by Thole *et al.* to determine the ground state expectation value of the orbital moment  $\langle L_z \rangle$  from XAS and XMCD measurements [127]. They were completed by Carra *et al.* the following year to obtain the effective spin moment  $\langle S_{z,eff} \rangle$  from the same data [128]. A year later, Chen *et al.* successfully applied the SR to iron and cobalt thin films with an error on the order of 5 to 10% [129]. Thus in the next sections we will describe how we have extracted values for the orbital and (effective) spin magnetic moments by applying the magneto-optical sum rules to our experimental XAS and XMCD spectra.

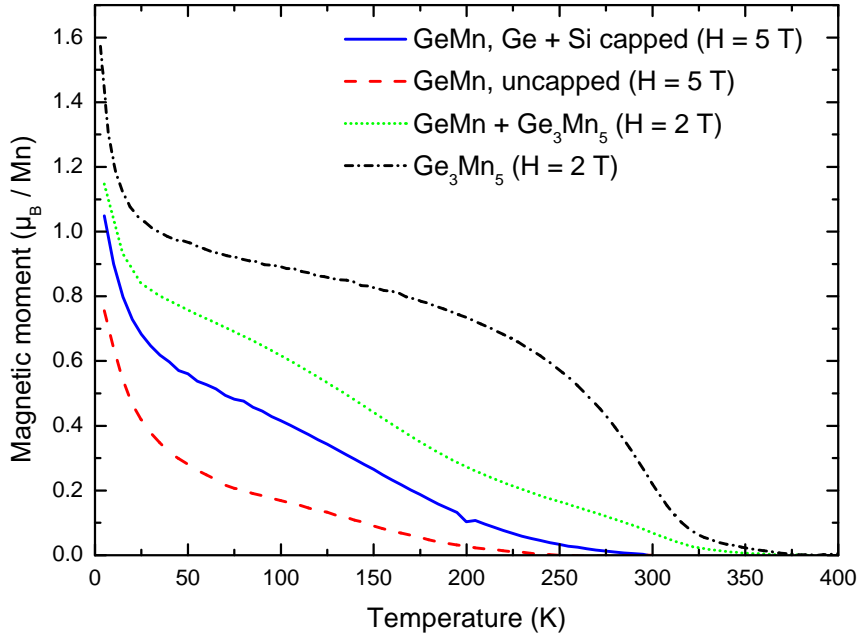


FIGURE 5.8: Magnetization *vs* temperature for different systems : GeMn nanocolumns protected by a capping layer (solid blue line), GeMn nanocolumns left unprotected (dashed red line), Ge<sub>3</sub>Mn<sub>5</sub> (black dot-dashed line) and GeMn nanocolumns containing Ge<sub>3</sub>Mn<sub>5</sub> clusters evidenced by TEM (green dotted line). Samples containing Ge<sub>3</sub>Mn<sub>5</sub> still exhibit a magnetization at 300 K, as opposed to the others. SQUID measurements performed by T. Devillers and M. Jamet.

#### 5.1.4 Magnetic (an)isotropy in the GeMn nanocolumns

Following the procedure described in Chapter 3, we have applied the XAS-XMCD sum rules to the experimental spectra. Figure 5.10 and figure 5.11 show the angular dependent XAS-XMCD spectra and the corresponding values extracted by using the sum rules, respectively. The different curves in figure 5.10 almost superimpose over both  $L_3$  and  $L_2$  absorption edges. The exception being the spectra measured at the most grazing incidence ( $30^\circ$ ) which are slightly more intense at both peaks. This tends to show that saturation effects are rather weak in this sample, as they would reduce the amplitude of the most intense peaks at grazing incidence [133]. Two more arguments against saturation effects in our measurements are : (i) self-absorption being non-linearly dependant on the intensity, it would affect differently the  $L_3$  and  $L_2$  peaks, however the BR is 0.67 in all cases (after Shirley background removal) ; (ii) given the calculations of Nakajima *et al.* in ref. [133] and taking the

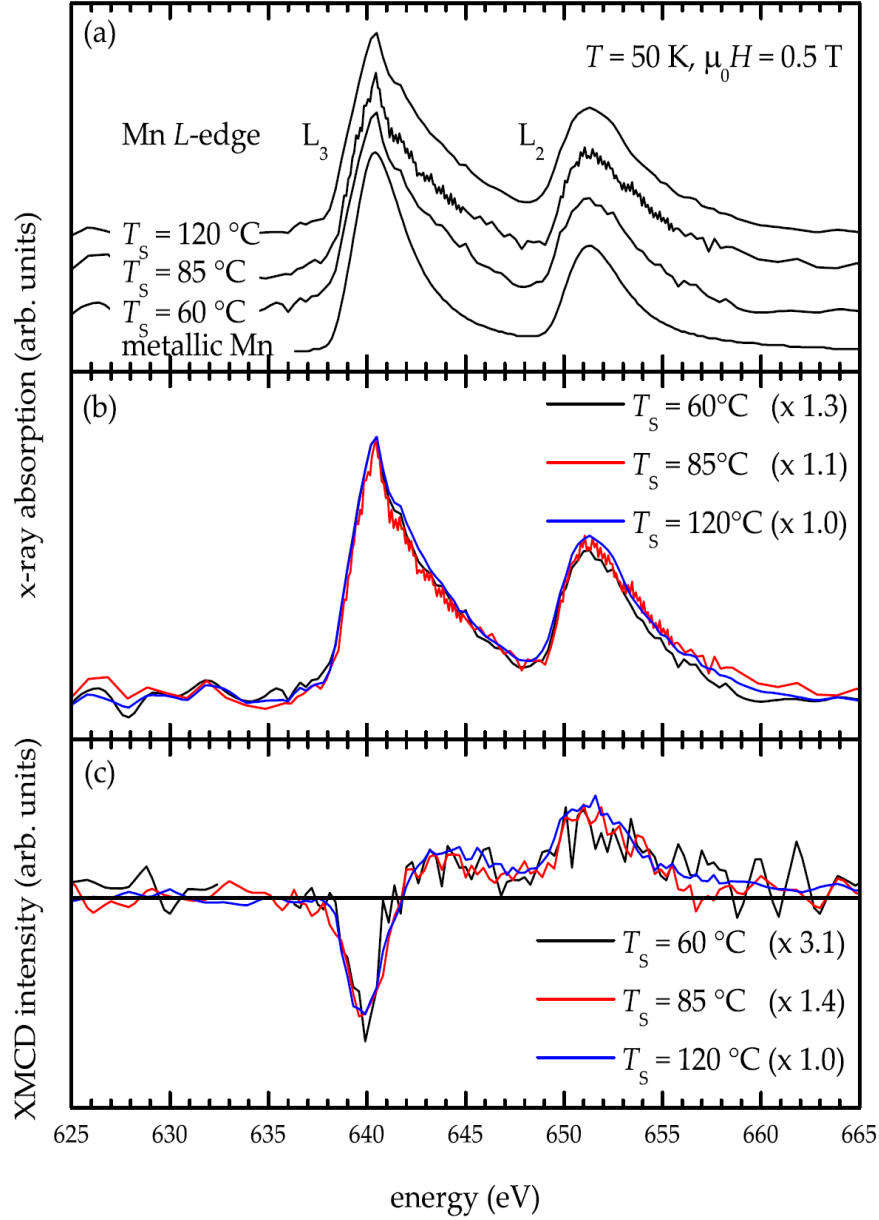


FIGURE 5.9: From ref. [158] : (a,b) XAS and (c) corresponding XMCD spectra of  $\text{Ge}_{97.2}\text{Mn}_{2.8}$  thin films measured at 50 K. For comparison, the absorption spectrum of metallic Mn is included (from ref. [37]). All spectra are normalized to the  $L_3$  peak intensity of the  $T_s=120^\circ \text{C}$  thin film in (b,c). The scaling factors are given in the figures.

worst-case scenario, namely the x-ray attenuation length at the edge in Mn-metal (70 nm) and an electron escape length of 3 nm, one finds a correction factor of a few percent at  $30^\circ$ .

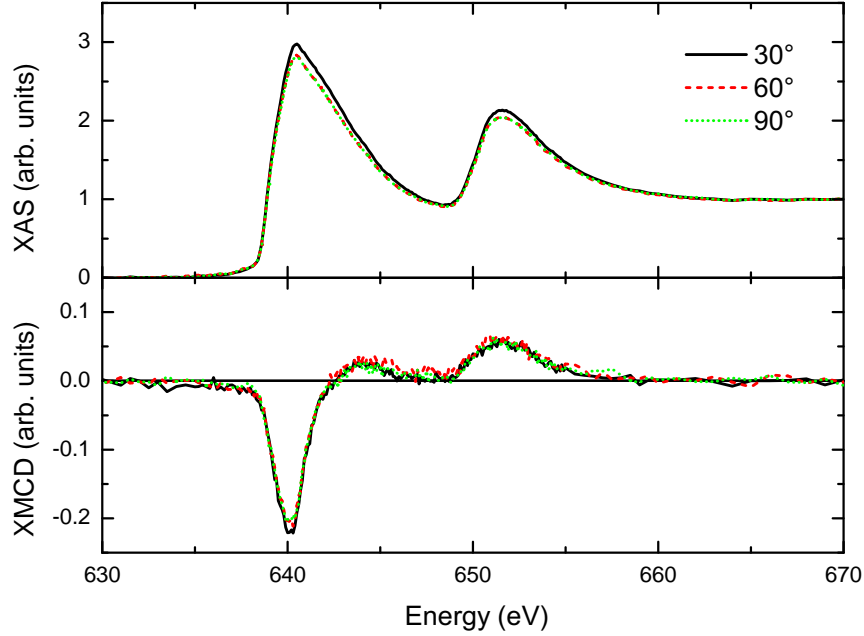


FIGURE 5.10: XAS and XMCD spectra measured at different incidence angles :  $30^\circ$  (black solid line),  $60^\circ$  (red dashed line),  $90^\circ$  (green dotted line).

Angular-dependent XAS-XMCD can provide very specific informations about the system. For example, Edmonds *et al.* have measured the angular dependence of the spectral features of XMCD measurements in (Ga,Mn)As. They were able to distinguish between two types of anisotropy, cubic and uniaxial, and to relate them respectively to localized atomic-like states far above the Fermi level and to states strongly hybridized with the strain-split valence band of the host [159]. In the case of the GeMn nanocolumns, no variation in the amplitude of the spectral features larger than the experimental noise can be observed (fig. 5.10)

As stated in the previous section, the XAS-XMCD sum rules have been applied to the experimental spectra. The results are presented in figure 5.11. The rather large error bars come from the significant amount of noise in our measurements : the signal originates from only a fraction of all atoms in the sample and the surface capping layer – even though absolutely necessary to prevent oxidation – further hinders the escape of the secondary electrons. It can be recalled that another

source of error is the estimated number of holes in the  $d$  shell  $N_h^{3d}$  (we have taken  $N_h^{3d} = 5$  in our case) because all calculated moments are proportional to  $N_h^{3d}$ . In the case of the different model structures examined by *ab initio* calculations (see section 5.4), calculated values for  $N_h^{3d}$  were comprised in the range of 4.2 – 4.8 holes.

As seen in figure 5.11, no clear anisotropy could be evidenced. The measured total magnetic moment on a Mn atom is comprised between 0.5 and 0.6  $\mu_B$ . The orbital moment remains quite low and represents only a few percent of the total magnetic moment, just as the orbital to spin moment ratio, is on the order of 0.1. This observation is consistent with a half-filled  $d$  shell and with our approximation of a number of five  $d$  holes in the sum rules. A small decrease in the orbital moment can also be observed around 60°, however its magnitude is comparable to the estimated error bars and it would be hazardous to try to provide an explanation for this.

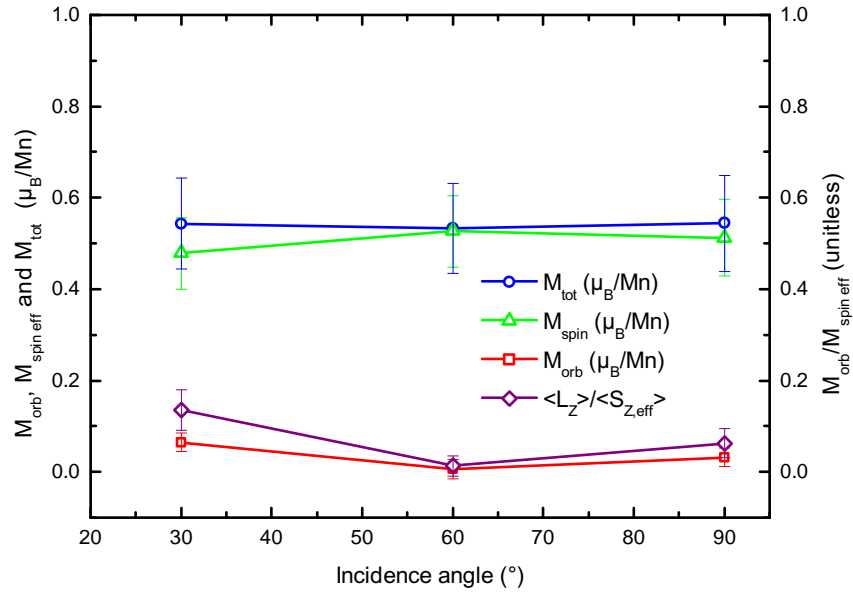


FIGURE 5.11: Orbital magnetic moment (red squares) and effective spin magnetic moment (green triangles), total magnetic moment  $M_{tot} = \langle L_z \rangle + 2 \langle S_z \rangle$  (blue circles) (in units of  $\mu_B/Mn$ ) and orbital to spin magnetic moment ratio (purple diamonds) as a function of the incidence angle at 5 K and 5 T.

In previous studies [153, 160], authors have found that experimental magnetic moment measured in  $Mn^{2+}$ -like system have to be corrected by a (multiplicative) factor 1/0.7 (hence the 30% error in the theoretical determination of the magnetic

moment for Mn using the sum rules). As a point of comparison, we also have corrected our results by a factor of 0.7, determined from a similar analysis as in [153, 160, 161] and both uncorrected and corrected values are reported. Note that only the spin magnetic moment is affected by this correction. Thus, figure 5.12 is the same as figure 5.11 where the spin mangnetic moment has been corrected : the total magnetic moment is independant of the angle and is equal to approximately  $0.8 \pm 0.1 \mu_B$ .

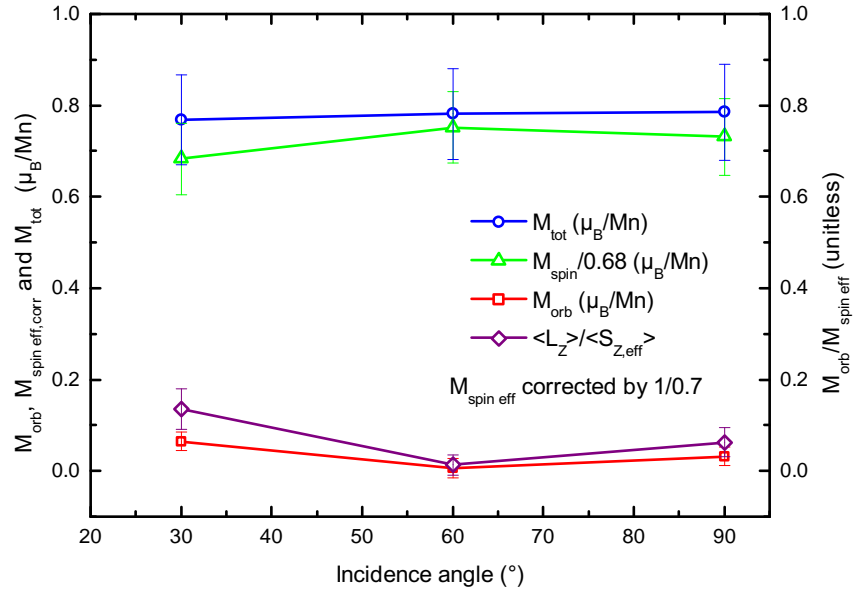


FIGURE 5.12: Orbital magnetic moment (red squares) and corrected effective spin magnetic moment (green triangles), total magnetic moment  $M_{tot} = \langle L_z \rangle + 2 \langle S_z \rangle$  (blue circles) (in units of  $\mu_B/Mn$ ) and orbital to spin magnetic moment ratio (purple diamonds) as a function of the incidence angle at 5 K and 5 T.

Considering the uncorrected values, in the case of uniaxial anisotropy (in-plane directions are equivalent), one expects the effective spin magnetic moment (in  $\mu_B/Mn$ ) to vary like [162] :

$$M_{s,eff}(\bar{\theta}) = \lambda + \beta \sin^2 \bar{\theta} \quad (5.2)$$

with  $\bar{\theta} = 90 - \theta$  in our experimental geometry and

$$\lambda = M_s - 7M_D^\perp \quad (5.3)$$

$$\beta = \frac{21}{2} M_D^\perp \quad (5.4)$$



$$M_D^\perp + 2M_D^\parallel = 0 \quad (5.5)$$

In order to estimate the correction on the effective spin moment, we have fitted the data extracted from the angular dependent measurements (fig. 5.11). Values of  $\lambda = 0.52 \pm 0.02 \mu_B/Mn$  and  $\beta = -0.05 \pm 0.04 \mu_B/Mn$  are found. The very small value of  $\beta$  indicates a vanishing value of  $M_D^\perp$  ( $M_D^\perp$  is less than one order of magnitude smaller than  $\beta$ ), within the experimental error. Hence  $M_D^\parallel$  is also negligible and in particular  $M_s = \lambda + \frac{2}{3}\beta \approx M_{s,eff}$ , in agreement with the fact that the magnetic dipole term can usually be safely ignored when applying the sum rules in a cubic system [163]. This conclusion holds if one considers the corrected values shown in fig.5.12, values of  $\lambda = 0.75 \pm 0.03 \mu_B/Mn$  and  $\beta = -0.08 \pm 0.06 \mu_B/Mn$  are found.

We observe what seems to be magnetic isotropy in this system. This is in opposition to what one's intuition, *i.e.* that the columnar shape anisotropy would dominate and set out-of-plane anisotropy. However, our measurements are consistent with magnetization measurements using SQUID by Devillers *et al.* on the same system, *i.e.* no or little difference between in-plane and out-of-plane orientations [82, 96]. The explanations proposed at that time [96] are still valid and recalled here :

- Magnetocrystalline anisotropy could compensate the shape anisotropy. In particular, strain might be significant in the nanocolumns and magneto-elastic anisotropy may compensate shape anisotropy.
- Coupling between the columns, in particular antiferromagnetic coupling, may also affect the overall anisotropy.

Since only in-plane and out-of-plane orientations are (easily) accessible in SQUID measurements, it was suggested by Devillers *et al.* that there might be an anisotropy axis in another direction [96]. However our observations cannot support that hypothesis as we did not observe any anisotropy in going from out-of-plane to in-plane.

### 5.1.5 Surface *vs* bulk measurement : comparison between XMCD and SQUID

As stated before, XAS-XMCD measurements, especially in total electron yield, are essentially sensitive to the surface. In order to be able to extend our observations to the bulk of the sample, we have compared the magnetic field dependence of the

XMCD signal to that of SQUID measurements in the same sample, at a temperature of 5 Kelvin. The results are plotted in figure 5.13. The agreement between both measurements is excellent as both SQUID and XMCD magnetic signals show the same dependence on the applied magnetic field.

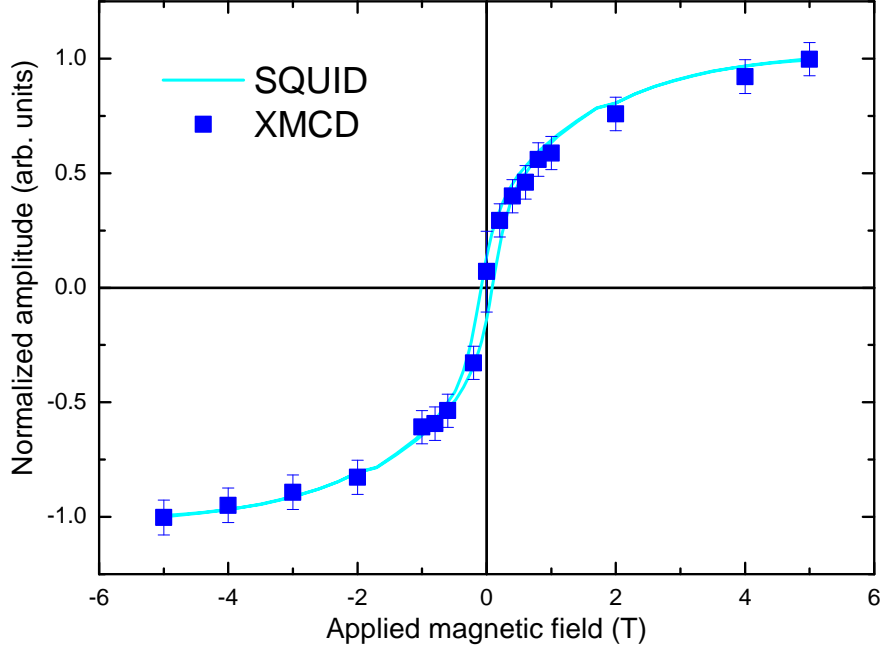


FIGURE 5.13: Normalized SQUID (solid cyan line) and XMCD (blue squares) signals as a function of the applied magnetic field. The SQUID signal is the measured magnetization, normalized to the value at 5 T. The XMCD signal is the amplitude of the XMCD at the  $L_3$  peak, normalized to the value at 5 T.

However, the scaling of the SQUID signal in Bohr magneton per manganese atom yields a magnetic moment of  $1.03 \mu_B/\text{Mn}$  in an applied field of 5 T and at a temperature of 5 K. This is quite different from the value of 0.5 to  $0.6 \mu_B/\text{Mn}$  extracted from the XAS-XMCD measurements by using the sum rules. One possible comment is that even though the magnetic behavior is similar in the surface and in the bulk, the normalization of the magnetic signal, *i.e.* the total number of Mn atoms may be different in the surface than in the bulk. Furthermore, considering the corrected values of  $\approx 0.8 \mu_B/\text{Mn}$ , as discussed in the previous paragraphs, the difference between the absolute SQUID and XMCD results is further reduced.

One can also note that the GeMn sample seems not to be completely saturated at the extreme applied magnetic fields of  $\pm 5$  T. This may be due to some paramagnetic substitutional Mn atoms in the Ge matrix that require higher magnetic

fields to be fully aligned.

### 5.1.6 Temperature dependence of the XAS-XMCD spectra

The previous section established the equivalence of the field dependence of the XAS-XMCD and SQUID measurements in the GeMn sample at 5 K. In order to examine the details of the evolution of the magnetic moments on the Mn atoms as a function of temperature, we have performed temperature-dependent XAS and XMCD measurements. The XAS spectra are shown in figure 5.14. No clear difference can be observed, except for a little variation in the amplitude of the  $L_3$  and  $L_2$  peaks, as illustrated in figure 5.15. However, the BR is equal to 0.67 for all temperatures. This small, energy-independent variations of the measured XAS signal could be due to variation of the escape length of the secondary electrons with the temperature. The calculated maximum variation of the integral of the (Shirley background-corrected) XAS signal at all temperatures are  $\pm 6\%$  with respect to the mean value, i.e. smaller than the error bar on the magnetic moment determination.

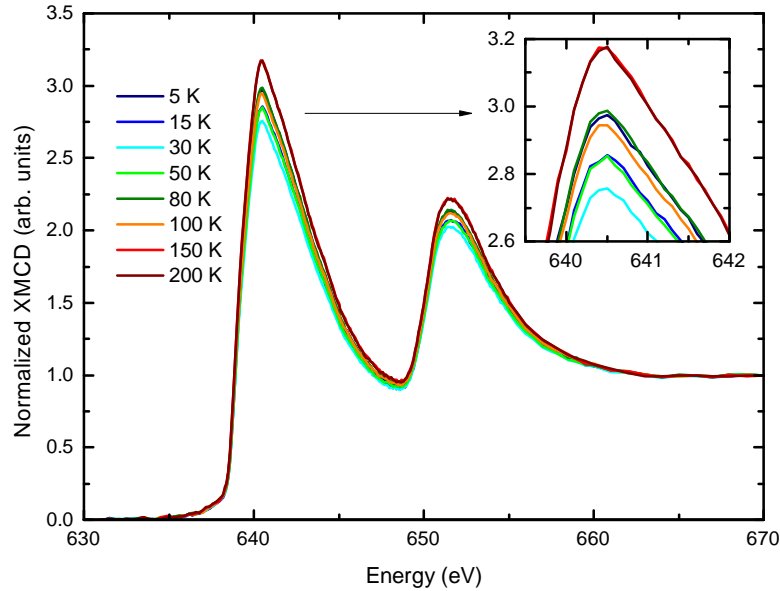


FIGURE 5.14: Corrected XAS spectra at the Mn  $L_{2,3}$  absorption edge, measured at different temperatures, with an applied magnetic field of 5 Tesla.

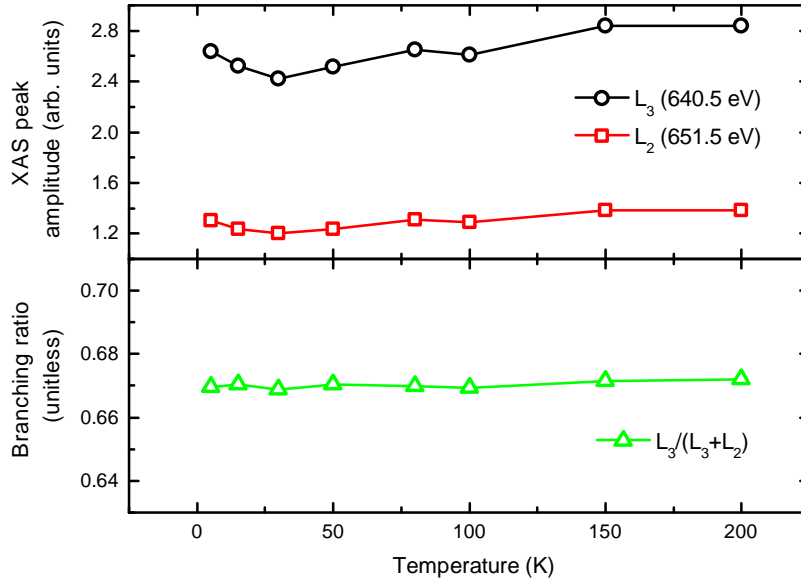


FIGURE 5.15: (top) Amplitude of the XAS at the Mn  $L_2$  (red circles) and  $L_3$  (black squares) absorption edges with an applied magnetic field of 5 Tesla, as a function of the temperature and (bottom) the corresponding BR. The mean value of the BR is  $0.670 \pm 0.001$ .

Quite similarly, the shape of the XMCD spectra does not depend on the temperature, as shown in figure 5.16. Only the spectrum measured at 150 Kelvin seems to be slightly different, however, as noise increases with temperature, it is hard to conclude on a single spectrum, especially since the spectrum measured at 200 K is again similar to the others.

Figure 5.17 shows on the same graph the evolution of the magnetic moment per Mn atom, as measured by SQUID and extracted from the XAS-XMCD spectra by the sum rules as function of temperature ( $M(T)$  curve). The SQUID signal decreases sharply between 5 and 30 K (probably due the contribution of the paramagnetic Mn), and then decreases linearly with temperature. The XMCD signal only seems to decrease linearly over the whole temperature range. However, the SQUID signal falls within most of the error bars from the XMCD measurements.

Considering the factor-corrected values from the sum rules gives a better agreement with the SQUID results, as shown in figure 5.18. The disagreement holds for the low temperature value, but for  $T \geq 15$  Kelvin, the agreement is much better and a similar linear decrease of the magnetic moment with increasing temperature is observed.

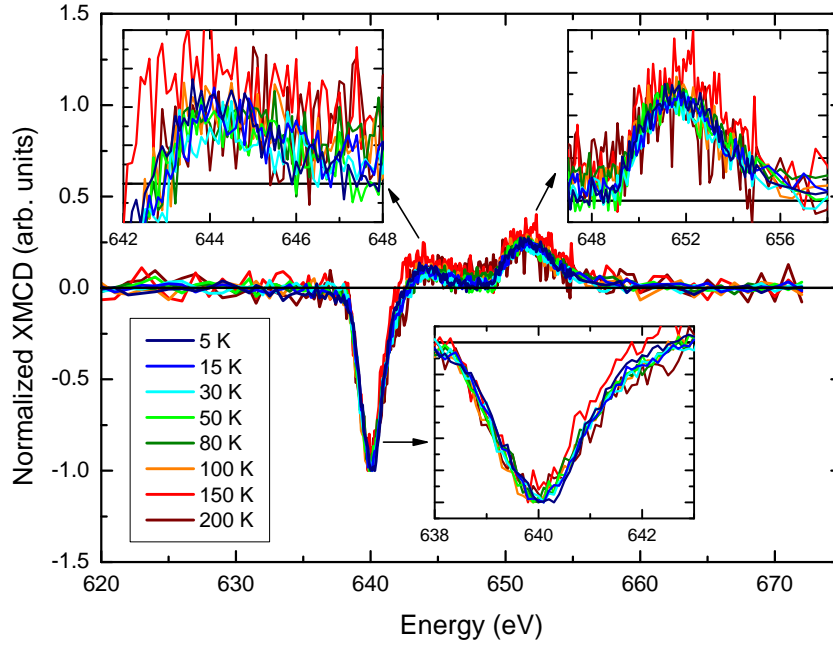


FIGURE 5.16: XMCD spectra at the Mn  $L_{2,3}$  absorption edge, measured at different temperatures, with an applied magnetic field of 5 Tesla. All spectra have been normalized to the XMCD  $L_3$  peak. Zoom on the different features of the XMCD spectra are shown in the insets.

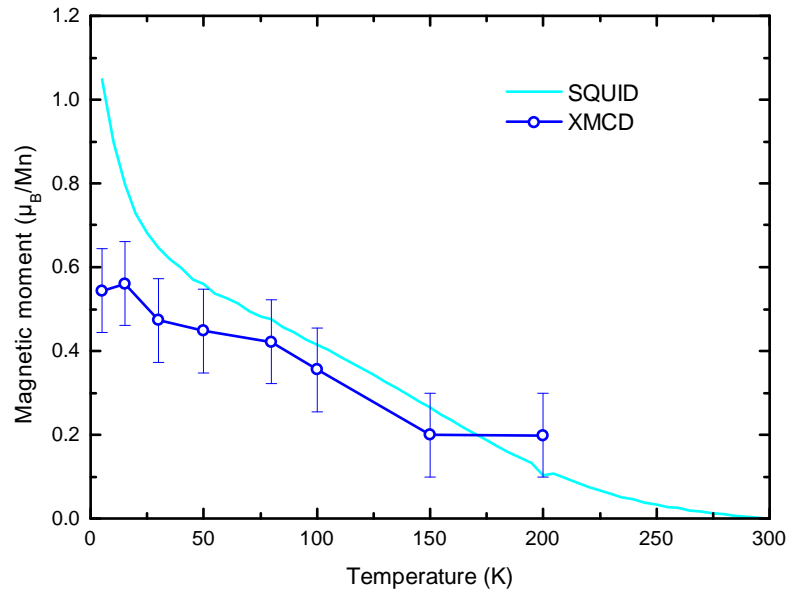


FIGURE 5.17: Magnetic moment measured by SQUID (solid cyan line) and by XAS-XMCD and sum rules (blue circles) as a function of temperature.

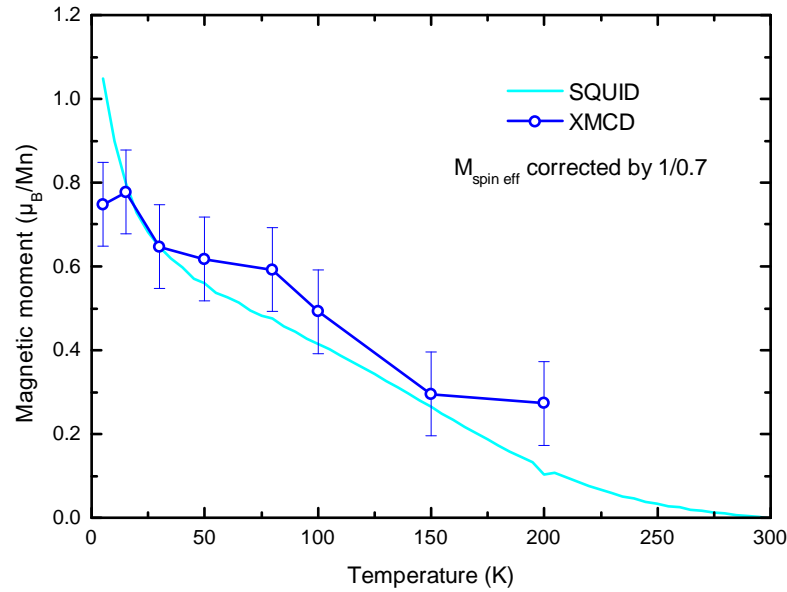


FIGURE 5.18: Magnetic moment measured by SQUID (solid cyan line) and by XAS-XMCD and sum rules with a corrective factor on the spin moment (blue circles) as a function of temperature.

### 5.1.7 Which manganese atoms are being measured ?

One simple question that is worth discussing is the type of manganese atoms that are actually being measured by XAS-XMCD in the GeMn samples. In the classical case of diluted (Ga,Mn)As, even if the system is homogeneous, all Mn atoms are not equivalent. Different types of environment have been considered (substitutionals, interstitials or dimers of both ...) [145, 164]. In the heterogenous case of GeMn nanocolumns, Mn atoms are located :

1. **in the Ge matrix** : this represents about 10% of total amount of Mn atoms. Mn atoms in the Ge matrix may assume any position discussed previously for (Ga,Mn)As, *i.e.* substitutionals, tetragonal or hexagonal interstitials or even dimers, or more complicated few atoms-clusters. It may also be recalled that the local Mn concentration in the Ge matrix is lower than 1%. It has been suggested that the Mn atoms in the matrix behave paramagnetically [22, 82, 96].
2. **in the nanocolumns** : the remaining 90% of the Mn atoms are located in the nanocolumns or at the interface with the matrix. The local concentration in the matrix is much higher than in the matrix and reaches around 30–40%.

3. **at the nanocolumns/matrix interface** : in the case of small nanocolumns (diameter on the order of 3 nm), the surface of the interface becomes quite significant, *e.g.*, it only takes a 0.514 Å-thick shell (= 0.9 lattice parameter) around a 3 nm-wide nanocolumns to obtain a shell :core surface ratio of 1. This means that interface effects will have to be kept in mind, in particular if the interface or if the core is disordered : it has been shown that Mn atoms in the environment of disordered group IV-atoms (amorphous Si) have their local magnetic moment quenched [38]. If such quenched magnetic moments exist in the GeMn nanocolumns system, it would indicate that the actual magnetic moment on the magnetic Mn atoms is higher than measured by XAS-XMCD or SQUID (since both are normalized by the *total* number of Mn atoms in the *probed volume* of the sample).

## 5.2 Influence of the surface oxide

### 5.2.1 Evidencing the surface oxide

As stated in the previous sections, we used different types of capping layer to protect our samples against oxidation. It appeared that the most efficient capping was made of 3 nm of amorphous Si on top of 0.5 nm of Ge. The XAS and XMCD spectra measured in samples with only the Ge part of the capping or with no capping layer at all are shown in figure 5.19. As described in the case of (Ga,Mn)As in section 5.1.1, both XAS and XMCD spectra of the uncapped are strikingly different from those measured in the Si+Ge-capped samples. In particular we observe much narrower absorption edges, corresponding to more localized *d* states and a multiplet structure (three sub-peaks at the  $L_3$  edge and two at the  $L_2$  edge, respectively noted A–C and D–E in figure 5.19) in the XAS spectra. The multiplet structure is also seen in the XMCD spectra and the maximum XMCD at the  $L_3$  edge is shifted  $\sim 0.3$  eV higher in energy, compared to the Ge+Si capped sample. The explanation for these differences is the formation of a MnO-like oxide layer on top of the GeMn layer, as can be inferred, for example, by comparing with results in various Mn oxides (figure 5.20, taken from refs. [37, 165]).

The comparison of the SQUID and XMCD signals also shows a strong discrepancy between both magnetization curves (figure 5.21). Using the same argument as in

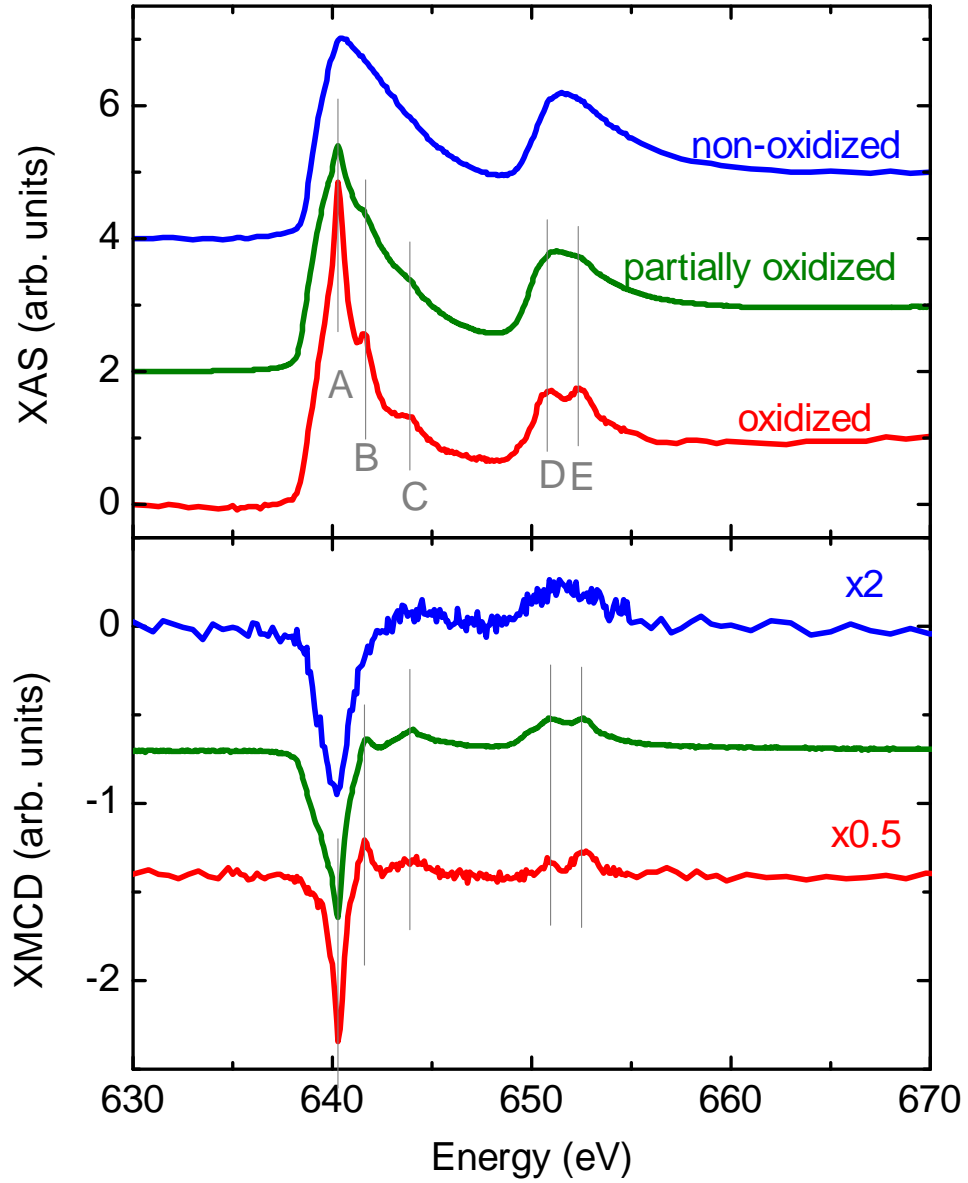


FIGURE 5.19: (top) Corrected and normalized isotropic x-ray absorption spectra at the Mn  $L_{2,3}$  absorption edges (from top to bottom) in the unoxidized GeMn nanocolumns (capped with 0.5 nm Ge + 3 nm Si), in the partially oxidized GeMn nanocolumns (capped with 0.5 nm Ge) and in oxidized GeMn nanocolumns (not capped). (bottom) Corresponding x-ray circular magnetic dichroism spectra. The XMCD spectrum for the non-oxidized sample has been magnified by a factor 2, the XMCD spectrum for the oxidized sample has been demagnified by a factor 1/2. All spectra were measured in the same conditions, *i.e.* in total electron yield mode, at 5 K with an applied magnetic field of 5 T. Spectra for the non-oxidized and oxidized sample were measured on beamline UE46.PGM-1 at BESSY. The partially oxidized sample was measured on beamline ID08 at the ESRF, the energy scale was adjusted by a rigid shift of +0.25 eV.



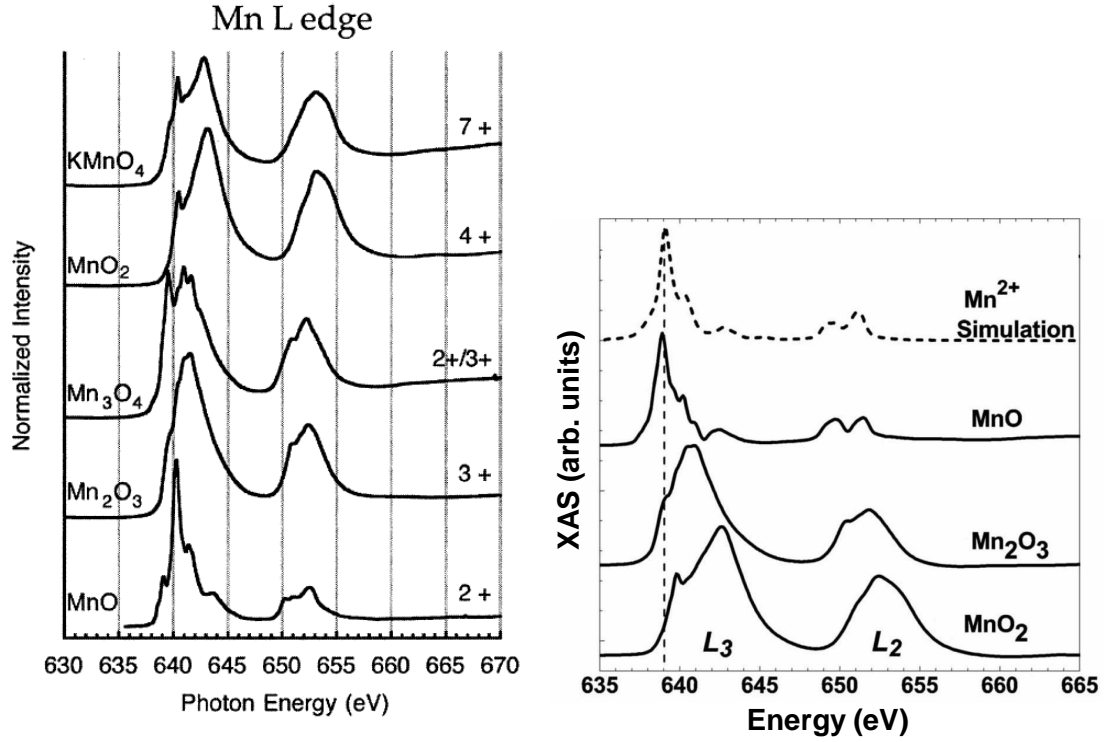


FIGURE 5.20: Experimental x-ray absorption spectra in different manganese oxide (left panel is adapted from [165], right panel is adapted from [37]). The spectra corresponding to the manganosite ( $\text{MnO}$ ) is similar to the spectra observed in oxidized GeMn samples.

section 5.1.5, we show that the observed effect is indeed due a different composition (*i.e.* oxidation) of the top part of the GeMn layer.

### 5.2.2 Probing the oxide/GeMn layer interface

In the case of the Ge capping layer, the XAS spectra look very similar to those measured in well-capped, non-oxidized samples (fig. 5.19). However, some shoulders can be observed at the same position as in the oxide layer. Moreover, the XMCD spectra shows the same features as in the case of the oxidized sample. A closer look at the XMCD at the Mn  $L_3$  absorption edge shows two sub peaks (noted A and B), with different dependences on the applied magnetic field (left panel in figure 5.22). Due to the overlap between both peaks it is rather hard to extract the magnetic field dependence of each peak simply by measuring their amplitude. This is shown in figure 5.23, where the lines are the measured XMCD signal at the two positions in energy while cycling the magnetic field. The difference between the two magnetic components is more obvious if instead we fit the XMCD

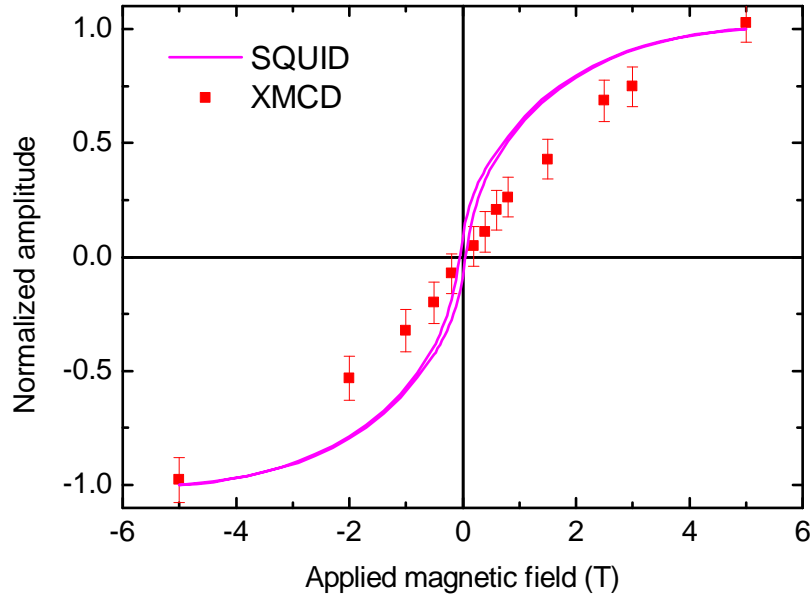


FIGURE 5.21: Normalized SQUID (solid magenta line) and XMCD (red squares) signals as a function of the applied magnetic field. The SQUID signal is the measured magnetization, normalized to the value at 5 T. The XMCD signal is the amplitude of the XMCD at the  $L_3$  peak, normalized to the value at 5 T.

spectra in the Ge capped sample (*i.e.* partially oxidized) by a weighted sum of the XMCD in the non-oxidized sample and of the XMCD in the oxidized sample, as shown in the right panel in figure 5.22. The good agreement between the fit and the experimental spectra is maintained over all the different applied magnetic fields. Hence, plotting the weight of each contribution as a function of the applied magnetic field (squares in fig. 5.23), a clear difference is recovered : the contribution to the fit of the GeMn layer (capped sample) is more ferromagnetic-like, while the oxidized part (uncapped sample) shows a rather paramagnetic-like behavior. Therefore, we show that using XAS and XMCD in the partially oxidized sample we can be sensible simultaneously to both the oxidized top layer as well as the underlying pristine nanocolumns.

### 5.2.3 Oxide and exchange bias in the nanocolumns

We have shown that the MnO-like oxide on top of the oxidized nanocolumns has an antiferromagnetic character that can be used to induce exchange bias in the

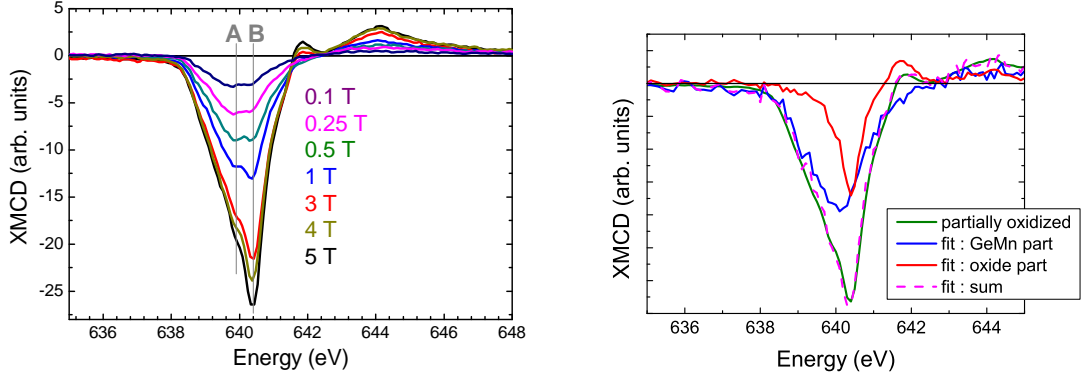


FIGURE 5.22: (left) X-ray magnetic circular dichroism spectra at the Mn  $L_3$  absorption edge in a partially oxidized (*i.e.* Ge capped) sample for applied magnetic fields ranging from 0.1 to 5 Tesla at a temperature of 5 Kelvin. Two overlapping peaks noted A and B can be observed, with different magnetic field dependence. (right) XMCD spectra at the Mn  $L_3$  edge in the partially oxidized sample (green line) at 5 K and 5 T, and its decomposition into a GeMn (non oxidized) component (blue) and an oxide component (red), as well as the result of the fit (pink dotted line).

underlying GeMn nanocolumns. All details of the study have been published in ref. [86], which is available in appendix B.

### 5.3 Conclusion about the experimental XAS-XMCD analysis in the GeMn nanocolumns

We have measured the x-ray absorption and magnetic circular dichroism spectra in GeMn nanocolumns samples using different experimental parameters. The results of this study can be summarized as follow :

- The capping layer on top of the GeMn nanocolumns is of critical importance. Sample left unprotected or poorly protected (*e.g.* with a 0.5 nm Ge capping) are prone to surface oxidation, which has dramatic effect on the measured XAS-XMCD spectra.
- The lineshape of the XAS spectra indicates that Mn  $3d$  are delocalized and hybridized with Ge states into bands.
- A good qualitative agreement of the lineshapes of the XAS and XMCD spectra was found with those measured in  $\text{Ge}_3\text{Mn}_5$  samples. However, all other experimental techniques used have shown no trace of such a compound in our samples.

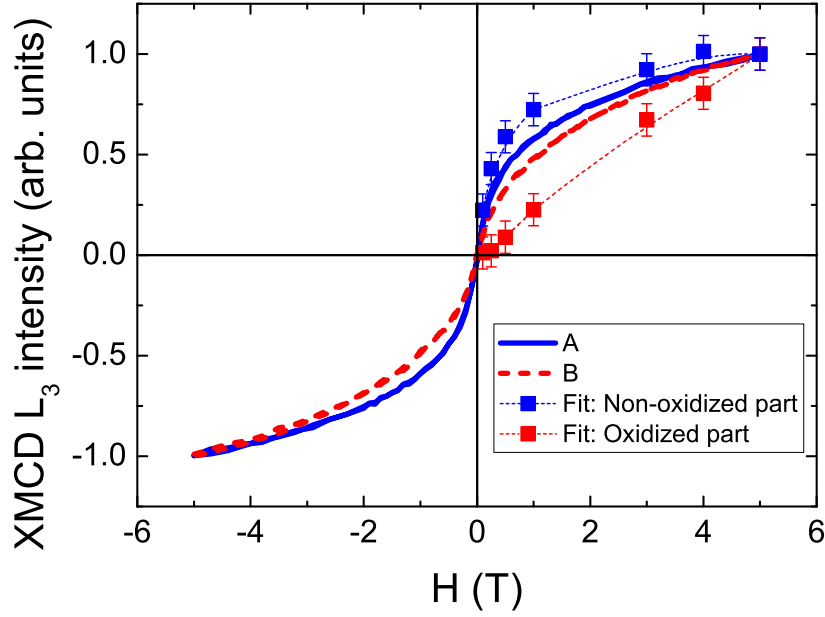


FIGURE 5.23: Magnetization curves for the two components A and B in the left panel in figure 5.22, as measured directly (solid line) and as extracted from the fits (squares). The dotted lines are guides to the eye.

In particular, no magnetic signal is observed below the Curie temperature of  $\text{Ge}_3\text{Mn}_5$  ( $\sim 300$  K).

- A quantitative analysis of the XAS-XMCD spectra in well protected samples has revealed a magnetic moment on the Mn atoms on the order of  $0.8 \mu_B$ . This small value, combined with the relatively high level of noise in our experimental spectra (partly due to the unavoidable capping layer) yields error bars of approximately  $\pm 0.1 \mu_B$ . In particular, the value of the magnetic moment is much lower than that in  $\text{Ge}_3\text{Mn}_5$ . The contribution of the orbital is small (less than  $0.1 \mu_B$ ).
- Angle-dependent measurements have shown no anisotropy, in agreement with previously obtained results using *bulk* methods in similar samples (ref. [96]). We show that the magnetic dipole term can safely be ignored, which is consistent with a cubic system. Temperature-dependent measurements show a linear decrease in the magnetization, in agreement with SQUID results.
- Comparison of magnetization curves measured by SQUID and XMCD show the same magnetic behavior in the bulk and in the top layers as a function of the applied magnetic field. All results from the XAS-XMCD analysis may then be extended to the whole length of the nanocolumns.

- We have shown that in the case of poorly capped samples, a partial oxidation occurs. It is qualified as *partial* in the sense that the interface between the shallow surface oxide layer and the underlying pristine GeMn nanocolumns can be accessed using XAS and XMCD. The surface oxide shows absorption spectra similar to MnO.
- The depth of the oxidation can be related to a decrease in the magnetic signal (see ref. [86]), due to an antiferromagnetic arrangement in the oxide. In particular, the antiferromagnetic character of the oxide can be used to induce an exchange bias effect in the underlying ferromagnetic nanocolumns. Its amplitude is comparable to that obtained in other magnetic semiconductors, or by using a entire MnO layer on top of the GeMn layer.

## 5.4 Calculation of the XAS-XMCD spectra

In order to understand the origin of the magnetic properties of the GeMn nanocolumns, we were interested in *ab initio* calculations. The aim of this work was to calculate the theoretical XAS and XMCD spectra in model structures and compare them to our experimental results. Hence, we could test the compatibility of the theoretical structures with experimental results. This work was done in close collaboration with Emmanuel Arras, Pascal Pochet and Frédéric Lançon at the L\_Sim laboratory (CEA-Grenoble), who calculated and provided me with the models of the crystalline structures most likely to form in the GeMn nanocolumns [89, 97]. Access to the codes and invaluable help in getting to use them was provided by Yves Joly (FDMNES [166]) and El-Kébir Hlil (SPRKKR [167, 168]) from the Institut Néel. Finalization of the work was done in collaboration with Andrey Titov (CEA-Grenoble), who provided expertise in the field of *ab initio* electronic properties calculations.

In this section, I will first describe the different structural models considered in this study, including the  $\text{Ge}_3\text{Mn}_5$  that will be used as a benchmark. Then the different results that were obtained are presented, as well as some of the important parameters to be considered in the calculations.

### 5.4.1 Calculation of the spectra

The XAS and XMCD spectra were calculated using different programs. The input parameters were simply the atomic positions and chemical species, as well as the unit cell parameters and space group. Two of the most important points to be considered in order to get the right absorption spectra are :

- A good description of the core states : the calculation of the spin-orbit splitting between the  $2p_{1/2}$  and  $2p_{3/2}$  core states, as well as the exchange splitting within each  $2p_{1/2}$  and  $2p_{3/2}$  state must be accurate because the transition probabilities (absorption rate) will be calculated for each core state before being combined in the total absorption spectra. An improper splitting between the  $p$  states will lead to an improper shift between all the energy-dependent transition probabilities and can even result in wrong features in the absorption spectra.
- A good calculation of the final states : in order to get the right absorption rates, one also need to have a good description of the final states, *i.e.* the Mn  $d$  band. This also includes a proper calculation of the Fermi level.

### 5.4.2 The $\text{Ge}_3\text{Mn}_5$ structure : a benchmark

As stated earlier, the  $\text{Ge}_3\text{Mn}_5$  structure is a stable phase in the (Ge,Mn) binary phase diagram. This phase is already well-known and numerous experimental results are available in the litterature [69, 169–171]. In particular, the XMCD spectra measured in  $\text{Ge}_3\text{Mn}_5$  samples look very similar to those observed in the GeMn nanocolumns. Therefore, we have used this structure as a benchmark for our calculations.

#### 5.4.2.1 Structural and magnetic properties of the $\text{Ge}_3\text{Mn}_5$ phase

The structural properties of the  $\text{Ge}_3\text{Mn}_5$  alloy are recalled in table 5.2 and the  $\text{Ge}_3\text{Mn}_5$  crystalline structure is illustrated in fig. 5.24. The magnetic properties are presented further, along with our results (see section 5.4.2.5)

TABLE 5.2: Structural parameters of the  $\text{Ge}_3\text{Mn}_5$  crystalline phase [69, 170].

Crystal system	Hexagonal
Space group	#193 $P6_3/mcm$
Lattice parameters	$a = b = 7.184 \text{ \AA}$ , $c = 5.053 \text{ \AA}$ $\alpha = \beta = 90^\circ$ , $\gamma = 120^\circ$
Mn1 positions	4(d) sites : $\pm(\frac{1}{3}, \frac{2}{3}, 0)$ ; $\pm(\frac{2}{3}, \frac{1}{3}, \frac{1}{2})$
Mn2 positions	6(g) sites : $\pm(x, 0, \frac{1}{4})$ ; $\pm(0, x, \frac{1}{4})$ ; $\pm(-x, -x, \frac{1}{4})$ with $x = 0.2397$
Ge positions	6(g) sites : $\pm(x, 0, \frac{1}{4})$ ; $\pm(0, x, \frac{1}{4})$ ; $\pm(-x, -x, \frac{1}{4})$ with $x = 0.6030$

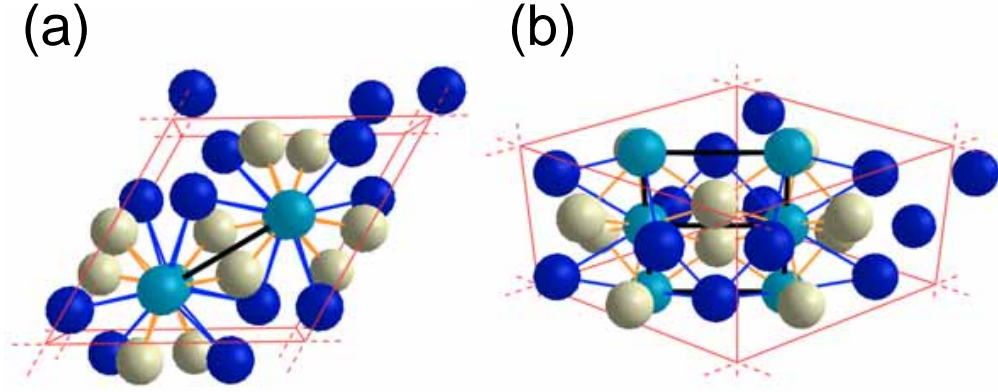


FIGURE 5.24: Balls and sticks representation of the Unit cell of the  $\text{Ge}_3\text{Mn}_5$  crystalline structure viewed (a) along the  $[001]$  direction and (b) along the  $[111]$  direction. The representation is consistent with that used in reference [97] : the Ge atoms (6) are the grey spheres, the  $\text{Mn}_1$  atoms (4) are pale blue and the  $\text{Mn}_2$  atoms (6) are dark blue.

#### 5.4.2.2 Calculation details

The calculation of the XAS-XMCD spectra for the  $\text{Ge}_3\text{Mn}_5$  crystalline structure was performed using the SPRKKR program package. Calculations were carried out within the density functional theory framework with the atomic sphere approximation (ASA), using the Von Barth-Hedin parametrization of the exchange-correlation potential, though similar results were obtained using the Vosko-Wilk-Nusair parametrization. Maximum size muffin tin radii (RMT) of 2.35 a.u. were used for both Ge and Mn atoms. Convergence was considered as achieved upon

deviation of the total energy of less than  $1 \times 10^{-5}$  Ry between two consecutive iterations on a k-mesh of up to  $16 \times 16 \times 20$ .

#### 5.4.2.3 Total and Mn-projected densities of states

Figure 5.25(a) shows the calculated total density of states (DOS) as well as its components projected on the Mn<sub>1</sub> and Mn<sub>2</sub> 3*d* states. The metallic character of Ge<sub>3</sub>Mn<sub>5</sub>, already mentionned in section 5.1.2, is confirmed here. The largest contribution near the Fermi level comes from the Mn *d* states. The majority states are almost completely filled at the Fermi level and most of the vacant Mn *d* states are in the minority channel. Mn<sub>1</sub> and Mn<sub>2</sub> have sensibly similar PDOS, the difference in intensity comes from the difference in stoichiometry ( $4 \times \text{Mn}_1$  vs  $6 \times \text{Mn}_2$ ). These results are consistent with those obtained by Picozzi *et al.*[171] and one can already see that the absorption properties will be dominated by the minority channel.

Integrating the total density of states up to the Fermi energy for all atoms in the unit cell gives a total of 93.4 electrons, very close to the expected value of 94.0 electrons<sup>3</sup> (fig.5.26). In particular, we obtain the number of 3*d* holes for each type of Mn using :

$$N_h^{3d} = 10 - \int_{-\infty}^{E_F} PDOS_{Mn_i}^{3d}(E) dE \quad (5.6)$$

where  $PDOS_{Mn_i}^{3d}(E)$  is the projected density of states on the 3*d* states of Mn<sub>*i*</sub> (*i*=1,2). The integral is illustrated in figure 5.26. We obtained a total of 4.3 holes in the *d* band for both Mn<sub>1</sub> and Mn<sub>2</sub>.

We note that the total number of states  $\int_{-\infty}^{+\infty} DOS(E) dE$  (fig.5.26) is smaller than expected : 149 valence electrons per unit cell, instead of 168, *i.e.* a deficit of 1.19 valence electron per atom on average. This is also observed in particular for the Mn *d* states : the total number of states are 8.72 and 8.80 for Mn<sub>1</sub> and Mn<sub>2</sub> respectively (fig.5.26). This shows that even by using maximum size RMTs for touching spheres, some states are still in the interstitial region and not described within the atomic spheres.

---

3. 4 valence electrons per Ge atom  $\times$  6 Ge atoms per unit cell + 7 valence electrons per Mn atom  $\times$  10 Mn atoms per unit cell = 94 electrons per unit cell



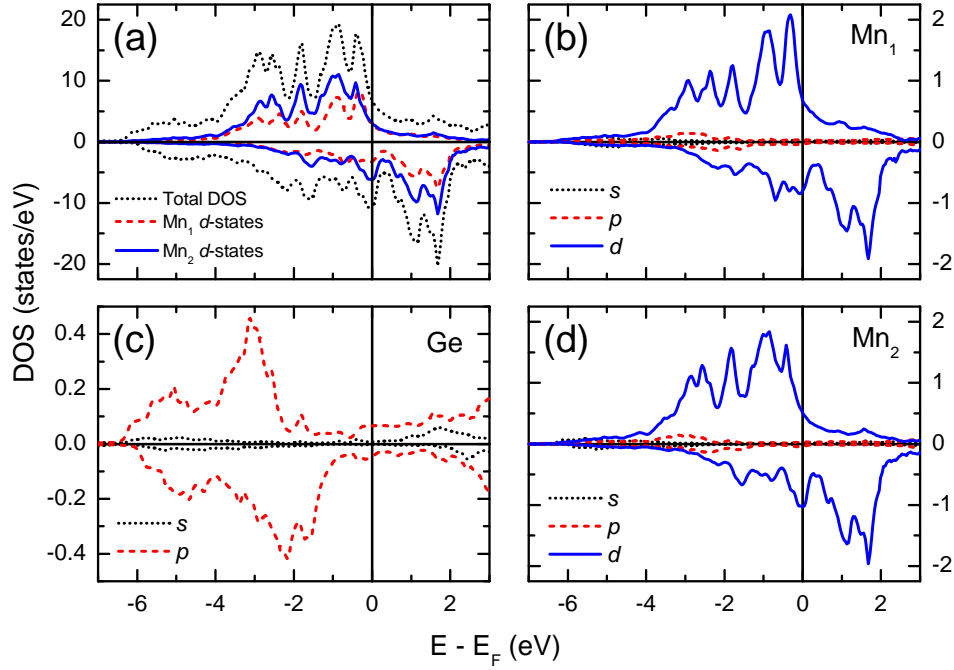


FIGURE 5.25: (a) Total density of states (dotted black line) and  $3d$  projected density of states for  $\text{Mn}_1$  (dashed red line) and  $\text{Mn}_2$  (solid blue line). (b)  $\text{Mn}_1$ , (c) Ge, and (d)  $\text{Mn}_2$   $s$ - (dotted black line),  $p$ - (dashed red line) and  $d$ - (solid blue line) PDOS. Curves corresponding to the majority (minority) spins are plotted along the positive (negative)  $y$ -axis. Units for the DOS are unit cell-wise in (a) and atom-wise in (b-d). The energy is given relative to the Fermi energy (indicated by a vertical black line).

#### 5.4.2.4 Absorption spectra : experiment *vs* theory

The absorption spectra for the  $\text{Ge}_3\text{Mn}_5$  structure were calculated using the program KKRGEN of the SPR-KKR package. This program outputs the absorption spectra for each of the six individual core-level (2 in  $2p_{1/2}$  and 4 in  $2p_{3/2}$ ) and for three polarizations (linear along  $z$ , circular left and circular right) for each of the Mn atom ( $\text{Mn}_1$  and  $\text{Mn}_2$ ). The corresponding spectra (for circularly polarized light) are plotted in figure 5.27 for  $\text{Mn}_1$ .

These individual spectra can then be summed over to obtain the total absorption spectra, which can in turn be convoluted with a broadening function to account for the core-level life-time, the experimental energy resolution and other experimental effects. The core-level life-time is well-known and can be modelled as Lorentzian

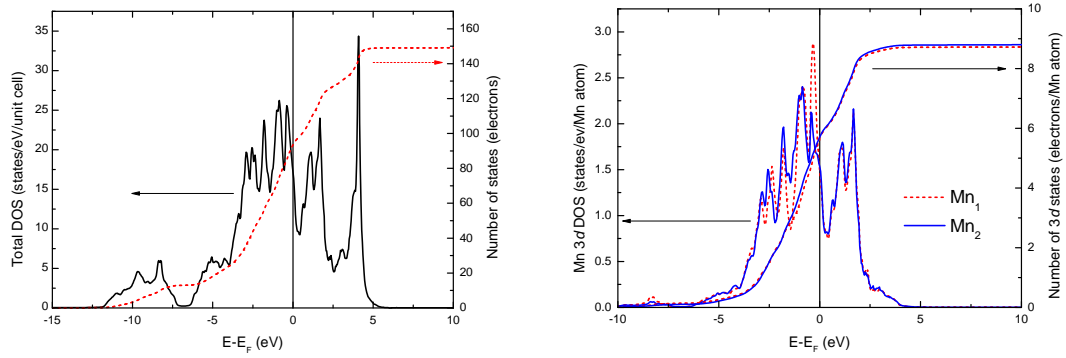


FIGURE 5.26: (*left*) Total DOS (spins up + spins down) (solid black line, left scale) and total number of valence states (dashed red line, right scale) per unit cell. (*right*) Total PDOS $_{Mn}^{3d}$  (spins up + spins down, left scale), as well as the total number of 3d states (right scale) for Mn $_1$  (dashed red line) and Mn $_2$  (solid blue line). The energy is given relative to the Fermi energy (indicated by a vertical black line).

function with FWHM = 0.34 and 0.32 eV at the Mn  $L_3$  and  $L_2$  edges respectively [172]. The typical energy resolution on a XAS-XMCD beamline is on the order of  $\Delta E/E = 10^{-4}$ , i.e. resulting in a Gaussian broadening of 0.6 to 0.7 eV at the Mn  $L_{2,3}$  absorption edges. To account for the broadening due to these effects (and possible others), different authors have used different types of functions to be convolved with the calculated spectra, *e.g.* Voigt functions (convolution of a Gaussian and Lorentzian)[173] or pure Lorentzian with FWHM ranging from 0.7 [171] to 1.0 eV [174]. In our case, we have used pure Gaussian functions. In all cases the best agreement was found for  $\sigma = 1.0$  eV.

The resulting spectra are plotted in figure 5.28, along the direct output of the KKRGEN program and experimental results digitized from the literature [69]. Some variance may be found in the reported XAS-XMCD spectra for Ge $_3$ Mn $_5$  [69, 157], but they consist mostly in small variations in the relative intensity of the XMCD features. One can see in figure 5.28 that the calculation reproduces quite well the experimental XAS and XMCD spectra : the number, the width (in particular for the manually-convoluted calculated spectra) and the relative amplitudes and positions in energy are reproduced. The main difference comes from the shape of the white lines at the  $L_3$  and  $L_2$  edges : in the experimental spectra, they are quite asymmetric and broader on the high energy side, whereas in the calculated spectra they are more symmetric.

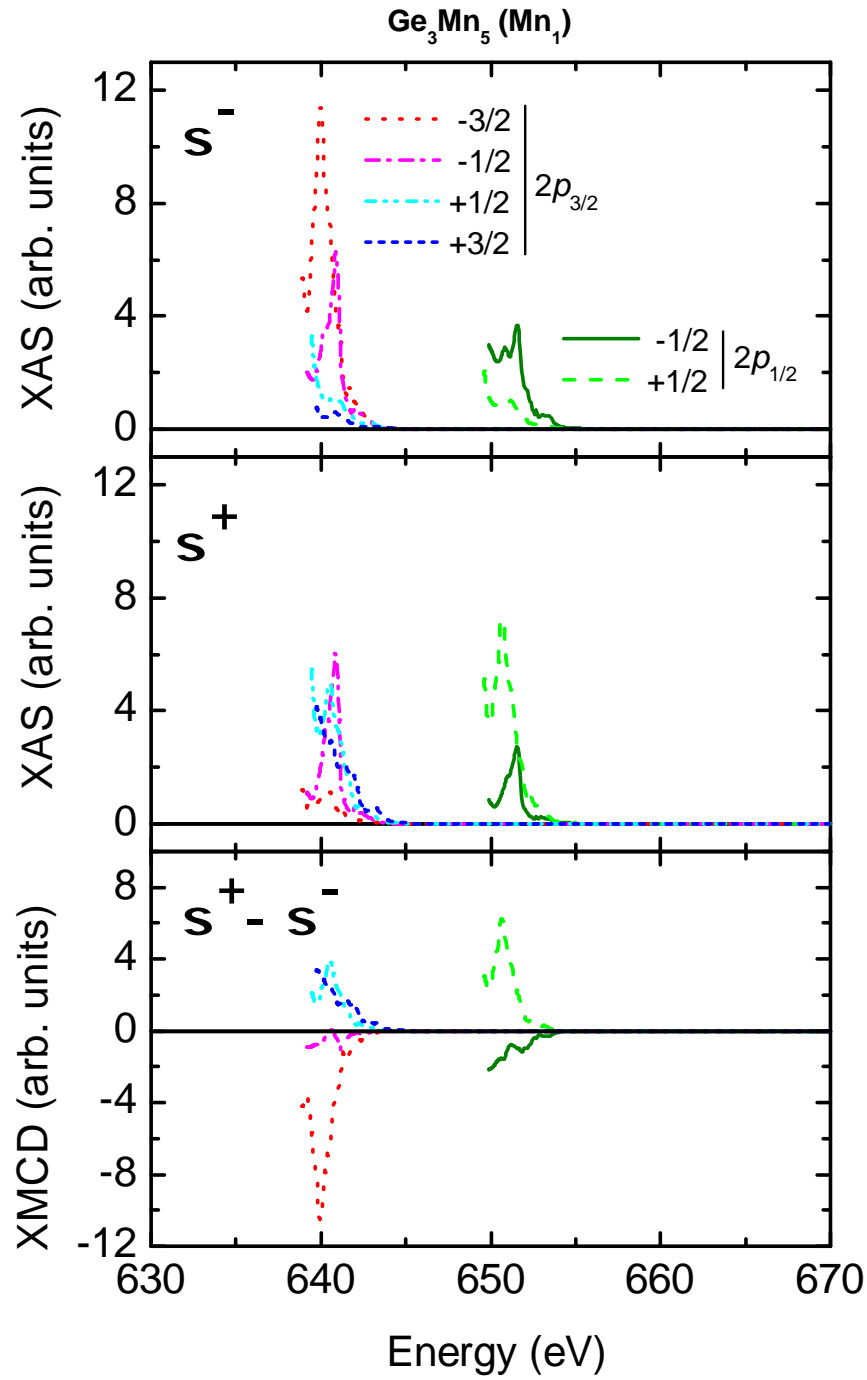


FIGURE 5.27: Absorption spectra for each individual core-level in Mn<sub>1</sub> in Ge<sub>3</sub>Mn<sub>5</sub> and the corresponding differences.

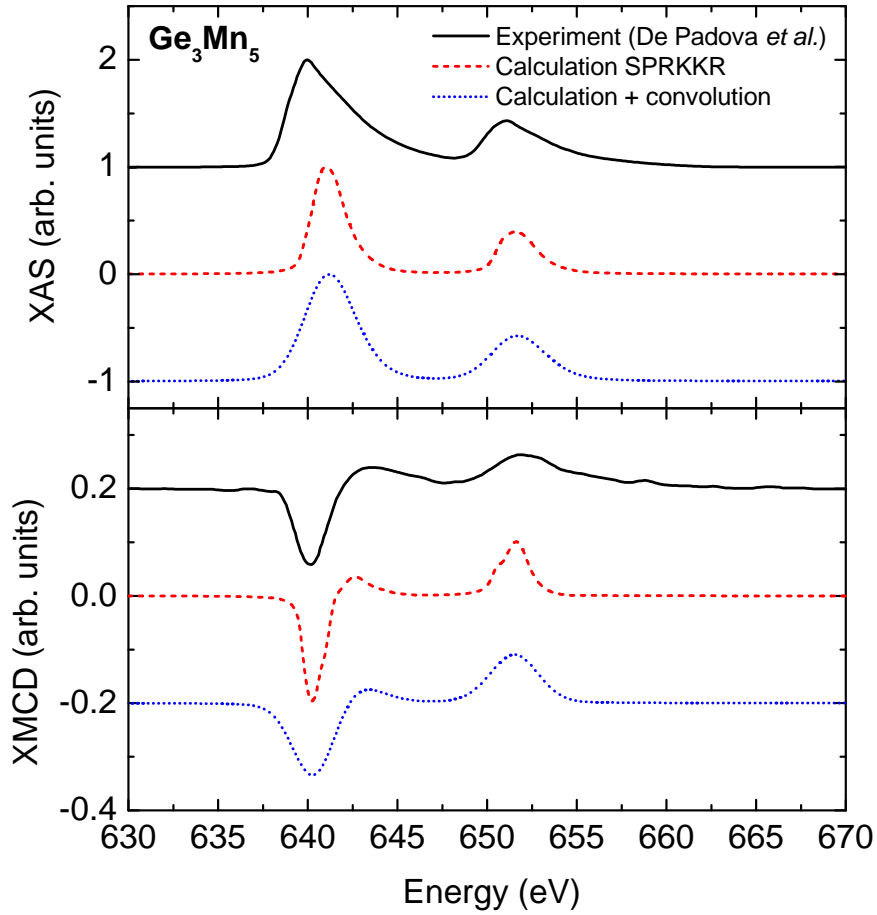


FIGURE 5.28: XAS (top) and XMCD (bottom) spectra in  $\text{Ge}_3\text{Mn}_5$ , as measured experimentally [69] (solid black line), result of the direct SPRKKR calculation (dashed red line) and results from the manually convoluted sum of the spectra corresponding to the individual core-levels (dotted blue line). The function used for the convolution in the latter case was a gaussian function with  $\sigma = 1$  eV.

For clarity, spectra have been shifted vertically.

#### 5.4.2.5 Quantitative analysis of the magnetic moments

The self-consistent calculation of the  $\text{Ge}_3\text{Mn}_5$  systems yields magnetic moments similar to those reported in previous experiments or calculations, as indicated in table 5.3. It appears that the magnetic moments calculated with SPRKKR are greater than those obtained in other *ab initio* calculations by about  $0.13 \mu_B$  in the case of  $\text{Mn}_1$ , and smaller by about  $0.55 \mu_B$  in the case of  $\text{Mn}_2$ . As a result, the SPRKKR-calculated total magnetic moment is smaller by about  $0.25 \mu_B/\text{Mn}$ .

TABLE 5.3: Calculated and measured magnetic moments for the  $\text{Ge}_3\text{Mn}_5$  phase. All results are given in units of  $\mu_B/\text{Mn}$ .

Reference	Method	Mn <sub>1</sub>	Mn <sub>2</sub>	Total
This work	SPRKKR	2.25	2.59	2.36
This work	KKRGEN+SR	1.76	1.66	1.70
[171]	FLAPW+GGA	2.12	3.16	2.59
[171]	FLAPW+GGA+SR	1.9	2.4	2.2
[175]	SPR-TB-KKR+ABINIT	2.11	3.11	2.63
[169]	Extraction	-	-	2.60
[170]	Neutron scattering	-	-	2.72
[69]	SQUID, exp. SR	-	-	2.6, 2.34

This discrepancy is probably due to the use of the local spin density approximation (LSDA) in our calculation, which is known to produce slightly higher and lower magnetic moment on the Mn<sub>1</sub> and Mn<sub>2</sub> respectively [171]. Furthermore, results from other reported *ab initio* calculations appear to be closer to the known experimental values. It can also be seen that when applying the sum rules to the theoretical spectra, the magnetic moments are systematically underestimated. This particular point will be discussed in more details further, along with the results in other structures.

#### 5.4.2.6 Conclusion

The *ab initio* study of the  $\text{Ge}_3\text{Mn}_5$  structure gives interesting results that can be summarized as follow :

- The SPRKKR calculated magnetic moments appear somewhat smaller than expected on average
- Using this method in a known system can yield a remarkable agreement between experimental and calculated XAS-XMCD spectra
- Moments extracted from the sum rules appear systematically lower than those calculated self-consistently (by a factor of  $\sim 0.72$  in our case), which is consistent with previous studies [153, 160].

The major conclusion from this study is that our mixed experimental and theoretical analysis is a possible route towards a deeper understanding of the experimental XAS-XMCD spectra in the GeMn nanocolumns. Hence, further insights with regards to the magnetic, electronic and crystalline structures in the nanocolumns may be obtained.

Now, we shall be interested in the results in the GeMn nanocolumns and proceed with the inspection of other suggested structures.

### 5.4.3 Simple defects

We have considered at first the most common simple defects in the Ge diamond lattice, *i.e.* the substitutional ( $\text{Mn}_S$ ) and the tetrahedral interstitial ( $\text{Mn}_T$ ). Two reasons can justify such a choice : firstly, previous results by Devillers *et al.* [96] tended to suggest that the GeMn nanocolumns might be formed by aggregations of such simple defects that would retain the average diamond crystalline structure. Diffraction results also argued in that way, as no clear crystalline contribution different from the diamond structure could be evidenced. Secondly, it is very likely that some Mn atoms may be located in the Ge matrix and participate in the magnetic signal. It was argued before (section 5.1.7) that their contribution to the overall magnetic signal should be rather small at sufficiently high temperatures. However, since we also have data at low temperatures (5 K), it is worth considering their theoretical XAS-XMCD spectroscopic characteristics.

#### 5.4.3.1 Structural properties of the Ge crystalline phase with simple defects

The corresponding unit cells used in the calculations are represented in figure 5.29. In both cases we considered the average Ge crystalline structure, as described in tabel 5.4. The interstitial and the substitutional cases correspond to a Mn atomic concentration of 11.1% and 12.5% respectively. Such values correspond to the overall Mn concentration in the considered samples. Note that the local concentration in the nanocolumns should be about 3 times higher, *i.e.* with 3 to 4 Mn atoms per unit cell. In this case, one would also have to take into account all the possible arrangement of the Mn atoms in the unit cell and average the different results. The cost in formation energy may be smaller than the mere addition of

the individual formation energy of each defect when considering special atomic arrangements, as shown by Arras *et al.* [97] and Continenza *et al.* [32], but it remains relatively high (more than 300 meV/atom). As a result, we decided to start with so-called simple defects structures<sup>4</sup> before moving on to more complex structures. Note that simple defects may also be used to describe the Mn atoms diluted in the matrix.

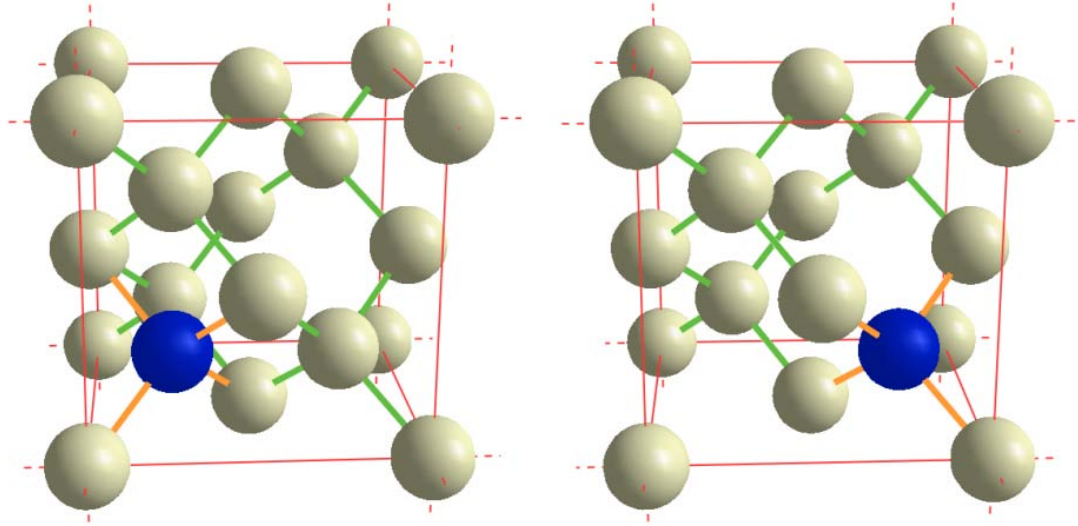


FIGURE 5.29: Balls and sticks representation of the unit cell in the case of a tetrahedral interstitial (left) and of a substitutional Mn (right) in the Ge diamond crystalline structure. Ge atoms are the grey spheres and Mn atoms are the dark blue spheres; Mn-Ge bonds are orange and Ge-Ge bonds are green.

#### 5.4.3.2 Calculation details

We used the same calculation procedure as described earlier for the  $\text{Ge}_3\text{Mn}_5$  crystalline structure (section 5.4.2.2). We used the maximum RMT for touching spheres, *i.e.* 2.32 a.u. in both interstitial and substitutional cases. The Ge diamond crystalline structure has a very small compacity<sup>5</sup> : 0.34 and 0.38, considering the interstitial and the substitutional case respectively, as opposed to 0.57 in the case of  $\text{Ge}_3\text{Mn}_5$ . Therefore, we had to introduce empty spheres to reduce the interstitial volume between the atomic spheres and take into account the interstitials electrons. The positions of the empty spheres (ES) are indicated in table 5.4. They

4. Some complementary results in these simple defect structures are already available in the literature [30, 32, 176–178].

5. The compacity is the ratio of the volume of the atomic spheres to the total volume of the unit cell.

TABLE 5.4: Structural parameters of the Ge diamond crystalline phase with simple defects.

Crystal system	Cubic
Space group	$\#227 Fd\bar{3}m$
Lattice parameters	$a = b = c = 5.657 \text{ \AA}$ $\alpha = \beta = \gamma = 90^\circ$
Ge positions	8(a) sites : $(0, 0, 0); (0, \frac{1}{2}, \frac{1}{2}); (\frac{1}{2}, 0, \frac{1}{2}); (\frac{1}{2}, \frac{1}{2}, 0);$ $(\frac{3}{4}, \frac{1}{4}, \frac{3}{4}); (\frac{3}{4}, \frac{3}{4}, \frac{1}{4}); (\frac{1}{4}, \frac{1}{4}, \frac{1}{4}); (\frac{1}{4}, \frac{3}{4}, \frac{3}{4})$
Mn <sub>S</sub> positions	one of the 8(a) sites : $(0, 0, 0); (0, \frac{1}{2}, \frac{1}{2}); (\frac{1}{2}, 0, \frac{1}{2}); (\frac{1}{2}, \frac{1}{2}, 0);$ $(\frac{3}{4}, \frac{1}{4}, \frac{3}{4}); (\frac{3}{4}, \frac{3}{4}, \frac{1}{4}); (\frac{1}{4}, \frac{1}{4}, \frac{1}{4}); (\frac{1}{4}, \frac{3}{4}, \frac{3}{4})$
Mn <sub>T</sub> positions	one of the 8(b) sites : $(\frac{1}{2}, \frac{1}{2}, \frac{1}{2}); (\frac{1}{2}, 0, 0); (0, \frac{1}{2}, 0); (0, 0, \frac{1}{2});$ $(\frac{1}{4}, \frac{3}{4}, \frac{1}{4}); (\frac{1}{4}, \frac{1}{4}, \frac{3}{4}); (\frac{3}{4}, \frac{3}{4}, \frac{3}{4}); (\frac{3}{4}, \frac{1}{4}, \frac{1}{4})$
Empty spheres positions	all unoccupied 8(b) sites : $(\frac{1}{2}, \frac{1}{2}, \frac{1}{2}); (\frac{1}{2}, 0, 0); (0, \frac{1}{2}, 0); (0, 0, \frac{1}{2});$ $(\frac{1}{4}, \frac{3}{4}, \frac{1}{4}); (\frac{1}{4}, \frac{1}{4}, \frac{3}{4}); (\frac{3}{4}, \frac{3}{4}, \frac{3}{4}); (\frac{3}{4}, \frac{1}{4}, \frac{1}{4})$

were a total of 8 ES in the substitutional case, and 7 ES in the interstitial one, bringing the compacity to 0.68 in both cases. The same RMT for the ES as for the Mn and Ge atoms were used. A k-mesh of up to  $16 \times 16 \times 16$  was considered.

#### 5.4.3.3 Total and Mn-projected densities of states

The resulting densities of states are plotted in figure 5.30 in the case of the interstitial defect and in figure 5.31 and in the case of the substitutional defect. In a similar fashion to the Ge<sub>3</sub>Mn<sub>5</sub> structure, in both interstitial and substitutional cases, the electronic states near the Fermi level are mostly of Mn 3*d* character. The spin up Mn 3*d* states are almost completely filled whereas most of the spin down states lay vacant just above the Fermi level. Contribution of the Mn *s* and *p* states near the Fermi level are very weak. The overall shape of the DOS, as well as the particular features related to the Mn atoms are in agreement with previously



published results using the more precise full-potential linearized augmented plane wave (FLPAW) method [176, 178].

Looking at the integrated PDOS $_{Mn}^{3d}$ , we find a total number of 5.8 electrons in the case of the interstitial Mn and 5.4 electrons in the case of the substitutional Mn. A very small deficit in Mn  $d$  states can be observed, as the PDOS $_{Mn}^{3d}$  for Mn $_T$  and Mn $_S$  reach the value of 9.83 and 9.96 electrons respectively. It is also worth mentioning that a particular feature appears in the Mn  $p$ -projected DOS : for energies higher than 10.2 eV and 11.3 eV above the Fermi level for Mn $_T$  and Mn $_S$  respectively, the PDOS $_{Mn}^p$  changes sign. This is obviously a artifact of the calculation. It should not really affect further analysis and in particular the XAS-XMCD calculation because the transition selection rules only allows transition with  $\Delta l = \pm 1$ , so these  $p$  states are transparent to the absorption.

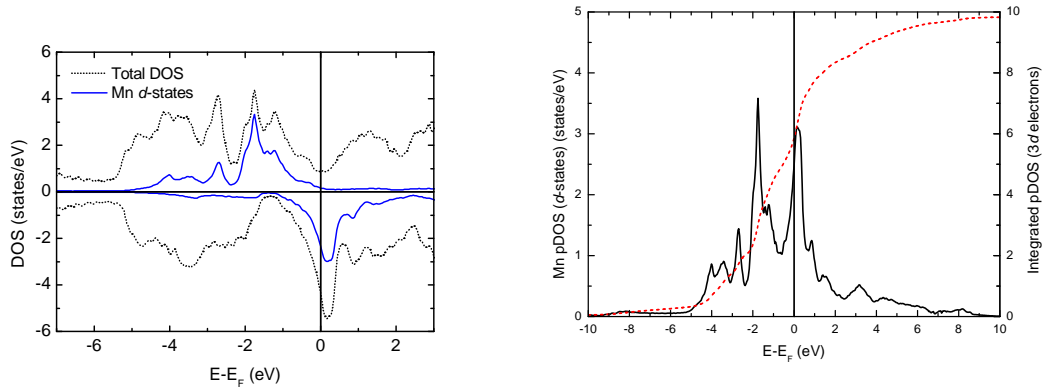


FIGURE 5.30: (left) Total DOS in the case of a tetrahedral interstitial Mn atom (solid black line) and Mn  $3d$ -projected DOS (dashed red line). Curves corresponding to the majority (minority) spins are plotted along the positive (negative)  $y$ -axis. (right) Total PDOS $_{Mn}^{3d}$  (spins up + spins down) (solid black line, left scale), as well as the total number of  $3d$  states (dashed red line, right scale).

#### 5.4.3.4 Absorption spectra : experiment *vs* theory

In the same fashion as described before, the XAS and XMCD spectra were calculated using KKRGEN. The calculated individual core-level spectra were summed up and convoluted with a Gaussian function of  $\sigma = 1.0$  eV. The corresponding spectra are plotted in figure 5.32 for the tetrahedral interstitial Mn and in figure 5.33 for the substitutional Mn, along with our experimental results in the GeMn nanocolumns.

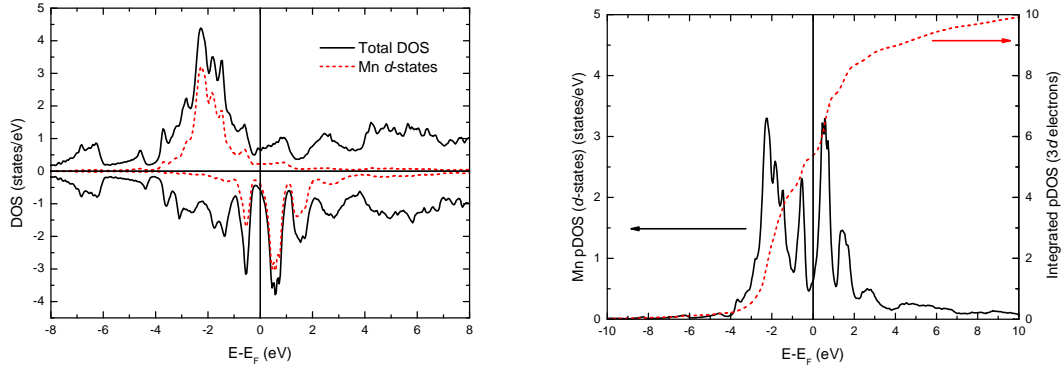


FIGURE 5.31: (left) Total DOS in the case of a substitutional Mn atom (solid black line) and Mn 3d-projected DOS (dashed red line). Curves corresponding to the majority (minority) spins are plotted along the positive (negative)  $y$ -axis. (right) Total  $\text{PDOS}_{Mn}^{3d}$  (spins up + spins down) (solid black line, left scale), as well as the total number of 3d states (dashed red line, right scale).

We observe that the absorption spectra are quite well reproduced : in both  $\text{Mn}_T$  and  $\text{Mn}_S$  cases, only two single peaks are seen at the Mn  $L_{2,3}$  absorption edges. The peaks are rather broad and in particular in the case of  $\text{Mn}_T$  (fig.5.32), they show a very similar asymmetry between the low and high energy side. In both cases, there is an overlap between the two absorption edges, similarly to the experimental results. For this reason, we calculated the branching ratio as described in section 5.1.2. Values of 0.69 and 0.68 are found for the  $\text{Mn}_T$  and the  $\text{Mn}_S$  case respectively, very close to the measured value of 0.67 and in agreement with the statistical value of  $2/3$ . The spin-orbit coupling in the  $2p$  states, measured as the energy spacing between the two absorption maxima, are found to be 10.6 and 10.4 eV for the  $\text{Mn}_T$  and the  $\text{Mn}_S$  case respectively. These values are slightly smaller than the measured value of 10.8 eV. Up to this point, only the qualitative argument of the lineshape provides better support for the interstitial case.

However, in both interstitial and substitutional cases, the dichroism spectra (bottom panels in fig.5.32 and fig.5.33) are in qualitative and quantitative disagreement. Firstly, the most striking point is the difference in amplitude in XMCD at the Mn  $L_3$  edge : it is much more intense in the case of the simple defects by a factor of 2.8 ( $\text{Mn}_T$ ) to 2.5 ( $\text{Mn}_S$ ). This is not completely unexpected, as magnetic moments are known to be on the order of  $3 \mu_B$  for these simple defects in germanium (the actual values will be discussed in more details in the next section). Such values are more than three times larger than the extracted moments from

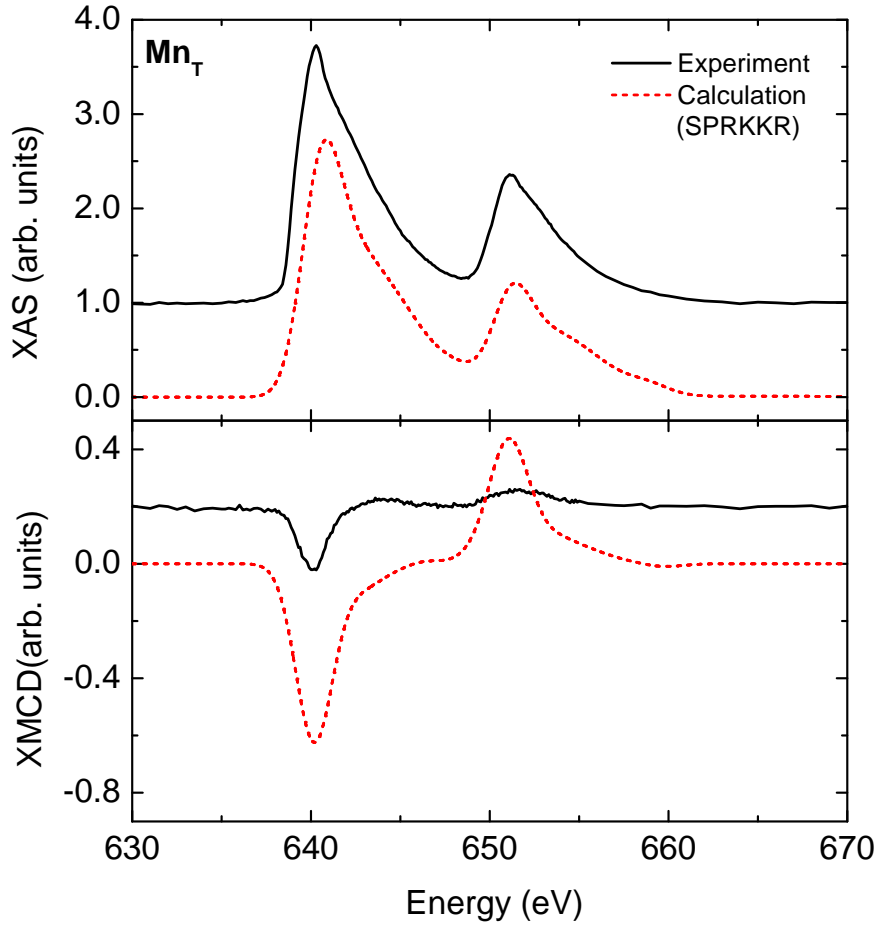


FIGURE 5.32: XAS (top) and XMCD (bottom) spectra in the GeMn nanocolumns samples, as measured experimentally (solid black line) and the result of the SPRKKR calculation for Ge with a  $\text{Mn}_T$  defect (dashed red line). For clarity, spectra have been shifted vertically.

the sum rules in our experimental results, and according to the same sum rules, larger XMCD signal at the  $L_3$  edge are correlated to larger magnetic signals. The calculated and measured ratio of the XMCD at the  $L_3$  and  $L_2$  edges are also very different. For example, if we consider the ratio of the maxima at the XMCD  $L_3$  and  $L_2$  edges, we obtain values of 1.2 and 1.4 for  $\text{Mn}_T$  and  $\text{Mn}_S$  respectively, as opposed to 3.7 in the experiment.<sup>6</sup> Finally, it can be seen that the small positive

6. One may again want to consider integrated intensities to take into account all the features in the spectra. If one considers the ratio of the amplitude integrated below 648.1 eV ( $L_3$  edge) to that integrated above 648.1 eV ( $L_2$  edge), one finds the following values : -1.17 and -1.05 for  $\text{Mn}_T$  and  $\text{Mn}_S$  respectively, and -1.67 for the experiment. The difference is not as obvious but can still be told.

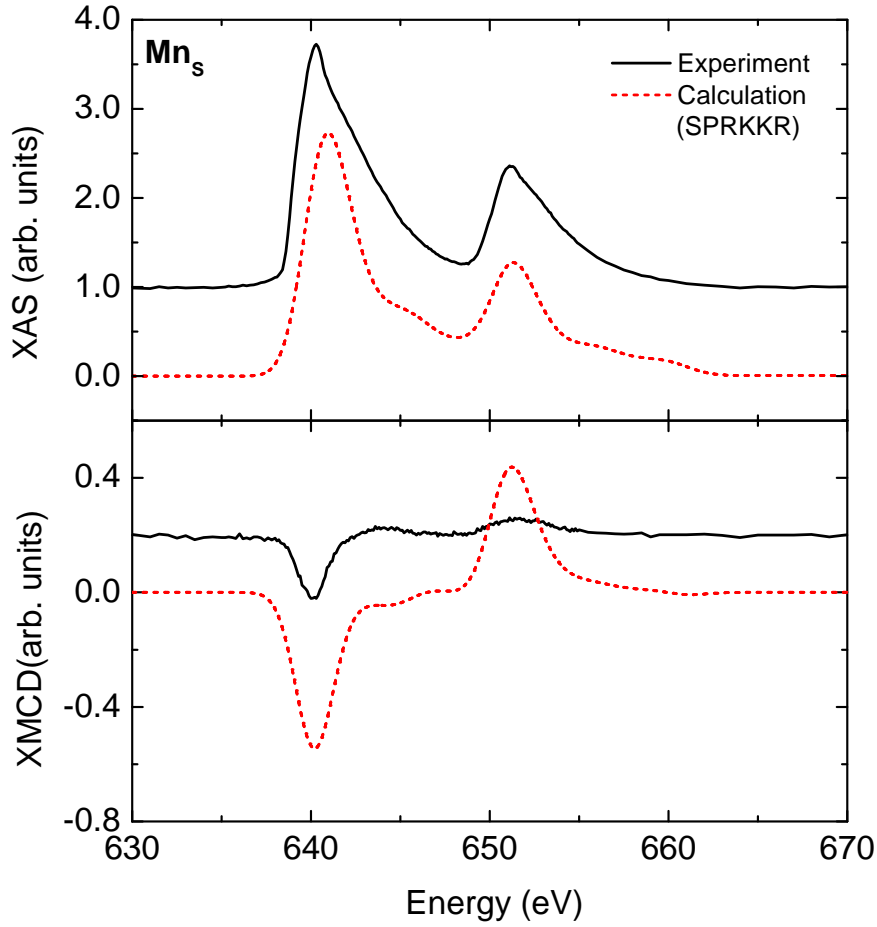


FIGURE 5.33: XAS (top) and XMCD (bottom) spectra in the GeMn nanocolumns samples, as measured experimentally (solid black line) and the result of the SPRKKR calculation for Ge with a  $\text{Mn}_S$  defect (dashed red line). For clarity, spectra have been shifted vertically.

hump on the high energy side of the XMCD  $L_3$  edge is not reproduced in the  $\text{Mn}_T$  nor in the  $\text{Mn}_S$  cases, whereas it was very clear for  $\text{Ge}_3\text{Mn}_5$ .

#### 5.4.3.5 Quantitative analysis of the magnetic moments

Even though the XAS-XMCD analysis seems to rule out the simple tetrahedral interstitial or substitution Mn defects in germanium, it is worth having a deeper look in the magnetic properties. Table 5.5 summarizes our results in terms of magnetic moments, as well as others that can be found in the litterature.

TABLE 5.5: Calculated magnetic moments for the Mn interstitial and substitutional defect in germanium. All results are given in units of  $\mu_B/\text{Mn}$ . The first result is the moment on the Mn atom, the result between parenthesis is the total moment in the unit cell per Mn atom.

Reference	Method	$\text{Mn}_T$	$\text{Mn}_S$
This work	SPRKKR	2.87 (3.18)	3.15 (2.87)
This work	KKRGEN+SR	2.08 (-)	2.25 (-)
[32]	FLAPW+LSDA	2.83 (3.22)	2.78 (3.00)
[32]	FLAPW+GGA	2.95 (3.20)	2.95 (3.00)
[178]	FLAPW+GGA		3.22 (3.00)

It appears that our SPRKKR results are in good agreement with the previously reported results, in particular in the case of the interstitial Mn. In the case of the substitutional Mn we obtained a slightly larger moment than with other LSDA-based calculations [32]. However the value is similar to those obtained in the generalized gradient approximation of the exchange-correlation potential. In particular we find a small negative magnetic polarisation ( $-0.09 \mu_B$ ) of the Ge atoms nearest to the Mn atom, which has also been reported by Titov using FLAPW calculations [178].

We also observed that sum rule derived values of the magnetic moment on the Mn atom are underestimated by about 30 % in both  $\text{Mn}_T$  and  $\text{Mn}_S$  cases, similarly to what was observed in the case of  $\text{Ge}_3\text{Mn}_5$  (section 5.4.2.5 and reported by others [153, 160]).

#### 5.4.3.6 Conclusion

The results obtained in the study of the simple tetrahedral interstitial and substitutional Mn defects in a germanium matrix can be summarized as follow :

- The SPRKKR calculated magnetic moments are in good agreement with other calculations, they appear quite similar on the  $\text{Mn}_T$  and the  $\text{Mn}_S$  atoms (around  $3 \mu_B$ ), while the total magnetic moment in the unit cell is slightly larger in the case of the interstitial defect. Note we have considered concentration of more than 10% and allowed for Mn  $3d$  hybridization. In the case of *isolated* interstitial defects, the theoretical moment on the Mn atoms should be equal to the ionic case, *i.e.*  $5 \mu_B$  (it should not change for  $\text{Mn}_S$  and stay at  $3 \mu_B$ ) [179].

- The calculated XAS spectra are quite in good agreement with the experimental results, in particular for the  $\text{Mn}_T$ . However, XMCD spectra are in strong disagreement with experimental data.
- Moments extracted from the sum rules appear systematically lower than those calculated self-consistently (by a factor of  $\sim 0.73$  and  $0.71$  for  $\text{Mn}_T$  and  $\text{Mn}_S$  respectively), which is consistent with previous studies [153, 160].

It appears that no reasonable agreement can be obtained with our experimental results by considering simple interstitial and substitutional defects. Even if non-magnetic Mn atoms were to contribute to the measured XAS signal and thus reduce the overall relative amplitude of the XMCD, the lineshapes of the calculated XMCD spectra would still differ from that of the measured XMCD spectrum. In particular an experimentally observed positive hump on the high energy side of the XMCD  $L_3$  edge (around 644 eV) is not reproduced in the calculations. Therefore, one need to consider different structures to account for the observed XAS-XMCD spectra.

#### 5.4.4 Crystalline phases

Among the different structures proposed by Arras *et al.* [89, 97], three main crystalline phases were considered based on different criteria : (i) their stoichiometry (close to  $\text{Ge}_2\text{Mn}$ ), (ii) their low energy of formation or (iii) their magnetic moment per Mn atom (on the order of  $1 \mu_B/\text{Mn}$ ). Namely, we considered :

- The **Hex** phase : this phase was built from the  $\text{Ge}_3\text{Mn}_5$  unit cell, considering only Ge and  $\text{Mn}_1$  atoms. In particular we investigated the Hex2 phase, which contains two Mn atoms.
- The **C<sub>16</sub>** phase : this phase has been described in a recent paper by Arras *et al.*[89]. This structure has already been observed in the case of  $\text{Ge}_2\text{Fe}$  by Regan *et al.*[180], who reported nanoscale phase separation in this system. Its name comes from the *Strukturbereich* notation.
- The  **$\alpha$**  phase : this phase was proposed by Arras and extensively studied in his thesis [97] and is named after the  $\text{FeSi}_2$   $\alpha$  phase from which it inherits its structure. This phase is very interesting from the point of view of its integration in germanium diamond, as described hereafter.

#### 5.4.4.1 Structural properties of the GeMn crystalline phases

The different unit cells corresponding to the crystalline structures introduced in the previous section are represented in figure 5.34 and the corresponding structural parameters are given in table 5.6.

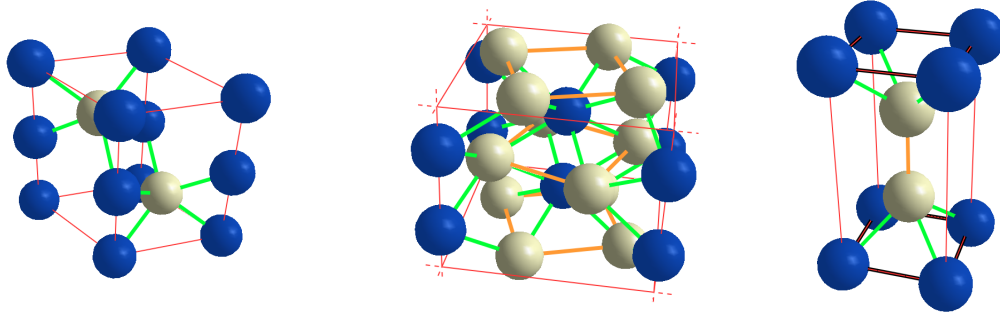


FIGURE 5.34: Balls and sticks representation of the unit cell for (left) the Hex2 phase, (middle) the C16 phase and (right) the  $\alpha$  phase. Ge atoms are the grey spheres and Mn atoms are the dark blue spheres; Mn-Ge bonds are orange, Mn-Mn bonds are black and Ge-Ge bonds are green.

The Hex2 phase has the particularity to be hexagonal. It is then expected to orient its  $[001]$  direction parallel to the  $\langle 111 \rangle$  orientation of the Ge diamond. In that case, its projection along the  $[001]_{Ge}$  is similar to that of the germanium, making it compatible with high-resolution TEM measurements. This structure contains 2 Mn atoms and 2 Ge atoms, *i.e.* a composition of 50% Mn. The compacity of this structure is already quite high (0.53) compared to the Ge diamond. However, since it contains only four atoms, we can make up for the unoccupied volume and use empty spheres (just like in the case of simple defects) without lengthening too much the calculation time. In this case, the presence of these 2 ES raises the compacity up to 0.62.

The C16 phase is tetragonal and, compared to the germanium diamond, it possesses lattice parameters respectively 5.7% larger in the  $(a, b)$  plane and 13% smaller in the  $c$  direction. In particular, this phase is very interesting for two reasons : it has the lowest formation energy of all the compounds studied by Arras [97] and its composition is exactly 33% Mn. There are 8 Ge atoms in the unit cell, as well as 4 Mn atoms. The structure is made up of a sequence of  $(a, b)$  planes containing only Ge or Mn. The compacity of this structure is 0.56.

The  $\alpha$  phase is made up of a pile of two cubes of simple cubic Ge, one of which is filled with a Mn atom in the middle. Hence, the transformation to go from

Ge diamond to the  $\alpha$  phase is to change the Ge in a simple cubic structure by displacing one of the Ge sublattice by  $(\frac{1}{2}, \frac{1}{2}, \frac{1}{2})$  and adding Mn atoms in half of the center of simple Ge cubes. This process is illustrated in figure 5.35. As a result of this transformation, the lattice parameter is kept constant at the Ge diamond value and only the Mn position is relaxed *ab initio* afterwards, yielding the positions indicated in table 5.6. The  $\alpha$  phase studied here is the simple building block represented in figure 5.34. It contains 33% Mn and has a compacity of 0.47. In order to perform the calculations, an ES was added at the center of the second Ge cube which raised the compacity to 0.62. Note that the last step of the process (*i.e.* the addition of Mn atoms) allows for some disorder to be taken into account by choosing which sites are filled with Mn atoms and which are left empty. In that way and using supercells, one may explore closely related compounds and in particular tune in the stoichiometry. This is very interesting because the composition of the nanocolumns is only *indirectly* measured (see refs [96, 97]). This aspect will be developed in more details in the next section.

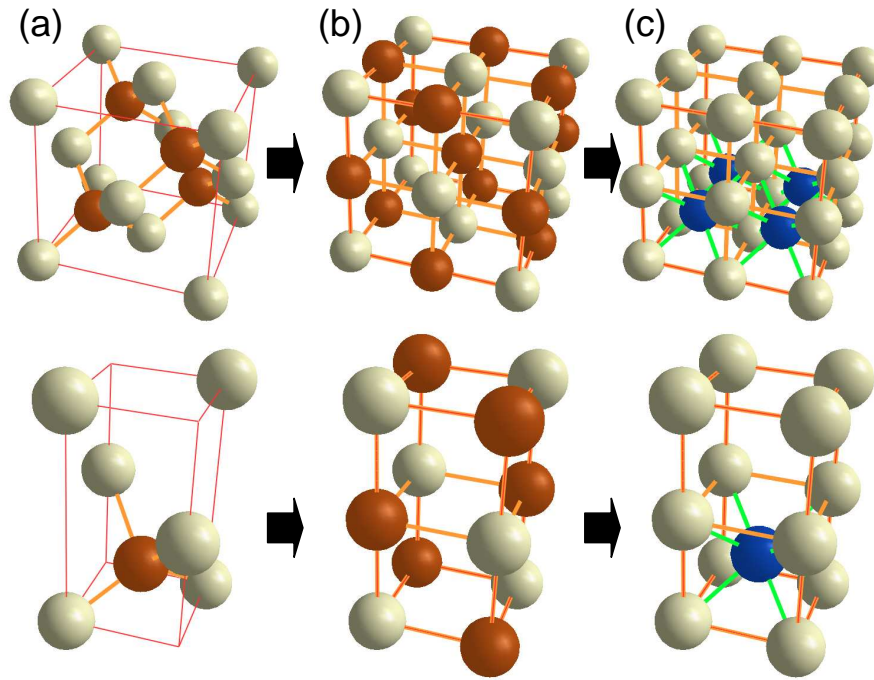


FIGURE 5.35: Construction of the  $\alpha$  structure : (top panel) one sublattice of Ge atoms (grey) is kept constant, while another one (orange) is moved by  $+(\frac{1}{2}, \frac{1}{2}, \frac{1}{2})$  (a), resulting in a new crystalline structure (b). Then Mn atoms are added at on half of the centers of the simple cubic Ge cells (c). The bottom panel display a zoom of the process on the  $\alpha$  unit cell.



TABLE 5.6: Structural parameters of the Hex2, the C16 and the  $\alpha$  crystalline phases.

<b>Hex2</b>	
Space group	#156 $P3m1$ (hexagonal)
Lattice parameters	$a = b = 3.652 \text{ \AA}$ , $c = 5.424 \text{ \AA}$ $\alpha = \beta = 90^\circ$ , $\gamma = 120^\circ$
Ge positions	1(a) site : $(0, 0, z)$ with $z = 0$ 1(b) site : $(\frac{1}{3}, \frac{2}{3}, z)$ with $z = \frac{1}{2}$
Mn positions	1(c) site ( $\text{Mn}_a$ ) : $(\frac{2}{3}, \frac{1}{3}, z)$ with $z = \frac{3}{4}$ 1(c) site ( $\text{Mn}_b$ ) : $(\frac{2}{3}, \frac{1}{3}, z)$ with $z = \frac{1}{4}$
ES positions	1(a) site : $(0, 0, z)$ with $z = \frac{1}{2}$ 1(b) site : $(\frac{1}{3}, \frac{2}{3}, z)$ with $z = 0$
<b>C16</b>	
Space group	#140 $I4/mcm$ (tetragonal)
Lattice parameters	$a = b = 5.9530 \text{ \AA}$ , $c = 5.026 \text{ \AA}$ $\alpha = \beta = \gamma = 90^\circ$
Ge positions	8(h) sites with $x = 0.157$ $(x, x + \frac{1}{2}, 0); (\bar{x}, \bar{x} + \frac{1}{2}, 0); (\bar{x} + \frac{1}{2}, x, 0); (x + \frac{1}{2}, \bar{x}, 0);$ $(x + \frac{1}{2}, x, \frac{1}{2}); (\bar{x} + \frac{1}{2}, \bar{x}, \frac{1}{2}); (\bar{x}, x + \frac{1}{2}, \frac{1}{2}); (x, \bar{x} + \frac{1}{2}, \frac{1}{2})$
Mn positions	4(a) sites : $(0, 0, \frac{1}{4}); (0, 0, \frac{3}{4}); (\frac{1}{2}, \frac{1}{2}, \frac{3}{4}); (\frac{1}{2}, \frac{1}{2}, \frac{1}{4})$
<b><math>\alpha</math></b>	
Space group	#123 $P4/mmm$ (tetragonal)
Lattice parameters	$a = b = 2.8285 \text{ \AA}$ , $c = 5.657 \text{ \AA}$ $\alpha = \beta = \gamma = 90^\circ$
Ge positions	2(h) sites with $z = 0.272$ : $(\frac{1}{2}, \frac{1}{2}, z); (\frac{1}{2}, \frac{1}{2}, \bar{z})$
Mn positions	1(a) site : $(0, 0, 0)$
ES positions	1(b) site : $(0, 0, \frac{1}{2})$

TABLE 5.7: Muffin-tin radius in atomic units used for the calculation of the Hex2, the C16 and the  $\alpha$  crystalline phases, as well as the maximum k-mesh used.

Structure	Ge	Mn	ES	k-mesh
Hex2 <sup>a</sup>	2.38	2.35	1.69	$20 \times 20 \times 12$
C16	2.37	2.37		$19 \times 19 \times 17$
$\alpha$	2.25	2.25	2.25	$23 \times 23 \times 12$

<sup>a</sup> The same RMT were used for both Mn<sub>a</sub> and Mn<sub>b</sub>

#### 5.4.4.2 Calculation details for the GeMn crystalline phases

Calculations were performed in the same fashion as described earlier. As stated in the previous section, in some cases we considered ES to help in the calculation. The different RMT used are recalled in table 5.7, along with the k-meshes.

#### 5.4.4.3 Total and Mn-projected densities of states

The DOS in the different structures (Hex2, C16,  $\alpha$ ) as well as their projection on the different Mn 3*d*-states are plotted in figure 5.36. In all three cases, the states around the Fermi level have mostly a Mn *d* character. The exchange splitting of the *d* band is larger for the Hex2 and the C16 structure than for the  $\alpha$  structure, consistent with a larger magnetic moment for the formers (the analysis of the magnetic moments will be given in the next section). The shape of the DOS and PDOS<sub>Mn</sub><sup>3*d*</sup> for the  $\alpha$  structure is agreement with that found by Arras using the ABINIT code [97].

TABLE 5.8: Number of holes in the Mn 3*d* band, as well the total number of calculated *d* states in the calculation energy range.

Structure	Mn <sub>a</sub>		Mn <sub>b</sub>	
	N <sup>3<i>d</i></sup> <sub>holes</sub>	N <sup>3<i>d</i></sup> <sub>states</sub>	N <sup>3<i>d</i></sup> <sub>holes</sub>	N <sup>3<i>d</i></sup> <sub>states</sub>
Hex2	4.52	10.38	4.32	10.44
C16	4.29	10.57		
$\alpha$	4.04	10.15		

By integrating the PDOS<sub>Mn</sub><sup>3*d*</sup> up to the Fermi level we find the number of holes in the *d* band, as reported in table 5.8. One can also see on all three PDOS<sub>Mn</sub><sup>3*d*</sup>

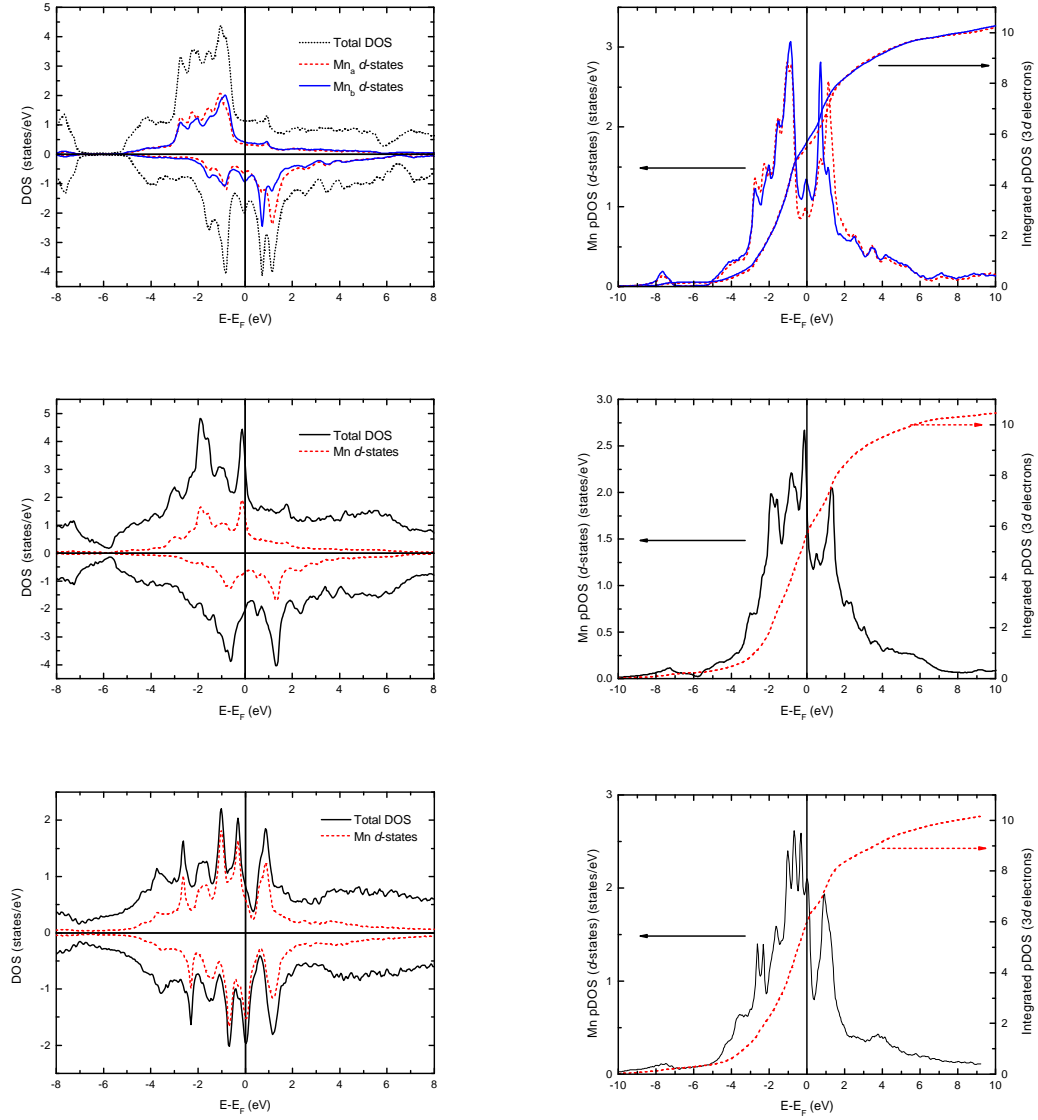


FIGURE 5.36: (from top to bottom) Density of states for the Hex2, C16 and  $\alpha$  structures. (left) Total DOS and Mn PDOS<sup>3d</sup> (for Mn<sub>a</sub> and Mn<sub>b</sub>, in the case of Hex2). Curves corresponding to the majority (minority) spins are plotted along the positive (negative)  $y$ -axis. Units are given cell-wise for the DOS and atom-wise for the PDOS. (right) Total PDOS<sub>Mn</sub><sup>3d</sup> (spins up + spins down, left scale) for Mn, as well as the total number of 3d states (right scale). In both panels the energy is given relative to the Fermi energy (indicated by a vertical black line).

in the right panels in figure 5.36 that there are still some Mn  $d$  states even more than 8 eV above the Fermi level. These non-zero values of the  $\text{PDOS}_{Mn}^{3d}$  translate into a number of  $d$  states (integrated  $\text{PDOS}_{Mn}^{3d}$ ) slightly higher than 10 electrons (see table 5.8, as opposed to the previously studied structure ( $\text{Ge}_3\text{Mn}_5$ ,  $\text{Mn}_T$ ,  $\text{Mn}_S$ ). Since the larger deviation in the total number of  $3d$  states in  $\text{Ge}_3\text{Mn}_5$  still allowed for a correct calculation of the XAS-XMCD spectra, we may suppose that the small error in the crystalline phases considered here will not affect much the corresponding XAS-XMCD spectra.

#### 5.4.4.4 Absorption spectra and magnetic moment in the Hex2 and C16 structures

Following the procedure described earlier, we calculated the absorption spectra for the three crystalline structures. The results for the Hex2 and the C16 structure are shown in figure 5.37 and 5.38. We encountered some specific difficulties in the case of the  $\alpha$  structures that will be described in the next section.

The lineshape of the XAS spectra for both Hex2 and C16 structures are in agreement with the experiments. Two single broad peaks can be observed at the Mn  $L_2$  and  $L_3$  edges and both a little asymmetry (broader on the high energy side) as experimentally observed. The branching ratio are respectively 0.64 and 0.65, close to the experimental and statistical value of 0.67.

On the other hand, the XMCD spectra are quite different : in the case of Hex2, the XMCD at the  $L_2$  and  $L_3$  edges are much more intense than experimentally measured (by a factor  $\sim 2.5$  at the  $L_3$  edge). In the case of the C16 structure, the difference in amplitude is much reduced at the  $L_3$  edge, however it is still much larger than experimentally measured at the  $L_2$  edge. This observation is consistent with the magnetic moment of the two structures : as shown on table 5.9, the C16 and the Hex2 structure have larger magnetic moments ( $\sim 1.5 \mu_B/\text{Mn}$  and  $\sim 2.6 \mu_B/\text{Mn}$ , respectively) than experimentally measured ( $0.8\text{-}1.0 \mu_B/\text{Mn}$ ), hence the larger XMCD signals. The XMCD spectra for the C16 and the Hex2 structure both lack the positive hump observed experimentally on the high energy side of the  $L_3$  absorption edge. This is similar to what was observed for the simple defects. So the overall lineshape of the XMCD spectra for both structures are quite in disagreement with the experiment.

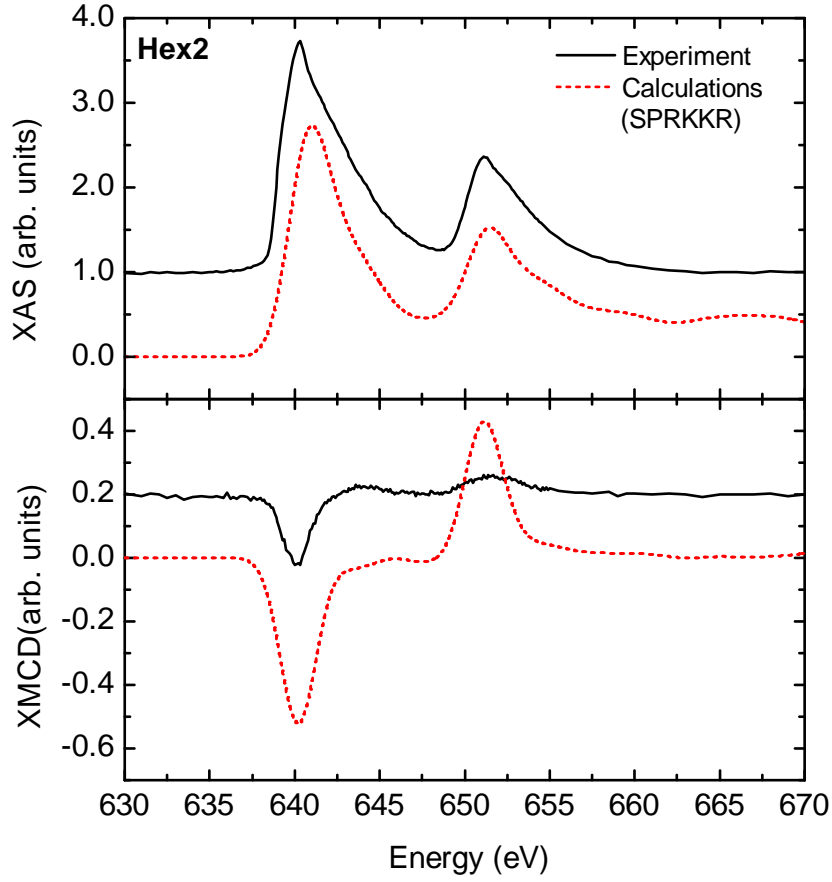


FIGURE 5.37: XAS (top) and XMCD (bottom) spectra in the GeMn nanocolumns samples, as measured experimentally (solid black line) and the result of the SPRKKR calculation for the Hex2 crystalline structure (dashed red line). For clarity, spectra have been shifted vertically.

The magnetic moments calculated using SPRKKR for the different structures are presented in table 5.9, along with the results of the sum rules applied to the theoretical spectra and the calculation using the ABINIT code by Arras. For the Hex2 structure we observe two different magnetic moments on the  $\text{Mn}_a$  and  $\text{Mn}_b$  (respectively  $2.67$  and  $2.06 \mu_B/\text{Mn}$ ) and the average moment ( $2.16 \mu_B/\text{Mn}$ ) is somewhat smaller than that calculated using the augmented plane wave method ( $2.6 \mu_B/\text{Mn}$ ). The values extracted from the sum rules applied to the KKRGEN calculated spectra are also smaller than those from the direct SPRKKR calculation by a factor  $0.56$  for both  $\text{Mn}_a$  and  $\text{Mn}_b$ , and  $0.62$  when the total magnetic moment is considered.

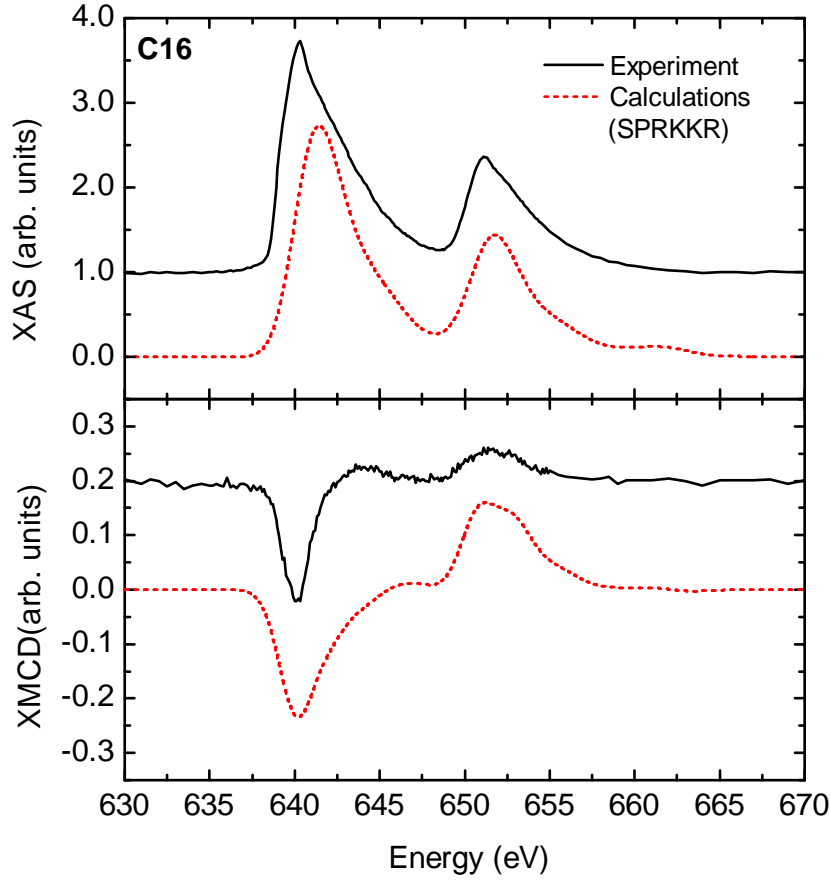


FIGURE 5.38: XAS (top) and XMCD (bottom) spectra in the GeMn nanocolumns samples, as measured experimentally (solid black line) and the result of the SPRKKR calculation for the C16 crystalline structure (dashed red line). For clarity, spectra have been shifted vertically.

In the case of the C16 structure, the moments calculated with SPRKKR are consistent with those calculated by Arras. However, the values extracted from the sum rules are yet again smaller those from the direct calculation by a factor 0.62.

#### 5.4.4.5 Particularities of the calculation for the $\alpha$ phase

As stated before, performing the calculations for the  $\alpha$  phase appeared more complex than for the other one, specially from the point of view of the calculation of

TABLE 5.9: Magnetic moments in the Hex2, C16 and  $\alpha$  crystalline phases. All moments are given in  $\mu_B/\text{Mn}$ , the  $M_{tot}$  is the total moment in the unit cell, divided by the number of Mn atoms.

		SPRKKR	KKRGEN+SR	ABINIT <sup>a</sup>
Hex2	Mn <sub>a</sub>	2.67	1.50	
	Mn <sub>b</sub>	2.06	1.16	
	Mn <sub>tot</sub>	2.16	1.33	2.6
C16	Mn	1.64	1.01	
	Mn <sub>tot</sub>	1.45	1.01	1.5
$\alpha$ + LSDA	Mn	0.50		
	Mn <sub>tot</sub>	0.49		
$\alpha$ + GGA	Mn	0.78		
	Mn <sub>tot</sub>	0.73		1.0

<sup>a</sup> Ref. [97]

the absorption spectra. The main issue can be seen in table 5.9, where the magnetic moment calculated using SPRKKR and the Von Barth-Hedin parametrization of the exchange-correlation potential is smaller by a factor of two with respect to the value calculated using ABINIT and a GGA-type exchange correlation potential. The absolute error ( $\sim 0.5 \mu_B/\text{Mn}$ ) is of the same magnitude as in the case of the Hex2 structure, however it represent 100% of the calculated value and is therefore expected to have a large impact on any further calculations. In order to circumvent this issue, we also turned to a GGA approximation of the exchange correlation potential by using the Perdew-Burke-Ernzerhof parametrization [181]. When comparing the GGA-calculated density of states to the LSDA (Von Barth-Hedin) one, we find that the PDOS<sub>Mn</sub><sup>3d</sup> are essentially the same, the only difference is a larger exchange splitting of the 3d band. The majority states are moved  $\sim 0.19$  eV towards lower energies, whereas the minority states are moved  $\sim 0.05$  eV towards higher energies (figure 5.39). This larger exchange splitting is consistent with the larger magnetic moment found (table 5.9) but the calculated magnetic moment is still  $0.27 \mu_B/\text{Mn}$  smaller than that calculated using ABINIT.

As a result, one way to try to correct the error of the self-consistent calculation in the absorption spectra would be to take into account the underestimation of the 3d exchange splitting by compensating on the core-levels splitting. The relationship between the core-level splitting and the local magnetic field (which is closely related

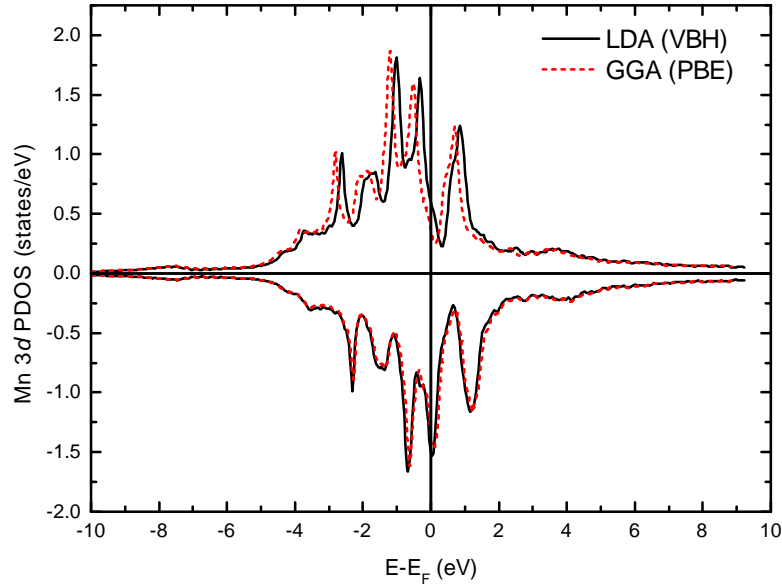


FIGURE 5.39: Mn 3*d*-projected density of states for a LSDA or a GGA approximation of the exchange-correlation potential. Spin up (down) are plotted along the positive (negative) *y*-axis. The energy is given relative to the Fermi energy (indicated by a vertical black line).

to the 3*d* exchange splitting) is plotted in figure 5.40. A clear linear relationship can be observed over a large range of magnetic moments, independantly of the considered structure. The splitting between the  $|\frac{3}{2}, +\frac{3}{2}\rangle$  and the  $|\frac{3}{2}, -\frac{3}{2}\rangle$  core states ( $\Delta_{3/2}$ ) can be calculated as a function of the local magnetic moment on the Mn atom ( $M$ ) using :

$$\Delta_{3/2} \text{ (eV)} = 0.36 \times M \text{ } (\mu_B) \quad (5.7)$$

An example of the result of the KKRGEN calculation is shown in figure 5.27 for the  $\text{Ge}_3\text{Mn}_5$  structure and in figure 5.42 for the  $\alpha$  structure. Shifting the core-levels to correct for the underestimated magnetic moment is almost the same as increasing the exchange splitting in the 3*d* band. However, some approximations are made and some errors are introduced. Firstly, the states near the Fermi level change as the 3*d* exchange splitting changes, whereas they are kept constant upon shifting the 2*p* core-levels. This means that calculated spectra will have some error at the absorption edge, however features further above the edge (*e.g.* the positive hump on the high-energy side of the XMCD  $L_3$  edge observed in the experiments)



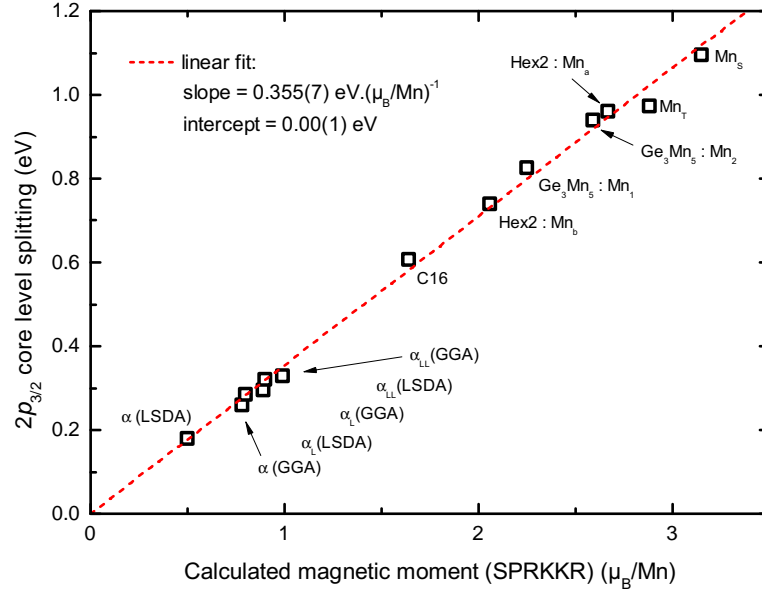


FIGURE 5.40: Mn  $2p_{3/2}$  core-level splitting (between  $|\frac{3}{2}, +\frac{3}{2}\rangle$  and  $|\frac{3}{2}, -\frac{3}{2}\rangle$ ) as a function of the SPRKKR calculated magnetic moment for different structures.

should not be affected by this approximation. Secondly, any mixing effect is not taken into account when shifting the core levels.

The core-level shifting procedure is illustrated in figure 5.41. The resulting XAS-XMCD spectra for an additional increase of the core-levels splitting of 0.0 to 0.6 eV are plotted in figure 5.43. It can be seen that increasing the splitting of the core-levels has little effect on the XAS spectra. On the opposite, the effects on the XMCD spectra are dramatic : as the splitting is increased, the XMCD at the Mn  $L_3$  edge is increased (which is consistent with a larger simulated exchange splitting of the  $3d$  band), the intensity  $L_2$  edge is slightly reduced and the peak is further broadened, and more interestingly, a positive XMCD signal on the high energy-side of the  $L_3$  edge appears. The spectra presented here correspond to our GGA calculations, hence the underestimation of the magnetic moment is  $\sim 0.2\text{-}0.3 \mu_B$  as indicated in table 5.9. Using equation 5.7, this translates in additional splitting of  $\sim 0.1$  eV.

We have plotted in figure 5.46 the experimental XAS-XMCD spectra against the results of the calculation for different values of the core-level splitting. The addition of a correction splitting of 0.1 eV does not appear to be enough to improve the agreement between the experimental and the calculated spectra. However the

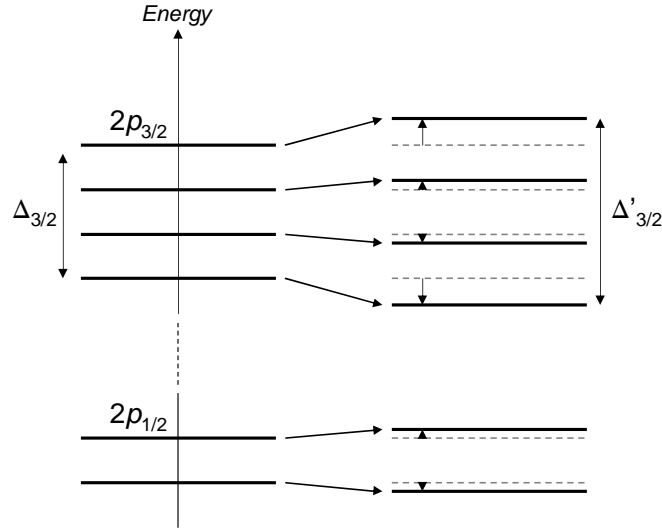


FIGURE 5.41: Simple picture of the core-level shifting procedure. We shift each single core-level in order to increase the splitting between two consecutive levels of the same sub-shell. This translates into a rigid shift of the corresponding absorption spectra in figure 5.42.

positive hump mentioned before appears for additional  $2p_{3/2}$  core-level splittings equal or higher than 0.3 eV, *i.e.* a correction on the magnetic moment of  $+0.83 \mu_B$ . Therefore it seems that a local enhancement of the magnetic moment would provide better agreement with the experimental spectra.

As a point of comparison we also applied the same procedure on the core states for the interstitial and the substitutional defects, in figure 5.44 and 5.45 respectively. In the same fashion as for the  $\alpha$  structure, the XAS spectra are not much affected by the shift of the core-levels. However in the case of the interstitial Mn, the XMCD spectra are also insensitive to the additional splitting of the core levels. In the case of the substitutional Mn, there is a small variation in the XMCD spectra at the  $L_3$  edge, where the XMCD is more intense and a small feature on the high energy-side starts to appear. Yet, it is much less spectacular than what was observed in the  $\alpha$  structure. The explanation for this insensitivity in the  $\text{Mn}_T$  and  $\text{Mn}_S$  structure is that these structures already have large magnetic moments (this can also be seen in amplitude of the XMCD spectra at the  $L_3$  edge). Therefore any change induced by a small additional core-level splitting ( $\sim 0.28 \mu_B$  per additional 0.1 eV) is not as dramatic as in the case of the  $\alpha$  phase.

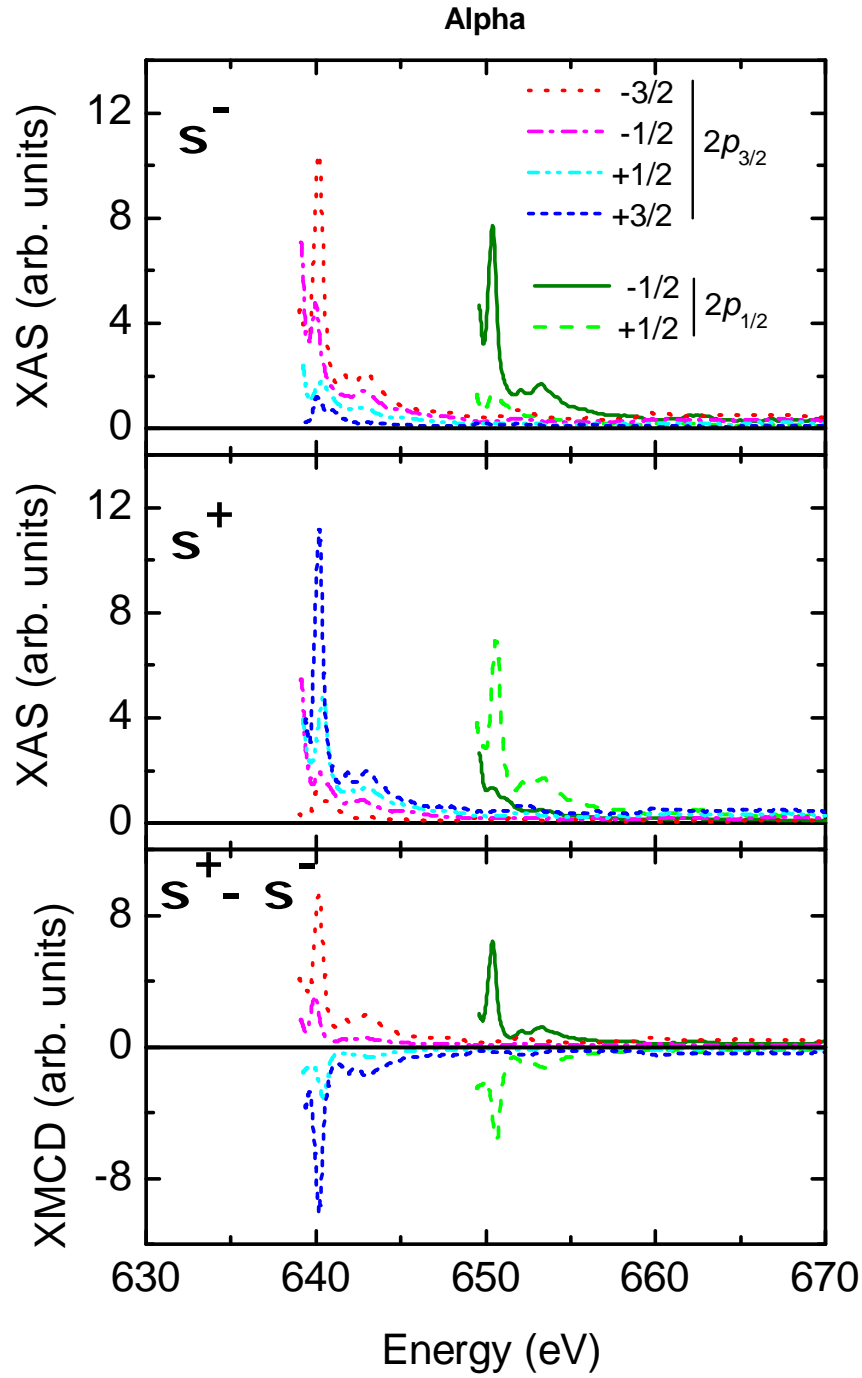


FIGURE 5.42: X-ray absorption spectra for each  $2p_{1/2}$  and  $2p_{3/2}$  core-level for both left and right circular polarisation, as well as the corresponding difference spectra for the  $\alpha$  crystalline phase.

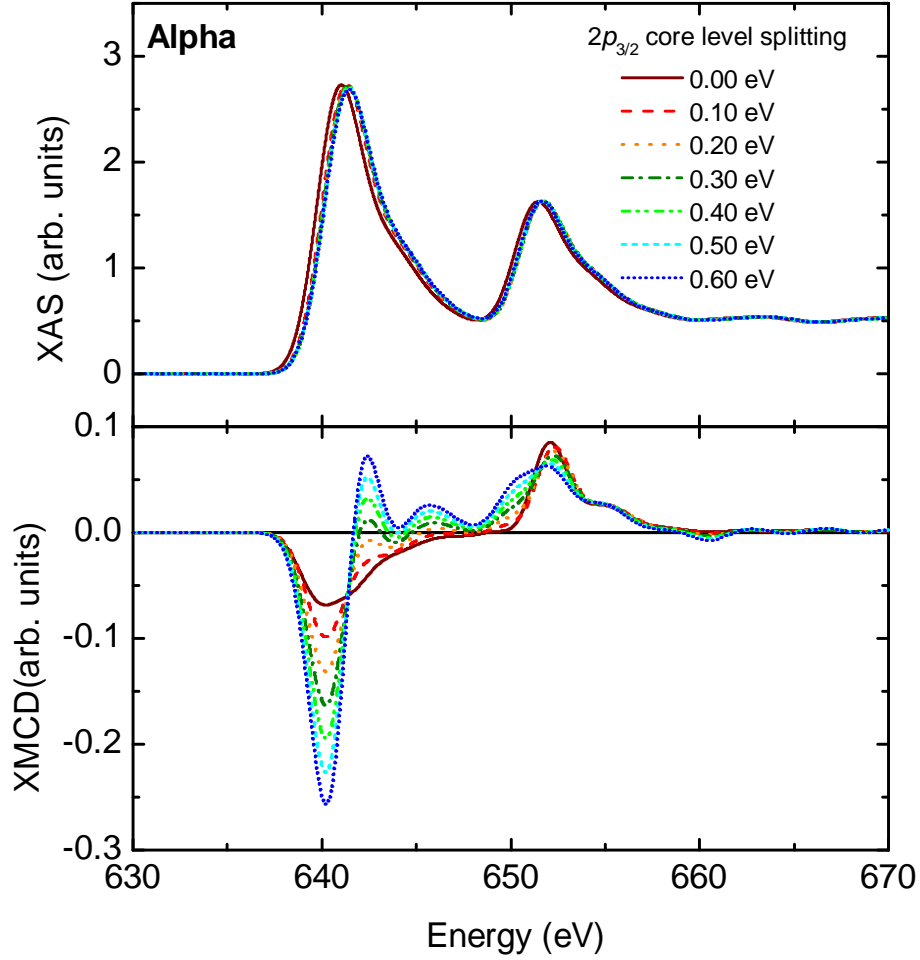


FIGURE 5.43: Calculated XAS and XMCD spectra for the  $\alpha$  phase for different values of the additional splitting in the  $2p$  core states (values are given in terms of total additional splitting in the  $2p_{3/2}$  sub-shell, *i.e* between the  $\left|\frac{3}{2}, +\frac{3}{2}\right\rangle$  and the  $\left|\frac{3}{2}, -\frac{3}{2}\right\rangle$  core states).

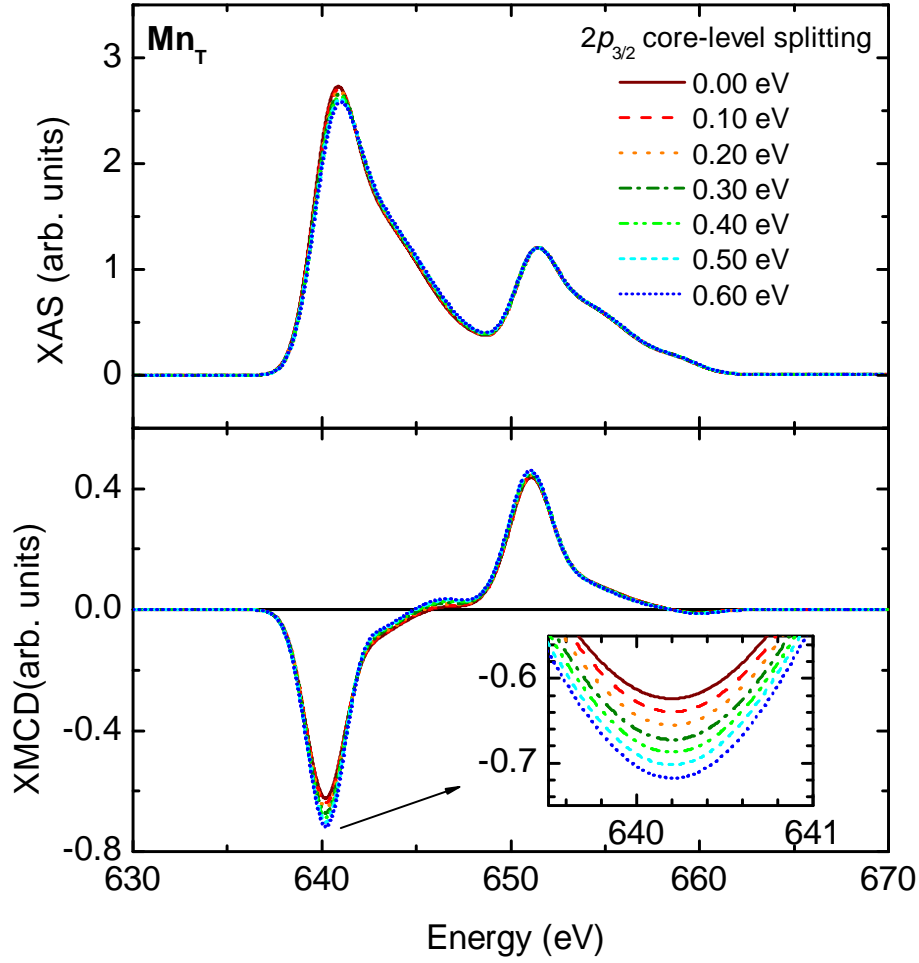


FIGURE 5.44: Calculated XAS and XMCD spectra for the interstitial Mn for different values of the additional splitting in the  $2p$  core states (values are given in terms of total additional splitting in the  $2p_{3/2}$  sub-shell, *i.e* between the

$\left|\frac{3}{2}, +\frac{3}{2}\right\rangle$  and the  $\left|\frac{3}{2}, -\frac{3}{2}\right\rangle$  core states).

#### 5.4.4.6 Conclusion

The consideration of the crystalline phases proposed by Arras *et al.* has shown a relatively good agreement of the calculated x-ray absorption spectra with the experimental ones. For all three considered structures, the agreement of the calculated XMCD spectra with those measured experimentally is not optimum, both in terms of amplitude and lineshape. However, in the case of the  $\alpha$  structure, the

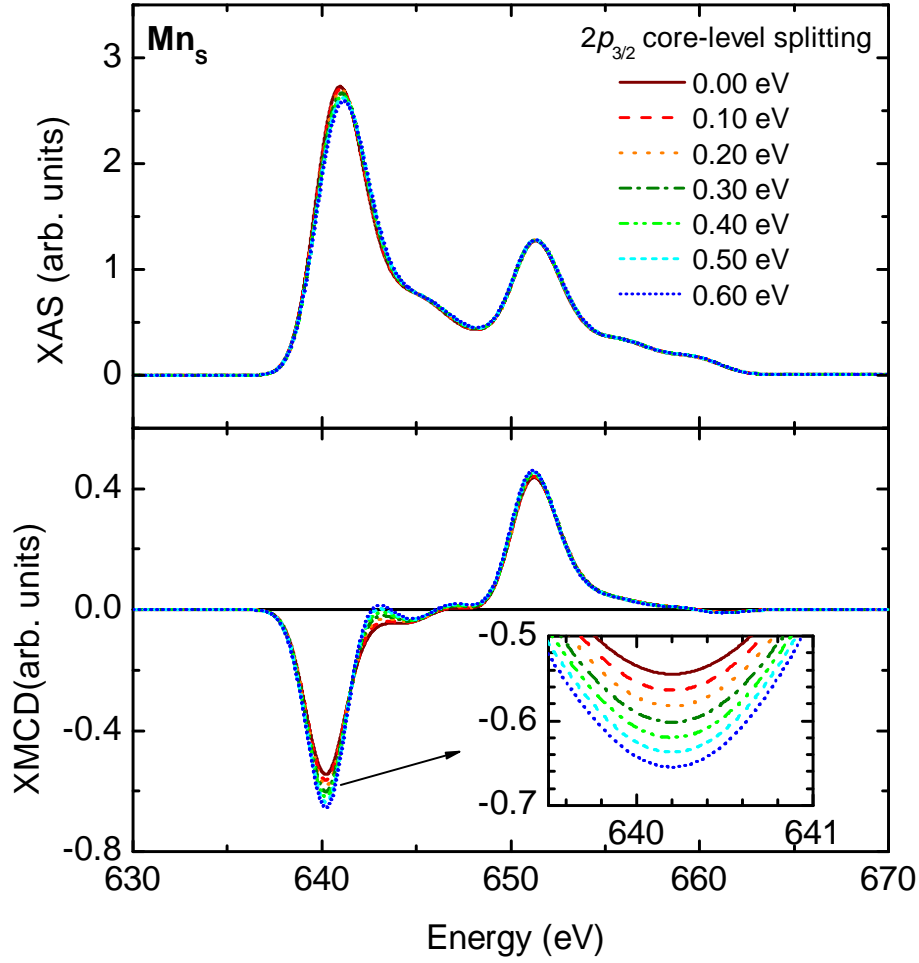


FIGURE 5.45: Calculated XAS and XMCD spectra for the substitutional Mn for different values of the additional splitting in the  $2p$  core states (values are given in terms of total additional splitting in the  $2p_{3/2}$  sub-shell, *i.e* between

the  $\left|\frac{3}{2}, +\frac{3}{2}\right\rangle$  and the  $\left|\frac{3}{2}, -\frac{3}{2}\right\rangle$  core states).

agreement could be improved by indirectly amplifying the local magnetic moment and splitting further apart the initial  $2p$  core-levels.

#### 5.4.5 Systematic error in the sum rules

The SPRKKR-KKRGGEN calculations in the different structures considered up to this point have revealed what seems to be a systematic error between the values

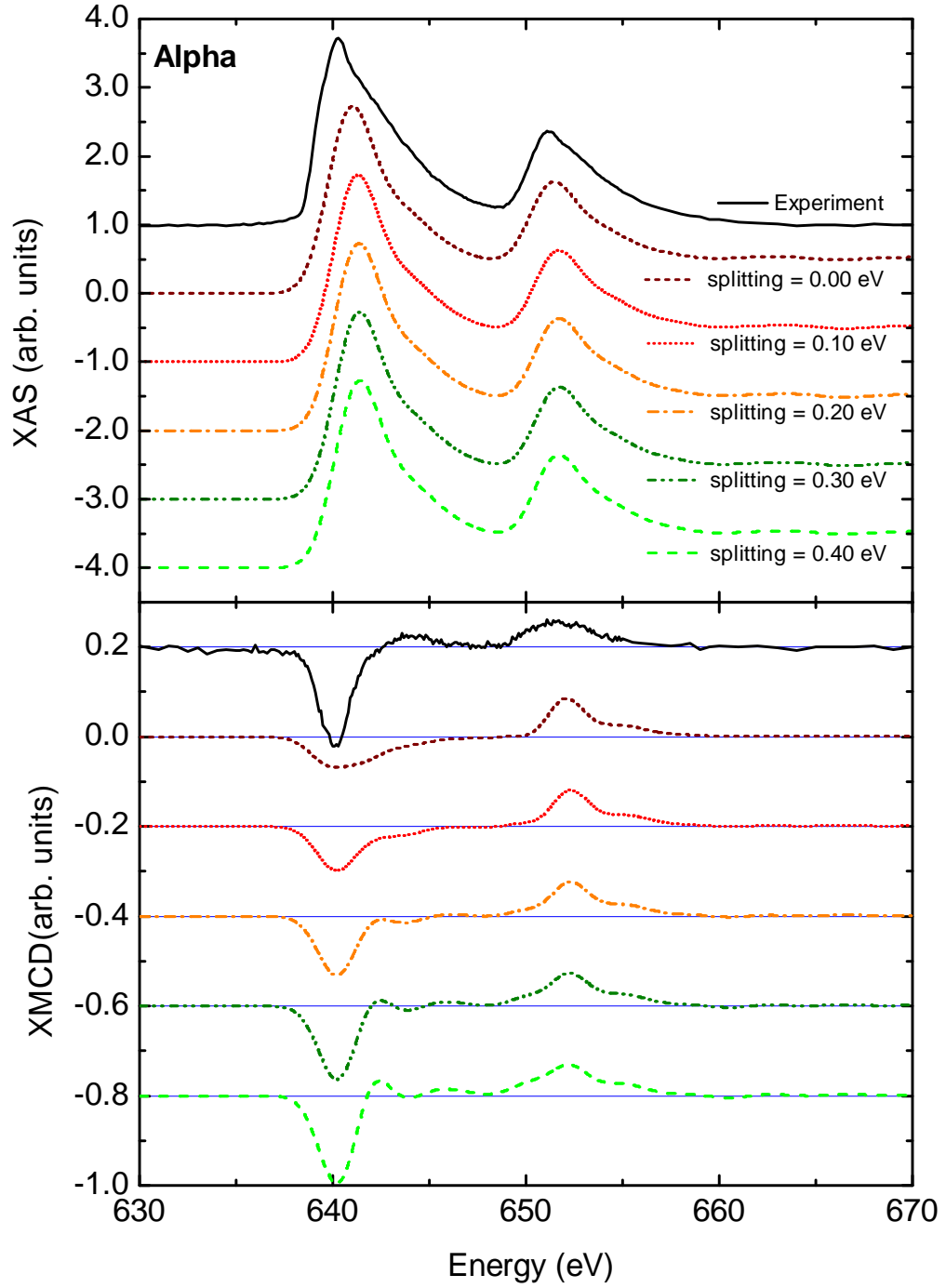


FIGURE 5.46: Experimental XAS and XMCD spectra (solid black line) and calculated XAS-XMCD spectra for different values of the additional splitting in the  $2p$  core states (values are given in terms of total additional splitting in the  $2p_{3/2}$  sub-shell, *i.e* between the  $|\frac{3}{2}, +\frac{3}{2}\rangle$  and the  $|\frac{3}{2}, -\frac{3}{2}\rangle$  core states.

of the magnetic moments extracted from the sum rules applied to the calculated spectra and the values directly calculated in the self-consistent cycles. Consistently with the very small orbital magnetic moment measured, we will see that this error is inherent to the effective spin moment sum rule in the case of  $\text{Mn}^{2+}$ -like configurations.

Let us denote the effective spin magnetic moment extracted from the sum rules applied to the calculated spectra by  $[SE_z^{sr}]$  and the expectation value of the spin magnetic moment calculated *ab initio* by  $\langle S_z \rangle$ . The deviation of the spin moment sum rule from the expectation value of the spin magnetic moment for  $\text{Mn}^{2+}$  was first theoretically investigated in 1996 by Teramura *et al.* [161], within years after the initial publication of the orbital and spin moment sum rules by Thole *et al.* and by Carra *et al.* [127, 128]. It was shown then that for  $\text{Mn}^{2+}$ , the ratio  $[SE_z^{sr}] / \langle S_z \rangle$  was 0.680. More recently, in 2008, Khanra *et al.* performed a theoretical and experimental studies of molecules having a  $\text{M}_4^{\text{II}}\text{O}_6$  core [160] and they found a ratio of 0.72 between the values of the spin magnetic moment extracted from the sum rules and those calculated *ab initio*. A year later, Piamonteze *et al.* published an extended theoretical study of the spin moment sum rule for the transition metals L-edges and found in particular a ratio  $[SE_z^{sr}] / \langle S_z \rangle$  between 0.68 and 0.74 for the  $3d^5$  initial state [153].

In figure 5.47, we have plotted the values of  $[SE_z^{sr}]$  *vs*  $\langle S_z \rangle$  from our calculations for various structures. A linear relationship links the two values : the ratio  $[SE_z^{sr}] / \langle S_z \rangle$  is approximately 0.7, which is consistent with the previously published studies. In particular, this shows that experimental XAS-XMCD values have to be corrected by a factor  $1/0.7$  to be compared with theoretical values or values obtained by other magnetometric methods.

#### 5.4.6 Conclusion of the theoretical XAS-XMCD analysis and how to obtain further insights

In this part we have compared our experimental XAS-XMCD spectra to those obtained using *ab initio* calculation. Our method was benchmarked using the known structure of  $\text{Ge}_3\text{Mn}_5$  and corresponding experimental spectra available in the literature [69]. Using the SPRKKR and KKRGEN code, we were able to calculate



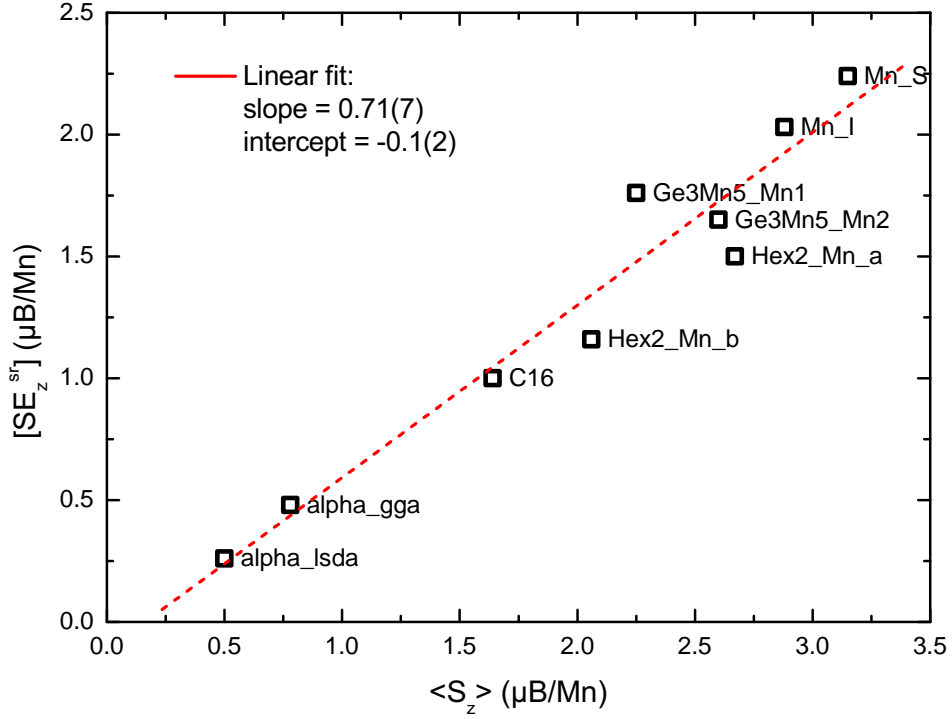


FIGURE 5.47: Effective spin magnetic moment extracted from the sum rules applied to the calculated spectra ( $[SE_z^{sr}]$ ) *vs* the corresponding expectation value of the spin magnetic moment calculated *ab initio* using SPRKKR ( $\langle S_z \rangle$ ).

XAS and XMCD spectra in qualitative and quantitative agreement with the experimental results.

In order to get more insights on the magnetic, electronic and crystalline structure of the nanocolumns, we have calculated the XAS-XMCD spectra of several structures : (i) simple defects (tetrahedral interstitial or substitutional Mn), because such configuration are likely to occur in our heterogeneous samples, and (ii) crystalline phases suggested as being the most stable by *ab initio* calculation [89, 97]. The concluding remarks of this section can be summarized as follow :

- Good agreement in terms of lineshape and relative amplitude of the different absorption edges between the calculated and the experimentally measured isotropic XAS spectra could be achieved in all cases. This indicates the possible presence of the different considered phases. However the calculated and experimental XMCD spectra where in disagreement for all cases (except for the particular  $\alpha$  phase) both in term of relative intensities and of lineshapes. This

last point is of particular importance, because if any of the above mentioned phase was to be present in the sample in domains that would interact antiferromagnetically, the overall intensity of the XMCD spectra (which is scaled to the absorption spectra) would be reduced but its lineshape would remain the same. Hence, if we cannot exclude the presence of simple defects  $\text{Mn}_S$  or  $\text{Mn}_T$ , or of the Hex2 or C16 phases, they cannot be responsible of the observed magnetic signal.

- The  $\alpha$  phase is an interesting solution : its *ab initio*-calculated magnetic moment is already close to the experimentally measured one and upon small variations of the  $2p$  core-level splitting related to this magnetic moment, XMCD spectra close to those experimentally measured could be calculated. In particular, any local enhancement of the magnetic moment in the  $\alpha$  phase would result in calculated XAS-XMCD spectra closer to the experimental ones.
- The previously mentioned result also shows the importance of a good calculation of the core states in order to produce reliable XMCD spectra. This is particularly important in the case of low magnetic moment structures ( $\leq 1 \mu_B$ ) because the SPRKKR code has proven to slightly underestimate already low magnetic moments. We have shown that one way to circumvent this issue is to consider exchange-correlation potentials in the generalized gradient approximation which, in particular, better describe the exchange splitting of the  $3d$  band. Yet the calculated moments were still lower than those calculated using augmented plane waves methods. In that sense, we propose to calculate the potential in our structures using such methods, using the WIEN2K code, while another multiple scattering code (FDMNES) offers to use those potentials to calculate the corresponding XAS-XMCD spectra. One would then expect larger magnetic moments and better agreement with the experiments.
- One last remark is related to the taking into account of the disorder. Due the low-temperature growth of the GeMn nanocolumns, one may expect defects to form during the growth. Moreover the broad x-ray absorption edges measured experimentally could be an indicator of variations in the local environment of the Mn atoms, *i.e.* structural or chemical disorder. True disorder is not easily taken into account in *ab initio* calculations. Simple ways to approach the variations in the local environment of the Mn atoms are (i) to introduce distortion by modifying the lattice parameters, (ii) to introduce chemical disorder as vacancies or as interstitials by removing or adding Mn atoms respectively, or (iii) to modify the periodicity of the structure by using supercells. Any of these three methods

can be combined to simulate disorder. Some promising results have already been obtained, using the suggested WIEN2K+FDMNES method and considering a faulted  $\alpha$  phase. Figure 5.48 shows the resulting XAS-XMCD spectra obtained in a double  $\alpha$  cell where one of the Mn atom is missing (resulting in 20% Mn composition, hence the notation  $\alpha_{20\%}$ ). This vacancy defect increases the magnetic moment on the remaining Mn atom to  $2.38 \mu_B$ . It still 4 times larger than the experimental magnetic moment. However, once rescaled to  $1/4$ , the calculated XMCD is in rather good agreement with the experimental one and in particular the positive hump on the high energy-side of the  $L_3$  is reproduced. This encourages further calculations considering other possible defects around the  $\alpha$  phase.

## 5.5 Résumé du chapitre 5

Nous avons discuté dans le chapitre 5 des résultats de l'étude par spectroscopie d'absorption de rayons X et dichroïsme magnétique circulaire de rayons X des propriétés magnétiques des nanocolonnes de GeMn. Dans un premier temps nous nous sommes attachés à analyser les résultats expérimentaux, résumés ci-après, puis dans un second temps nous avons complété cette étude par une approche théorique en calculant et discutant les spectres XAS-XMCD théoriques pour différentes structures cristallines des nanocolonnes.

Nous avons vu que l'aspect des spectres XAS-XMCD mesurés aux seuils  $L_{2,3}$  du Mn indique des états  $3d$  du Mn délocalisés et hybridés sous forme de bandes avec les états du Ge. Les spectres sont très similaires à ceux mesurés dans des échantillons de  $\text{Ge}_3\text{Mn}_5$ , bien que toutes les autres techniques expérimentales excluent la présence de cette phase dans l'échantillon (en particulier aucun signal magnétique n'est observé en dessous de la température de Curie de  $\text{Ge}_3\text{Mn}_5$ , autour de 300 K). L'analyse quantitative des spectres XAS-XMCD donne un moment magnétique total sur les atomes de Mn de l'ordre de  $0.8 \pm 0.1 \mu_B$ , bien plus faible que pour  $\text{Ge}_3\text{Mn}_5$ . Comme attendu pour une configuration proche de  $3d^5$ , la contribution orbitale est faible (moins de  $0.1 \mu_B$ ). Les mesures à différents angles ne montrent aucune anisotropie, confirmant que le terme dipolaire magnétique peut être ignoré lors de l'application des règles de sommes. Une dépendance linéaire de l'aimantation en fonction de la température est également rapportée et confirmée par des mesures SQUID. La comparaison des courbes d'aimantation mesurées par

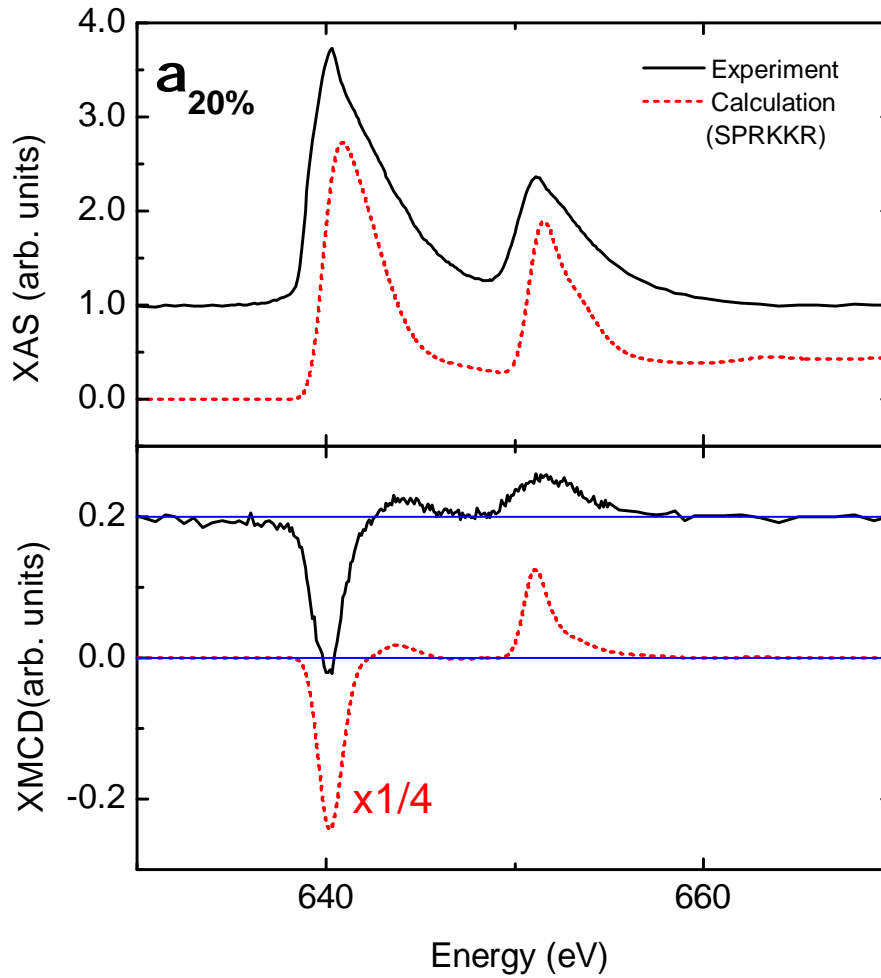


FIGURE 5.48: Experimental XAS and XMCD spectra (solid black line) and calculated XAS-XMCD spectra for a faulted  $\alpha$  phase where one in two Mn atoms is missing (red dashed line). The XMCD spectra has been scaled down by a factor 0.25 in order to facilitate the lineshape comparison.

XAS-XMCD (surface) et SQUID (volume) permettent d'ailleurs de confirmer l'homogénéité magnétique des échantillons.

Nous avons aussi montré que la présence d'une couche de protection (typiquement 3 nm de Si amorphe) recouvrant la couche de GeMn est absolument essentielle pour prévenir toute oxydation. Les échantillons laissés sans protection ou mal protégé (par exemple par 0.5 nm de Ge) s'oxydent dès qu'exposés à l'air et présentent alors des spectres XAS-XMCD caractéristiques du Mn dans un état oxydé. Dans le cas d'échantillon protégé par 0.5 nm de Ge, l'oxydation est *partielle* au sens

où l'interface entre l'oxyde et les nanocolonnes est accessible par XAS-XMCD. L'oxyde montre certaines caractéristique du MnO, avec notamment une composante antiferromagnétique se traduisant d'une part par la diminution du signal magnétique global après oxydation, et d'autre part par la mise en évidence d'un effet de décalage d'échange.

Afin d'obtenir de plus amples informations sur la structure locale des nanocolonnes, nous avons calculé à l'aide de code *ab initio* les spectres XAS-XMCD correspondant à de potentielles structures présentes dans les nanocolonnes, telles que proposé par nos collaborateurs du L\_Sim au CEA-Grenoble. Un bon accord général pour les spectres d'absorption a pu être obtenu pour la majorité des structures considérées, ne permettant donc pas de discriminer une structures cristalline préférentielle. Cependant, l'allure des spectres XMCD est en désaccord pour toutes les structures, sauf pour la phase  $\alpha$ . La phase  $\alpha$  est d'un intérêt particulier car le calcul *ab initio* à l'aide du code WIEN2K (formalisme FLAPW) permet de déterminer un moment magnétique du même ordre de grandeur que celui mesuré ( $\sim 1 \mu_B/\text{Mn}$ ). De plus, une légère variation de la valeur de l'écart entre les états de coeur  $2p$  permet d'améliorer l'accord avec l'expérience. Cette modification de l'écart entre les états de coeur est justifiée par la sous-estimation du moment magnétique lors du calcul des spectres XAS-XMCD avec le code SPR-KKR. Nous avons cherché à améliorer la précision du calcul en considérant un formalisme GGA pour le potentiel d'échange-corrélation, ce qui a permis d'obtenir un meilleur accord avec l'expérience. L'accord a été encore affiné en utilisant un code FLAPW (WIEN2K) pour le calcul du potentiel, et un code de diffusion multiple (FDMNES) pour le calcul des spectres d'absorption.

Enfin, nous avons soulevé l'importance de la prise en compte du désordre dans les structures considérées, en calculant notamment les spectres XAS-XMCD dans des structure contenant des défauts tels que des lacunes ou des atomes interstitiels. Nous avons alors pu observé pour certaines de ces structures une augmentation du moment magnétique locale et un accord qualitatif de l'allure des spectres XAS et XMCD.



# General Conclusion and Outlook

In this thesis, the electronic, magnetic and structural properties of self-assembled GeMn nanocolumns were studied using synchrotron radiation. The GeMn nanocolumns system is an heterogeneous ferromagnetic semiconductor and as such, it appears as a very promising candidate for spintronics applications. Synchrotron techniques are highly suited for the study of nanoscale objects, due to the high intensity, high brilliance, and tunable polarization and energy of the synchrotron light. The different results obtained during this thesis are summarized in the following.

## Conclusion

The crystalline structure of various types of GeMn was investigated using grazing-incidence x-ray scattering techniques. The main focus was to study the crystalline phase inside the nanocolumns, in order to determine whether it consisted in a Ge diamond structure with a large concentration of defects (30–40%) or in a new and different crystalline structure. No clear sign of a crystalline phase different from Ge diamond could be observed in samples free from intermetallic precipitates (such as  $\text{Ge}_3\text{Mn}_5$ ), which supported the former hypothesis. However, a strong diffuse scattering was observed, indicating a relatively high degree of disorder in the nanocolumns. The conclusion on the high degree of disorder inside the nanocolumns was further supported by complementary atomistic calculations<sup>7</sup>.

The presence of intermetallic nanoclusters was evidenced in some samples. We observed the characteristic hexagonal crystalline structure of  $\text{Ge}_3\text{Mn}_5$  and were able to determine the orientation of the clusters. In particular we confirmed the observations by Lechner *et al.* [74] that the vast majority of the clusters close to

---

7. Collaboration with F. Lançon, CEA-Grenoble.

the surface have their  $c$ -axis oriented parallel to the surface, along the  $a$ -axis of the Ge diamond structure.

The measurements of the small angle x-ray scattering around Bragg reflections have shown diffuse rings around the Bragg peaks, with larger intensity on the high- $Q$  side along the OH and OK-axis. This particular shape of the scattered intensity was interpreted as stemming from the strain in the Ge matrix. While collaborating with Frédéric Lançon from the CEA-Grenoble for *ab initio* simulations, we were able to explain the influence of the spatially correlated strain fields from the nanocolumns on the Ge matrix and on the corresponding scattered intensity. In particular, we were able to measure the strain in the Ge matrix in a quantitative way. Ageing (*i.e.* oxidation) of the samples was shown to relax the strain in the matrix, indicating large structural modifications in the nanocolumns.

Several attempts using original diffraction techniques were also performed. In the case of the Bragg-GISAXS technique, we were able to enhance the small GISAXS signal from the nanocolumns (due to the small Z-contrast) by measuring it around Bragg reflections, thus adding a strain contrast. In particular, we were able to measure the contribution of in-plane correlations due to the surface roughness ( $\sim 40$ – $50$  nm) and to the inter-columns spacing ( $\sim 10$  nm), as well as oscillations in the latter, due to the finite thickness of the GeMn layer.

Other techniques were used to try to provide further insights about the internal structure of the nanocolumns. Anomalous scattering measurements were performed at the Mn K-edge to enhance the chemical contrast, however no clear signal could be observed *in-plane* or *out-of-plane*. Original in-plane pair distribution function measurements were also performed, to determine the in-plane 2D distribution of distances. Though the technique has been shown to work properly in 3D, data processing for the 2D case has proven more difficult. High-energy total scattering measurements were also performed using large 2D detectors. It was shown that the observed diffuse ring around the Bragg peaks discussed above lies indeed parallel to the plane, even in out-of-plane reflections. This confirmed our interpretation. Further analysis requires a complete correction of the signal, including background effect such as the thermal diffuse scattering of the Ge substrate.

XAS-XMCD measurements in ordered GeMn nanocolumns have shown that the Mn  $d$  states are rather delocalized and metallic-like. A stunning resemblance was observed with results in  $\text{Ge}_3\text{Mn}_5$ . However, the presence of such clusters in the



sample was excluded by complementary characterizations (TEM, SQUID, XRD). Moreover, the magnetic moment per Mn atom (on the order of  $0.8 \mu_B$ ) was shown to be much lower than that expected in  $\text{Ge}_3\text{Mn}_5$  (around  $2.6 \mu_B$ ). The measured magnetic moment is also much smaller than that expected for substitutional Mn (around  $3 \mu_B$ ). A small but non zero orbital magnetic moment was observed, on the order of  $0.1 \mu_B$ .

Contrary to what could be expected from the nanocolumns aspect ratio, no magnetic anisotropy was found. This confirms previous results found by T. Devillers in similar samples, using SQUID magnetometry. A possible explanation is that shape anisotropy is compensated by magnetocrystalline anisotropy. This explanation is further supported by the fact that out-of-plane anisotropy was indeed observed in amorphous nanocolumns.

It was also shown that upon oxidation, the topmost part of the nanocolumns is oxidized and possess some antiferromagnetic character. This was used to induce exchange bias in the underlying ferromagnetic segment of the nanocolumns.

Our collaborators E. Arras and P. Pochet from the CEA-Grenoble proposed different possible crystalline structures using the results of *ab initio* calculations. The theoretical XAS-XMCD spectra of these structures were calculated in collaboration with A. Titov and compared to the experimental results.

All calculated structures have shown XAS spectra in rather good agreement with the experiment. However, the XMCD appeared compatible in both relative intensity and lineshape only for the  $\alpha$  structure. The presence of defects in the  $\alpha$  structure also appeared to improve the agreement.

During the calculations, several points of importance were noticed. It appeared that a precise calculation of the core states is required to produce consistent XMCD spectra, especially in the case of structures with small magnetic moments. We also observed a systematic underestimation of the magnetic moment by applying the sum rules to the theoretical spectra, when compared to the values calculated in the self-consistent cycle. This effect is ascribed to *jj*-mixing in the case of Mn and illustrates the difficulty of applying the theoretical sum rules to this element. The deduced correction factor is in agreement with values previously reported in the literature.

## Short summary

*We have characterized the structural and magnetic properties of self-assembled GeMn nanocolumns using synchrotron techniques and *ab initio* calculations. We observed in particular that the nanocolumns exert a compressive strain on the surrounding Ge matrix. The resulting displacement field is influenced by the positional correlations of the nanocolumns and yields a distinctive diffuse scattering around the Bragg peaks. The coherent nanocolumns still contain some degree of inner disorder that prevent the identification of a different crystalline phase within the nanocolumns. In particular, disordered structures considered using *ab initio* calculation are shown to be in agreement with experimental results. The local magnetic moment measured on the Mn atoms by XAS-XMCD is found to be rather low ( $0.8 \mu_B$ ), even when corrected from the underestimation of the theoretical sum rules applied to the Mn L absorption edges. Investigated possible explanations for this low average moment include new low-magnetic-moment crystalline phases, compatible with diffraction measurements. It is observed that a precise calculation of the individual core states is essential to accurately calculate the lineshape of the XMCD spectra. Finally, we have shown a high sensitivity of the nanocolumns to air, as well as a modification of both structural and magnetic properties upon oxidation.*

## Outlook

It appears that properly taking into account the disorder *inside* the nanocolumns is crucial. Further development of the *ab initio* structural models of the nanocolumns are currently underway<sup>8</sup>. Resulting models may be tested by calculating the theoretical XAS-XMCD spectra<sup>9</sup> and comparing with experimental results, as done during this thesis.

2D-PDF data analysis requires the development of a specific data processing procedure. Otherwise, if much thicker samples could be grown on thin substrates, one may resort to classical PDF measurements by grinding the sample to powder. This would require a large amount of GeMn, since the volume fraction of the nanocolumns is already on the order of 10–20% in the layer. This task would be

---

8. Collaboration with E. Arras and P. Pochet, L\_Sim, CEA-Grenoble

9. Collaboration with A. Titov, L\_Sim, CEA-Grenoble

rather challenging, due to high reactivity of the nanocolumns to air. Total scattering data acquired during this thesis also require more processing to extract useful information about the inner structure of the nanocolumns. In particular, background effects such as thermal diffuse scattering from the Ge, would need to be carefully defined and corrected.

Magnetotransport studies performed in the GeMn nanocolumns were not described in this manuscript. However, the reader may find additional information in references [22, 182, 183]. A strong anomalous Hall effect, as well as a large positive magnetoresistance was observed in samples containing GeMn nanocolumns [22]. However, samples containing metallic  $\text{Ge}_3\text{Mn}_5$  clusters have shown weaker to negligible magnetoresistance and anomalous Hall effect [182, 183]. A deeper understanding is then required to fully apprehend the band structure in the nanocolumns and their alignment with respect to the semiconducting host. In particular, an analysis of confined states in the nanocolumns to observe the possible presence of quasi-1D spin polarized states in the bandgap may also provide further insights about the couplings between the nanocolumns, as suggested in reference [40].

Individual characterization of a single nanocolumn would be highly desirable. In order to do so, procedures to selectively etch the Ge matrix have to be developed. Several etching ways are possible, using either chemical or physical means. Initial work using a focussed ion-beam technique was done by S. Cherifi. One of the main issue remains the oxidation of the exposed nanocolumns. Solutions include *in situ* preparation, or *in situ* capping using, *e.g.*, amorphous Si. XAS-XMCD measurements in etched nanocolumns (not shown in this manuscript) have demonstrated that efficient capping is critical.



# Conclusion Générale et Perspectives

Nous avons caractérisé les propriétés structurales et magnétiques de nanocolonnes auto-organisées de GeMn à l'aide du rayonnement synchrotron et de calculs *ab initio*. Nous avons observé en particulier que les nanocolonnes exercent une contrainte en compression sur la matrice de Ge environnante. Le champ de déplacement résultant est influencé par les corrélations de positions des nanocolonnes et se traduit par un anneau diffus distinctif autour des pics de Bragg du Ge. Les nanocolonnes cohérentes avec la matrice de Ge diamant contiennent un certain degré de désordre interne, prévenant l'identification d'une phase cristalline différente au sein des nanocolonnes. En particulier, des structures (partiellement) désordonnées considérée à l'aide calculs *ab initio* montre un accord avec les résultats expérimentaux. Le moment magnétique local mesuré sur les atomes de Mn par XAS et XMCD est relativement faible ( $0.8 \pm 0.1 \mu_B$ ) comparé à ce que serait attendu pour des atomes uniquement en substitution du Ge ( $\sim 3 \mu_B$ ). Cette différence persiste même après correction de la sous-estimation du moment magnétique par les règles de sommes théoriques au seuil  $L$  du Mn, telle que déterminée au cours de ce travail. Les explications possibles pour une faible valeur du moment magnétique comprennent la présence de nouvelles phases cristalline, portant un faible moment magnétique et compatibles avec les résultats de diffraction. Nous notons aussi qu'un calcul précis des états de coeurs individuels (et en particulier de leurs écarts en énergie) est essentiel au calcul précis des spectres XAS-XMCD. Enfin, nous avons montré la forte sensibilité des nanocolonnes à l'air, ainsi que les modifications des propriétés magnétiques et structurales lors de l'oxydation.

Les perspectives de poursuite de ce travail sont multiples. Tout d'abord il apparait crucial de tenir compte du désordre au sein des nanocolonnes de façon adéquate.

De tels développement des modèles structuraux des nanocolonnes<sup>10</sup>, ainsi que des calculs des spectres XAS-XMCD sont actuellement en cours<sup>11</sup>. D'un point de vue structural, l'analyse des données de 2D-PDF requiert le développement d'outils spécifiques. Autrement, une approche de PDF classique pourrait être utilisée avec des couches de GeMn beaucoup plus épaisses. Les données des mesures de diffusion totales pourraient aussi être utiles pour extraire un supplément d'information sur le désordre local, toutefois les effets parasites, tel que la diffusion diffuse thermique dû au Ge doivent être correctement définis et corrigés. Les expériences de magnéto-transport n'ont pas été décrites dans ce manuscrit ; Toutefois, le lecteur intéressé pourra trouver un supplément d'information dans les références [22, 182, 183]. Un fort effet Hall anomal, ainsi qu'une forte magnétoresistance positive ont été observés dans les nanocolonnes de GeMn[22]. Toutefois, les échantillons contenant des clusters métalliques de  $\text{Ge}_3\text{Mn}_5$  ont montré une forte réduction de ces effets [182, 183]. Une connaissance plus approfondie est donc requise pour permettre une description correcte de la structure de bandes des nanocolonnes et leur alignement par rapport à la matrice semiconductrice. En particulier, une étude des états confinés dans les nanocolonnes pour observer la présence possible d'états polarisés en spin quasi-1D dans la bande interdite pourrait apporter de nouveaux éléments sur les couplages entre nanocolonnes, tel que suggéré dans la référence [40]. Enfin, une caractérisation individuelle des nanocolonnes serait hautement souhaitable. Pour ce faire, une méthode de gravure sélective de la matrice de Ge doit être développée. Un travail initial à l'aide de faisceau focalisés d'ion Ga a été proposé par S. Cherifi. Le problème majeur reste alors l'oxydation des nanocolonnes exposés. Les solutions à cela peuvent résider dans la préparation *in situ* des colonnes ou la protection par une surcouche, telle que décrite au cours de cette étude. Des mesures XAS-XMCD réalisées dans de tels échantillons (non décrites dans ce manuscrit) ont le caractère critique d'une protection efficace des nanocolonnes ainsi isolées.

---

10. Collaboration avec E. Arras et P. Pochet, L.Sim, CEA-Grenoble

11. Collaboration A. Titov, L.Sim, CEA-Grenoble

# Annexe A

## Synchrotron radiation : generalities

Synchrotron radiation and in particular the development of third generation synchrotron radiation sources have offered physicists a whole new range of techniques. Synchrotron radiation was first used in a parasitic way in particle accelerators [184]. The idea was to take advantage of the radiation emitted by the relativistic particles (*e.g.*, electrons or positrons) traveling on an orbit. Since the first uses, dedicated facilities have been built, giving birth to the second generation facilities. Further development of insertion devices (wiggler and undulators) has led to current “third generation” synchrotron sources used worldwide. Next generation synchrotron radiation facilities will likely consist in intense and coherent x-ray sources such as free-electron lasers. Future developments will also most likely include femtosecond time-resolution in pump-probe experiments<sup>1</sup>, going beyond the picosecond timescale of the electron bunch.

In current 3rd gen. synchrotron facilities, the x-rays are produced by electrons moving around a closed path (the storage ring). The storage ring consists in straight line sections, connected by magnetic devices used to bend the path of the electrons. At each bending point, intense x-ray light is emitted and directed along a beamline. Experimental setups (endstations) are placed at the end of each beamline to use the radiation. Figure A.1 represent the layout of the European Synchrotron Radiation Facility in Grenoble, France.

---

1. see, *e.g.*, ref. [185] for the first demonstration of fs-resolved x-ray absorption spectroscopy at the ALS, or ref. [186] for details about the *femto-slicing* technique developed at BESSY.

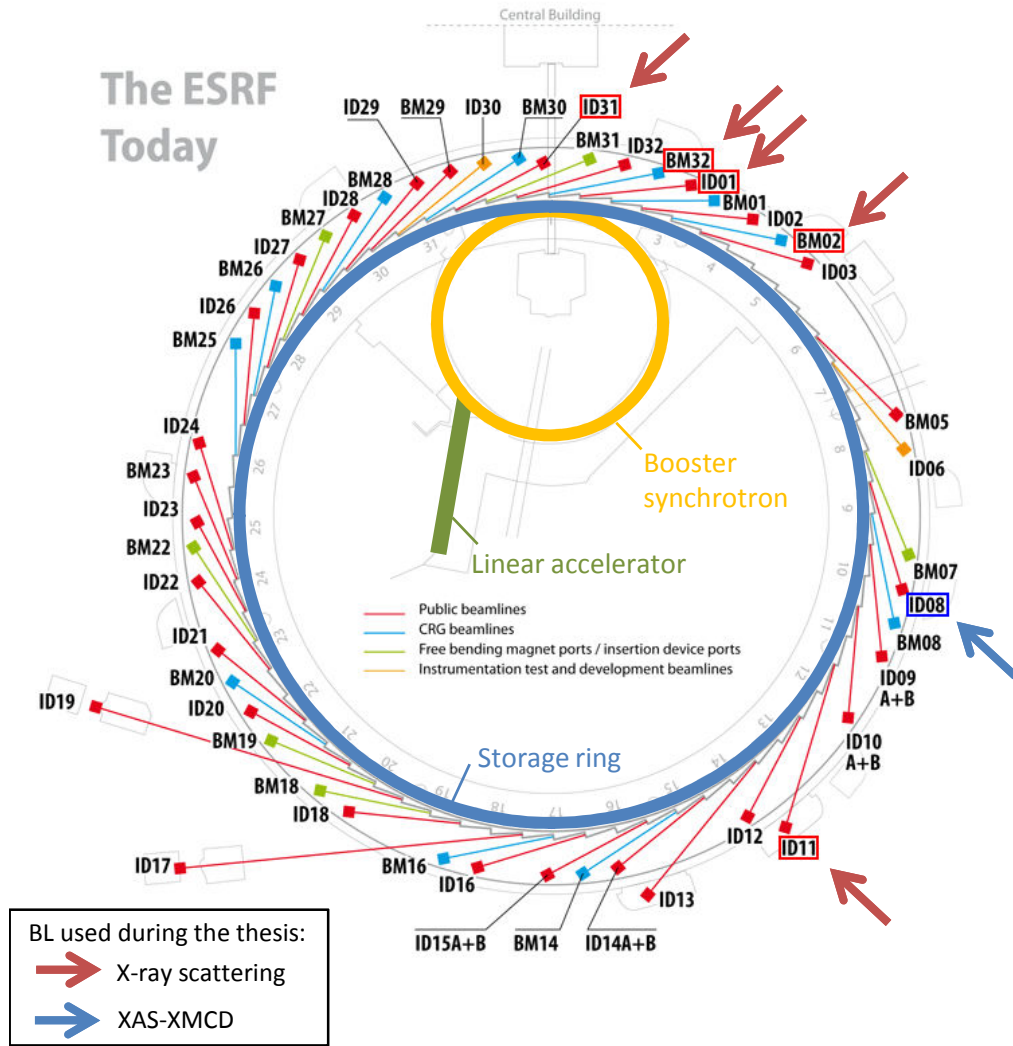


FIGURE A.1: Layout of the European Synchrotron Radiation Facility in Grenoble, France. The prefix of each beamline indicates the type of radiation delivered : bending magnet (BM) or insertion device (ID). From ref. [187].

Depending on the devices along the path of the electron, the spectral shape of the emitted radiation can be very different, for example the typical photon energy can range from the far infra-red (below 0.5 eV) up to the very hard x-ray regime (on the order of  $10^6$  eV). Thus a very wide range of applications are in use in today's synchrotron radiation facilities.



## Annexe B

### Exchange bias in GeMn nanocolumns : The role of surface oxidation

## Exchange bias in GeMn nanocolumns: The role of surface oxidation

S. Tardif,<sup>1,2</sup> S. Cherifi,<sup>1,3,a)</sup> M. Jamet,<sup>2</sup> T. Devillers,<sup>2</sup> A. Barski,<sup>2</sup> D. Schmitz,<sup>4</sup> N. Darowski,<sup>4</sup> P. Thakur,<sup>5</sup> J. C. Cezar,<sup>5</sup> N. B. Brookes,<sup>5</sup> R. Mattana,<sup>6</sup> and J. Cibert<sup>1</sup>

<sup>1</sup>*Institut Néel, CNRS and UJF, 25 rue des Martyrs, BP166, F-38042 Grenoble, France*

<sup>2</sup>*INAC, CEA-Grenoble, 17 rue des Martyrs, F-38054 Grenoble, France*

<sup>3</sup>*IPCMS, CNRS and UdS, 23 rue du Loess, BP43, F-67034 Strasbourg, France*

<sup>4</sup>*Helmholtz Centre Berlin, Albert-Einstein-Str. 15, D-12489 Berlin, Germany*

<sup>5</sup>*European Synchrotron Radiation Facility, BP 220, F-38043 Grenoble, France*

<sup>6</sup>*Unité Mixte de Physique CNRS-Thales, Route départementale 128, F-91767 Palaiseau, France*

(Received 4 May 2010; accepted 19 July 2010; published online 9 August 2010)

We report on the exchange biasing of self-assembled ferromagnetic GeMn nanocolumns by GeMn-oxide caps. The x-ray absorption spectroscopy analysis of this surface oxide shows a multiplet fine structure that is typical of the  $\text{Mn}^{2+}$  valence state in MnO. A magnetization hysteresis shift  $|H_E| \sim 100$  Oe and a coercivity enhancement  $\Delta H_c \sim 70$  Oe have been obtained upon cooling (300–5 K) in a magnetic field as low as 0.25 T. This exchange bias is attributed to the interface coupling between the ferromagnetic nanocolumns and the antiferromagnetic MnO-like caps. The effect enhancement is achieved by depositing a MnO layer on the GeMn nanocolumns. © 2010 American Institute of Physics. [doi:10.1063/1.3476343]

The electrical control of the magnetization is presently one of the most explored aspects in modern magnetism. In addition to the understanding of fundamental aspects, this possibility offers a probable direction toward the development of hybrid devices using, e.g., magnetic multiferroics<sup>1</sup> or taking advantage of the carrier-mediated magnetism in magnetic semiconductor based architectures.<sup>2</sup> In fact, the experimental demonstration of a pure electric field manipulation of the magnetization in (Mn,Ga)As (Ref. 3) shows the outstanding possibility of controlling magnetism in dilute magnetic semiconductors through electrical gates. The prospect of inducing an exchange bias (EB) in magnetic semiconductors<sup>4</sup> adds also an exceptional functionality to these materials. Moreover, the electric current-controlled EB (Ref. 5) or the electric field-controlled EB (Refs. 6 and 7) show a promising potential for advanced applications such as fully electric-controlled memory devices.

We have recently demonstrated the ferromagnetic behavior of self-organized GeMn nanocolumns surrounded by a quaspure Ge matrix.<sup>8,9</sup> We report here on the possibility of inducing an EB in these nanocolumns by controlling their surface oxidation and by following a regular magnetic field-cooling (FC) procedure. The magnetic and spectroscopic properties of nonoxidized and partially oxidized nanocolumns are studied by means of polarized x-ray absorption spectroscopy (XAS) and superconducting quantum interference device (SQUID) magnetometry.

The GeMn nanocolumns were grown on Ge(001) by using solid sources molecular beam epitaxy. A 30-nm-thick Ge buffer layer was grown first at 250 °C on an epi-ready Ge(001) wafer. Subsequently, 80-nm-thick GeMn films containing a total amount of about 10% of Mn were grown at 90 °C by coevaporating Ge and Mn at low deposition rates (about 0.15 Å/s). A two-dimensional spinodal decomposition<sup>10</sup> occurring during the growth leads to the formation of Mn-rich nanocolumns. In these growth condi-

tions, self-organized nanocolumns of about 3 nm in diameter with a density of about  $3 \times 10^4$  columns/ $\mu\text{m}^2$  are estimated from transmission electron microscopy (TEM) observations. Figure 1 shows typical TEM transverse and plane views of the self-assembled GeMn nanocolumns (dark regions). These GeMn nanocolumns are found to be Mn-rich and they are surrounded by a quaspure Ge matrix (Mn contents <1%), as evidenced by local electron energy loss spectroscopy measurements.<sup>9</sup>

The magnetic properties of the nanocolumns have been analyzed by means of a SQUID magnetometer and by using XAS and x-ray magnetic circular dichroism (XMCD) measurements at the Mn  $2p \rightarrow 3d$  resonance peaks ( $L_{2,3}$  edges). The XAS and XMCD experiments have been performed at the electron storage rings BESSY II (beamline UE-46-PGM1) and ESRF (beamline ID08). All the measurements were carried out in the total electron yield detection mode at 5 K in superconducting magnets allowing the application of a magnetic field of 5 T. The field was applied in the direction of propagation of the incident x-rays with the sample oriented at 30° with respect to the incident photon beam.

Three different samples, prepared under the same growth conditions, i.e., same columns size and density (diameter 3 nm, length 80 nm, and spacing 6–7 nm), have been studied. The only difference was the surface capping as follows: (i) uncapped-GeMn, leading to 20-nm-thick oxide caps after

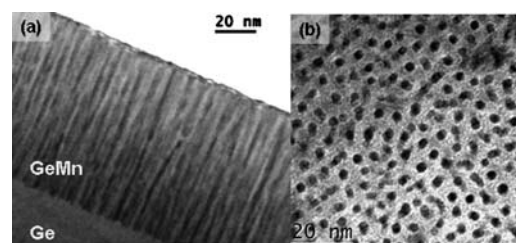


FIG. 1. TEM observations in cross-section (a) and plane view (b) of a GeMn film containing 10% of Mn and grown at about 100 °C on Ge(001). We can clearly observe self-assembled nanocolumns.

<sup>a)</sup> Author to whom correspondence should be addressed. Electronic mail: cherifi@ipcms.u-strasbg.fr.

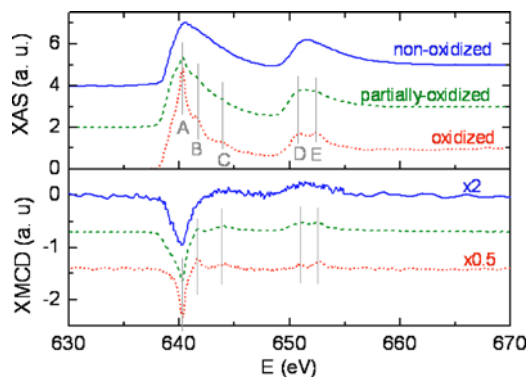


FIG. 2. (Color online) Isotropic XAS (top) and the corresponding XMCD (bottom) measured at 5 K and 5 T in following: nonoxidized GeMn nanocolumns (solid line), GeMn-oxide(5 nm)/GeMn(75 nm) (dashed line), and GeMn-oxide(20 nm)/GeMn(60 nm) (dotted line). The spectra have been vertically shifted. The spectra obtained in nonoxidized and oxidized samples have been measured with two different experimental setups at BESSY II and ESRF storage rings, respectively. Therefore, no information about the energy shift after oxidation could be extracted from the measurements.

water treatment for 15 min; (ii) Ge-capped GeMn, leading to about 5-nm-thick oxide caps after water treatment for 15 min; and (iii) GeSi-capped GeMn, where an amorphous Si(3 nm) layer in addition to the Ge(0.5 nm) capping allows an efficient protection of the nanocolumns against oxidation. The de-ionized water treatment permits the dissolution of the native germanium dioxide<sup>11</sup> and induces a local oxidation of the Mn-rich nanocolumns. The oxidation of Mn:Ge upon oxygen incorporation and the formation of Mn–O–Mn complexes has been predicted to decrease the system net magnetization.<sup>12</sup> In the GeMn nanocolumns, the magnetic signal measured by SQUID magnetometry before water treatment has to be multiplied by a numerical factor ( $<1$ ) to fit the magnetic signal after water cleaning, while the magnetization remains unaltered in the well-protected (SiGe capped) samples. The indirect estimation of the manganese oxide amount by measuring the decay of the magnetic signal upon oxidation is found to be most suitable for this system where the oxidized Mn caps represents only a small fraction of the 10% Mn atoms that are distributed in the GeMn layer.

The x-ray absorption spectra measured at the Mn  $L_{2,3}$  edges in the well-protected GeMn nanocolumns shows single broad peaks full width at half maximum (FWHM=5.7 eV) related to the metallic character of the GeMn nanocolumns and to the probable hybridization with Ge. Upon oxidation, the XAS and XMCD line shapes become strikingly different as they develop a multiplet fine structure (Fig. 2). In the oxidized nanocolumns, the Mn  $L_3$  absorption edge displays several peaks labeled A (640.3 eV), B (641.5 eV), and C (644.0 eV) and the Mn  $L_2$  edge displays two peaks labeled D (651.0 eV) and E (652.4 eV). The XAS multiplet structure and the spacing between A-B(1.2 eV) and A-C(3.7 eV) are typical for the  $Mn^{2+}$  valence state in MnO as discussed by Gilbert *et al.*<sup>13</sup> and observed in different XAS measurements.<sup>14,15</sup> Although the oxidation of the Mn-rich GeMn nanocolumns surrounded by a quasipure Ge matrix could form complex (Ge,Mn)O oxides, the gradual formation of the typical  $Mn^{2+}$  multiplet fine structure upon oxidation is the signature of manganositelike (i.e., a MnO-like oxide) caps forming at the surface the GeMn nanocolumns.

In the well-protected nonoxidized nanocolumns, the magnetic field-dependent intensity of the XMCD signal at

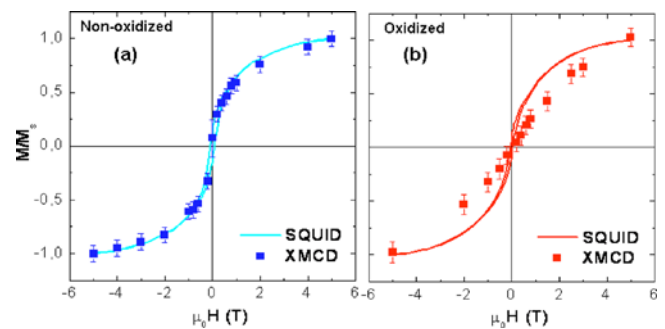


FIG. 3. (Color online) Magnetization curves measured by using SQUID (solid line) and XMCD (circles) in following: (a) nonoxidized GeMn (80 nm) and (b) GeMn-oxide(20 nm)/GeMn(60 nm) measured at 5 K and normalized to the magnetization value measured at 5 T. The XMCD signal is the magnetic field-dependent amplitude of the dichroism at the Mn  $L_3$  edge.

the Mn  $L_3$  peak closely follows the magnetization loop  $M(H)$  measured by SQUID magnetometry [Fig. 3(a)], suggesting that the topmost layers (about 5–7 nm) probed by XMCD are indeed representative of the properties of the whole GeMn nanocolumns length. When the columns are oxidized over 20 nm [Fig. 3(b)], a clear difference in the field-dependent signal measured by the two methods is observed. This is due to the in-depth sensitivity of the SQUID magnetometer that allows us to probe the whole film thickness, i.e., the oxidized caps as well as the ferromagnetic GeMn nanocolumns underneath versus the surface sensitivity of soft x-ray magnetic dichroism that mostly probes the oxidized caps.

We have exploited these GeMn-oxide caps (20 nm) to induce EB with the base ferromagnetic column layer (60 nm) following the well-established FC procedure below the MnO blocking temperature (118 K). The detailed ferromagnetic properties of the nonoxidized GeMn nanocolumns could be found in Refs. 8 and 9. To precisely determine any modification in the magnetization hysteresis loops (shift or coercive field increase),  $M(H)$  measurements have been performed before and after FC from 300 to 5 K at different magnetic field values applied in the film plane (i.e., perpendicular to the columns).

As shown in Fig. 4 and Fig. 5, a positive cooling field shifts the magnetization curve toward the negative field values ( $H_E$  negative) while cooling the system under a negative magnetic field shifts the magnetization toward the positive field values ( $H_E$  positive). The shift in the hysteresis loop

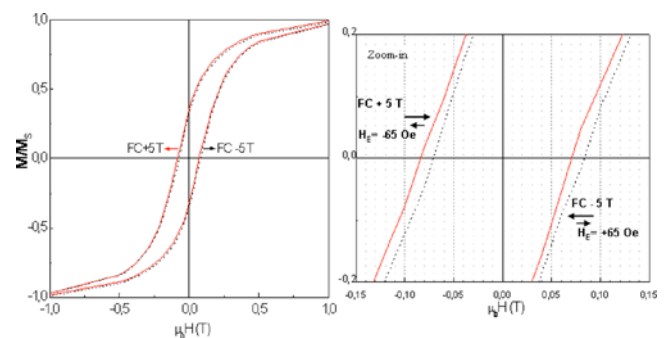


FIG. 4. (Color online) Magnetization curves after cooling the sample from room temperature to 5 K under a magnetic field of 5 T (solid line) and  $-5$  T (dashed line). The loops are symmetrically shifted by  $H_E=65$  Oe in the direction opposite to the cooling field while the coercive field increases by  $\Delta H_C \sim 60$  Oe with respect to the zero-field cooled value ( $H_C(ZFC) = 650$  Oe).

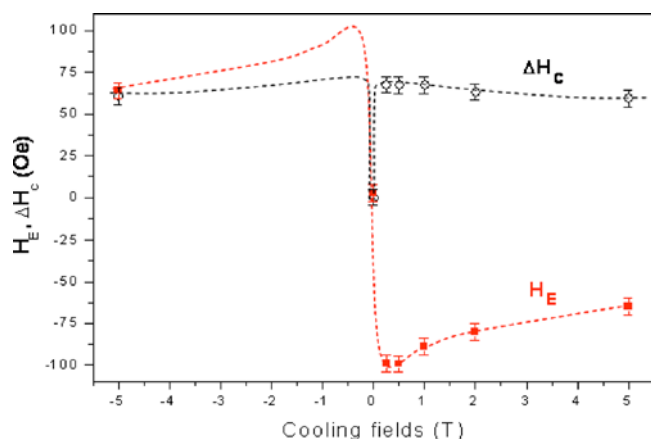


FIG. 5. (Color online) Variation in the exchange field  $H_E$  (squares) and the coercive field variation  $\Delta H_C$  (open circles) as a function of the cooling field. All the measurements were performed at 5 K. The dashed lines are guides of the eyes.

upon the FC procedure is accompanied by an enhancement of the coercive field. These two effects are the signature of a clear EB. The same result was obtained in different GeMn samples where the exchange field was in the range of 65–100 Oe. Only the coercive field varied from 30–100 Oe, depending on the oxide layer thickness. Our study revealed in addition that cooling under a field as low as 0.25 T is sufficient to induce EB in the GeMn nanocolumns with an exchange field  $|H_E|=100$  Oe and a coercive field enhancement of about 70 Oe (Fig. 5) with respect to the zero field-cooling value (650 Oe). A similarly enhanced EB at low-cooling fields has been reported by Pan *et al.*<sup>16</sup> in cobalt oxide. This effect was ascribed to the relative orientation between the cooling field and measurement field and the (intrinsic) easy magnetization axis of the system.

The exchange field obtained in our GeMn-oxide/GeMn nanocolumns is comparable to the exchange field values previously reported in other ferromagnetic semiconductor-based heterostructures as follows: 90–180 Oe in MnO/(Ga,Mn)As and IrMn/(Ga,Mn)As (Refs. 17–19) and around 70 Oe in MnO/Cr-doped GaN.<sup>20</sup>

A MnO(3 nm)/GeMn(40 nm) bilayer has been prepared by naturally oxidizing in ambient atmosphere a pure Mn film deposited on GeMn nanocolumns. An exchange field  $H_E$  (MnO/GeMn) = −70 Oe and  $\Delta H_C$  (MnO/GeMn) = 410 Oe was obtained in this case upon a similar FC procedure under a positive field. Annealing in air at 200 °C for 150 s induces an additional coercive field increase of 660 Oe and a shift in the magnetization curve of −150 Oe. This enhanced EB is explained by the presence of a more defined antiferromagnetic Mn–O compound in the system and by the thicker antiferromagnetic layer (MnO+oxidized-GeMn caps) that is obtained upon annealing in air. This result supports also that

MnO is indeed at the origin of the observed EB in GeMn-oxide caps/GeMn nanocolumns.

In conclusion, exchange biasing of self-organized ferromagnetic GeMn nanocolumns by oxidized-GeMn caps is reported. The XAS measurements performed in GeMn-oxides shows a multiplet structure that is typical of the  $Mn^{2+}$  valence state in MnO. The magnetic measurements show a clear EB revealed by the hysteresis shift toward negative magnetic fields upon positive FC (and vice versa) that is accompanied by the enhancement of the coercive field. The observed EB is attributed to the exchange coupling at the interface between the ferromagnetic GeMn nanocolumns and the antiferromagnetic MnO-like caps.

This work has been supported by the French National Research Agency (ANR) under Project No. ANR-07-NANO-003-02.

- <sup>1</sup>N. A. Spaldin and M. Fiebig, *Science* **309**, 391 (2005).
- <sup>2</sup>D. D. Awschalom and M. E. Flatté, *Nat. Phys.* **3**, 153 (2007).
- <sup>3</sup>D. Chiba, M. Sawicki, Y. Nishitani, Y. Nakatani, F. Matsukura, and H. Ohno, *Nature (London)* **455**, 515 (2008).
- <sup>4</sup>K. F. Eid, M. B. Stone, K. C. Ku, O. Maksimov, P. Schiffer, N. Samarth, T. C. Shih, and C. J. Palmström, *Appl. Phys. Lett.* **85**, 1556 (2004).
- <sup>5</sup>Z. Wei, A. Sharma, A. S. Nunez, P. M. Haney, R. A. Duine, J. Bass, A. H. MacDonald, and M. Tsoi, *Phys. Rev. Lett.* **98**, 116603 (2007).
- <sup>6</sup>X. Chen, A. Hochstrat, P. Borisov, and W. Kleemann, *Appl. Phys. Lett.* **89**, 202508 (2006).
- <sup>7</sup>V. Laukhin, V. Skumryev, X. Marti, D. Hrabovsky, F. Sanchez, M. V. Garcia-Cuenca, C. Ferrater, M. Varela, U. Lüders, J. F. Bobo, and J. Fontcuberta, *Phys. Rev. Lett.* **97**, 227201 (2006).
- <sup>8</sup>M. Jamet, A. Barski, T. Devillers, V. Poydenot, R. Dujardin, P. Bayle-Guillemaud, J. Rothman, E. Bellet-Amalric, A. Marty, J. Cibert, R. Matana, and S. Tatarenko, *Nature Mater.* **5**, 653 (2006).
- <sup>9</sup>T. Devillers, M. Jamet, A. Barski, V. Poydenot, P. Bayle-Guillemaud, E. Bellet-Amalric, S. Cherifi, and J. Cibert, *Phys. Rev. B* **76**, 205306 (2007).
- <sup>10</sup>T. Fukushima, K. Sato, H. Katayama-Yoshida, and P. H. Dederichs, *Jpn. J. Appl. Phys., Part 1* **45**, L416 (2006).
- <sup>11</sup>*The Oxide Handbook*, edited by G. V. Samsonov (Plenum, New York, 1973).
- <sup>12</sup>A. Continenza and G. Profeta, *Phys. Rev. B* **78**, 085215 (2008).
- <sup>13</sup>B. Gilbert, B. H. Frazer, A. Belz, P. G. Conrad, K. H. Neilson, D. Haskel, J. C. Lang, G. Srajer, and G. De Stasio, *J. Phys. Chem. A* **107**, 2839 (2003).
- <sup>14</sup>S. Andrieu, E. Foy, H. Fischer, M. Alnot, F. Chevrier, G. Krill, and M. Picuch, *Phys. Rev. B* **58**, 8210 (1998).
- <sup>15</sup>P. Gambardella, L. Claude, S. Rusponi, K. J. Franke, H. Brune, J. Raabe, F. Nolting, P. Bencok, A. T. Hanbicki, B. T. Jonker, C. Grazioli, M. Veronese, and C. Carbone, *Phys. Rev. B* **75**, 125211 (2007).
- <sup>16</sup>M. Pan, B. Youa, Y. Zhao, S. Wang, M. Lu, A. Hu, H. Zhai, S. Zhou, *Phys. Lett. A* **313**, 442 (2003).
- <sup>17</sup>K. F. Eid, M. B. Stone, O. Maksimov, T. C. Shih, K. C. Ku, W. Fadgen, C. J. Palmström, P. Schiffer, and N. Samarth, *J. Appl. Phys.* **97**, 10D304 (2005).
- <sup>18</sup>H. T. Lin, Y. F. Chen, P. W. Huang, S. H. Wang, J. H. Huang, C. H. Lai, W. N. Lee, and T. S. Chin, *Appl. Phys. Lett.* **89**, 262502 (2006).
- <sup>19</sup>Z. Ge, W. L. Lim, S. Shen, Y. Y. Zhou, X. Liu, J. K. Furdyna, and M. Dobrowolska, *Phys. Rev. B* **75**, 014407 (2007).
- <sup>20</sup>H. X. Liu, S. Y. Wu, R. K. Singh, and N. Newman, *J. Appl. Phys.* **98**, 046106 (2005).

# Bibliographie

- [1] M. N. Baibich, J. M. Broto, A. Fert, F. Nguyen Van Dau, F. Petroff, P. Etienne, G. Creuzet, A. Friederich, and J. Chazelas. Giant magnetoresistance of (001)Fe/(001)Cr magnetic superlattices. *Physical Review Letters*, 61(21) :2472, November 1988. doi : 10.1103/PhysRevLett.61.2472. URL <http://link.aps.org/abstract/PRL/v61/p2472>. Copyright (C) 2009 The American Physical Society ; Please report any problems to [prola@aps.org](mailto:prola@aps.org).
- [2] G. Binasch, P. Grünberg, F. Saurenbach, and W. Zinn. Enhanced magnetoresistance in layered magnetic structures with antiferromagnetic interlayer exchange. *Physical Review B*, 39(7) :4828, March 1989. doi : 10.1103/PhysRevB.39.4828. URL <http://link.aps.org/abstract/PRB/v39/p4828>. Copyright (C) 2009 The American Physical Society ; Please report any problems to [prola@aps.org](mailto:prola@aps.org).
- [3] B. Dieny, B. A. Gurney, S. E. Lambert, D. Mauri, S. S. P. Parkin, V. S. Speriosu, D. R. Wilhoit, M Hill, and International Business Machines. Magnetoresistive sensor based on the spin valve effect, April 1993. URL <http://www.google.fr/patents?hl=fr&lr=&vid=USPAT5206590&id=PkAnAAAAEBAJ&oi=fnd&dq=dieny+spin-valve&printsec=abstract>. undefinedFiling Date : 11 Dec 1990.
- [4] wikimedia commons. URL <http://commons.wikimedia.org/>.
- [5] M. Julliere. Tunneling between ferromagnetic films. *Physics Letters A*, 54(3) :225–226, September 1975. ISSN 0375-9601. doi : 10.1016/0375-9601(75)90174-7. URL <http://www.sciencedirect.com.gate4.inist.fr/science/article/B6TVM-46R3N46-10D/2/90703cfc684b0679356dce9a76b2e942>.

- [6] Stuart S. P. Parkin, Christian Kaiser, Alex Panchula, Philip M. Rice, Brian Hughes, Mahesh Samant, and See-Hun Yang. Giant tunnelling magnetoresistance at room temperature with MgO (100) tunnel barriers. *Nature Materials*, 3(12) :862–867, December 2004. ISSN 1476-1122. doi : 10.1038/nmat1256. URL <http://dx.doi.org/10.1038/nmat1256>.
- [7] Supriyo Datta and Biswajit Das. Electronic analog of the electro-optic modulator. *Applied Physics Letters*, 56(7) :665, 1990. ISSN 00036951. doi : 10.1063/1.102730. URL <http://link.aip.org/link/APPLAB/v56/i7/p665/s1&Agg=doi>.
- [8] J. M. Kikkawa and D. D. Awschalom. Lateral drag of spin coherence in gallium arsenide. *Nature*, 397(6715) :139–141, January 1999. ISSN 0028-0836. doi : 10.1038/16420. URL <http://dx.doi.org/10.1038/16420>.
- [9] Georges Lampel. Nuclear dynamic polarization by optical electronic saturation and optical pumping in semiconductors. *Physical Review Letters*, 20(10) :491, March 1968. doi : 10.1103/PhysRevLett.20.491. URL <http://link.aps.org/doi/10.1103/PhysRevLett.20.491>.
- [10] G. Schmidt, D. Ferrand, L. W. Molenkamp, A. T. Filip, and B. J. van Wees. Fundamental obstacle for electrical spin injection from a ferromagnetic metal into a diffusive semiconductor. *Physical Review B*, 62(8) :R4790, 2000. doi : 10.1103/PhysRevB.62.R4790. URL <http://link.aps.org/doi/10.1103/PhysRevB.62.R4790>.
- [11] A. Fert and H. Jaffrès. Conditions for efficient spin injection from a ferromagnetic metal into a semiconductor. *Physical Review B*, 64(18) : 184420, October 2001. doi : 10.1103/PhysRevB.64.184420. URL <http://link.aps.org/doi/10.1103/PhysRevB.64.184420>.
- [12] Ian Appelbaum, Biqin Huang, and Douwe J. Monsma. Electronic measurement and control of spin transport in silicon. *Nature*, 447(7142) : 295–298, May 2007. ISSN 0028-0836. doi : 10.1038/nature05803. URL <http://dx.doi.org/10.1038/nature05803>.
- [13] Biqin Huang, Lai Zhao, Douwe J. Monsma, and Ian Appelbaum. 35% magnetocurrent with spin transport through si. *Applied Physics Letters*, 91(5) :052501, 2007. ISSN 00036951. doi : 10.1063/1.2767198. URL [http://apl.aip.org/resource/1/applab/v91/i5/p052501\\_s1](http://apl.aip.org/resource/1/applab/v91/i5/p052501_s1).



- [14] FZU. Ferromagnetic semiconductor spintronics website. URL [http://unix12.fzu.cz/ms/navigate.php?cont=public\\_in](http://unix12.fzu.cz/ms/navigate.php?cont=public_in).
- [15] T. Dietl, H. Ohno, F. Matsukura, J. Cibert, and D. Ferrand. Zener model description of ferromagnetism in Zinc-Blende magnetic semiconductors. *Science*, 287(5455) :1019–1022, February 2000. doi : 10.1126/science.287.5455.1019. URL <http://www.sciencemag.org/cgi/content/abstract/287/5455/1019>.
- [16] Kazunori Sato, Hiroshi Katayama-Yoshida, and Peter H. Dederichs. High curie temperature and Nano-Scale spinodal decomposition phase in dilute magnetic semiconductors. *Japanese Journal of Applied Physics*, 44(30) : L948–L951, 2005. doi : 10.1143/JJAP.44.L948. URL <http://jjap.ipap.jp/link?JJAP/44/L948/>.
- [17] H. Katayama-Yoshida, K. Sato, T. Fukushima, M. Toyoda, H. Kizaki, V.A. Dinh, and P.H. Dederichs. Computational nano-materials design for high-TC ferromagnetism in wide-gap magnetic semiconductors. *Journal of Magnetism and Magnetic Materials*, 310(2, Part 3) :2070–2077, March 2007. ISSN 0304-8853. doi : 10.1016/j.jmmm.2006.10.1120. URL <http://www.sciencedirect.com.gate4.inist.fr/science/article/B6TJJ-4MFTTDJ-5/2/6cd9beecf8df5bf49bc25a12c8718fa4>.
- [18] K Sato, T Fukushima, and H Katayama-Yoshida. Ferromagnetism and spinodal decomposition in dilute magnetic nitride semiconductors. *Journal of Physics : Condensed Matter*, 19(36) :365212, 2007. ISSN 0953-8984. doi : 10.1088/0953-8984/19/36/365212. URL <http://iopscience.iop.org/0953-8984/19/36/365212/>.
- [19] Shinji Kuroda, Nozomi Nishizawa, Koki Takita, Masanori Mitome, Yoshio Bando, Krzysztof Osuch, and Tomasz Dietl. Origin and control of high-temperature ferromagnetism in semiconductors. *Nature Materials*, 6(6) : 440–446, June 2007. ISSN 1476-1122. doi : 10.1038/nmat1910. URL <http://dx.doi.org/10.1038/nmat1910>.
- [20] A. Bonanni, A. Navarro-Quezada, Tian Li, M. Wegscheider, Z. Matecaronj, V. Holý, R. T. Lechner, G. Bauer, M. Rovezzi, F. D’Acapito, M. Kiecana, M. Sawicki, and T. Dietl. Controlled aggregation of magnetic ions in a semiconductor : An experimental demonstration. *Physical Review Letters*,

- 101(13) :135502, 2008. doi : 10.1103/PhysRevLett.101.135502. URL <http://link.aps.org/doi/10.1103/PhysRevLett.101.135502>.
- [21] Pham Nam Hai, Shinobu Ohya, Masaaki Tanaka, Stewart E. Barnes, and Sadamichi Maekawa. Electromotive force and huge magnetoresistance in magnetic tunnel junctions. *Nature*, 458(7237) :489–492, 2009. ISSN 0028-0836. doi : 10.1038/nature07879. URL [http://ovidsp.tx.ovid.com.gate4.inist.fr/sp-3.2.4b/ovidweb.cgi?&S=DHNAFPNMBHDDHDOPNCDLAHGCHHMAAA00&Link+Set=S.sh.15.17.22.27%7c61%7csl\\_10](http://ovidsp.tx.ovid.com.gate4.inist.fr/sp-3.2.4b/ovidweb.cgi?&S=DHNAFPNMBHDDHDOPNCDLAHGCHHMAAA00&Link+Set=S.sh.15.17.22.27%7c61%7csl_10).
- [22] Matthieu Jamet, Andre Barski, Thibaut Devillers, Valier Poydenot, Romain Dujardin, Pascale Bayle-Guillemaud, Johan Rothman, Edith Bellet-Amalric, Alain Marty, Joel Cibert, Richard Mattana, and Serge Tatarenko. High-Curie-temperature ferromagnetism in self-organized Ge<sub>1-x</sub>Mn<sub>x</sub> nanocolumns. *Nature Materials*, 5(8) :653–659, 2006. ISSN 1476-1122. doi : 10.1038/nmat1686. URL <http://dx.doi.org/10.1038/nmat1686>.
- [23] Yong Jae Cho, Chang Hyun Kim, Han Sung Kim, Wang Su Lee, Seong-Hun Park, Jeunghye Park, Seung Yong Bae, Bongsoo Kim, Hangil Lee, and Jae-Young Kim. Ferromagnetic Ge<sub>1-x</sub>M<sub>x</sub> (M = mn, fe, and co) nanowires. *Chemistry of Materials*, 20(14) :4694–4702, July 2008. doi : 10.1021/cm7035635. URL <http://dx.doi.org/10.1021/cm7035635>.
- [24] T. B. Massalski. *Binary Alloy Phase Diagrams*. ASM International(OH), 2nd (3 volumes) edition, December 1990. ISBN 087170403X.
- [25] T. Ohba, N. Watanabe, and Y. Komura. Temperature dependence of the lattice constants and the structure of Mn<sub>11</sub>Ge<sub>8</sub> at 295 and 116 k. *Acta Crystallographica Section B Structural Science*, 40(4) :351–354, 1984. ISSN 0108-7681. doi : 10.1107/S0108768184002287. URL <http://scripts.iucr.org/cgi-bin/paper?S0108768184002287>.
- [26] L. Castelliz. Kristallstruktur von Mn<sub>5</sub>Ge<sub>3</sub> und einiger ternärer phasen mit zwei Übergangselementen. *Monatshefte für Chemie*, 84(4) :765–776, 1953. ISSN 0026-9247. doi : 10.1007/BF00902776. URL <http://www.springerlink.com.gate4.inist.fr/content/n33kk52u1244m5w0/>.
- [27] Tetuo Ohoyama. X-ray and magnetic studies of the Manganese-Germanium system. *Journal of the Physical Society of Japan*, 16 :1995–2002, 1961. ISSN



- 0031-9015. doi : 10.1143/JPSJ.16.1995. URL <http://jpsj.ipap.jp/link?JPSJ/16/1995>.
- [28] Tetuo Ohoyama, Kō Yasukōchi, and Kazuo Kanematsu. A new phase of an intermetallic compound  $\text{Mn}_{3.4}\text{Ge}$  and its magnetism. *Journal of the Physical Society of Japan*, 16 :352–353, 1961. ISSN 0031-9015. doi : 10.1143/JPSJ.16.352. URL <http://jpsj.ipap.jp/link?JPSJ/16/352>.
- [29] T. Dietl, H. Ohno, and F. Matsukura. Hole-mediated ferromagnetism in tetrahedrally coordinated semiconductors. *Physical Review B*, 63(19) :195205, April 2001. doi : 10.1103/PhysRevB.63.195205. URL <http://link.aps.org/doi/10.1103/PhysRevB.63.195205>.
- [30] T. C. Schulthess and W. H. Butler. Electronic structure and magnetic interactions in mn doped semiconductors. *Journal of Applied Physics*, 89(11) :7021, 2001. ISSN 00218979. doi : 10.1063/1.1359456. URL <http://link.aip.org/link/JAPIAU/v89/i11/p7021/s1&Agg=doi>.
- [31] Yu-Jun Zhao, Tatsuya Shishidou, and A. J. Freeman. Ruderman-Kittel-Kasuya-Yosida-like ferromagnetism in  $\text{Mn}_x\text{Ge}_{1-x}$ . *Physical Review Letters*, 90(4) :047204, January 2003. doi : 10.1103/PhysRevLett.90.047204. URL <http://link.aps.org/doi/10.1103/PhysRevLett.90.047204>.
- [32] A. Continenza, G. Profeta, and S. Picozzi. Transition metal impurities in ge : Chemical trends and codoping studied by electronic structure calculations. *Physical Review B*, 73(3) :035212, January 2006. doi : 10.1103/PhysRevB.73.035212. URL <http://link.aps.org/doi/10.1103/PhysRevB.73.035212>.
- [33] A. Continenza, G. Profeta, and S. Picozzi. Transition metal doping and clustering in ge. *Applied Physics Letters*, 89(20) :202510–3, November 2006. doi : 10.1063/1.2388894. URL <http://link.aip.org/link/?APL/89/202510/1>.
- [34] Alessandra Continenza, Gianni Profeta, and Silvia Picozzi. Transition metal doping in ge. *Journal of Magnetism and Magnetic Materials*, 310(2, Part 3) : 2147–2149, March 2007. ISSN 0304-8853. doi : 10.1016/j.jmmm.2006.10.940. URL <http://www.sciencedirect.com.gate4.inist.fr/science/article/B6TJJ-4MCW7NJ-P/2/681d5f4b4fc8d826a4d61e13599fbc34>.
- [35] Silvia Picozzi and Marjana Lezaic. Ab-initio study of exchange constants and electronic structure in diluted magnetic group-IV semiconductors. *New*

- Journal of Physics*, 10(5) :055017, 2008. ISSN 1367-2630. URL <http://www.iop.org/EJ/abstract/1367-2630/10/5/055017/>.
- [36] S. Decoster, S. Cottenier, U. Wahl, J. G. Correia, L. M. C. Pereira, C. Lacasta, M. R. Da Silva, and A. Vantomme. Diluted manganese on the bond-centered site in germanium. *Applied Physics Letters*, 97(15) :151914, 2010. ISSN 00036951. doi : 10.1063/1.3501123. URL <http://link.aip.org/link/APPLAB/v97/i15/p151914/s1&Agg=doi>.
- [37] Li Zeng, A. Huegel, E. Helgren, F. Hellman, C. Piamonteze, and E. Arenholz. X-ray absorption study of the electronic structure of mn-doped amorphous si. *Applied Physics Letters*, 92(14) :142503, 2008. doi : 10.1063/1.2908050. URL <http://link.aip.org/link/?APL/92/142503/1>.
- [38] Li Zeng, E. Helgren, M. Rahimi, F. Hellman, R. Islam, B. J. Wilkens, R. J. Culbertson, and David J. Smith. Quenched magnetic moment in mn-doped amorphous si films. *Physical Review B*, 77(7) :073306, February 2008. doi : 10.1103/PhysRevB.77.073306. URL <http://link.aps.org/doi/10.1103/PhysRevB.77.073306>.
- [39] Alessandra Continenza and Gianni Profeta. Mn doping in model amorphous si and ge : A theoretical investigation. *Journal of Physics : Conference Series*, 200(3) :032014, 2010. ISSN 1742-6596. doi : 10.1088/1742-6596/200/3/032014. URL <http://iopscience.iop.org/1742-6596/200/3/032014?fromSearchPage=true>.
- [40] S. Caprara, V. N. Men'shov, V. V. Tugushev, P. M. Echenique, and E. V. Chulkov. Effect of carrier confinement on exchange coupling in dilute magnetic semiconductors with self-organized nanocolumns. *Physical Review B*, 79(3) :035202, January 2009. doi : 10.1103/PhysRevB.79.035202. URL <http://link.aps.org/doi/10.1103/PhysRevB.79.035202>.
- [41] J. T. Arantes, Antônio J. R. da Silva, and A. Fazzio. Structural, electronic, and magnetic properties of mn-doped ge nanowires by ab initio calculations. *Physical Review B*, 75(11) :115113, March 2007. doi : 10.1103/PhysRevB.75.115113. URL <http://link.aps.org/doi/10.1103/PhysRevB.75.115113>.
- [42] Y. D. Park, A. T. Hanbicki, S. C. Erwin, C. S. Hellberg, J. M. Sullivan, J. E. Mattson, T. F. Ambrose, A. Wilson, G. Spanos, and B. T. Jonker. A Group-IV ferromagnetic semiconductor :  $\text{Mn}_x\text{Ge}_{1-x}$ . *Science*, 295(5555) :

- 651–654, January 2002. doi : 10.1126/science.1066348. URL <http://www.sciencemag.org/cgi/content/abstract/295/5555/651>.
- [43] F. D’Orazio, F. Lucari, S. Santucci, P. Picozzi, A. Verna, M. Passacantando, N. Pinto, L. Morresi, R. Gunnella, and R. Murri. Magneto-optical properties of epitaxial  $\text{Mn}_x\text{Ge}_{1-x}$  films. *Journal of Magnetism and Magnetic Materials*, 262(1) :158–161, May 2003. ISSN 0304-8853. doi : 10.1016/S0304-8853(03)00041-6. URL <http://www.sciencedirect.com.gate4.inist.fr/science/article/B6TJJ-47T84T2-2/2/f6a909a49957147566f10e03dc380656>.
- [44] F. D’Orazio, F. Lucari, N. Pinto, L. Morresi, and R. Murri. Toward room temperature ferromagnetism of Ge :Mn systems. *Journal of Magnetism and Magnetic Materials*, 272-276(Part 3) :2006–2007, May 2004. ISSN 0304-8853. doi : 10.1016/j.jmmm.2004.01.014. URL <http://www.sciencedirect.com.gate4.inist.fr/science/article/B6TJJ-4BHT558-2F/2/02f6666906071770c4df2409f0213dc6>.
- [45] N. Pinto, L. Morresi, R. Murri, F. D’Orazio, F. Lucari, M. Passacantando, and P. Picozzi. Growth process and characterization of magnetic semiconductors based on GeMn alloy films. *physica status solidi (c)*, 1(7) :1748–1751, 2004. doi : 10.1002/pssc.200304409. URL <http://dx.doi.org/10.1002/pssc.200304409>.
- [46] N. Pinto, L. Morresi, M. Ficcadenti, R. Murri, F. D’Orazio, F. Lucari, L. Boarino, and G. Amato. Magnetic and electronic transport percolation in epitaxial  $\text{Ge}_{1-x}\text{Mn}_x$  films. *Physical Review B*, 72(16) :165203, October 2005. doi : 10.1103/PhysRevB.72.165203. URL <http://link.aps.org/doi/10.1103/PhysRevB.72.165203>.
- [47] S. Picozzi, L. Ottaviano, M. Passacantando, G. Profeta, A. Continenza, F. Priolo, M. Kim, and A. J. Freeman. X-ray absorption spectroscopy in  $\text{Mn}_x\text{Ge}_{1-x}$  diluted magnetic semiconductor : Experiment and theory. *Applied Physics Letters*, 86(6) :062501, 2005. ISSN 00036951. doi : 10.1063/1.1861127. URL <http://link.aip.org/link/APPLAB/v86/i6/p062501/s1&Agg=doi>.
- [48] L. Morresi, N. Pinto, M. Ficcadenti, R. Murri, F. D’Orazio, and F. Lucari. Magnetic and transport polaron percolation in diluted

- GeMn films. *Materials Science and Engineering : B*, 126(2-3) :197–201, January 2006. ISSN 0921-5107. doi : 10.1016/j.mseb.2005.09.025. URL <http://www.sciencedirect.com.gate4.inist.fr/science/article/B6TXF-4HDP77C-F/2/fe5e0fa979d5cacd5b01d6bb1a35eb4b>.
- [49] P. De De Padova, C. Quaresima, P. Perfetti, N. Zema, C. Grazioli, M. Veronese, B. Olivieri, M.C. Richter, O. Heckmann, F. D’Orazio, F. Lucari, and K. Hricovini. Structural and magnetic properties of ge Mn/Ge(001) 2 1 diluted magnetic semiconductors. *Journal de Physique IV (Proceedings)*, 132 : 5 pages, 2006. doi : 10.1051/jp4:2006132044.
- [50] P. De Padova, A. Generosi, B. Paci, V. Rossi Albertini, P. Perfetti, C. Quaresima, B. Olivieri, M.C. Richter, O. Heckmann, F. D’Orazio, F. Lucari, and K. Hricovini. Morphological and magnetic properties of Ge/MnxGe1-x/Ge(0 0 1)2x1 diluted magnetic semiconductor. *Surface Science*, 600(18) : 4190–4194, September 2006. ISSN 0039-6028. doi : 10.1016/j.susc.2006.02.071. URL <http://www.sciencedirect.com.gate4.inist.fr/science/article/B6TVX-4K0FDMR-7/2/5df4f13bd16f07f5fe031a357e134844>.
- [51] L. Ottaviano, M. Passacantando, A. Verna, R. Gunnella, E. Principi, A. Di Cicco, G. Impellizzeri, and F. Priolo. Direct structural evidences of mn dilution in ge. *Journal of Applied Physics*, 100(6) :063528, 2006. ISSN 00218979. doi : 10.1063/1.2337388. URL <http://link.aip.org/link/JAPIAU/v100/i6/p063528/s1&Agg=doi>.
- [52] A. Verna, L. Ottaviano, M. Passacantando, S. Santucci, P. Picozzi, F. D’Orazio, F. Lucari, M. De Biase, R. Gunnella, M. Berti, A. Gasparotto, G. Impellizzeri, and F. Priolo. Ferromagnetism in ion implanted amorphous and nanocrystalline Mn<sub>x</sub>Ge<sub>1-x</sub>. *Physical Review B*, 74(8) :085204, 2006. doi : 10.1103/PhysRevB.74.085204. URL <http://link.aps.org/doi/10.1103/PhysRevB.74.085204>.
- [53] L. Ottaviano, M. Passacantando, A. Verna, F. D’Amico, and R. Gunnella. Mn l<sub>[sub 2,3]</sub> x-ray absorption spectra of a diluted Mn–Ge alloy. *Applied Physics Letters*, 90(24) :242105, 2007. ISSN 00036951. doi : 10.1063/1.2746063. URL <http://link.aip.org/link/APPLAB/v90/i24/p242105/s1&Agg=doi>.
- [54] R. B. Morgunov, A. I. Dmitriev, and O. L. Kazakova. Percolation ferromagnetism and spin waves in Ge :Mn thin films. *Physical Review B*,

- 80(8) :085205, 2009. doi : 10.1103/PhysRevB.80.085205. URL <http://link.aps.org/doi/10.1103/PhysRevB.80.085205>.
- [55] Yong Wang, Jin Zou, Zuoming Zhao, Xinhai Han, Xiaoyu Zhou, and Kang L. Wang. Mn behavior in  $\text{Ge}_{0.96}\text{Mn}_{0.04}$  magnetic thin films grown on si. *Journal of Applied Physics*, 103(6) :066104, 2008. ISSN 00218979. doi : 10.1063/1.2875110. URL <http://link.aip.org/link/JAPIAU/v103/i6/p066104/s1&Agg=doi>.
- [56] Sunglae Cho, Sungyoul Choi, Soon Cheol Hong, Yunki Kim, John B. Ketterson, Bong-Jun Kim, Y. C. Kim, and Jung-Hyun Jung. Ferromagnetism in mn-doped ge. *Physical Review B*, 66(3) :033303, July 2002. doi : 10.1103/PhysRevB.66.033303. URL <http://link.aps.org/doi/10.1103/PhysRevB.66.033303>.
- [57] Sung-Kyu Kim, S Park, K J Yee, Jong Yeog Son, Young-Han Shin, Moon-Ho Jo, and Tae Eun Hong. Electrical and optical observations of ferromagnetism in  $\text{Ge}_{0.7}\text{Mn}_{0.3}$  semiconductor. *Journal of Physics D : Applied Physics*, 42(8) :085005, 2009. ISSN 0022-3727. doi : 10.1088/0022-3727/42/8/085005. URL <http://iopscience.iop.org/0022-3727/42/8/085005/>.
- [58] Changgan Zeng, Zhenyu Zhang, Klaus van Benthem, Matthew F. Chisholm, and Hanno H. Weitering. Optimal doping control of magnetic semiconductors via subsurfactant epitaxy. *Physical Review Letters*, 100(6) :066101, February 2008. doi : 10.1103/PhysRevLett.100.066101. URL <http://link.aps.org/doi/10.1103/PhysRevLett.100.066101>.
- [59] Y. X. Chen, Shi shen Yan, Y. Fang, Y. F. Tian, S. Q. Xiao, G. L. Liu, Y. H. Liu, and L. M. Mei. Magnetic and transport properties of homogeneous  $\text{Mn}_x\text{Ge}_{1-x}$  ferromagnetic semiconductor with high mn concentration. *Applied Physics Letters*, 90(5) :052508, 2007. ISSN 00036951. doi : 10.1063/1.2436710. URL <http://link.aip.org/link/APPLAB/v90/i5/p052508/s1&Agg=doi>.
- [60] Jiang xia Deng, Yu feng Tian, Shi shen Yan, Qiang Cao, Guo lei Liu, Yan xue Chen, Liang mo Mei, Gang Ji, and Ze Zhang. Magnetism of amorphous  $\text{Ge}_{1-x}\text{Mn}_x$  magnetic semiconductor films. *Journal of Applied Physics*, 104(1) :013905, 2008. ISSN 00218979. doi : 10.1063/1.2951460. URL <http://link.aip.org/link/JAPIAU/v104/i1/p013905/s1&Agg=doi>.

- [61] F A Ferri and A R Zanatta. Structural, optical and morphological characterization of amorphous  $\text{Ge}_{100-x}\text{Mn}_x$  films deposited by sputtering. *Journal of Physics D : Applied Physics*, 42(3) :035005, 2009. ISSN 0022-3727. doi : 10.1088/0022-3727/42/3/035005. URL <http://iopscience.iop.org/0022-3727/42/3/035005/>.
- [62] Shinsuke Yada, Satoshi Sugahara, and Masaaki Tanaka. Magneto-optical and magnetotransport properties of amorphous ferromagnetic semiconductor  $\text{Ge}_{1-x}\text{Mn}_x$  thin films. *Applied Physics Letters*, 93(19) :193108, 2008. ISSN 00036951. doi : 10.1063/1.3023070. URL <http://link.aip.org/link/APPLAB/v93/i19/p193108/s1&Agg=doi>.
- [63] Y. D. Park, A. Wilson, A. T. Hanbicki, J. E. Mattson, T. Ambrose, G. Spanos, and B. T. Jonker. Magnetoresistance of Mn :Ge ferromagnetic nanoclusters in a diluted magnetic semiconductor matrix. *Applied Physics Letters*, 78(18) :2739, 2001. ISSN 00036951. doi : 10.1063/1.1369151. URL <http://link.aip.org/link/APPLAB/v78/i18/p2739/s1&Agg=doi>.
- [64] R. Gunnella, L. Morresi, N. Pinto, R. Murri, L. Ottaviano, M. Pasacantando, F. D’Orazio, and F. Lucari. Magnetization of epitaxial MnGe alloys on  $\text{Ge}(1\ 1\ 1)$  substrates. *Surface Science*, 577(1) :22–30, February 2005. ISSN 0039-6028. doi : 10.1016/j.susc.2004.12.021. URL <http://www.sciencedirect.com.gate4.inist.fr/science/article/B6TVX-4F9SVXH-4/2/ee6c6fcf8f4d0c9b9ce87c17b7b39654>.
- [65] L. Morresi, J.P. Ayoub, N. Pinto, M. Ficcadenti, R. Murri, A. Ronda, and I. Berbezier. Formation of  $\text{Mn}_5\text{Ge}_3$  nanoclusters in highly diluted  $\text{Mn}_x\text{Ge}_{1-x}$  alloys. *Materials Science in Semiconductor Processing*, 9(4-5) : 836–840, August 2006. ISSN 1369-8001. doi : 10.1016/j.mssp.2006.08.056. URL <http://www.sciencedirect.com.gate4.inist.fr/science/article/B6VPK-4KXWK3X-2/2/f91e3a7fadb6ebfd5241a2a86ee3d094>.
- [66] L. Morresi, J.P. Ayoub, N. Pinto, M. Ficcadenti, R. Murri, A. Ronda, I. Berbezier, F. D’Orazio, and F. Lucari. Structural, magnetic and electronic transport properties of  $\text{Mn}_x\text{Ge}_{1-x}/\text{Ge}(0\ 0\ 1)$  films grown by MBE at 350 °C. *Surface Science*, 601(13) :2632–2635, July 2007. ISSN 0039-6028. doi : 10.1016/j.susc.2006.11.077. URL <http://www.sciencedirect.com.gate4.inist.fr/science/article/B6TVX-4MRG27T-5/2/21735a3bc3f79db3e73ec6533bd2ca43>.

- [67] P. De Padova, J.-P. Ayoub, I. Berbezier, J.-M. Mariot, A. Taleb-Ibrahimi, M.C. Richter, O. Heckmann, A.M. Testa, D. Fiorani, B. Olivieri, S. Piccozzi, and K. Hricovini.  $\text{Mn}_x\text{Ge}_{1-x}$  thin layers studied by TEM, x-ray absorption spectroscopy and SQUID magnetometry. *Surface Science*, 601(13) :2628–2631, July 2007. ISSN 0039-6028. doi : 10.1016/j.susc.2006.11.076. URL <http://www.sciencedirect.com.gate4.inist.fr/science/article/B6TVX-4MRG27T-4/2/d9cb09adc9b68fe2eaa803cbb3b2b6ee>.
- [68] P. De Padova, L. Favre, I. Berbezier, B. Olivieri, A. Generosi, B. Paci, V. Rossi Albertini, P. Perfetti, C. Quaresima, J.-M. Mariot, A. Taleb-Ibrahimi, M.C. Richter, O. Heckmann, F. D’Orazio, F. Lucari, and K. Hricovini. Structural and magnetic properties of  $\text{Mn}_5\text{Ge}_3$  nanoclusters dispersed in  $\text{Mn}_x\text{Ge}_{1-x}/\text{Ge}(0\ 0\ 1)_{2\times 1}$  diluted magnetic semiconductors. *Surface Science*, 601(18) :4370–4374, September 2007. ISSN 0039-6028. doi : 10.1016/j.susc.2007.06.020. URL <http://www.sciencedirect.com.gate4.inist.fr/science/article/B6TVX-4P06C89-1/2/c6bbbd0d2cdc2c7ddafa4132f1bc65d4>.
- [69] P. De Padova, J.-P. Ayoub, I. Berbezier, P. Perfetti, C. Quaresima, A. M. Testa, D. Fiorani, B. Olivieri, J.-M. Mariot, A. Taleb-Ibrahimi, M. C. Richter, O. Heckmann, and K. Hricovini.  $\text{Mn}_{0.06}\text{Ge}_{0.94}$  diluted magnetic semiconductor epitaxially grown on  $\text{ge}(001)$  : Influence of  $\text{Mn}_5\text{Ge}_3$  nanoscopic clusters on the electronic and magnetic properties. *Physical Review B (Condensed Matter and Materials Physics)*, 77(4) :045203–7, January 2008. doi : 10.1103/PhysRevB.77.045203. URL <http://link.aps.org/abstract/PRB/v77/e045203>.
- [70] R Gunnella, L Morresi, N Pinto, A Di Cicco, L Ottaviano, M Passacantando, A Verna, G Impellizzeri, A Irrera, and F d’Acapito. Localization of the dopant in Ge :Mn diluted magnetic semiconductors by x-ray absorption at the mn k edge. *Journal of Physics : Condensed Matter*, 22(21) :216006, 2010. ISSN 0953-8984. doi : 10.1088/0953-8984/22/21/216006. URL <http://iopscience.iop.org/0953-8984/22/21/216006>.
- [71] E. Biegger, L. Stäheli, M. Fonin, U. Rüdiger, and Yu. S. Dedkov. Intrinsic ferromagnetism versus phase segregation in mn-doped ge. *Journal of Applied Physics*, 101(10) :103912, 2007. ISSN 00218979. doi : 10.1063/1.2718276. URL <http://link.aip.org/link/JAPIAU/v101/i10/p103912/s1&Agg=doi>.

- [72] Yong Wang, Jin Zou, Zuoming Zhao, Xinhai Han, Xiaoyu Zhou, and Kang L. Wang. Direct structural evidences of  $\text{mn}_{11}\text{Ge}_8$  and  $\text{mn}_5\text{Ge}_2$  clusters in  $\text{ge}_{0.96}\text{Mn}_{0.04}$  thin films. *Applied Physics Letters*, 92(10) :101913, 2008. ISSN 00036951. doi : 10.1063/1.2884527. URL <http://link.aip.org/link/APPLAB/v92/i10/p101913/s1&Agg=doi>.
- [73] C. Bihler, C. Jaeger, T. Vallaitis, M. Gjukic, M. S. Brandt, E. Pippel, J. Woltersdorf, and U. Gösele. Structural and magnetic properties of  $\text{mn}_5\text{Ge}_3$  clusters in a dilute magnetic germanium matrix. *Applied Physics Letters*, 88(11) :112506, 2006. ISSN 00036951. doi : 10.1063/1.2185448. URL <http://link.aip.org/link/APPLAB/v88/i11/p112506/s1&Agg=doi>.
- [74] R. T. Lechner, V. Holy, S. Ahlers, D. Bougeard, J. Stangl, A. Trampert, A. Navarro-Quezada, and G. Bauer. Self-assembled  $\text{mn}_5\text{Ge}_3$  nanomagnets close to the surface and deep inside a  $\text{ge}_{1-x}\text{Mn}_x$  epilayer. *Applied Physics Letters*, 95(2) :023102, 2009. ISSN 00036951. doi : 10.1063/1.3159827. URL <http://link.aip.org/link/APPLAB/v95/i2/p023102/s1&Agg=doi>.
- [75] S. Ahlers, D. Bougeard, H. Riedl, G. Abstreiter, A. Trampert, W. Kipferl, M. Sperl, A. Bergmaier, and G. Dollinger. Ferromagnetic  $\text{Ge}(\text{Mn})$  nanostructures. *Physica E : Low-dimensional Systems and Nanostructures*, 32 (1-2) :422–425, May 2006. ISSN 1386-9477. doi : 10.1016/j.physe.2005.12.129. URL <http://www.sciencedirect.com.gate4.inist.fr/science/article/B6VMT-4J6X4PV-4/2/3b2af909bccd042a76c4d9679e58447e>.
- [76] S. Ahlers, D. Bougeard, N. Sircar, G. Abstreiter, A. Trampert, M. Opel, and R. Gross. Magnetic and structural properties of  $\text{ge}_{1-x}\text{mn}_x$  films : Precipitation of intermetallic nanomagnets. *Physical Review B*, 74(21) : 214411, December 2006. doi : 10.1103/PhysRevB.74.214411. URL <http://link.aps.org/doi/10.1103/PhysRevB.74.214411>.
- [77] Shengqiang Zhou, Danilo Bürger, Manfred Helm, and Heidemarie Schmidt. Anomalous hall resistance in  $\text{Ge}:\text{Mn}$  systems with low  $\text{mn}$  concentrations. *Applied Physics Letters*, 95(17) :172103, 2009. ISSN 00036951. doi : 10.1063/1.3257363. URL <http://link.aip.org/link/APPLAB/v95/i17/p172103/s1&Agg=doi>.
- [78] Shengqiang Zhou, Artem Shalimov, Kay Potzger, Nicole M. Jeutter, Carsten Baetz, Manfred Helm, Jürgen Fassbender, and Heidemarie Schmidt.



- Memory effect of  $\text{Mn}_{0.5}\text{Ge}_{0.3}$  nanomagnets embedded inside a  $\text{Mn}$ -diluted  $\text{Ge}$  matrix. *Applied Physics Letters*, 95(19) :192505, 2009. ISSN 00036951. doi : 10.1063/1.3264076. URL <http://link.aip.org/link/APPLAB/v95/i19/p192505/s1&Agg=doi>.
- [79] Satoshi Sugahara, Kok Leong Lee, Shinsuke Yada, and Masaaki Tanaka. Precipitation of amorphous ferromagnetic semiconductor phase in epitaxially grown  $\text{Mn}$ -Doped  $\text{Ge}$  thin films. *Japanese Journal of Applied Physics*, 44 : L1426–L1429, 2005. ISSN 0021-4922. doi : 10.1143/JJAP.44.L1426. URL <http://jjap.ipap.jp/link?JJAP/44/L1426/>.
- [80] D. Bougeard, S. Ahlers, A. Trampert, N. Sircar, and G. Abstreiter. Clustering in a Precipitate-Free  $\text{GeMn}$  magnetic semiconductor. *Physical Review Letters*, 97(23) :237202, December 2006. doi : 10.1103/PhysRevLett.97.237202. URL <http://link.aps.org/doi/10.1103/PhysRevLett.97.237202>.
- [81] D. Bougeard, N. Sircar, S. Ahlers, V. Lang, G. Abstreiter, A. Trampert, J. M. LeBeau, S. Stemmer, D. W. Saxey, and A. Cerezo.  $\text{Ge}_{1-x}\text{Mn}_x$  clusters : Central structural and magnetic building blocks of nanoscale Wire-Like Self-Assembly in a magnetic semiconductor. *Nano Letters*, 9(11) :3743–3748, November 2009. doi : 10.1021/nl901928f. URL <http://dx.doi.org/10.1021/nl901928f>.
- [82] T. Devillers, M. Jamet, A. Barski, V. Poydenot, P. Bayle-Guillemaud, E. Bellet-Amalric, S. Cherifi, and J. Cibert. Structure and magnetism of self-organized  $\text{Ge}_{1-x}\text{Mn}_x$  nanocolumns on  $\text{Ge}(001)$ . *Physical Review B (Condensed Matter and Materials Physics)*, 76(20) :205306–12, November 2007. doi : 10.1103/PhysRevB.76.205306. URL <http://link.aps.org/abstract/PRB/v76/e205306>.
- [83] T. Devillers, M. Jamet, A. Barski, V. Poydenot, R. Dujardin, P. Bayle-Guillemaud, J. Rothman, E. Bellet Amalric, J. Cibert, R. Mattana, and S. Tatarenko. Structural and magnetic properties of  $\text{GeMn}$  layers; high curie temperature ferromagnetism induced by self organized  $\text{GeMn}$  nano-columns. *physica status solidi (a)*, 204(1) : 130–135, 2007. ISSN 18626300. doi : 10.1002/pssa.200673026. URL <http://onlinelibrary.wiley.com/doi/10.1002/pssa.200673026/abstract;jsessionid=01CC348278124098A0D42C63840A3FFA.d03t01>.

- [84] S. Tardif, Ing-Song Yu, T. Devillers, M. Jamet, S. Cherifi, J. Cibert, A. Barski, P. Bayle-Guillemaud, and E. Bellet-Amalric. From diluted magnetic semiconductors to self-organized nanocolumns of GeMn in germanium. In Manijeh Razeghi, Henri-Jean M. Drouhin, and Jean-Eric Wegrowe, editors, *Spintronics*, volume 7036, pages 703615–10, San Diego, CA, USA, 2008. SPIE. URL <http://link.aip.org/link/?PSI/7036/703615/1>.
- [85] M. Rovezzi, T. Devillers, E. Arras, F. d’Acapito, A. Barski, M. Jamet, and P. Pochet. Atomic structure of mn-rich nanocolumns probed by x-ray absorption spectroscopy. *Applied Physics Letters*, 92(24) :242510, 2008. ISSN 00036951. doi : 10.1063/1.2949077. URL <http://link.aip.org/link/APPLAB/v92/i24/p242510/s1&Agg=doi>.
- [86] S. Tardif, S. Cherifi, M. Jamet, T. Devillers, A. Barski, D. Schmitz, N. Darowski, P. Thakur, J. C. Cezar, N. B. Brookes, R. Mattana, and J. Cibert. Exchange bias in GeMn nanocolumns : The role of surface oxidation. *Applied Physics Letters*, 97(6) :062501, 2010. ISSN 00036951. doi : 10.1063/1.3476343. URL <http://link.aip.org/link/APPLAB/v97/i6/p062501/s1&Agg=doi>.
- [87] S. Tardif, V. Favre-Nicolin, F. Lançon, E. Arras, M. Jamet, A. Barski, C. Porret, P. Bayle-Guillemaud, P. Pochet, T. Devillers, and M. Rovezzi. Strain and correlation of self-organized Ge<sub>1-x</sub>Mn<sub>x</sub> nanocolumns embedded in ge (001). *Physical Review B*, 82(10) :104101, 2010. doi : 10.1103/PhysRevB.82.104101. URL <http://link.aps.org/doi/10.1103/PhysRevB.82.104101>.
- [88] M. Jamet, T. Devillers, I-S. Yu, A. Barski, P. Bayle-Guillemaud, J. Rothman, V. Favre-Nicolin, S. Tardif, S. Cherifi, J. Cibert, L. Grenet, P. Noe, V. Calvo, P. Warin, J-M. Hartmann, B. Rodmacq, and S. Au. (Ge,Mn) : a ferromagnetic semiconductor for spin injection in silicon. *International Journal of Nanotechnology*, 7(4/5/6/7/8) :575 – 590, 2010. doi : 10.1504/IJNT.2010.031734. URL [http://www.inderscience.com/search/index.php?action=record&rec\\_id=31734&prevQuery=&ps=10&m=or](http://www.inderscience.com/search/index.php?action=record&rec_id=31734&prevQuery=&ps=10&m=or).
- [89] E. Arras, I. Slipukhina, M. Torrent, D. Caliste, T. Deutsch, and P. Pochet. First principles prediction of the metastability of the ge[<sub>2</sub>]Mn phase and its synthesis pathways. *Applied Physics Letters*, 96(23) :231904, 2010. ISSN 00036951. doi : 10.1063/1.3446837. URL <http://link.aip.org/link/APPLAB/v96/i23/p231904/s1&Agg=doi>.

- [90] A. P. Li, C. Zeng, K. van Benthem, M. F. Chisholm, J. Shen, S. V. S. Nageswara Rao, S. K. Dixit, L. C. Feldman, A. G. Petukhov, M. Foygel, and H. H. Weitering. Dopant segregation and giant magnetoresistance in manganese-doped germanium. *Physical Review B (Condensed Matter and Materials Physics)*, 75(20) :201201–4, May 2007. doi : 10.1103/PhysRevB.75.201201. URL <http://link.aps.org/abstract/PRB/v75/e201201>.
- [91] Yong Wang, Faxian Xiu, Jin Zou, Kang L. Wang, and Ajey P. Jacob. Tadpole shaped  $\text{Ge}_{0.96}\text{Mn}_{0.04}$  magnetic semiconductors grown on si. *Applied Physics Letters*, 96(5) :051905, 2010. ISSN 00036951. doi : 10.1063/1.3297880. URL <http://link.aip.org/link/APPLAB/v96/i5/p051905/s1&Agg=doi>.
- [92] Faxian Xiu, Yong Wang, Kin Wong, Yi Zhou, Xufeng Kou, Jin Zou, and Kang L Wang. MnGe magnetic nanocolumns and nanowells. *Nanotechnology*, 21(25) :255602, 2010. ISSN 0957-4484. doi : 10.1088/0957-4484/21/25/255602. URL <http://iopscience.iop.org/0957-4484/21/25/255602?fromSearchPage=true>.
- [93] Faxian Xiu, Yong Wang, Jiyoung Kim, Augustin Hong, Jianshi Tang, Ajey P. Jacob, Jin Zou, and Kang L. Wang. Electric-field-controlled ferromagnetism in high-Curie-temperature  $\text{Mn}_{0.05}\text{Ge}_{0.95}$  quantum dots. *Nat Mater*, 9(4) : 337–344, April 2010. ISSN 1476-1122. doi : 10.1038/nmat2716. URL <http://dx.doi.org/10.1038/nmat2716>.
- [94] Olga Kazakova, Jaideep S. Kulkarni, Justin D. Holmes, and Sergej O. Demokritov. Room-temperature ferromagnetism in  $\text{Ge}_{1-x}\text{Mn}_x$  nanowires. *Physical Review B*, 72(9) :094415, 2005. doi : 10.1103/PhysRevB.72.094415. URL <http://link.aps.org/doi/10.1103/PhysRevB.72.094415>.
- [95] Tomasz Dietl. From our readers : Self-organized growth controlled by charge states of magnetic impurities. *Nat Mater*, 5(9) :673, 2006. ISSN 1476-1122. doi : 10.1038/nmat1721. URL <http://dx.doi.org/10.1038/nmat1721>.
- [96] Thibaut Devillers. *Etude des propriétés physiques des phases de  $\text{Ge}_{1-x}\text{Mn}_x$  ferromagnétiques pour l'électronique de spin*. PhD thesis, Université Joseph Fourier Grenoble I, November 2008. URL [http://tel.archives-ouvertes.fr/index.php?halsid=m0sbfu2ma2pkqe6vpnvrrrdh5&view\\_this\\_doc=tel-00367396&version=2](http://tel.archives-ouvertes.fr/index.php?halsid=m0sbfu2ma2pkqe6vpnvrrrdh5&view_this_doc=tel-00367396&version=2).

- [97] Emmanuel Arras. *Etude théorique de la structure et de la stabilité des alliages GeMn dans le cadre de la spintronique*. PhD thesis, Université Joseph Fourier Grenoble I, April 2010. URL [http://tel.archives-ouvertes.fr/index.php?halsid=dvi4amv85bio83tblfub42ipo3&view\\_this\\_doc=tel-00489879&version=2](http://tel.archives-ouvertes.fr/index.php?halsid=dvi4amv85bio83tblfub42ipo3&view_this_doc=tel-00489879&version=2).
- [98] D. T. Cromer and J. B. Mann. X-ray scattering factors computed from numerical Hartree–Fock wave functions. *Acta Crystallographica Section A*, 24(2) :321–324, 1968. ISSN 0567-7394. doi : 10.1107/S0567739468000550. URL <http://scripts.iucr.org/cgi-bin/quickfind>.
- [99] *Tables for X-Ray Crystallography*, volume C. AJC Wilson, kluwer academic publishing edition, 1995.
- [100] B L Henke, E M Gullikson, and J C Davis. *X-ray interactions : photoabsorption, scattering, transmission, and reflection at E=50-30000 eV, Z=1-92*, volume 54 of *Atomic Data and Nuclear Data Tables*. July 1993.
- [101] Mauro Rovezzi. *Study of the local order around magnetic impurities in semiconductors for spintronics*. PhD thesis, Université Joseph Fourier Grenoble I, October 2009. URL [http://tel.archives-ouvertes.fr/index.php?halsid=7sscdahaq9sr5m5opp4iv91jq3&view\\_this\\_doc=tel-00442852&version=1](http://tel.archives-ouvertes.fr/index.php?halsid=7sscdahaq9sr5m5opp4iv91jq3&view_this_doc=tel-00442852&version=1).
- [102] John S. Toll. Causality and the dispersion relation : Logical foundations. *Physical Review*, 104(6) :1760, December 1956. doi : 10.1103/PhysRev.104.1760. URL <http://link.aps.org/doi/10.1103/PhysRev.104.1760>.
- [103] Don T. Cromer. Relativistic calculation of anomalous scattering factors for x rays. *The Journal of Chemical Physics*, 53(5) :1891, 1970. ISSN 00219606. doi : 10.1063/1.1674266. URL <http://link.aip.org/link/?JCP/53/1891/1&Agg=doi>.
- [104] J. O. Cross, M. Newville, J. J. Rehr, L. B. Sorensen, C. E. Bouldin, G. Watson, T. Gouder, G. H. Lander, and M. I. Bell. Inclusion of local structure effects in theoretical x-ray resonant scattering amplitudes using ab initio x-ray-absorption spectra calculations. *Physical Review B*, 58(17) :11215, November 1998. doi : 10.1103/PhysRevB.58.11215. URL <http://link.aps.org/doi/10.1103/PhysRevB.58.11215>.

- [105] Helmut Dosch. *Critical Phenomena at Surfaces and Interfaces : Evanescent X-Ray and Neutron Scattering*. Springer, 1 edition, June 1992. ISBN 3540545344.
- [106] R. James. *Optical Principles of the Diffraction of X-Rays*. Ox Bow Press, June 1982. ISBN 0918024234.
- [107] Gilles Renaud, Rémi Lazzari, and Frédéric Leroy. Probing surface and interface morphology with grazing incidence small angle X-Ray scattering. *Surface Science Reports*, 64(8) :255–380, August 2009. ISSN 0167-5729. doi : 10.1016/j.surfrep.2009.07.002. URL <http://www.sciencedirect.com.gate4.inist.fr/science/article/B6TVY-4X36TK4-1/2/4b814e9c3f0ed2eb564018d156727c6e>.
- [108] M. A. Krivoglaz. *X-Ray and Neutron Diffraction in Nonideal Crystals*. Springer-Verlag Telos, January 1996. ISBN 0387505644.
- [109] K. Huang. X-Ray reflexions from dilute solid solutions. *Proceedings of the Royal Society of London. Series A. Mathematical and Physical Sciences*, 190 (1020) :102–117, June 1947. doi : 10.1098/rspa.1947.0064. URL <http://rspa.royalsocietypublishing.org/content/190/1020/102.abstract>.
- [110] Mikhail. A. Krivoglaz. *Theory of X-Ray and Thermal-Neutron Scattering By Real Crystals*. Plenum, first edition edition, January 1969.
- [111] V. Holy, U. Pietsch, and T. Baumbach. *High-Resolution X-Ray Scattering from Thin Films and Multilayers*. Springer-Verlag Berlin and Heidelberg GmbH & Co. K, December 1998. ISBN 354062029X.
- [112] Ulrich Pietsch, Vaclav Holy, and Tilo Baumbach. *High-Resolution X-Ray Scattering : From Thin Films to Lateral Nanostructures*. Springer-Verlag New York Inc., 2nd revised edition edition, September 2004. ISBN 0387400923.
- [113] M. J. Capitan, D. Thiaudiere, L. Goirand, R. Taffut, and S. Lequien. The ID01 beamline at the E.S.R.F. : the diffuse scattering technique applied to surface and interface studies. *Physica B : Condensed Matter*, 283(1-3) :256–261, June 2000. ISSN 0921-4526. doi : 10.1016/S0921-4526(99)01990-0. URL <http://www.sciencedirect.com.gate4.inist.fr/science/article/B6TVH-400WR74-K9/2/d22aa32139f9b76c441fd2144a578ded>.

- [114] ID1 - anomalous scattering, March 2010. URL <http://www.esrf.eu/UsersAndScience/Experiments/StructMaterials/ID01>.
- [115] A. Barbier, R. Baudoing-Savois, G. Renaud, M. de Santis, O. Robach, M.-C. Saint-Lager, P. Jeantet, P. Taunier, J.-P. Roux, O. Ulrich, A. Mougin, G. Berard, and O. Geaymond. Présentation des possibilités de la diffraction de surface en ultra-vide sur les lignes françaises à l'ESRF. *Le Journal de Physique IV*, 06(C4) :9, 1996. doi : 10.1051/jp4:1996431.
- [116] BM32 - CRG-IF - the french collaborating research group, September 2010. URL <http://www.esrf.eu/UsersAndScience/Experiments/CRG/BM32/>.
- [117] Marie-Ingrid Richard. *Etudes in situ et ex situ par rayonnement synchrotron de la croissance d'îlots de Ge sur substrats de Si(001) nominiaux et préstructurés*. PhD thesis, Université Joseph Fourier Grenoble I, Grenoble, December 2007. URL [http://tel.archives-ouvertes.fr/index.php?halsid=1n61q5k935d61igksbu7cm8mk3&view\\_this\\_doc=tel-00264059&version=1](http://tel.archives-ouvertes.fr/index.php?halsid=1n61q5k935d61igksbu7cm8mk3&view_this_doc=tel-00264059&version=1).
- [118] BM 2 - the D2AM french CRG beamline at ESRF, July 2010. URL <http://www.esrf.eu/UsersAndScience/Experiments/CRG/BM02>.
- [119] Johann Coraux. *Etude par spectroscopie X en condition de diffraction de la croissance et de l'encapsulation de boites quantiques GaN/AlN*. PhD thesis, Université Joseph Fourier Grenoble I, Grenoble, October 2006. URL [http://tel.archives-ouvertes.fr/index.php?halsid=13g5npgbqjnaad2gh4q86blgm4&view\\_this\\_doc=tel-00105778&version=4](http://tel.archives-ouvertes.fr/index.php?halsid=13g5npgbqjnaad2gh4q86blgm4&view_this_doc=tel-00105778&version=4).
- [120] Luciana Capello. *Etude par des méthodes de diffusion de rayons X des propriétés structurales du silicium après implantation ionique*. PhD thesis, Université Joseph Fourier Grenoble I, Grenoble, May 2005. URL [http://tel.archives-ouvertes.fr/index.php?halsid=26onjta1krt20qslf8kdtfvnq1&view\\_this\\_doc=tel-00009791&version=1](http://tel.archives-ouvertes.fr/index.php?halsid=26onjta1krt20qslf8kdtfvnq1&view_this_doc=tel-00009791&version=1).
- [121] The maxipix detector, March 2009. URL <http://www.esrf.eu/UsersAndScience/Experiments/TBS/ISG/maxipix>.

- [122] XPAD : a photon counting pixel detector for materials science, September 2010. URL <http://www.esrf.eu/UsersAndScience/Experiments/CRG/BM02/detectors/xpad>.
- [123] Claude Cohen-Tannoudji, Bernard Diu, and Franck Laloë. *Mécanique quantique I*. Hermann, October 1997. ISBN 2705660747.
- [124] J. L. Erskine and E. A. Stern. Calculation of the m<sub>23</sub> magneto-optical absorption spectrum of ferromagnetic nickel. *Physical Review B*, 12(11) : 5016, December 1975. doi : 10.1103/PhysRevB.12.5016. URL <http://link.aps.org/doi/10.1103/PhysRevB.12.5016>.
- [125] Anne Lehnert. *Magnetism of Individual Adatoms and of Epitaxial Monolayers*. PhD thesis, EPFL, Lausanne, June 2009.
- [126] J. Stohr. In *New Directions in Research with Third-Generation Soft X-Ray Synchrotron Radiation Sources (NATO Science Series E :)*. Kluwer Academic, 1 edition, April 1994. ISBN 0792326237.
- [127] B. T. Thole, P. Carra, F. Sette, and G. van der Laan. X-ray circular dichroism as a probe of orbital magnetization. *Physical Review Letters*, 68(12) :1943, March 1992. doi : 10.1103/PhysRevLett.68.1943. URL <http://link.aps.org/doi/10.1103/PhysRevLett.68.1943>.
- [128] Paolo Carra, B. T. Thole, Massimo Altarelli, and Xindong Wang. X-ray circular dichroism and local magnetic fields. *Physical Review Letters*, 70(5) :694, February 1993. doi : 10.1103/PhysRevLett.70.694. URL <http://link.aps.org/doi/10.1103/PhysRevLett.70.694>.
- [129] C. T. Chen, Y. U. Idzerda, H.-J. Lin, N. V. Smith, G. Meigs, E. Chaban, G. H. Ho, E. Pellegrin, and F. Sette. Experimental confirmation of the X-Ray magnetic circular dichroism sum rules for iron and cobalt. *Physical Review Letters*, 75(1) :152, July 1995. doi : 10.1103/PhysRevLett.75.152. URL <http://link.aps.org/doi/10.1103/PhysRevLett.75.152>.
- [130] H.P.J. Wijn, editor. *3d, 4d and 5d Elements, Alloys and Compounds*, volume 19a. Springer-Verlag, Berlin/Heidelberg, 1986. ISBN 3-540-15904-5. URL [http://www.springermaterials.com/navigation/navigation.do?m=1\\_2\\_109051\\_Magnetic+Properties+%C2%B7+Magnetic+Properties+of+Metals+%C2%B7+3d%2C+4d+and+5d+Elements%2C+Alloys+and+Compounds](http://www.springermaterials.com/navigation/navigation.do?m=1_2_109051_Magnetic+Properties+%C2%B7+Magnetic+Properties+of+Metals+%C2%B7+3d%2C+4d+and+5d+Elements%2C+Alloys+and+Compounds).

- [131] S. Eisebitt, T. Böske, J.-E. Rubensson, and W. Eberhardt. Determination of absorption coefficients for concentrated samples by fluorescence detection. *Physical Review B*, 47(21) :14103, June 1993. doi : 10.1103/PhysRevB.47.14103. URL <http://link.aps.org/doi/10.1103/PhysRevB.47.14103>.
- [132] E. Goering, S. Gold, A. Bayer, and G. Schuetz. Non-symmetric influences in the total electron yield x-ray magnetic circular dichroism signal in applied magnetic fields. *Journal of Synchrotron Radiation*, 8(2) :434–436, 2001. ISSN 09090495. doi : 10.1107/S0909049500018343. URL <http://scripts.iucr.org/cgi-bin/paper?S0909049500018343>.
- [133] Reiko Nakajima, J. Stöhr, and Y. U. Idzerda. Electron-yield saturation effects in l-edge x-ray magnetic circular dichroism spectra of fe, co, and ni. *Physical Review B*, 59(9) :6421, March 1999. doi : 10.1103/PhysRevB.59.6421. URL <http://link.aps.org/doi/10.1103/PhysRevB.59.6421>.
- [134] Reiko Nakajima. *X-ray Magnetic Circular Dichroism Spectroscopy in Transition Metal Thin Films*. PhD thesis, Stanford University, Stanford, CA, USA, January 1998. URL <http://ssrl.slac.stanford.edu/stohr/>.
- [135] U Englisch, H Rossner, H Maletta, J Bahrdt, S Sasaki, F Senf, K.J.S Sawhney, and W Gudat. The elliptical undulator UE46 and its monochromator beam-line for structural research on nanomagnets at BESSY-II. *Nuclear Instruments and Methods in Physics Research Section A : Accelerators, Spectrometers, Detectors and Associated Equipment*, 467-468(Part 1) :541–544, July 2001. ISSN 0168-9002. doi : 10.1016/S0168-9002(01)00407-7. URL <http://www.sciencedirect.com.gate4.inist.fr/science/article/B6TJM-43N61TY-4S/2/14e65e9bd9dce147aa8ebed8ce8d3ed1>.
- [136] Beamline UE46 PGM1. URL [http://www.bessy.de/bit/bit\\_show\\_object.html.php?i\\_bit\\_id\\_object=24](http://www.bessy.de/bit/bit_show_object.html.php?i_bit_id_object=24).
- [137] Shigemi Sasaki. Analyses for a planar variably-polarizing undulator. *Nuclear Instruments and Methods in Physics Research Section A : Accelerators, Spectrometers, Detectors and Associated Equipment*, 347(1-3) :83–86, August 1994. ISSN 0168-9002. doi : 10.1016/0168-9002(94)91859-7. URL <http://www.sciencedirect.com.gate4.inist.fr/science/article/B6TJM-46XYDK0-M/2/d8c81fd49878d4640cd4bf60b7194c80>.



- [138] Undulator - messplätze bei BESSY für untersuchungen an magnetischen nanostrukturen. URL [http://www.helmholtz-berlin.de/forschung/magma/magnetismus/instrumentierung-und-projekte/synchrotron-strahlung/bessy-aktivitaeten/undulator-messplaetze-bei-bessy\\_de.html](http://www.helmholtz-berlin.de/forschung/magma/magnetismus/instrumentierung-und-projekte/synchrotron-strahlung/bessy-aktivitaeten/undulator-messplaetze-bei-bessy_de.html).
- [139] Rolf Follath and Friedmar Senf. New plane-grating monochromators for third generation synchrotron radiation light sources. *Nuclear Instruments and Methods in Physics Research Section A : Accelerators, Spectrometers, Detectors and Associated Equipment*, 390(3) :388–394, May 1997. ISSN 0168-9002. doi : 10.1016/S0168-9002(97)00401-4. URL <http://www.sciencedirect.com.gate4.inist.fr/science/article/B6TJM-3SPKX96-4R/2/2892d1d04ea3e6593957c92b93c9f64f>.
- [140] V. Holy, R. T. Lechner, S. Ahlers, L. Horak, T. H. Metzger, A. Navarro-Quezada, A. Trampert, D. Bougeard, and G. Bauer. Diffuse x-ray scattering from inclusions in ferromagnetic gel-x mnx layers. *Physical Review B*, 78(14) :144401, October 2008. doi : 10.1103/PhysRevB.78.144401. URL <http://link.aps.org/doi/10.1103/PhysRevB.78.144401>.
- [141] J. J. Wortman and R. A. Evans. Young’s modulus, shear modulus, and poisson’s ratio in silicon and germanium. *Journal of Applied Physics*, 36(1) : 153, 1965. ISSN 00218979. doi : 10.1063/1.1713863. URL <http://link.aip.org/link/JAPIAU/v36/i1/p153/s1&Agg=doi>.
- [142] P. H. Dederichs. Diffuse scattering from defect clusters near bragg reflections. *Physical Review B*, 4(4) :1041, 1971. doi : 10.1103/PhysRevB.4.1041. URL <http://link.aps.org/doi/10.1103/PhysRevB.4.1041>.
- [143] Frank H. Stillinger and Thomas A. Weber. Computer simulation of local order in condensed phases of silicon. *Physical Review B*, 31(8) :5262, April 1985. doi : 10.1103/PhysRevB.31.5262. URL <http://link.aps.org/doi/10.1103/PhysRevB.31.5262>.
- [144] Kejian Ding and Hans C. Andersen. Molecular-dynamics simulation of amorphous germanium. *Physical Review B*, 34(10) :6987, November 1986. doi : 10.1103/PhysRevB.34.6987. URL <http://link.aps.org/doi/10.1103/PhysRevB.34.6987>.

- [145] H. Ohldag, V. Solinus, F. U. Hillebrecht, J. B. Goedkoop, M. Finazzi, F. Matsukura, and H. Ohno. Magnetic moment of mn in the ferromagnetic semiconductor (Ga<sub>0.98</sub>Mn<sub>0.02</sub>)As. *Applied Physics Letters*, 76(20) :2928, 2000. ISSN 00036951. doi : 10.1063/1.126519. URL <http://link.aip.org/link/APPLAB/v76/i20/p2928/s1&Agg=doi>.
- [146] S. Ueda, S. Imada, T. Muro, Y. Saitoh, S. Suga, F. Matsukura, and H. Ohno. Magnetic circular dichroism in mn 2p core absorption of Ga<sub>1-x</sub>Mn<sub>x</sub>As. *Physica E : Low-dimensional Systems and Nanostructures*, 10(1-3) :210–214, May 2001. ISSN 1386-9477. doi : 10.1016/S1386-9477(01)00084-4. URL <http://www.sciencedirect.com/science/article/B6VMT-433WBN6-1H/2/00785f071a196ec96a77bc77f2470117>.
- [147] Y. Ishiwata, M. Watanabe, R. Eguchi, T. Takeuchi, Y. Harada, A. Chainani, S. Shin, T. Hayashi, Y. Hashimoto, S. Katsumoto, and Y. Iye. Manganese concentration and low-temperature annealing dependence of Ga<sub>1-x</sub>Mn<sub>x</sub>As by x-ray absorption spectroscopy. *Physical Review B*, 65(23) :233201, May 2002. doi : 10.1103/PhysRevB.65.233201. URL <http://link.aps.org/doi/10.1103/PhysRevB.65.233201>.
- [148] Y. L. Soo, G. Kioseoglou, S. Kim, X. Chen, H. Luo, Y. H. Kao, H.-J. Lin, H. H. Hsieh, T. Y. Hou, C. T. Chen, Y. Sasaki, X. Liu, and J. K. Furdyna. Local environment surrounding ferromagnetically ordered mn in Mn/GaAs digital alloys and (Mn, Ga)As random alloys. *Physical Review B*, 67(21) : 214401, June 2003. doi : 10.1103/PhysRevB.67.214401. URL <http://link.aps.org/doi/10.1103/PhysRevB.67.214401>.
- [149] K. W. Edmonds, N. R. S. Farley, R. P. Campion, C. T. Foxon, B. L. Gallagher, T. K. Johal, G. van der Laan, M. MacKenzie, J. N. Chapman, and E. Arenholz. Surface effects in mn l<sub>3,2</sub> x-ray absorption spectra from (Ga,Mn)As. *Applied Physics Letters*, 84(20) :4065, 2004. ISSN 00036951. doi : 10.1063/1.1751619. URL <http://link.aip.org/link/APPLAB/v84/i20/p4065/s1&Agg=doi>.
- [150] P. Gambardella, L. Claude, S. Rusponi, K. J. Franke, H. Brune, J. Raabe, F. Nolting, P. Bencok, A. T. Hanbicki, B. T. Jonker, C. Grazioli, M. Veronese, and C. Carbone. Surface characterization of mn<sub>x</sub> ge<sub>1-x</sub> and cry mn<sub>x</sub> ge<sub>1-x-y</sub> dilute magnetic semiconductors. *Physical Review B*, 75(12) :

- 125211, March 2007. doi : 10.1103/PhysRevB.75.125211. URL <http://link.aps.org/doi/10.1103/PhysRevB.75.125211>.
- [151] S. Andrieu, E. Foy, H. Fischer, M. Alnot, F. Chevrier, G. Krill, and M. Piecuch. Effect of o contamination on magnetic properties of ultrathin mn films grown on (001) fe. *Physical Review B*, 58(13) :8210, October 1998. doi : 10.1103/PhysRevB.58.8210. URL <http://link.aps.org/abstract/PRB/v58/p8210>. Copyright (C) 2009 The American Physical Society ; Please report any problems to [prola@aps.org](mailto:prola@aps.org).
- [152] M. Morita, T. Ohmi, E. Hasegawa, M. Kawakami, and M. Ohwada. Growth of native oxide on a silicon surface. *Journal of Applied Physics*, 68(3) :1272, 1990. ISSN 00218979. doi : 10.1063/1.347181. URL <http://link.aip.org/link/JAPIAU/v68/i3/p1272/s1&Agg=doi>.
- [153] Cinthia Piamonteze, Piter Miedema, and Frank M. F. de Groot. Accuracy of the spin sum rule in XMCD for the transition-metal l edges from manganese to copper. *Physical Review B*, 80(18) :184410, November 2009. doi : 10.1103/PhysRevB.80.184410. URL <http://link.aps.org/doi/10.1103/PhysRevB.80.184410>.
- [154] E. Goering. X-ray magnetic circular dichroism sum rule correction for the light transition metals. *Philosophical Magazine*, 85(25) :2895, 2005. ISSN 1478-6435. doi : 10.1080/14786430500155221. URL <http://www.informaworld.com/10.1080/14786430500155221>.
- [155] S. Gold, A. Bayer, and E. Goering. Ground-State-Moment-Analysis : a quantitative tool for x-ray magnetic circular dichroism analysis for 3d transition metals. *Applied Physics A : Materials Science & Processing*, 78(6) :855–865, 2004. ISSN 0947-8396. doi : 10.1007/s00339-003-2442-8. URL <http://www.springerlink.com/gate4.inist.fr/content/bfg3pu8rumqdhmk/>.
- [156] K. H. J. Buschow. *Handbook of magnetic materials*. Gulf Professional Publishing, 2001. ISBN 9780444506665.
- [157] C. Hirai, H. Sato, A. Kimura, K. Yaji, K. Iori, M. Taniguchi, K. Hiraoka, T. Muro, and A. Tanaka. Mn 2p-3d soft x-ray magnetic circular dichroism study of Mn<sub>5</sub>Ge<sub>3</sub>. *Physica B : Condensed Matter*, 351(3-4) : 341–343, September 2004. ISSN 0921-4526. doi : 10.1016/j.physb.2004.06.

048. URL <http://www.sciencedirect.com.gate4.inist.fr/science/article/B6TVH-4CXDT6D-6/2/6364f286cb36d676252a3b044c2f5c6a>.
- [158] S. Ahlers, P. R. Stone, N. Sircar, E. Arenholz, O. D. Dubon, and D. Bougeard. Comparison of the magnetic properties of GeMn thin films through mn l-edge x-ray absorption. *Applied Physics Letters*, 95(15) :151911, 2009. ISSN 00036951. doi : 10.1063/1.3232245. URL <http://link.aip.org/link/APPLAB/v95/i15/p151911/s1&Agg=doi>.
- [159] K. W. Edmonds, G. van der Laan, A. A. Freeman, N. R. S. Farley, T. K. Johal, R. P. Champion, C. T. Foxon, B. L. Gallagher, and E. Arenholz. Angle-Dependent X-Ray magnetic circular dichroism from (Ga,Mn)As : anisotropy and identification of hybridized states. *Physical Review Letters*, 96(11) : 117207, March 2006. doi : 10.1103/PhysRevLett.96.117207. URL <http://link.aps.org/doi/10.1103/PhysRevLett.96.117207>.
- [160] Sumit Khanra, Karsten Kuepper, Thomas Weyhermüller, Manuel Prinz, Michael Raekers, Sebastian Voget, Andrei V. Postnikov, Frank M. F. de Groot, Simon J. George, Marin Coldea, Manfred Neumann, and Phalguni Chaudhuri. Star-Shaped molecule of MnII4O6 core with an  $s = 10$  High-Spin state. a theoretical and experimental study with XPS, XMCD, and other magnetic methods. *Inorganic Chemistry*, 47(11) :4605–4617, June 2008. doi : 10.1021/ic7023007. URL <http://dx.doi.org/10.1021/ic7023007>.
- [161] Yoshiki Teramura, Arata Tanaka, and Takeo Jo. Effect of coulomb interaction on the X-Ray magnetic circular dichroism spin sum rule in 3 d transition elements. *Journal of the Physical Society of Japan*, 65 : 1053–1055, 1996. ISSN 0031-9015. doi : 10.1143/JPSJ.65.1053. URL <http://jpsj.ipap.jp/link?JPSJ/65/1053/>.
- [162] W. Grange, M. Maret, J.-P. Kappler, J. Vogel, A. Fontaine, F. Petroff, G. Krill, A. Rogalev, J. Goulon, M. Finazzi, and N. B. Brookes. Magnetocrystalline anisotropy in (111) CoPt<sub>3</sub> thin films probed by x-ray magnetic circular dichroism. *Physical Review B*, 58(10) :6298, 1998. doi : 10.1103/PhysRevB.58.6298. URL <http://link.aps.org/doi/10.1103/PhysRevB.58.6298>.
- [163] Ruqian Wu and A. J. Freeman. Limitation of the Magnetic-Circular-Dichroism spin sum rule for transition metals and importance of the magnetic dipole term. *Physical Review Letters*, 73(14) :1994, October 1994.

- doi : 10.1103/PhysRevLett.73.1994. URL <http://link.aps.org/doi/10.1103/PhysRevLett.73.1994>.
- [164] D. Wu, D. J. Keavney, Ruqian Wu, E. Johnston-Halperin, D. D. Awschalom, and Jing Shi. Concentration-independent local ferromagnetic mn configuration in gal-x mnx as. *Physical Review B*, 71(15) :153310, April 2005. doi : 10.1103/PhysRevB.71.153310. URL <http://link.aps.org/doi/10.1103/PhysRevB.71.153310>.
- [165] B. Gilbert, B. H. Frazer, A. Belz, P. G. Conrad, K. H. Neelson, D. Haskell, J. C. Lang, G. Srajer, and G. De Stasio. Multiple scattering calculations of bonding and x-ray absorption spectroscopy of manganese oxides. *The Journal of Physical Chemistry A*, 107(16) :2839–2847, April 2003. doi : 10.1021/jp021493s. URL <http://dx.doi.org/10.1021/jp021493s>.
- [166] Y. Joly. X-ray absorption near-edge structure calculations beyond the muffin-tin approximation. *Physical Review B*, 63(12) :125120, March 2001. doi : 10.1103/PhysRevB.63.125120. URL <http://link.aps.org/doi/10.1103/PhysRevB.63.125120>.
- [167] H Ebert. The munich SPR-KKR package, version 5.4, . URL <http://olymp.cup.uni-muenchen.de/ak/ebert/SPRKKR>.
- [168] H Ebert. *Fully relativistic band structure calculations for magnetic solids – Formalism and Application, in Electronic Structure and Physical Properties of Solids*,, volume 535 of *Lecture Notes in Physics*. H. Dreyssé, Berlin, springer edition, .
- [169] G. Kappel, G. Fischer, and A. Jaegle. On the saturation magnetization of mn<sub>5</sub> ge<sub>3</sub>. *Physics Letters A*, 45(3) :267–268, September 1973. ISSN 0375-9601. doi : 10.1016/0375-9601(73)90199-0. URL <http://www.sciencedirect.com.gate4.inist.fr/science/article/B6TVM-46S5J3F-2TW/2/dc87387f2080cf7faa2a5c7be7d7f461>.
- [170] J B Forsyth and P J Brown. The spatial distribution of magnetisation density in Mn<sub>5</sub>Ge<sub>3</sub>. *Journal of Physics : Condensed Matter*, 2(11) :2713–2720, March 1990. doi : 10.1088/0953-8984/2/11/014. URL [/cgi-bin/sciserv.pl?collection=iop&journal=09538984&issue=v02i0011&article=2713\\_tsdmdim](http://cgi-bin/sciserv.pl?collection=iop&journal=09538984&issue=v02i0011&article=2713_tsdmdim).

- [171] S. Picozzi, A. Continenza, and A. J. Freeman. First-principles characterization of ferromagnetic  $\text{Mn}_{0.5}\text{Ge}_{0.3}$  for spintronic applications. *Physical Review B*, 70(23) :235205, December 2004. doi : 10.1103/PhysRevB.70.235205. URL <http://link.aps.org/doi/10.1103/PhysRevB.70.235205>.
- [172] M. O. Krause and J. H. Oliver. Natural widths of atomic k and l levels, ka x-ray lines and several KLL auger lines. *Journal of Physical and Chemical Reference Data*, 8(2) :329, 1979. ISSN 00472689. doi : 10.1063/1.555595. URL <http://link.aip.org/link/JPCRBV/v8/i2/p329/s1&Agg=doi>.
- [173] G. Vaitheeswaran, V. Kanchana, M. Alouani, and A. Delin. Ab initio calculated x-ray magnetic circular dichroism of  $\text{Sr}_2\text{CrReO}_6$ . *EPL*, 84(4) :4, 2008. doi : 10.1209/0295-5075/84/47005.
- [174] K. Miyamoto, K. Iori, A. Kimura, T. Xie, M. Taniguchi, S. Qiao, and K. Tsuchiya. Soft x-ray magnetic circular dichroism of heusler-type alloy  $\text{Co}_2\text{MnGe}$ . *Solid State Communications*, 128(5) :163–166, October 2003. ISSN 0038-1098. doi : 10.1016/j.ssc.2003.08.007. URL <http://www.sciencedirect.com.gate4.inist.fr/science/article/B6TVW-499F0B3-5/2/ced551664253d965dcd3d406902c0e39>.
- [175] I. Slipukhina, E. Arras, Ph. Mavropoulos, and P. Pochet. Simulation of the enhanced curie temperature in  $\text{Mn}_{0.5}\text{Ge}_{0.3}\text{C}_x$  compounds. *Applied Physics Letters*, 94(19) :192505–3, May 2009. doi : 10.1063/1.3134482. URL <http://link.aip.org/link/?APL/94/192505/1>.
- [176] A. Stroppa, S. Picozzi, A. Continenza, and A. J. Freeman. Electronic structure and ferromagnetism of mn-doped group-IV semiconductors. *Physical Review B*, 68(15) :155203, October 2003. doi : 10.1103/PhysRevB.68.155203. URL <http://link.aps.org/doi/10.1103/PhysRevB.68.155203>.
- [177] L. Ottaviano, M. Passacantando, S. Picozzi, A. Continenza, R. Gunnella, A. Verna, G. Bihlmayer, G. Impellizzeri, and F. Priolo. Phase separation and dilution in implanted  $\text{Mn}_x\text{Ge}_{1-x}$  alloys. *Applied Physics Letters*, 88(6) :061907, 2006. ISSN 00036951. doi : 10.1063/1.2171485. URL <http://link.aip.org/link/APPLAB/v88/i6/p061907/s1&Agg=doi>.
- [178] Andrey Titov. *Propriétés électroniques des semiconducteurs magnétiques dilués :  $\text{Ga}_{1-x}\text{Mn}_x\text{N}$ ,  $\text{Ga}_{1-x}\text{Mn}_x\text{As}$ ,  $\text{Ge}_{1-x}\text{Mn}_x$* . PhD thesis, Université Joseph Fourier Grenoble I, Grenoble, December

2006. URL [http://tel.archives-ouvertes.fr/index.php?halsid=o1lvucqdbcokateeeecs4o1aar1&view\\_this\\_doc=tel-00113864&version=1](http://tel.archives-ouvertes.fr/index.php?halsid=o1lvucqdbcokateeeecs4o1aar1&view_this_doc=tel-00113864&version=1).
- [179] T. Dietl, A. Haury, and Y. Merle d'Aubigné. Free carrier-induced ferromagnetism in structures of diluted magnetic semiconductors. *Physical Review B*, 55(6) :R3347, February 1997. doi : 10.1103/PhysRevB.55.R3347. URL <http://link.aps.org/doi/10.1103/PhysRevB.55.R3347>.
- [180] Michael J. Regan, Marybeth Rice, Marcela B. Fernandez van Raap, and Arthur Bienenstock. Anisotropic phase separation through the Metal-Insulator transition in amorphous alloys. *Physical Review Letters*, 73(8) :1118, 1994. doi : 10.1103/PhysRevLett.73.1118. URL <http://link.aps.org/doi/10.1103/PhysRevLett.73.1118>.
- [181] John P. Perdew, Kieron Burke, and Matthias Ernzerhof. Generalized gradient approximation made simple. *Physical Review Letters*, 77(18) :3865, October 1996. doi : 10.1103/PhysRevLett.77.3865. URL <http://link.aps.org/doi/10.1103/PhysRevLett.77.3865>.
- [182] Ing-Song Yu. *Etude des propriétés des magnéto-transport de (Ge,Mn) semiconducteur ferromagnétique sur GaAs(001) pour l'électronique de spin*. PhD thesis, Université Joseph Fourier Grenoble I, Grenoble, July 2010. URL [http://tel.archives-ouvertes.fr/index.php?halsid=cej9neh81ngk9fe16i9k86heb2&view\\_this\\_doc=tel-00526338&version=1](http://tel.archives-ouvertes.fr/index.php?halsid=cej9neh81ngk9fe16i9k86heb2&view_this_doc=tel-00526338&version=1).
- [183] I.-S. Yu, M. Jamet, T. Devillers, A. Barski, P. Bayle-Guillemaud, C. Beigné, J. Rothman, V. Baltz, and J. Cibert. Spinodal decomposition to control magnetotransport in (Ge,Mn) films. *Physical Review B*, 82(3) :035308, July 2010. doi : 10.1103/PhysRevB.82.035308. URL <http://link.aps.org/doi/10.1103/PhysRevB.82.035308>.
- [184] D. H. Tomboulion and P. L. Hartman. Spectral and angular distribution of ultraviolet radiation from the 300-Mev cornell synchrotron. *Physical Review*, 102(6) :1423, June 1956. doi : 10.1103/PhysRev.102.1423. URL <http://link.aps.org/doi/10.1103/PhysRev.102.1423>.
- [185] A. Cavalleri, M. Rini, H. H. W. Chong, S. Fourmaux, T. E. Glover, P. A. Heilmann, J. C. Kieffer, and R. W. Schoenlein. Band-Selective measurements of

- electron dynamics in VO<sub>2</sub> using femtosecond Near-Edge X-Ray absorption. *Physical Review Letters*, 95(6) :067405, 2005. doi : 10.1103/PhysRevLett.95.067405. URL <http://link.aps.org/doi/10.1103/PhysRevLett.95.067405>.
- [186] S. Khan, K. Holldack, T. Kachel, R. Mitzner, and T. Quast. Femtosecond undulator radiation from sliced electron bunches. *Physical Review Letters*, 97(7) :074801, 2006. doi : 10.1103/PhysRevLett.97.074801. URL <http://link.aps.org/doi/10.1103/PhysRevLett.97.074801>.
- [187] ESRF layout. URL <http://www.esrf.eu/UsersAndScience/Experiments/Beamlines>.





## Résumé

Le système des nanocolonnes auto-assemblées de GeMn, riches en Mn et entourées d'une matrice de germanium quasi pure, est un matériau prometteur pour la spintronique. Selon les paramètres de croissance, les échantillons contiennent des nanocolonnes de type cohérents sur la matrice de Ge, de type amorphe, ou/et des nanoinclusions de  $\text{Ge}_3\text{Mn}_5$ . Ce manuscrit présente notre étude des propriétés électroniques, magnétiques et structurales des nanocolonnes de GeMn à l'aide du rayonnement synchrotron. Les mesures de la diffusion et diffraction des rayons X en incidence rasante dans des échantillons contenant des nanocolonnes cohérentes et sans précipités de  $\text{Ge}_3\text{Mn}_5$  montrent un certain désordre dans les nanocolonnes. Les cartographies de l'espace réciproque ont pu être quantitativement expliquées en considérant la déformation de la matrice de germanium due à l'inclusion des nanocolonnes dans celle-ci, ainsi que par leurs corrélations de position, sans avoir recours à d'autres phases cristallines. La spectroscopie d'absorption et le dichroïsme circulaire magnétique de rayons X ont permis de sonder spécifiquement les propriétés magnétiques des atomes de Mn dans des échantillons sans précipités de  $\text{Ge}_3\text{Mn}_5$ . On observe une allure des spectres XAS-XMCD des nanocolonnes très similaire à celle observée dans le cas de  $\text{Ge}_3\text{Mn}_5$ . Le moment magnétique local sur le manganèse possède une composante orbitale faible mais non-nulle et une amplitude totale ( $0.8 \pm 0.1 \mu_B$ ) plus faible que celle attendue pour  $\text{Ge}_3\text{Mn}_5$  ( $\sim 2.6 \mu_B$ ) ou pour des atomes de Mn substitutionnels ( $\sim 3 \mu_B$ ). Ceci indique une origine différente de la phase des nanocolonnes. Les spectres XAS-XMCD ont été calculés pour différentes structures modèles, incluant des défauts simples ainsi de nouvelles phases cristallines, les paramètres critiques des calculs ayant été identifiés. Le meilleur accord est observé pour une nouvelle phase de type  $\text{Ge}_2\text{Mn}$ .

## Abstract

The system of self-assembled Mn-rich GeMn nanocolumns embedded in a Mn-poor germanium matrix is a promising material for spintronics applications. Depending on the growth parameters, coherent GeMn nanocolumns, amorphous GeMn nanocolumns and/or  $\text{Ge}_3\text{Mn}_5$  nanoclusters can be observed. In this manuscript, we report on the investigation on the electronic, magnetic and structural properties of the GeMn nanocolumns using synchrotron techniques. Measurements using grazing incidence x-ray scattering techniques in samples containing coherent nanocolumns, free from  $\text{Ge}_3\text{Mn}_5$  precipitates, show some disorder in the nanocolumns. Reciprocal space maps are quantitatively explained by considering the scattering of the Ge matrix strained by the inclusion of the nanocolumns in the matrix and their correlations in position, without requiring the consideration of different additional phases. X-ray absorption spectroscopy and x-ray magnetic circular dichroism allow for the specific probing of the Mn magnetic properties in samples free of  $\text{Ge}_3\text{Mn}_5$  clusters. The lineshapes of the XAS-XMCD spectra in the nanocolumns are found to be very similar to those in  $\text{Ge}_3\text{Mn}_5$ . The local magnetic moment on the Mn atom possess a small but non-zero orbital component and its total magnitude is much smaller ( $0.8 \pm 0.1 \mu_B$ ) than that in  $\text{Ge}_3\text{Mn}_5$  ( $\sim 2.6 \mu_B$ ) or than that expected for fully substitutional Mn atoms ( $\sim 3 \mu_B$ ). This points to a different nature of the nanocolumns. The XAS-XMCD spectra have been calculated for several structural models, including simple defects and new crystalline phases, and critical parameters for the calculations have been identified. The best agreement is found for a new  $\text{Ge}_2\text{Mn}$  crystalline phase.